

Ministry of Education and Science of the Russian Federation
Saint Petersburg National Research University of Information
Technologies, Mechanics, and Optics

NANOSYSTEMS:
PHYSICS, CHEMISTRY, MATHEMATICS

2021, volume 12(5)

Наносистемы: физика, химия, математика

2021, том 12, № 5



NANOSYSTEMS:

PHYSICS, CHEMISTRY, MATHEMATICS

ADVISORY BOARD MEMBERS

Chairman: V.N. Vasiliev (*St. Petersburg, Russia*),
V.M. Buznik (*Moscow, Russia*); V.M. Ievlev (*Voronezh, Russia*), P.S. Kop'ev (*St. Petersburg, Russia*), N.F. Morozov (*St. Petersburg, Russia*), V.N. Parmon (*Novosibirsk, Russia*),
A.I. Rusanov (*St. Petersburg, Russia*),

EDITORIAL BOARD

Editor-in-Chief: I.Yu. Popov (*St. Petersburg, Russia*)

Section Co-Editors:

Physics – V.M. Uzdin (*St. Petersburg, Russia*),
Material science – V.V. Gusarov (*St. Petersburg, Russia*),
Chemistry – V.K. Ivanov (*Moscow, Russia*),
Mathematics – I.Yu. Popov (*St. Petersburg, Russia*).

Editorial Board Members:

V.M. Adamyan (*Odessa, Ukraine*); O.V. Al'myasheva (*St. Petersburg, Russia*);
A.P. Alodjants (*Vladimir, Russia*); S. Bechta (*Stockholm, Sweden*); J. Behrndt (*Graz, Austria*);
M.B. Belonenko (*Volgograd, Russia*); A. Chatterjee (*Hyderabad, India*); A.V. Chizhov
(*Dubna, Russia*); A.N. Enyashin (*Ekaterinburg, Russia*), P.P. Fedorov (*Moscow, Russia*);
E.A. Gudilin (*Moscow, Russia*); H. Jónsson (*Reykjavik, Iceland*); A.A. Kiselev (*Durham, USA*);
Yu.S. Kivshar (*Canberra, Australia*); S.A. Kozlov (*St. Petersburg, Russia*);
P.A. Kurasov (*Stockholm, Sweden*); A.V. Lukashin (*Moscow, Russia*); I.V. Melikhov
(*Moscow, Russia*); G.P. Miroshnichenko (*St. Petersburg, Russia*); I.Ya. Mittova (*Voronezh, Russia*);
Nguyen Anh Tien (*Ho Chi Minh, Vietnam*); V.V. Pankov (*Minsk, Belarus*);
K. Pankrashkin (*Orsay, France*); A.V. Ragulya (*Kiev, Ukraine*); V. Rajendran (*Tamil Nadu, India*);
A.A. Rempel (*Ekaterinburg, Russia*); V.Ya. Rudyak (*Novosibirsk, Russia*);
D Shoikhet (*Karmiel, Israel*); P Stovicek (*Prague, Czech Republic*); V.M. Talanov
(*Novocherkassk, Russia*); A.Ya. Vul' (*St. Petersburg, Russia*); A.V. Yakimansky
(*St. Petersburg, Russia*), V.A. Zagrebnov (*Marseille, France*).

Editors:

I.V. Blinova; A.I. Popov; A.I. Trifanov; E.S. Trifanova (*St. Petersburg, Russia*),
R. Simoneaux (*Philadelphia, Pennsylvania, USA*).

Address: ITMO University, Kronverkskiy pr., 49, St. Petersburg 197101, Russia.

Phone: +7(812)607-02-54, **Journal site:** <http://nanojournal.ifmo.ru/>,

E-mail: nanojournal.ifmo@gmail.com

AIM AND SCOPE

The scope of the journal includes all areas of nano-sciences. Papers devoted to basic problems of physics, chemistry, material science and mathematics inspired by nanosystems investigations are welcomed. Both theoretical and experimental works concerning the properties and behavior of nanosystems, problems of its creation and application, mathematical methods of nanosystem studies are considered.

The journal publishes scientific reviews (up to 30 journal pages), research papers (up to 15 pages) and letters (up to 5 pages). All manuscripts are peer-reviewed. Authors are informed about the referee opinion and the Editorial decision.

CONTENT

MATHEMATICS

- A.S. Bagmutov
Bound states for Laplacian perturbed by varying potential supported by line in \mathbb{R}^3 549
- E.G. Fedorov
Properties of an oriented ring of neurons with the FitzHugh-Nagumo model 553

PHYSICS

- N.M. Khatamov
Holliday junctions in the HC Blume-Capel model in "one case" on DNA 563
- J. Gulomov, R. Aliev
Numerical analysis of the effect of illumination intensity on photoelectric parameters of the silicon solar cell with various metal nanoparticles 569
- H.A. Zain, M. Batumalay, H.R.A. Rahim, Z. Harith, M. Yasin, S.W Harun
Surface plasmon resonance optical sensor for COVID-19 detection 575
- Ratna Chakrabarty, Nirranjan Kumar Mandal
Realization of combinational logic circuits using standard functions in quantum dot cellular automata 583
- M.A. Baranov, E.N. Velichko, E.K. Nepomnyashchaya, I.V. Pleshakov
Energy relaxation in molecular systems containing salt ions 598
- I.A. Nesterenko, I.Y. Popov
Modeling the evolution of surface nanobubbles 603

CHEMISTRY AND MATERIAL SCIENCE

- B. Khoshbayan, A. Morsali, M.R. Bozorgmehr, S.A. Beyramabadi
Structural and energetic analysis of cyclic peptide-gold nano-drug delivery system: a DFT study 612
- A.A. Krasilin
The influence of edge specific surface energy on the direction of hydrosilicate layers scrolling 623

M.V. Kaneva, V.P. Tolstoy The "rolling up" effect of platinum layer obtained on nickel surface by interaction with solution of H_2PtCl_6 and its electrocatalytic properties in hydrogen evolution reaction during water electrolysis in alkaline medium	630
K.D. Martinson, V.I. Popkov Two-step combustion synthesis of nanocrystalline $Zn_{1-x}Mn_xFe_2O_4$ ($0 \leq x \leq 1$) spinel ferrites with linear tuning of magnetic parameters	634
Yu.A. Avdeeva, I.V. Luzhkova, A.N. Ermakov Formation of titanium-cobalt nitride $Ti_{0.7}Co_{0.3}N$ under plasma-chemical synthesis conditions in a low-temperature nitrogen plasma	641
Information for authors	650

Bound states for Laplacian perturbed by varying potential supported by line in \mathbb{R}^3

A. S. Bagmutov

ITMO University, Kronverkskiy, 49, Saint Petersburg, 197101, Russia

bagmutov94@mail.ru

DOI 10.17586/2220-8054-2021-12-5-549-552

We investigate a system with attracting δ -potential located along a straight line in 3D. It has constant intensity, except for a local region. We prove the existence of discrete spectrum and construct an upper bound on the number of bound states, using Birman-Schwinger method.

Keywords: operator extension theory, singular potential, spectrum.

Received: 17 July 2021

Revised: 10 October 2021

1. Introduction

The system under investigation is an example of an extensively studied class of models. It can be described as Schrodinger operator in 3D, with singular δ -interactions, supported on a set of zero measure, with codimension two, and often referred to as leaky quantum wires. These models, composed of δ -interaction, concentrated on one-dimensional manifolds, are meant to approximate the behaviour of such physical systems, as quantum wires. The operator can be formally written as $-\Delta - \alpha\delta(x - \gamma)$, where the γ represents the curve of the wire. A prominent feature of the model is the potential for tunnelling between different parts of the wire, which reflects the behaviour of modelled systems. A region outside of the curve is classically-forbidden, therefore, for bound states, the probability of finding a particle far from the wire declines exponentially and all energies of bound states are negative. An overview of different graph model types, their comparison and some results can be found in [16].

One of the important characteristics of leaky wire systems is the existence and number of bound states, which correspond to localized states of particles. For the investigation of operator spectrum, we use a well-established method, which includes the description of the operator resolvent through a Krein-like formula, which represents the effect of a wire, as a perturbation. This allows the usage of the relevant perturbation theorems. The first appearance of the method, applied to leaky wires model, was in the works [17, 18], where the straight line in 3D was considered, and Krein type resolvent formula was used. For a general description of the method dealing with singular interactions, see [2], or for curves in \mathbb{R}^3 - more recent work [6]. The Krein-like formula was fully described in [3]. There are a number of works, which use this procedure for different types of curves [8, 10–12, 19, 20]. Existing results also include works considering the case of \mathbb{R}^2 and codimension one [1, 4, 5] on bent curves or loops [7, 9], as well as finite curves and different types of interaction along the curve [13–15]. A model of line-like window in the domain boundary was suggested in [22–25]. It can be considered as a generalization of potential supported by line. For investigation of our system, we will mostly follow the progression of the paper [10].

The system studied in the present paper consists of a straight line in \mathbb{R}^3 , with an attractive δ potential, generally of constant intensity, except for a finite region, where it is varied.

The paper organized as follows: in section 2 we describe an operator and write a resolvent formula. In section 3 we prove the existence of at least one bound state. In section 4 we construct a Birman-Schwinger operator, and show a method for calculating an upper bound on the number of discrete spectrum points.

2. Hamiltonian construction

Let us describe a system. An attractive delta potential is located along a straight line in \mathbb{R}^3 . The intensity is equal to $-(\alpha + \beta(s))$, where $\alpha > 0$ is a constant, and $0 \leq \beta(s) \in C(a, b) \setminus \{0\}$ – is a localized function of the distance s along the line, which equals to zero outside of arbitrary finite region $[a, b]$. We choose the 0 point on the line, so that $\beta(0) \neq 0$. Note, that the space for β potentially could be expanded.

First, following [10], we describe an operator $-\Delta_{\alpha, \beta}$, which is a self-adjoint extension of the symmetric operator $-\Delta : C_0^\infty(\mathbb{R}^3 \setminus \Gamma) \rightarrow L^2(\mathbb{R}^3)$, and then we construct its resolvent. Consider a straight line Γ , defined by a function $\gamma(s) = (0, 0, s) : \mathbb{R} \rightarrow \mathbb{R}^3$. Let's introduce the shifted curve Γ_r , which corresponds to $\gamma_r(s) = (\xi, \eta, s); (\xi^2 + \eta^2)^{1/2} = r$. Let $f \in H_{\text{loc}}^2(\mathbb{R}^3 \setminus \Gamma)$, and $f_{\Gamma_r}(s)$, its embedding in $\Gamma_r; r > 0$.

Definition 2.1. A function $f \in H_{\text{loc}}^2(\mathbb{R}^3 \setminus \Gamma) \cap L^2(\mathbb{R}^3)$ belongs to $D(-\Delta_{\alpha,\beta})$ if the following conditions are satisfied:
1) The limits

$$\begin{aligned}\Xi(f)(s) &= -\lim_{r \rightarrow 0} \frac{1}{\ln r} f_{\Gamma_r}(s), \\ \Upsilon(f)(s) &= -\lim_{r \rightarrow 0} (f_{\Gamma_r}(s) + \Xi(f)(s) \ln r),\end{aligned}$$

exist a.e. in \mathbb{R} , are independent of the direction $\frac{1}{r}(\xi, \eta)$, and define functions from $L^2(\mathbb{R})$,

2) The condition takes place:

$$2\pi(\alpha + \beta(s))\Xi(f)(s) = \Upsilon(f)(s).$$

Finally we define operator $-\Delta_{\alpha,\beta} : D(-\Delta_{\alpha,\beta}) \rightarrow L^2(\mathbb{R}^3)$ which acts as

$$-\Delta_{\alpha,\beta} f(x) = -\Delta f(x), \quad x \in \mathbb{R}^3 \setminus \Gamma.$$

For description of the $\sigma(-\Delta_{\alpha,\beta})$ will be useful the following statement from [1]:

Remark 2.2. A system with one point interaction in \mathbb{R}^2 , has the following spectrum with a single discrete point:

$$\begin{aligned}\sigma_{\text{ess}} &= [0, \infty), \\ \sigma_{\text{disc}} &= \{\xi_{1,\alpha}\}, \\ \xi_{1,\alpha} &= -4e^{2(-2\pi\alpha + \psi(1))},\end{aligned}$$

where $\psi(x) = \Gamma'(x)/\Gamma(x)$, $\Gamma(x)$ is the Euler Gamma-function, $-\psi(1) \approx 0.5772$ is Euler's number.

Now we will construct a resolvent of $-\Delta_{\alpha,\beta}$. The free resolvent is $R_z = (-\Delta - z)^{-1} : L^2(\mathbb{R}^3) \rightarrow H^2(\mathbb{R}^3)$, z is in resolvent set $z \in \rho(-\Delta)$.

We define the bounded trace map operator of the line:

$$(\tau\phi)(s) = \phi(s, 0, 0) : H^2(\mathbb{R}^3) \rightarrow L^2(\mathbb{R}).$$

Its adjoint $\tau^* : L^2(\mathbb{R}) \rightarrow H^{-2}(\mathbb{R}^3)$ is determined by

$$\langle \tau^* h, \omega \rangle = (h, \tau\omega), \quad h \in L^2(\mathbb{R}), \omega \in H^{-2}(\mathbb{R}^3),$$

where $\langle \cdot, \cdot \rangle$ stands for duality between $H^{-2}(\mathbb{R}^3)$ and $H^2(\mathbb{R}^3)$.

Lets introduce a self-adjoint operator

$$\begin{aligned}T_\kappa f(s) &= \int_{\mathbb{R}} (\tilde{T}_\kappa(s-s') + \frac{1}{2\pi}(\ln 2 + \psi)) f(s') ds' = F^{-1} \left[\frac{1}{2\pi} (-\ln [(p^2 + \kappa^2)^{0.5}] + (\ln 2 + \psi)\delta(p)) \hat{f}(p) \right], \\ \tilde{T}_\kappa(s-s') &= -\frac{1}{(2\pi)^2} \int_{\mathbb{R}} \ln [(p^2 + \kappa^2)^{0.5}] e^{ip(s-s')} dp,\end{aligned}$$

with the domain $D(T_\kappa) = f \in L^2(\mathbb{R}) : \int_{\mathbb{R}} \tilde{T}_\kappa(s-s') f(s') ds' \in L^2(\mathbb{R})$, where $-\psi \approx 0.577$ is Euler's number and $Ff = \hat{f}$ is a Fourier transform.

Finally, we define self-adjoint operator

$$Q^\kappa f(s) = (T_\kappa - \beta(s))f(s) : D(T_\kappa) \rightarrow L^2(\mathbb{R}).$$

Now we can construct a resolvent of the main operator, following theorems from [10]:

$$R_{\beta,\alpha}^\kappa = R^\kappa - R^{\kappa*} \tau^* (Q^\kappa - \alpha) \tau R^\kappa. \quad (1)$$

3. Existence of bound states

Let us denote as $\beta_0 > 0$ and $\beta_w > 0$, any two small enough numbers, so that $\beta(x) > \beta_0; \forall |x| < \beta_w/2$, and $\sup \beta(s) = \beta_s$.

First, lets notice that $\beta(s)$, being a local perturbation of a potential, does not change essential spectrum of the main operator:

$$\sigma_{\text{ess}}(-\Delta_{\alpha,\beta}) = \sigma_{\text{ess}}(-\Delta_\alpha) = [\xi_{1,\alpha}, \infty) = [-4e^{2(-2\pi\alpha + \psi)}, \infty).$$

Using the momentum representation of T_κ and locality of $\beta(s)$, we can get

$$\begin{aligned}\sigma_{\text{ess}}(T_\kappa) &= \sigma_{\text{ess}}(Q^\kappa) = (-\infty, s_\kappa], \\ s_\kappa &= \frac{1}{2\pi} \left(\psi(1) - \ln \frac{\kappa}{2} \right).\end{aligned}$$

Note that $s_\kappa = \alpha$ corresponds to $-\kappa^2 = \xi_{1,\alpha}$ of the main operator.

Lemma 3.1. $\sup \sigma(Q^\kappa) = \sup \sigma(T_\kappa - \beta(s)) > s_\kappa$.

Proof. The lemma is equivalent to

$$(Q^\kappa \phi, \phi) - s_\kappa(\phi, \phi) > 0,$$

for any $\phi \in D(Q^\kappa)$. Let $\phi \in C_0^\infty(\mathbb{R})$, such that $\exists C > 0, \delta > 0 : \phi(s) > C, |s| < \delta$ and we will use $\phi_\lambda(s) = \lambda^{0.5} \phi(\lambda s); \lambda > 0$, notice, still $\phi(\lambda s) > C, |s| < \delta$, and $\|\phi_\lambda\| = \|\phi\|$. We get

$$\frac{1}{2\pi} \int_{\mathbb{R}} \ln \left[\left(1 + \frac{\lambda^2 u^2}{\kappa} \right)^{0.5} \right] |F\phi(u)|^2 du + \lambda \int_{\mathbb{R}} \beta(s) |\phi(\lambda s)|^2 ds > 0,$$

where the first term can be expanded as $-\frac{1}{4\pi} \left(\frac{\lambda}{\kappa} \right)^2 \int_{\mathbb{R}} u^2 |F\phi(u)|^2 du + \mathcal{O}(\lambda^4)$, and the second one:

$\lambda \int_{\mathbb{R}} \beta(s) |\phi(\lambda s)|^2 ds > \lambda \int_{-\delta}^{\delta} \beta(s) C^2 ds > 2\delta C \beta_0 \beta_w$. So for the λ small enough, the second term sways the sum in the positive direction. \square

Lemma 3.2. The function $\kappa \rightarrow Q^\kappa$ is continuous in the norm operator sense on (κ_0, ∞) , and

$$\lim_{\kappa \rightarrow \infty} \sup \sigma(Q^\kappa) = -\infty. \tag{2}$$

Proof. Function, $\kappa \rightarrow T_\kappa$ is continuous in the norm-operator sense:

$$\|(T_\kappa - T_{\kappa'})f\| = \frac{1}{4(2\pi)^3} \int_{\mathbb{R}} \left(\ln \frac{p^2 + \kappa^2}{p^2 + \kappa'^2} \right)^2 |Ff(p)|^2 dp \leq \frac{1}{4(2\pi)^3} \left(\ln \frac{\kappa}{\kappa'} \right)^2 \|f\|^2 \xrightarrow{\kappa' \rightarrow \kappa} 0$$

and $\beta(s)$ is independent of κ , so $Q^\kappa = T_\kappa - \beta(s)$ is continuous. Limit (2) follows from:

$$\begin{aligned} (Q^\kappa f, f) &= \frac{1}{(2\pi)^{3/2}} \int_{\mathbb{R}} \left(-\ln \sqrt{p^2 + \kappa^2} + \ln 2 + \psi(1) \right) |\hat{f}(p)|^2 dp + (\beta(s)f, f) \leq \\ &\leq \frac{1}{(2\pi)^{3/2}} \left(-\ln \frac{\kappa}{2} + \psi(1) \right) \|f\|^2 + \beta_s * \|f\|^2. \end{aligned}$$

\square

Now, analogous to theorem 5.6 of [10], we are ready to prove the existence of at least one bound state.

Theorem 3.1. The operator $-\Delta_{\alpha,\beta}$ has at least one isolated eigenvalue in $(-\infty, \xi_{1,\alpha})$.

Proof. The addition of localized potential $\beta(s)$ can alter only discrete part of a spectrum, i. e. for the main operator - the part that lies in $(-\infty, \xi_{1,\alpha})$ and for Q^κ , it lies in (s_κ, ∞) . Then by Lemma 3.1, there exists at least one discrete point of spectrum for $Q^\kappa, \lambda(\kappa)$. By Lemma 3.2, $\lambda(\kappa)$ is continuous and $\lambda \rightarrow -\infty$ as $\kappa \rightarrow \infty$. Therefore $\exists \kappa' > |\xi_{1,\alpha}|^{0.5} : \lambda(\kappa') = \alpha$. The point $-\kappa'^2$ is a pole of resolvent (1), and therefore is an eigenvalue of the main operator. \square

4. Upper bound on number of bound states

Now we can utilize the Birman-Schwinger method (see [21]) to get an upper bound on the number of bound states for the main operator.

Let's construct a Birman-Schwinger operator, which we will use to count eigenvalues.

$$\begin{aligned} Q^\kappa f - \alpha f &= 0, \\ T_\kappa f - \alpha f - \beta(s)f &= 0, \\ K_\kappa f \equiv (T_\kappa - \alpha)^{-1} (\beta(s)f) &= f. \end{aligned} \tag{3}$$

Here, if f is an eigenvector of Q^κ , corresponding to the eigenvalue $\lambda_Q = \alpha$, then it is an eigenvector of K_κ , corresponding to the eigenvalue $\lambda_K = 1$. Also, note that eigenvalues of Q^κ are monotonically decreasing as functions of κ , and so are eigenvalues of K_κ , therefore, if we fix κ , for each discrete point of spectrum of the main operator $-\Delta_{\alpha,\beta}$, there is a corresponding eigenvalue of Q^κ , bigger then α , and corresponding eigenvalue of K_κ , bigger then 1. Summing up all these eigenvalues of K_κ , we get an upper bound on the number of eigenvalues $\lambda(Q^\kappa) > \alpha$ and number of discrete points of $-\Delta_{\alpha,\beta}$, smaller then $-\kappa^2$. To cover all $\sigma_{disc}(-\Delta_{\alpha,\beta})$, we approach the $\sigma_{ess}(-\Delta_{\alpha,\beta})$ threshold and get the final bound:

Proposition 4.1. The number of points in $\sigma_{disc}(-\Delta_{\alpha,\beta})$, has the following upper bound

$$\#\sigma_{disc}(-\Delta_{\alpha,\beta}) \leq \lim_{-\kappa^2 \uparrow \xi_{1,\alpha}} \int_{\mathbb{R}^2} \left(\int \frac{e^{2\pi i(s-p)w}}{-\ln \sqrt{w^2 + \kappa^2} + (-\ln \frac{\kappa}{2} + \psi(1) - \alpha)\delta(w)} dw \beta(p) \right)^2 ds ds'.$$

Acknowledgements

The reported study was funded by RFBR, project number 20-31-90050.

References

- [1] Albeverio S., Gesztesy F., Høegh-Krohn R., Holden H. *Solvable Models in Quantum Mechanics*, Springer, Heidelberg, 1988.
- [2] Brasche J., Exner P., Kuperin Yu.A., Seba P. Schrödinger operator with singular interactions. *J. Math. Anal. Appl.*, 1994, **184**, P. 112–139.
- [3] Posilicano A. A Krein-like formula for singular perturbations of self-adjoint operators and applications. *J. Funct. Anal.*, 2001, **183**, P. 109–147.
- [4] Shondin Yu. On the semiboundedness of delta-perturbations of the Laplacian on curves with angular points. *Theor. Math. Phys.*, 1995, **105**, P. 1189–1200.
- [5] Behrndt J., Langer M. Boundary value problems for elliptic partial differential operators on bounded domains. *J. Funct. Anal.*, 2007, **243**, P. 536–565.
- [6] Behrndt J., Frank R.L., Kuhn Ch., Lotoreichik V., Rohleder J. Spectral theory for Schroedinger operators with δ -interactions supported on curves in \mathbb{R}^3 . *Ann. H. Poincar'e*, 2017, **18**, P. 1305–1347.
- [7] Exner P., Ichinose T. Geometrically induced spectrum in curved leaky wires. *J. Phys.*, 2001, **A34**, P. 1439–1450.
- [8] Exner P., Kondej S. Gap asymptotics in a weakly bent leaky quantum wire. *J. Phys.*, 2015, **A48**, P. 495301.
- [9] Exner P., Yoshitomi K. Asymptotics of eigenvalues of the Schroedinger operator with a strong delta-interaction on a loop. *J. Geom. Phys.*, 2002, **41**, P. 344–358.
- [10] Exner P., Kondej S. Curvature-induced bound states for a delta interaction supported by a curve in R^3 . *Ann. H. Poincare*, 2002, **3**, P. 967–981.
- [11] Exner P., Kondej S. Hiatus perturbation for a singular Schrödinger operator with an interaction supported by a curve in \mathbb{R}^3 . *J. Math. Phys.*, 2008, **49**, P. 032111.
- [12] Exner P., Kondej S. Scattering by local deformations of a straight leaky wire. *J. Phys.*, 2005, **A38**, P. 4865–4874.
- [13] Exner P., Jex M. Spectral asymptotics of a strong δ' interaction on a planar loop. *J. Phys.*, 2013, **A46**, P. 345201.
- [14] Exner P., Tater M. Spectra of soft ring graphs. *Waves Random Media*, 2003, **14**, P. S47–S60.
- [15] Behrndt J., Langer M., Lotoreichik V. Schroedinger operators with δ and δ' -potentials supported on hypersurfaces. *Ann. Henri Poincar'e*, 2013, **14**, P. 385–423.
- [16] Exner P. Leaky quantum graphs: a review, Analysis on Graphs and its Applications. Selected papers based on the Isaac Newton Institute for Mathematical Sciences programme, Cambridge, UK, 2007, *Proc. Symp. Pure Math.*, 2008, **77**, P. 523–564.
- [17] Kurylev Ya. Boundary conditions on curves for the three-dimensional Laplace operator. *Journal of Soviet Mathematics*, 1983, **22**(1), P. 1072–1082.
- [18] Blagovescenskii A.S., Lavrent'ev K.K. A three-dimensional Laplace operator with a boundary condition on the real line (in Russian). *Vestn. Leningr. Univ., Math. Mekh. Astron.*, 1977, **1**, P. 9–15.
- [19] Exner P., Kondej S. Strong coupling asymptotics for Schroedinger operators with an interaction supported by an open arc in three dimensions. *Rep. Math. Phys.*, 2016, **77**, P. 1–17.
- [20] Eremin D.A., Ivanov D.A., Popov I.Yu. Regular Potential Approximation for delta-Perturbation Supported by Curve of the Laplace-Beltrami Operator on the Sphere. *Zeitschrift für Analysis und Ihre Anwendungen*, 2012, **31**(2), P. 125–137.
- [21] Reed M., Simon B. *Methods of Modern Mathematical Physics. IV. Analysis of Operators*. Academic Press, New York, 1978.
- [22] Pavlov B.S., Popov I.Y. Model of diffraction on an infinitely-narrow slit and the theory of extensions. *Vestnik Leningrad. Univ. Ser. Mat., Mekh., Astr.*, 1983, **4**, P. 36–44.
- [23] Popov I.Yu. The extension theory and localization of resonances for the domain of trap type. *Matematicheskii sbornik*, 1990, **181**(10), P. 1366–1390. English: *Mathematics of the USSR-Sbornik*, 1992, **71**(1), P. 209–234.
- [24] Popov I.Y. The resonator with narrow slit and the model based on the operator extensions theory. *J. Math. Phys.*, 1992, **33**(11), P. 3794–3801.
- [25] Popov I.Yu. Helmholtz resonator and the operator extension theory in a space with an indefinite metrics. *Matematicheskii sbornik*, 1992, **183**(3), P. 2–38. English translation in Russian *Acad. Sci. Sb. Math.*, 1993, **75**(2), P. 285–315.

Properties of an oriented ring of neurons with the FitzHugh-Nagumo model

E. G. Fedorov

ITMO University, Kronverkskiy, 49, St. Petersburg, 197101, Russia

FedorovEGe@gmail.com

PACS 87.19.La, 87.18.Sn

DOI 10.17586/2220-8054-2021-12-5-553-562

The transmission of an impulse through a neuron is provided by processes that occur at the nanoscale level. This paper will build a model for an oriented ring of connected neurons. To describe the process of impulse transmission through a neuron, the FitzHugh-Nagumo model is used, which allows one to set a higher abstraction level by simulating an impulse. In this case, when transmitting impulses between neurons, the delay is taken into account. For the constructed model, the dependence of the number of neurons on the dynamics of the network as a whole is studied, and local bifurcations are found. All results are verified numerically. It is shown that the period of self-oscillations of such a network depends on the number of neurons.

Keywords: Neural networks, Hopf bifurcations, FitzHugh-Nagumo system, communication delay, stability.

Received: 15 July 2021

Revised: 19 September 2021

1. Introduction

The time delay can greatly affect the network of neurons and significantly expand the range of possible behaviors of the network. Because of this, models of networks are actively being investigated, where transmission between neurons occurs with a delay. There are works here on a network of connected neurons with an identical delay [1, 2]. And works on different transmission lag times [3–6]. Most often, in such studies, a pair of connected neurons is considered.

The transmission of an impulse through a neuron is provided by processes that occur at the nanoscale level, for example, via the overflow of sodium, potassium, chlorine and calcium ions through ion channels. In this work, we study the effect of the delay in the transmission of an impulse between connected neurons on the dynamics of the system of neurons as a whole. The FitzHugh-Nagumo model will be used to describe one neuron. And the system as a whole will be an oriented ring of neurons connected one after another. In this case, any connection between neurons will be considered with a constant delay. The main goal is to determine the type of behavior depending on the delay time, as well as to test the hypothesis that there is no direct relationship between the number of neurons and the period of self-oscillation of the impulse in the system. For this, in the first part of the work, the analysis of equilibrium states and their stability is carried out. In the second part of the work, the results obtained are verified numerically.

2. Neuron network

We will consider a group of neurons, where each neuron can have unidirectional connections with other neurons. That is, the axon of a neuron can be called its output, and for another neuron it will be an input (through a bunch of synapses and dendrites). To describe one neuron, will use the FitzHugh-Nagumo model [7–9]:

$$\begin{cases} \dot{u} &= -au + (a + 1)u^2 - u^3 - v + I, \\ \dot{v} &= bu - \gamma v, \end{cases} \quad (1)$$

where $u(t)$ corresponds to the potential of the neuron at time t , and $v(t)$ is the function of the internal state at time t , a, b, γ are positive constant parameters of the neuron, and I is the external current to the neuron.

As an external current I for a neuron, we will consider the total impact of other neurons, and the output will be the value of the potential of a neuron with a delay τ (delay for the transmission of an impulse through an axon). In this case, the effect between neurons will be sigmoidal (that is, it does not depend on the postsynaptic neuron). Thus, the model of the i -th neuron will be as follows:

$$\begin{cases} \dot{u}_i &= -au_i + (a + 1)u_i^2 - u_i^3 - v_i + \sum_{j=1, j \neq i}^n c \tanh(u_j^\tau), \\ \dot{v}_i &= bu_i - \gamma v_i. \end{cases} \quad (2)$$

2.1. Ring of connected neurons

In this section, we will consider a specific network of neurons in the form of an oriented ring. That is, the input of the neuron i will be the output of the neuron $i - 1$ ($i \geq 2$), and the input of the neuron 1 will be the output of the neuron n . Moreover, all neurons are identical in their parameters. A schematic representation of the considered network in Fig. 1. We will write a model of the considered network of neurons:

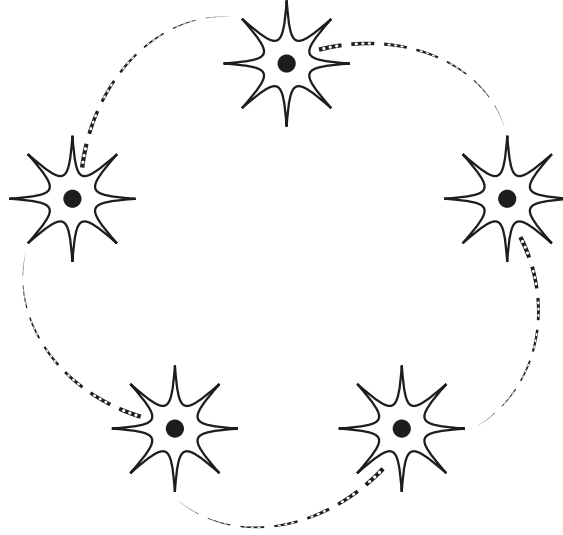


FIG. 1. Schematic representation of an oriented ring of connected neurons

$$\begin{cases} \dot{u}_1 &= -au_1 + (a+1)u_1^2 - u_1^3 - v_1 + c \tanh(u_n^\tau), \\ \dot{v}_1 &= bu_1 - \gamma v_1, \\ \dot{u}_2 &= -au_2 + (a+1)u_2^2 - u_2^3 - v_2 + c \tanh(u_1^\tau), \\ \dot{v}_2 &= bu_2 - \gamma v_2, \\ &\dots \\ \dot{u}_n &= -au_n + (a+1)u_n^2 - u_n^3 - v_n + c \tanh(u_{n-1}^\tau), \\ \dot{v}_n &= bu_n - \gamma v_n, \end{cases} \quad (3)$$

where $u_i(t)$ corresponds to the potential of the i -th neuron at time t , and $v_i(t)$ is the function of the internal state at time t , a, b, γ are positive constant parameters of neurons, c positive constant, connection strength, $u_i^\tau(t) = u_i(t - \tau)$, $i = 1, 2, \dots, n$.

2.1.1. *Find equilibrium states.* To search for equilibrium states of the system, it is necessary to solve:

$$\begin{cases} 0 &= -au_1 + (a+1)u_1^2 - u_1^3 - v_1 + c \tanh(u_n), \\ 0 &= bu_1 - \gamma v_1, \\ 0 &= -au_2 + (a+1)u_2^2 - u_2^3 - v_2 + c \tanh(u_1), \\ 0 &= bu_2 - \gamma v_2, \\ &\dots \\ 0 &= -au_n + (a+1)u_n^2 - u_n^3 - v_n + c \tanh(u_{n-1}), \\ 0 &= bu_n - \gamma v_n, \end{cases} \quad (4)$$

$$\begin{cases} v_i &= \frac{b}{\gamma} u_i, \quad i \in [1 \dots n], \\ c \tanh(u_{i-1}) &= u_i^3 - (a+1)u_i^2 + \left(a + \frac{b}{\gamma}\right) u_i, \quad i \in [2 \dots n], \\ c \tanh(u_n) &= u_1^3 - (a+1)u_1^2 + \left(a + \frac{b}{\gamma}\right) u_1. \end{cases} \quad (5)$$

Some of the equations in the system can be represented as:

$$\begin{cases} f(u_{i-1}) = g(u_i), \\ f(u_n) = g(u_1), \end{cases} \tag{6}$$

where $f(u) = c \tanh(u)$, $g(u) = u^3 - (a + 1)u^2 + \left(a + \frac{b}{\gamma}\right)u$. Let $\frac{b}{\gamma} \geq \frac{1}{3}(a^2 - a + 1)$. This assumption fits the main parameters of the neurons under consideration [2, 10], where $a < 1$, and b roughly the same γ . Throughout the rest of this section, we will assume everywhere that the assumption is fulfilled.

Proposition 1. *In the described system, the equilibrium states of neurons are the same, that is $u_i = u_j, v_i = v_j \forall i, j$.*

For the proof, we show that the function $g(x)$ will be increasing. Derivative $g(x)$: $g'(u) = 3u^2 - 2(a+1)u + a + \frac{b}{\gamma}$. Then, if $\frac{b}{\gamma} \geq \frac{1}{3}(a^2 - a + 1)$, then $(a + 1)^2 - 3\left(a + \frac{b}{\gamma}\right) \leq 0$, which coincides with the determinant $g(u)/2$. Hence, $g(u)$ is an increasing function (the leading coefficient is positive). Now, for the system (6), the functions $f(u)$ and $g(u)$ are increasing, which means that the assumption that some two connected neurons have different values of the equilibrium state potential leads to contradiction. That is, $u_i = u_j \forall i, j$, hence $v_i = v_j \forall i, j$. ■

Now, the system (5) can be reduced to an equivalent:

$$\begin{cases} v_i = \frac{b}{\gamma}u_i, & i \in [1 \dots n], \\ u_i = u_1, & i \in [2 \dots n], \\ c \tanh(u_1) = u_1^3 - (a + 1)u_1^2 + \left(a + \frac{b}{\gamma}\right)u_1. \end{cases} \tag{7}$$

Now the search for equilibrium states has been reduced to finding the roots of the equation $c \tanh(u_1) = u_1^3 - (a + 1)u_1^2 + \left(a + \frac{b}{\gamma}\right)u_1$. Note that $u_1 = 0$ is always a root. The right side of the equation has only one inflection point and it is located on the right semiaxis. Now let's highlight a few cases:

- 1) $a + \frac{b}{\gamma} > c$, then the considered equation has no negative solutions, but positive solutions can be 0, 1 or 2 (as c grows, the number of roots grows from 0 to 2, 1 root at the only critical value of c).
- 2) $a + \frac{b}{\gamma} < c$, then the considered equation has only one negative and one positive solution.

2.1.2. Define the stability of equilibrium states. To determine the stability of the equilibrium states of the system of neurons under consideration, we linearize the system in the general equilibrium state $u_i = u_1, v_i = v_1, i \in [2 \dots n]$. For this, we rewrite the system (3) as $\dot{U}(t) = AU(t) + BU(t - \tau)$, where $U(t) = (u_1(t), v_1(t), \dots, u_n(t), v_n(t))^T$:

$$A = \begin{pmatrix} -\alpha & -1 & 0 & 0 & \dots & 0 & 0 \\ b & -\gamma & 0 & 0 & \dots & 0 & 0 \\ 0 & 0 & -\alpha & -1 & \dots & 0 & 0 \\ 0 & 0 & b & -\gamma & \dots & 0 & 0 \\ & & & \dots & & & \\ 0 & 0 & 0 & 0 & \dots & -\alpha & -1 \\ 0 & 0 & 0 & 0 & \dots & b & -\gamma \end{pmatrix}, \quad B = \begin{pmatrix} 0 & 0 & \dots & 0 & 0 & c' & 0 \\ 0 & 0 & \dots & 0 & 0 & 0 & 0 \\ c' & 0 & \dots & 0 & 0 & 0 & 0 \\ 0 & 0 & \dots & 0 & 0 & 0 & 0 \\ & & & \dots & & & \\ 0 & 0 & \dots & c' & 0 & 0 & 0 \\ 0 & 0 & \dots & 0 & 0 & 0 & 0 \end{pmatrix}, \tag{8}$$

where $\alpha = 3u_1^2 - 2u_1(a + 1) + a, c' = \frac{c}{\cosh^2(u_1)}$.

Next, we find solutions to the characteristic equation $\det(A - \lambda I + Be^{-\lambda\tau}) = 0$ to determine stability:

$$\begin{vmatrix} -\alpha - \lambda & -1 & 0 & 0 & \dots & 0 & 0 & c'e^{-\lambda\tau} & 0 \\ b & -\gamma - \lambda & 0 & 0 & \dots & 0 & 0 & 0 & 0 \\ c'e^{-\lambda\tau} & 0 & -\alpha - \lambda & -1 & \dots & 0 & 0 & 0 & 0 \\ 0 & 0 & b & -\gamma - \lambda & \dots & 0 & 0 & 0 & 0 \\ & & & \dots & & & & & \\ 0 & 0 & 0 & 0 & \dots & c'e^{-\lambda\tau} & 0 & -\alpha - \lambda & -1 \\ 0 & 0 & 0 & 0 & \dots & 0 & 0 & b & -\gamma - \lambda \end{vmatrix} = 0. \tag{9}$$

To find the determinant, let's write it down on the top line. The first two elements will reduce the problem to a similar one with a lower dimension and this part of the determinant is equal to $((-\alpha - \lambda)(-\gamma - \lambda) + b)^n$. The third element in the top line is unique and sets a set of elements in the matrix and the part corresponding to it is equal to $-(c'e^{-\lambda\tau}(-\gamma - \lambda))^n$. As a result:

$$((-\alpha - \lambda)(-\gamma - \lambda) + b)^n - (c'e^{-\lambda\tau}(-\gamma - \lambda))^n = 0, \quad (10)$$

$$(\alpha + \lambda)(\gamma + \lambda) + b = c'e^{-\lambda\tau + \frac{2\pi k}{n}i}(\gamma + \lambda), \quad k \in [0 \dots n - 1]. \quad (11)$$

To determine stability in the system in the absence of delay, take $\tau = 0$. Then:

$$\lambda^2 + \lambda(\alpha + \gamma - c'e^{\frac{2\pi k}{n}i}) + \alpha\gamma + b - c'\gamma e^{\frac{2\pi k}{n}i} = 0, \quad k \in [0 \dots n - 1]. \quad (12)$$

For even odd n , these equations can be split into pairs $(k; -k)$ and there remains one equation for $k = 0$. For even n these equations can be split into pairs $(k; -k)$ and there will remain two equations for $k = 0$ and $k = \frac{n}{2}$. Next, we define the stability of the selected groups.

For $k = 0$:

$$\lambda^2 + \lambda(\alpha + \gamma - c') + \alpha\gamma + b - c'\gamma = 0. \quad (13)$$

This pair of roots will be stable if and only if:

$$\begin{cases} \alpha + \gamma - c' > 0, \\ \alpha + \frac{b}{\gamma} - c' > 0. \end{cases} \quad (14)$$

That is $\alpha + \min\left(\gamma, \frac{b}{\gamma}\right) > c'$. And, for the zero state of equilibrium:

$$a + \min\left(\gamma, \frac{b}{\gamma}\right) > c. \quad (15)$$

For $k = \frac{n}{2}$ ($n:2$):

$$\lambda^2 + \lambda(\alpha + \gamma + c') + \alpha\gamma + b + c'\gamma = 0. \quad (16)$$

This pair of roots will be stable if and only if:

$$\begin{cases} \alpha + \gamma + c' > 0, \\ \alpha + \frac{b}{\gamma} + c' > 0. \end{cases} \quad (17)$$

That is $\alpha + \min\left(\gamma, \frac{b}{\gamma}\right) > -c'$. For a zero equilibrium state, this condition is automatically satisfied, since $c > 0$.

For couple $(k; -k)$ ($k \neq 0, k \neq \frac{n}{2}$):

$$\begin{aligned} & \left(\lambda^2 + \lambda(\alpha + \gamma - c'e^{-\frac{2\pi k}{n}i}) + \alpha\gamma + b - c'\gamma e^{-\frac{2\pi k}{n}i} \right) \times \\ & \left(\lambda^2 + \lambda(\alpha + \gamma - c'e^{\frac{2\pi k}{n}i}) + \alpha\gamma + b - c'\gamma e^{\frac{2\pi k}{n}i} \right) = 0, \end{aligned} \quad (18)$$

$$(\lambda^2 + \lambda(\alpha + \gamma) + \alpha\gamma + b)^2 - 2(\lambda^2 + \lambda(\alpha + \gamma) + \alpha\gamma + b)c'(\gamma + \lambda)\cos\frac{2\pi k}{n} + c'^2(\gamma + \lambda)^2 = 0, \quad (19)$$

$$\begin{aligned} & \lambda^4 + 2\left(\alpha + \gamma - c'\cos\frac{2\pi k}{n}\right)\lambda^3 + \left((\alpha + \gamma)^2 + 2(\alpha\gamma + b) - 2(\alpha + 2\gamma)c'\cos\frac{2\pi k}{n} + c'^2\right)\lambda^2 + \\ & 2\left((\alpha + \gamma)(\alpha\gamma + b) - (\alpha + \gamma)c'\gamma\cos\frac{2\pi k}{n} - (\alpha\gamma + b)c'\cos\frac{2\pi k}{n} + c'^2\gamma\right)\lambda + \\ & (\alpha\gamma + b)^2 - 2(\alpha\gamma + b)c'\gamma\cos\frac{2\pi k}{n} + c'^2\gamma^2 = 0. \end{aligned} \quad (20)$$

An equation of the 4-th degree with real coefficients is obtained, its stability can be checked by the Hurwitz or Mikhailov criterion.

Now, we will find candidates for bifurcation from stable to unstable equilibrium or vice versa (when there is a purely imaginary eigenvalue). To do this, we take $\lambda = i\omega$:

$$(\alpha + i\omega)(\gamma + i\omega) + b = c'e^{-i\omega\tau + \frac{2\pi k}{n}i}(\gamma + i\omega), \quad (21)$$

$$\begin{cases} \alpha\gamma - \omega^2 + b + i\omega(\alpha + \gamma) = c'(\gamma\cos\tau' + \omega\sin\tau' + i(\omega\cos\tau' - \gamma\sin\tau')), \\ \tau' = \omega\tau - \frac{2\pi k}{n}, \end{cases} \quad (22)$$

$$\begin{cases} \alpha\gamma - \omega^2 + b = c'(\gamma \cos \tau' + \omega \sin \tau'), \\ \omega(\alpha + \gamma) = c'(\omega \cos \tau' - \gamma \sin \tau'), \\ \tau' = \omega\tau - \frac{2\pi k}{n}, \end{cases} \quad (23)$$

$$\begin{cases} c'(\omega^2 + \gamma^2) \cos \tau' = \alpha(\omega^2 + \gamma^2) + b\gamma, \\ c'(\omega^2 + \gamma^2) \sin \tau' = -\omega(\omega^2 + \gamma^2) + b\omega, \\ \tau' = \omega\tau - \frac{2\pi k}{n}, \end{cases} \quad (24)$$

let $\tau' \neq \frac{\pi}{2} + \pi k, k \in \mathbb{Z}$, then:

$$\begin{cases} \tan(\omega\tau - \frac{2\pi k}{n}) = \frac{-\omega(\omega^2 + \gamma^2) + b\omega}{\alpha(\omega^2 + \gamma^2) + b\gamma}, \\ \text{sign}(\cos(\omega\tau - \frac{2\pi k}{n})) = \text{sign}(\alpha(\omega^2 + \gamma^2) + b\gamma), \\ c'^2(\omega^2 + \gamma^2)^2 = (\alpha(\omega^2 + \gamma^2) + b\gamma)^2 + (-\omega(\omega^2 + \gamma^2) + b\omega)^2, \end{cases} \quad (25)$$

$$\begin{cases} \tan(\omega\tau - \frac{2\pi k}{n}) = \frac{-\omega(\omega^2 + \gamma^2) + b\omega}{\alpha(\omega^2 + \gamma^2) + b\gamma}, \\ \text{sign}(\cos(\omega\tau - \frac{2\pi k}{n})) = \text{sign}(\alpha(\omega^2 + \gamma^2) + b\gamma), \\ c'^2(\omega^2 + \gamma^2) = \alpha^2(\omega^2 + \gamma^2) + 2b\alpha\gamma + b^2 + \omega^2(\omega^2 + \gamma^2) - 2b\omega^2, \end{cases} \quad (26)$$

$$\begin{cases} \tan(\omega\tau - \frac{2\pi k}{n}) = \frac{-\omega(\omega^2 + \gamma^2) + b\omega}{\alpha(\omega^2 + \gamma^2) + b\gamma}, \\ \text{sign}(\cos(\omega\tau - \frac{2\pi k}{n})) = \text{sign}(\alpha(\omega^2 + \gamma^2) + b\gamma), \\ \omega^4 + (\alpha^2 + \gamma^2 - c'^2 - 2b)\omega^2 + \alpha^2\gamma^2 + 2b\alpha\gamma + b^2 - c'^2\gamma^2 = 0. \end{cases} \quad (27)$$

This means that the system can have 0, 1, or 2 series of decisions. Under the condition $\alpha(\omega^2 + \gamma^2) + b\gamma > 0$ (which is always true for the zero equilibrium state), we obtain (if the condition is not true, then the series for τ' must be offset by π):

$$\begin{cases} \omega = \left(\frac{1}{2} \left(-(\alpha^2 + \gamma^2 - c'^2 - 2b) \pm \sqrt{(\alpha^2 - \gamma^2 - c'^2)^2 - 4b((\alpha + \gamma)^2 - c'^2)} \right) \right)^{\frac{1}{2}}, \\ \tau = \frac{1}{\omega} \arctan \left(\frac{-\omega(\omega^2 + \gamma^2) + b\omega}{\alpha(\omega^2 + \gamma^2) + b\gamma} \right) + \frac{2\pi m}{\omega} + \frac{2\pi k}{n\omega}, \quad k, m \in \mathbb{Z}, \end{cases} \quad (28)$$

$$\begin{cases} \omega = \left(\frac{1}{2} \left(-(\alpha^2 + \gamma^2 - c'^2 - 2b) \pm \sqrt{(\alpha^2 - \gamma^2 - c'^2)^2 - 4b((\alpha + \gamma)^2 - c'^2)} \right) \right)^{\frac{1}{2}}, \\ \tau = \frac{1}{\omega} \arctan \left(\frac{-\omega(\omega^2 + \gamma^2) + b\omega}{\alpha(\omega^2 + \gamma^2) + b\gamma} \right) + \frac{2\pi k}{n\omega}, \quad k \in \mathbb{Z}. \end{cases} \quad (29)$$

Next, we define the conditions for the presence of candidates for a local bifurcation. That is, the conditions under which (27) has a real or positive root for ω^2 . If:

- 1) $c' > |\alpha + \frac{b}{\gamma}|$, in for $\omega = 0$ (27) is negative, therefore, with respect to ω^2 there is exactly one positive solution.
- 2) $c' < |\alpha + \frac{b}{\gamma}|$, (27) will be positive at 0, then it is necessary and sufficient that the roots are (the discriminant is positive) and the coefficient at ω^2 was negative. That is:

$$\begin{cases} (\alpha^2 + \gamma^2 - c'^2 - 2b)^2 - 4(\alpha^2\gamma^2 + 2b\alpha\gamma + b^2 - c'^2\gamma^2) > 0, \\ \alpha^2 + \gamma^2 - c'^2 - 2b < 0, \end{cases} \quad (30)$$

$$\begin{cases} c'^4 - 2(\alpha^2 - \gamma^2 - 2b)c'^2 + \alpha^4 - 2\alpha^2\gamma^2 + \gamma^4 - 4\alpha^2b - 8\alpha b\gamma - 4b\gamma^2 > 0, \\ c'^2 > \alpha^2 + \gamma^2 - 2b. \end{cases} \quad (31)$$

For $2\alpha b\gamma + 2b\gamma^2 + b^2 < 0$, the system is equivalent to $c'^2 > \alpha^2 + \gamma^2 - 2b$, otherwise:

$$\begin{cases} \left[\begin{array}{l} c'^2 < \alpha^2 - \gamma^2 - 2b - 2\sqrt{2\alpha b\gamma + 2b\gamma^2 + b^2}, \\ c'^2 > \alpha^2 - \gamma^2 - 2b + 2\sqrt{2\alpha b\gamma + 2b\gamma^2 + b^2}, \end{array} \right. \\ c'^2 > \alpha^2 + \gamma^2 - 2b, \end{cases} \quad (32)$$

$$c'^2 > \alpha^2 - \gamma^2 - 2b + 2\sqrt{2\alpha b\gamma + 2b\gamma^2 + b^2}. \quad (33)$$

Next, it is necessary to determine for each candidate for bifurcation its effect on stability (increases or decreases the number of eigenvalues with a positive real part). Let τ_0 be a candidate for bifurcation, $\omega_0, \lambda_0 = i\omega_0$ correspond to it. Define the sign of the expression $\frac{\partial \Re(\lambda)}{\partial \tau} \Big|_{\tau=\tau_0}$, where $\Re(x)$ is the real part of the number x , D – characteristic equation (10):

$$\frac{\partial \Re(\lambda)}{\partial \tau} \Big|_{\tau=\tau_0} = -\Re \left(\frac{\partial D}{\partial \tau} / \frac{\partial D}{\partial \lambda} \right) \Big|_{\tau=\tau_0} = -\Re \left(\frac{n (c' e^{-\lambda_0 \tau_0} (\gamma + \lambda_0))^n \lambda_0}{d_1} \right), \tag{34}$$

where

$$d_1 = n((\alpha + \lambda_0)(\gamma + \lambda_0) + b)^{n-1}(\gamma + \alpha + 2\lambda_0) - n c'^n e^{-n\lambda_0 \tau_0} (\gamma + \lambda_0)^{n-1} (-\tau_0(\gamma + \lambda_0) + 1). \tag{35}$$

Since τ_0 and λ_0 satisfy the characteristic equation, then

$$(c' e^{-\lambda_0 \tau_0} (-\gamma - \lambda_0))^n = ((-\alpha - \lambda_0)(-\gamma - \lambda_0) + b)^n, \tag{36}$$

then

$$\frac{\partial \Re(\lambda)}{\partial \tau} \Big|_{\tau=\tau_0} = -\Re \left(\frac{((\alpha + \lambda_0)(\gamma + \lambda_0) + b)^n \lambda_0}{d_2} \right) = -\Re \left(\frac{((\alpha + \lambda_0)(\gamma + \lambda_0) + b) \lambda_0 (\gamma + \lambda_0)}{d_3} \right), \tag{37}$$

where

$$d_2 = ((\alpha + \lambda_0)(\gamma + \lambda_0) + b)^{n-1}(\gamma + \alpha + 2\lambda_0) - ((\alpha + \lambda_0)(\gamma + \lambda_0) + b)^n \left(-\tau_0 + \frac{1}{\gamma + \lambda_0} \right), \tag{38}$$

$$d_3 = \tau_0 \lambda_0^3 + (\alpha \tau_0 + 2\gamma \tau_0 + 1) \lambda_0^2 + (2\alpha \gamma \tau_0 + \gamma^2 \tau_0 + b \tau_0 + 2\gamma) \lambda_0 + \alpha \gamma^2 \tau_0 + b \gamma \tau_0 + \gamma^2 - b. \tag{39}$$

Multiply in (37) the numerator and denominator by the conjugate of d_3 and multiply the whole expression by the square of the modulus d_3 :

$$\text{sign} \left(\frac{\partial \Re(\lambda)}{\partial \tau} \Big|_{\tau=\tau_0} \right) = \text{sign} \left((\omega_0^2 + \gamma^2)^2 - (b^2 + 2\alpha b \gamma + 2b \gamma^2) \right). \tag{40}$$

Now, we can see that the condition for increasing/decreasing the number of roots with a positive real part does not depend on a specific representative of the τ series, but is a property of the entire series or depends only on ω . ω_0 is the root of (27):

$$\omega_0^4 + (\alpha^2 + \gamma^2 - c'^2 - 2b) \omega_0^2 + \alpha^2 \gamma^2 + 2b\alpha\gamma + b^2 - c'^2 \gamma^2 = 0, \tag{41}$$

in another view:

$$(\omega_0^2 + \gamma^2)^2 + (\alpha^2 - c'^2 - \gamma^2 - 2b) (\omega_0^2 + \gamma^2) + b^2 + 2\alpha b \gamma + 2b \gamma^2 = 0. \tag{42}$$

Lemma 2. *Let $x^2 + ax + b = 0$ have two real roots x_1, x_2 ($x_1 < x_2$) and $b > 0$, then $x_1^2 - b$ and $x_2^2 - b$ will have different signs. And if $a > 0$, then $x_2^2 - b < 0$, and if $a < 0$, then $x_1^2 - b < 0$.*

Let $x^2 + ax + b = 0$ have two real roots x_1, x_2 ($x_1 < x_2$) and $b < 0$, then $x_1^2 - b$ and $x_2^2 - b$ will always be positive.

Substitute the values of the roots in $x^2 - b$:

$$\left(\frac{(-a \pm \sqrt{a^2 - 4b})}{2} \right)^2 - b = \frac{a^2 - 4b \mp a\sqrt{a^2 - 4b}}{2}, \tag{43}$$

then $\text{sign}(x^2 - b) = \text{sign}(\sqrt{a^2 - 4b} \mp a)$. This implies the assertions of the lemma. ■

As previously received, if $|\alpha + \frac{b}{\gamma}| < c'$, that is, one solution (27) for ω (up to sign). $|\alpha + \frac{b}{\gamma}| < c'$, so, $\alpha < c'$, and therefore $\alpha^2 - c'^2 - \gamma^2 - 2b < 0$. That is, among the two roots (27) for ω^2 ours is larger in absolute value. If $|\alpha + \frac{b}{\gamma}| > c'$, then $\alpha^2 + \gamma^2 - c'^2 - 2b < 0$, hence $\alpha^2 - \gamma^2 - c'^2 - 2b < 0$.

Applying lemma (2), the expression for $\text{sign} \left(\frac{\partial \Re(\lambda)}{\partial \tau} \Big|_{\tau=\tau_0} \right)$, the inequalities obtained above for ω_0 and the equation (let there be at least one solution for ω_0) obtain that $\text{sign} \left(\frac{\partial \Re(\lambda)}{\partial \tau} \Big|_{\tau=\tau_0} \right) = -1$, if and only if there are two roots (up to a sign) for ω and $b^2 + 2\alpha b \gamma + 2b \gamma^2 > 0$ for all τ , corresponding to a smaller ω (larger period of the series).

Then, we can conclude that:

1) If $c > a + \frac{b}{\gamma}$, that is, there are three equilibrium states ($u < 0, u = 0, u > 0$), while the zero equilibrium state will be unstable for $\tau = 0$, and will remain unstable with increasing τ (there is one series of values that changes the number of roots with a positive real part, but it only increases this number).

2) If $c < a + \frac{b}{\gamma}$, that is, either one equilibrium state ($u = 0$), or three ($u = 0, u > 0, u > 0$).

For equilibrium states, the following results were obtained:

1) If $c' > \alpha + \gamma$ or $c' > \alpha + \frac{b}{\gamma}$, then the equilibrium state is unstable at $\tau = 0$. If $c' < \alpha + \gamma$ and $c' < \alpha + \frac{b}{\gamma}$, then it is asymptotically stable.

2) If $c' > |\alpha + \frac{b}{\gamma}|$, then (the equilibrium state is unstable at $\tau = 0$) the equilibrium state will be unstable for any τ (there is one series of values, which changes the number of roots with a positive real part, but it only increases this number).

3) Otherwise, if $2\alpha\gamma + 2\gamma^2 + b < 0$ and $c'^2 > \alpha^2 + \gamma^2 - 2b$, that is, two series of changing the number of roots with positive real part, both of which increase this number. If $2\alpha\gamma + 2\gamma^2 + b > 0$ and $c'^2 > \alpha^2 - \gamma^2 - 2b + 2\sqrt{2\alpha b\gamma + 2b\gamma^2 + b^2}$, that is, two series of changing the number of roots with a positive real part, one of which decreases the number of roots, the other increases (the one with a shorter period). Otherwise, there are no succession series, the asymptotic stability of the equilibrium state does not depend on τ .

As a special case, for the zero equilibrium state:

1) If $c > a + \frac{b}{\gamma}$, then the equilibrium state will be unstable for any τ and there are two other equilibrium states.

2) If $a + \frac{b}{\gamma} > c > a + \gamma$, then the equilibrium state is unstable at $\tau = 0$ and there are two series of changing the number of roots with a positive real part, one of which decreases the number roots, the other increases.

3) If $c < a + \gamma$, then the equilibrium state is asymptotically stable for $\tau = 0$, for $c^2 < \alpha^2 - \gamma^2 - 2b + 2\sqrt{2\alpha b\gamma + 2b\gamma^2 + b^2}$ it will remain so for any τ , otherwise there are two series of changing the number of roots with a positive real part, one of which decreases the number of roots, the other increases.

In the results obtained, it can be noted that the number and the states of equilibrium themselves do not depend on the number of neurons in the ring. Also, the main criteria for determining the stability of a series of candidates do not depend on the number of neurons. Only the period in this series depends: the period is equal to $\frac{2\pi}{n\omega}$. Thus, the direct relationship between the number of neurons in the ring and the pulse propagation period was not confirmed analytically.

2.1.3. Numerical verification of conclusion. Let us introduce several definitions: a sequence of the first kind is a sequence $\{\tau_k\}$ such that for the characteristic equation (10) passing through the value of this sequence leads to an increase by two the number of roots with a positive real part. Similarly, introduce a sequence of the second kind – one that reduces by two the number of roots with a positive real part.

To obtain numerical solutions of the system, the Wolfram Mathematica package and the NDSolve method were used. The initial values were zero functions and a jump at the time $t = 0$ for the first neuron by 0.01. That is, $u_1(t|t < 0) = v_1(t|t \leq 0) = 0, u_1(0) = 0.01, u_i(t|t \leq 0) = v_i(t|t \leq 0) = 0, i \in [2, \dots, n]$.

Consider the following values of neuron parameters: $a = 0.15, b = \gamma = 0.02, c = 0.18$.

The value $c = 0.18$ lies between the value $c = 0.890512$, which separates one state of equilibrium from three, and between $c = a + \gamma = 0.17$. That is, from the results obtained earlier, we can conclude that, regardless of the number of neurons, there is one equilibrium state ($u = 0$), which is unstable at $\tau = 0$. For this state of equilibrium, there is a series of both the first and second kind.

Next, we consider the different number of neurons in the ring:

1) A ring of two neurons. Then two series of candidates are $\tau_{1,k} \approx 1.70691 + 25.715009k$ of the second kind, and $\tau_{2,k} \approx 14.431569 + 16.895513k$ of the first kind. Then, for this unique equilibrium state, we obtain four Hopf bifurcations: at $\tau \approx 1.70691$ – a transition from an unstable equilibrium to an asymptotically stable one (Fig. 2, 3), then for $\tau \approx 14.431569, \tau \approx 27.42192$ and $\tau \approx 31.327082$ (Fig. 4, 5).

2) A ring of three neurons. Then two series of candidates are $\tau_{1,k} \approx 1.70691 + 17.143339k$ of the second kind, and $\tau_{2,k} \approx 8.799731 + 11.263675k$ of the first kind. Then, for this unique equilibrium state, we obtain four Hopf bifurcations: at $\tau \approx 1.70691$ – a transition from an unstable equilibrium to an asymptotically stable one (Fig. 6, 7), then for $\tau \approx 8.799731, \tau \approx 18.850249$ and $\tau \approx 20.063406$ (Fig. 8, 9).

2 neurons in a ring

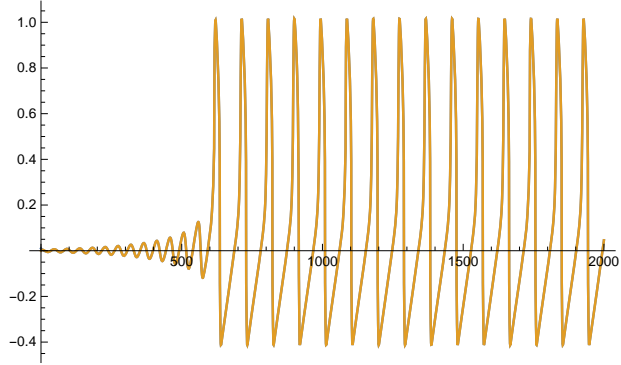


FIG. 2. $\tau = 0$

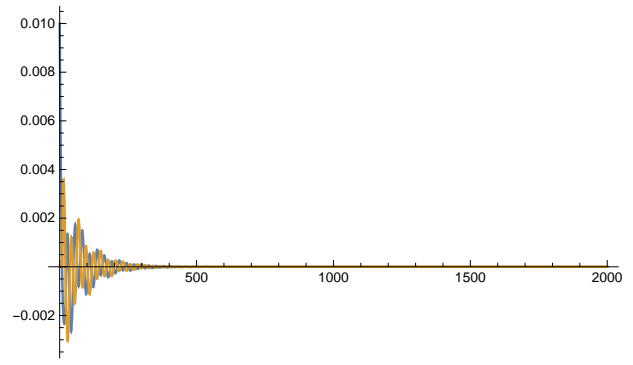


FIG. 3. $\tau = 10$

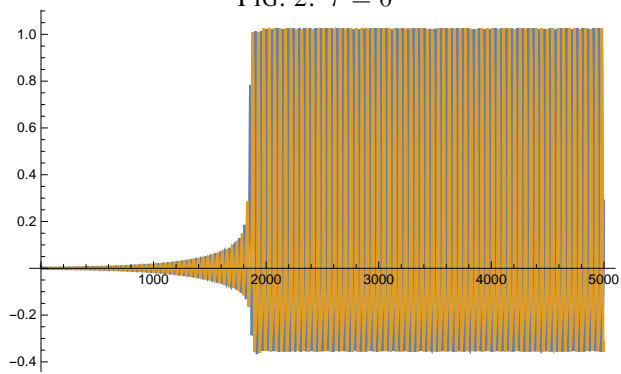


FIG. 4. $\tau = 20$

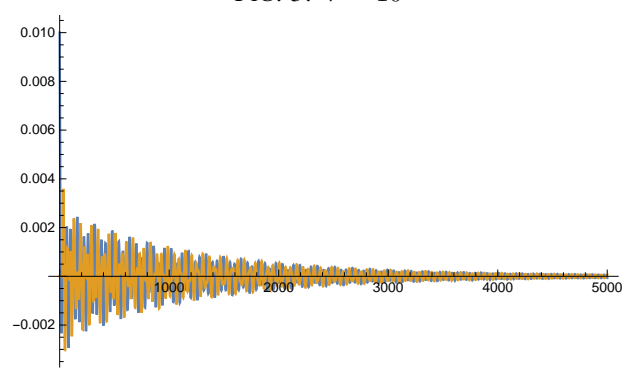


FIG. 5. $\tau = 29$

3 neurons in a ring

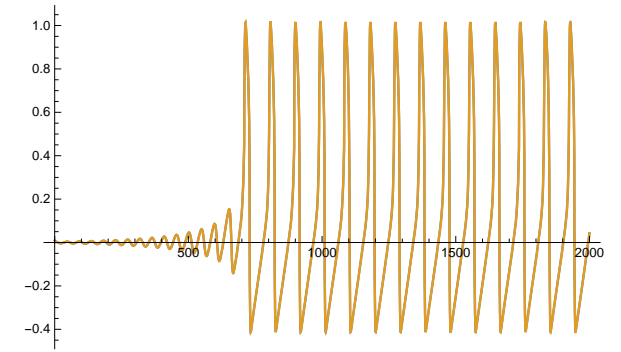


FIG. 6. $\tau = 0$

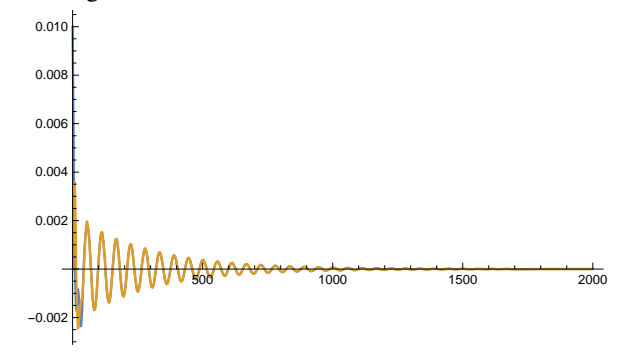


FIG. 7. $\tau = 3$

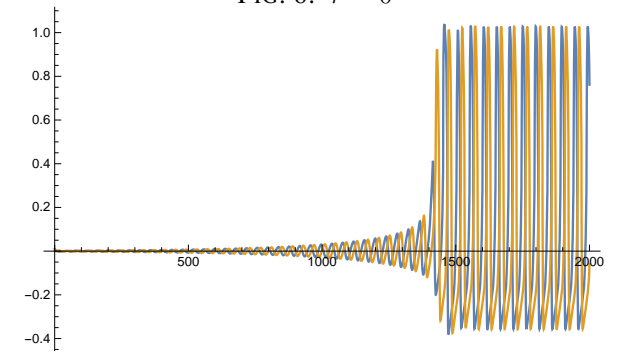


FIG. 8. $\tau = 12$

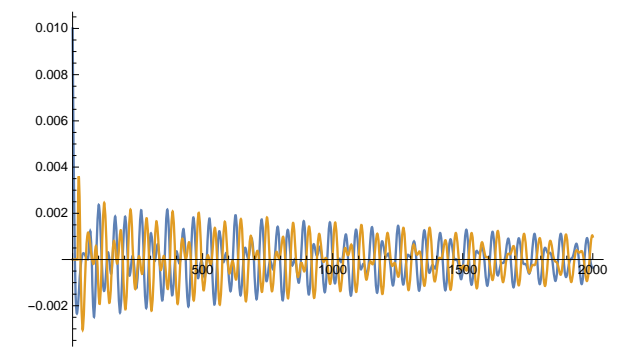


FIG. 9. $\tau = 19.3$

3) A ring of four neurons. Then two series of candidates are $\tau_{1,k} \approx 1.70691 + 12.857505k$ of the second kind, and $\tau_{2,k} \approx 5.983812 + 8.447756k$ of the first kind. Then, for this unique equilibrium state, obtain two Hopf bifurcations: at $\tau \approx 1.70691$ – a transition from an unstable equilibrium to an asymptotically stable one (Fig. 10, 11), then at $\tau \approx 5.983812$ (Fig. 12).

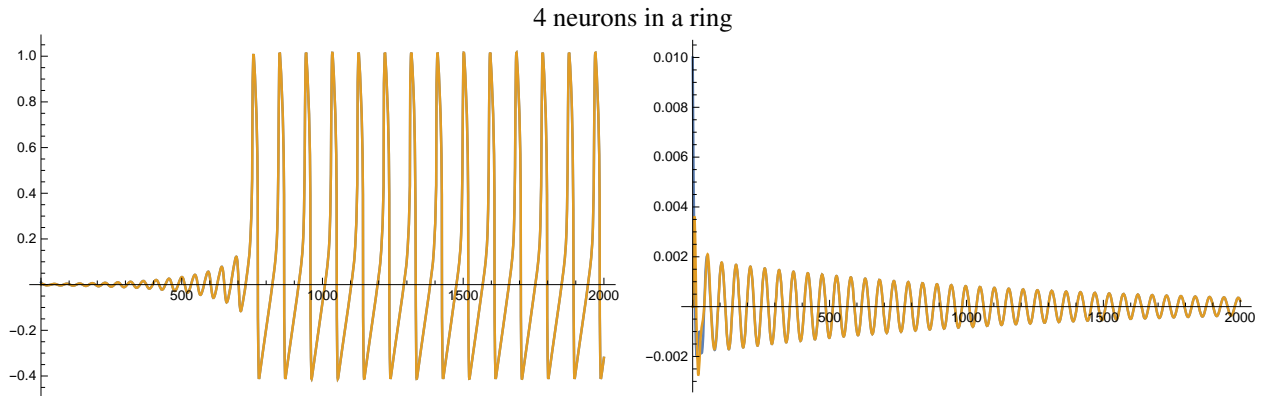


FIG. 10. $\tau = 0$

FIG. 11. $\tau = 2$

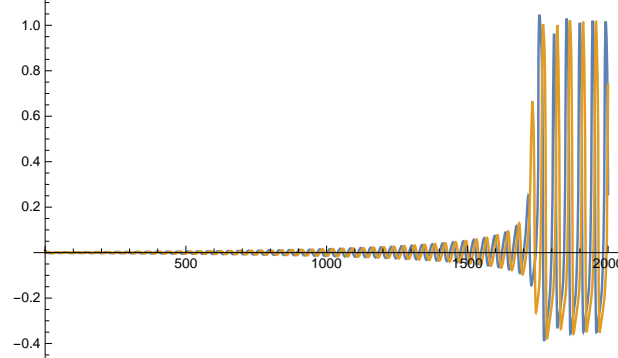


FIG. 12. $\tau = 7$

3. Conclusion

In this work, a system in the form of an oriented ring of neurons was considered. Connection between the two neurons was delayed. To describe the behavior of one neuron, the FitzHugh-Nagumo model was used, and on its basis, the final model for the system in the form of a ring of neurons was built. For this system, the equilibrium states were determined, criteria for determining the stability of equilibrium states and, as a consequence, criteria for the presence of periodic solutions in the system were obtained. It has been shown that the period of self-oscillations in the ring of neurons does not have a linear dependence on the number of neurons in the ring. In this case, for a fixed number of neurons, the dynamics will be affected only by the total delay in the transmission of an impulse along the ring, and not by individual pairs of neurons. All results are then verified numerically.

Acknowledgements

This work was supported by the Russian Foundation for Basic Research (RFBR) project number 20-31-90036.

References

- [1] Schöll E., Hiller G., Hövel P., Dahlem M. Time-delayed feedback in neurosystems. *Philosophical Transactions of the Royal Society A: Mathematical, Physical and Engineering Sciences*. 2009. **1891** (367). 1079–1096.
- [2] Burić N., Todorović D. Dynamics of FitzHugh-Nagumo excitable systems with delayed coupling. *Physical Review E*. 2003. **6** (67). 066222 p.
- [3] Song Z., Xu J., Zhen B. Multitype activity coexistence in an inertial two-neuron system with multiple delays. *International Journal of Bifurcation and Chaos*. 2015. **13** (25). 1530040 p.
- [4] Xu C., Zhang Q., Wu Y. Bifurcation analysis in a three-neuron artificial neural network model with distributed delays. *Neural Processing Letters*. 2016. **2** (44). 343–373.
- [5] Karaoğlu E., Yılmaz E., Merdan H. Stability and bifurcation analysis of two-neuron network with discrete and distributed delays. *Neurocomputing*. 2016. **182**. 102–110.
- [6] Xu C. Local and global Hopf bifurcation analysis on simplified bidirectional associative memory neural networks with multiple delays. *Mathematics and Computers in Simulation*. 2018. **149**. 69–90.
- [7] FitzHugh R. Impulses and physiological states in theoretical models of nerve membrane. *Biophysical journal*. 1961. **6** (1). 445–466.
- [8] Nagumo J., Arimoto S., Yoshizawa S. An active pulse transmission line simulating nerve axon. *Proceedings of the IRE*. 1962. **10** (50). 2061–2070.
- [9] Fedorov E.G., Popov A.I., Popov I.Y. Metric graph version of the FitzHugh-Nagumo model. *Nanosystems: Physics, Chemistry, Mathematics*. 2019. **10** (6). 623–626.
- [10] Burić N., Grozdanović I., Vasović N. Type I vs. type II excitable systems with delayed coupling. *Chaos, Solitons and Fractals*. 2005. **5** (23). 1221–1233.

Holliday junctions in the HC Blume–Capel model in “one case” on DNA

N. M. Khatamov

Institute of mathematics, 4B, St. University, 100174, Tashkent, Uzbekistan

nxatamov@mail.ru

DOI 10.17586/2220-8054-2021-12-5-563-568

We consider a DNA as a configuration of HC Blume–Capel model and embed it on a path of Cayley tree. To study thermodynamic properties of the model of DNAs, we describe the corresponding translation-invariant Gibbs measures (TIGM) of the model on the Cayley tree. It is shown that, for $k \geq 2$, for any temperature $T > 0$ there is a unique TIGM. Using these results, we study the distributions of the Holliday junctions DNA. For very high and very low temperatures, we give stationary distributions and typical configurations of the Holliday junctions.

Keywords: DNA, Cayley tree, Blume–Capel model, Gibbs measure, Holliday junction.

Received: 23 June 2021

Revised: 30 June 2021

1. Introduction and definitions

It is known that each DNA molecule is a double helix formed by two complementary strands of nucleotides held together by hydrogen bonds between $C + G$ and $A + T$ base pairs, where cytosine (C), guanine (G), adenine (A) and thymine (T). The genetic information, stored in an organism’s DNA, contains instructions for all proteins the organism will ever synthesize [1].

Holliday junctions [2] are cruciform structures that form during genetic recombination when two double-stranded DNA molecules split into four strands to exchange segments of genetic information.

In articles [3], [4–7] the Ising, Potts and Blume–Capel DNA models were considered in order to study their thermodynamics by Gibbs measures. Note that the non-uniqueness of the Gibbs measure corresponds to phase coexistence in the DNA system. By the properties of Markov chains (corresponding to TIGM) Holliday junctions and DNA branches are studied.

On the Cayley tree, the results for DNA were obtained only for cases $k = 2$. In this paper, the results are obtained for the case $k \geq 2$. For other results on the Blume–Capel model, see [8], [3, 9, 10].

In our model, we consider a set of DNA, as in [4], which “lives” on a tree graph. Suppose that on the edge l of this graph there is a function $\sigma(l)$ with three possible values $-1, 0, 1$ (an analog of the spin values in physical systems) in the case $\sigma(l) = 0$, we say that the edge l doesn’t belong to DNA. If this l separates two DNAs, then the value $\sigma(l) = 1$ or $\sigma(l) = -1$ means that the two DNAs have a Holliday junction.

Now, following [4, 5, 12], we recall some definitions.

The Cayley tree Γ^k of order $k \geq 1$ is an infinite tree, i.e., a graph without cycles, such that exactly $k + 1$ edges originate from each vertex. Let $\Gamma^k = (V, L, i)$, where V is the set of vertices Γ^k , L the set of edges and i is the incidence function setting each edge $l \in L$ into correspondence with its endpoints $x, y \in V$. If $i(l) = \{x, y\}$, then, the vertices x and y are called the nearest neighbors, denoted by $l = \langle x, y \rangle$. The distance $d(x, y)$, $x, y \in V$ on the Cayley tree is the number of edges of the shortest path from x to and y :

$$d(x, y) = \min\{d : \exists x = x_0, x_1, \dots, x_{d-1}, x_d = y \in V \text{ such that } \langle x_0, x_1 \rangle, \dots, \langle x_{d-1}, x_d \rangle\}.$$

For a fixed $x^0 \in V$ we set $W_n = \{x \in V : d(x^0, x) = n\}$,

$$V_n = \{x \in V : d(x^0, x) \leq n\}, L_n = \{l = \langle x, y \rangle \in L | x, y \in V_n\}.$$

Let $\mathbb{Z} = \{\dots, -2, -1, 0, 1, 2, \dots\}$. It was proved in [11] that all vertices of a Cayley tree can be partitioned into equivalence classes labeled by integers and that through each vertex belonging to the m -th equivalence class, there passes a unique path such that the labels of the equivalence classes to which successive vertices belong form an integer sequence $\dots, m - 2, m - 1, m, m + 1, m + 2, \dots$, which is infinite in both directions. Each such path is called a \mathbb{Z} -path.

Let L be the set of edges of the Cayley tree. Consider the function σ , which assigns each edge $l \in L$ to the values $\sigma(l) \in \{-1, 0, 1\}$. The value $\sigma(l) = -1$ (respectively $+1$) means that the edge l is “occupied” $-1 = A + T$ (respectively $1 = C + G$) and $\sigma(l) = 0$ means that l is “vacant”.

The configuration $\sigma = \{\sigma(l), l \in L\}$ on edges of the Cayley tree is given by a function from L to $\{-1, 0, 1\}$. The set of all configurations in L is denoted by Ω . Configurations in L_n are defined similarly and the set of all configurations in L_n are denoted by Ω_n .

In the case of a “one case”, the configuration $\sigma = \{\sigma(l), l \in L\}$ is called *admissible*, if

- 1) $\sigma(l) \neq 0$ for any $l \in \mathbb{Z}$ -path;
- 2) $\{\sigma(l), \sigma(t)\} \in \{\{0, 0\}, \{0, -1\}, \{0, +1\}, \{-1, 0\}, \{-1, +1\}\}$;

The restriction of an admissible configuration on a \mathbb{Z} -path is called a *DNA*.

We consider the following Blume–Capel model of energy configuration σ of a DNA set (see [4]):

$$H(\sigma) = J \sum_{\langle l,t \rangle \in L \times L} (\sigma(l) - \sigma(t))^2, \tag{1}$$

where $J > 0$ is a coupling constant, $\sigma(l) \in \{-1, 0, 1\}$ and $\langle l, t \rangle$ denote the nearest neighboring edges, that is, the edges that have a common endpoint.

Let Ω_n^a (respectively Ω^a) be the set of all admissible configurations on L_n (respectively L).

Let us introduce designations as [4]:

$$E_n = \{\langle x, y \rangle \in L : x \in W_{n-1}, y \in W_n\},$$

$$\Omega_n^{ba} = \text{the set of admissible configurations on } E_n.$$

For $l \in E_{n-1}$ denote:

$$S(l) = \{t \in E_n : \langle l, t \rangle\}.$$

It is easy to see that:

$$S(l) \cap \mathbb{Z}\text{-path} = \begin{cases} \{l_0, l_1\} \subset L, & \text{if } l \notin \mathbb{Z}\text{-path,} \\ \{l_1\} \subset L, & \text{if } l \in \mathbb{Z}\text{-path.} \end{cases}$$

We denote:

$$S_0(l) = S(l) \setminus \{l_0, l_1\}, \quad l \notin \mathbb{Z}\text{-path,}$$

$$S_1(l) = S(l) \setminus \{l_1\}, \quad l \in \mathbb{Z}\text{-path.}$$

Let $\tilde{L}(G)$ be the set of “edge” of G . We define adjacency matrix of G by $A \equiv A^G = (\alpha_{ij})_{i,j=-1,0,+1}$, i.e.:

$$\alpha_{ij} \equiv \alpha_{ij}^G = \begin{cases} 1, & \text{if } \{i, j\} \in \tilde{L}(G), \\ 0, & \text{if } \{i, j\} \notin \tilde{L}(G). \end{cases}$$

In a standard way (see [4, 5, 12]), one can reduce the study of the Gibbs measures of the Blume–Capel model to the problem of finding solutions to the following system of functional equations:

$$\begin{aligned} z_{0,l} &= \frac{\alpha_{0,+1}\lambda z_{l_0} + \alpha_{0,-1}\lambda}{\alpha_{-1,+1}\lambda^4 z_{l_0} + \alpha_{-1,-1}} \cdot \frac{\alpha_{0,+1}\lambda z_{l_1} + \alpha_{0,-1}\lambda}{\alpha_{-1,+1}\lambda^4 z_{l_1} + \alpha_{-1,-1}} \cdot \prod_{t \in S_0(l)} \frac{\alpha_{0,+1}\lambda z_{+1,t} + \alpha_{0,-1}\lambda + \alpha_{0,0}z_{0,t}}{\alpha_{-1,+1}\lambda^4 z_{+1,t} + \alpha_{-1,-1} + \alpha_{-1,0}\lambda z_{0,t}}, \\ & \hspace{25em} l \notin \mathbb{Z}\text{-path,} \\ z_{1,l} &= \frac{\alpha_{+1,+1}z_{l_0} + \alpha_{+1,-1}\lambda^4}{\alpha_{-1,+1}\lambda^4 z_{l_0} + \alpha_{-1,-1}} \cdot \frac{\alpha_{+1,+1}z_{l_1} + \alpha_{+1,-1}\lambda^4}{\alpha_{-1,+1}\lambda^4 z_{l_1} + \alpha_{-1,-1}} \cdot \prod_{t \in S_0(l)} \frac{\alpha_{+1,+1}z_{+1,t} + \alpha_{+1,-1}\lambda^4 + \alpha_{+1,0}\lambda z_{0,t}}{\alpha_{-1,+1}\lambda^4 z_{+1,t} + \alpha_{-1,-1} + \alpha_{-1,0}\lambda z_{0,t}}, \\ & \hspace{25em} l \notin \mathbb{Z}\text{-path,} \\ z_l &= \frac{\alpha_{+1,+1}z_l + \alpha_{+1,-1}\lambda^4}{\alpha_{-1,+1}\lambda^4 z_l + \alpha_{-1,-1}} \cdot \prod_{t \in S_1(l)} \frac{\alpha_{+1,+1}z_{+1,t} + \alpha_{+1,-1}\lambda^4 + \alpha_{+1,0}\lambda z_{0,t}}{\alpha_{-1,+1}\lambda^4 z_{+1,t} + \alpha_{-1,-1} + \alpha_{-1,0}\lambda z_{0,t}}, \quad l \in \mathbb{Z}\text{-path,} \end{aligned} \tag{2}$$

where:

$$\lambda = \exp(-J\beta). \tag{3}$$

Moreover, this means that for any set of vectors $\mathbf{z} = \{(z_{0,l}, z_{1,l}, z_t), l \notin \mathbb{Z}\text{-path}, t \in \mathbb{Z}\text{-path}\}$ satisfying the system of functional equations (2), there exists the only Gibbs measure μ and vice versa. However, analyzing the (2) solutions is not easy. Here are some solutions (2).

2. TIGMs of the set of DNAs

Now, in this section, we find solutions \mathbf{z}_l to the system of functional equations (2), which does not depend on l , i.e.:

$$z_{0,l} = u, z_{1,l} = v, \forall l \notin \mathbb{Z}\text{-path}; \quad z_l = w, \forall l \in \mathbb{Z}\text{-path}. \tag{4}$$

where $u, v, w > 0$ (by (2)) satisfy:

$$\begin{aligned} u &= \left(\frac{\alpha_{0,+1}\lambda v + \alpha_{0,-1}\lambda + \alpha_{0,0}u}{\alpha_{-1,+1}\lambda^4 v + \alpha_{-1,-1} + \alpha_{-1,0}\lambda u} \right)^{k-2} \left(\frac{\alpha_{0,+1}\lambda w + \alpha_{0,-1}\lambda}{\alpha_{-1,+1}\lambda^4 w + \alpha_{-1,-1}} \right)^2, \\ v &= \left(\frac{\alpha_{+1,+1}v + \alpha_{+1,-1}\lambda^4 + \alpha_{+1,0}\lambda u}{\alpha_{-1,+1}\lambda^4 v + \alpha_{-1,-1} + \alpha_{-1,0}\lambda u} \right)^{k-2} \left(\frac{\alpha_{+1,+1}w + \alpha_{+1,-1}\lambda^4}{\alpha_{-1,+1}\lambda^4 w + \alpha_{-1,-1}} \right)^2, \\ w &= \left(\frac{\alpha_{+1,+1}v + \alpha_{+1,-1}\lambda^4 + \alpha_{+1,0}\lambda u}{\alpha_{-1,+1}\lambda^4 v + \alpha_{-1,-1} + \alpha_{-1,0}\lambda u} \right)^{k-1} \left(\frac{\alpha_{+1,+1}w + \alpha_{+1,-1}\lambda^4}{\alpha_{-1,+1}\lambda^4 w + \alpha_{-1,-1}} \right). \end{aligned} \tag{5}$$

Consider in “one case”:

$$\begin{aligned} \alpha_{-1,-1} &= 0, & \alpha_{-1,0} &= 1, & \alpha_{-1,1} &= 1, \\ \alpha_{0,-1} &= 1, & \alpha_{0,0} &= 1, & \alpha_{0,1} &= 1, \\ \alpha_{1,-1} &= 1, & \alpha_{1,0} &= 1, & \alpha_{1,1} &= 0, \end{aligned} \tag{6}$$

then system (5) we obtain:

$$\begin{aligned} u &= \left(\frac{\lambda v + \lambda + u}{\lambda^4 v + \lambda u} \right)^{k-2} \cdot \left(\frac{\lambda w + \lambda}{\lambda^4 w} \right)^2 \\ v &= \left(\frac{\lambda^4 + \lambda u}{\lambda^4 v + \lambda u} \right)^{k-2} \cdot \frac{1}{w^2} \\ w &= \left(\frac{\lambda^4 + \lambda u}{\lambda^4 v + \lambda u} \right)^{k-1} \cdot \frac{1}{w}. \end{aligned} \tag{7}$$

We have the equation:

$$w^2 = \left(\frac{\lambda^4 + \lambda u}{\lambda^4 v + \lambda u} \right)^{k-1}, \tag{8}$$

from the last equation of the system (7). Then, from the second equation of the system (7), $v = 1$. From equation (8) we obtain $w = 1$. If we put them to the first equation of the system (7), then we have:

$$u = \frac{4}{\lambda^6} \left(\frac{u + 2\lambda}{\lambda^4 + \lambda u} \right)^{k-2}. \tag{9}$$

For $k \geq 2$ true the following.

Lemma 1. *If $k \geq 2$ and $0 < \lambda < 1$, then system (7) has unique solution:*

$$\mathbf{z} = (u, v, w) = (u_*, 1, 1),$$

where u_* is solution of equation (9).

Proof. We have seen above that at $k = 2$, equation (9) has a unique solution $u_* = \frac{4}{\lambda^6}$. Then in this case $\mathbf{z} = (u_*, 1, 1) = \left(\frac{4}{\lambda^6}, 1, 1 \right)$. We write equation (9) in the form:

$$u = f(u), \tag{10}$$

where:

$$f(u) = \frac{4}{\lambda^6} \left(\frac{u + 2\lambda}{\lambda^4 + \lambda u} \right)^{k-2}.$$

Note that the derivative of the function $f(u)$:

$$f'(u) = (k - 2) \frac{4}{\lambda^4} \left(\frac{u + 2\lambda}{\lambda^4 + \lambda u} \right)^{k-3} \frac{(\lambda - \sqrt{2})(\lambda + \sqrt{2})}{(\lambda^4 + \lambda u)^2} < 0$$

at the $0 < \lambda < 1$, i.e. the function $f(u)$ is decreasing for $u > 0$. Hence, equation (10) has a unique solution u_* for any $\lambda \in (0, 1)$. Then system (7) has unique solution $\mathbf{z} = (u, v, w) = (u_*, 1, 1)$. Lemma 1 is proved.

For some values of k one can give explicit form of the unique solution to (9). For example, if $k = 2$ then the unique solution of equation (7) is with:

$$u_*^{(2)} = \frac{4}{\lambda^6}, \tag{11}$$

i.e.:

$$\mathbf{z} = (u, v, w) = (u_*^{(2)}, 1, 1).$$

For $k = 3$ the system of equation (7) has unique solution for any $\lambda > 0$:

$$\mathbf{z} = (u, v, w) = (u_*^{(3)}, 1, 1),$$

where:

$$u_*^{(3)} = \frac{\sqrt{(\lambda^{10} - 4)^2 + 32\lambda^8} - (\lambda^{10} - 4)}{2\lambda^7}. \tag{12}$$

For $k = 4$ the system of equation (7) has unique solution:

$$\mathbf{z} = (u, v, w) = (u_*^{(4)}, 1, 1),$$

where:

$$u_*^{(4)}(\lambda) = \frac{1}{3\lambda^8} \left(\sqrt[3]{A + 6\sqrt{3B}} + \frac{C}{\sqrt[3]{A + 6\sqrt{3B}}} - 2\lambda^{11} + 4 \right), \tag{13}$$

here:

$$\begin{aligned} A &= \lambda^{33} + 30\lambda^{22} - 144\lambda^{20} + 216\lambda^{18} - 96\lambda^{11} + 288\lambda^9 + 64, \\ B &= \frac{(\lambda^{24} - \lambda^{13} - 36\lambda^{11} + 108\lambda^9 + 32)(\lambda^2 - 2)^2}{\lambda}, \\ C &= \lambda^{22} - 16\lambda^{11} + 48\lambda^9 + 16. \end{aligned}$$

On the cases $k > 4$, it is not possible to find an explicit form of the solution to equation (9).

Denote by μ the Gibbs measure which, by (2), correspond to the solution \mathbf{z} .

Thus we obtain the following.

Theorem 1. For the HC Blume–Capel model in “one case” of DNAs on the Cayley tree of order $k \geq 2$ at the $T = \frac{J}{\ln \frac{1}{\lambda}} > 0$ there is unique translation-invariant Gibbs measure μ .

3. Markov chains of TIGMs and Holliday junction of DNA

For marginals on the two-edge sets consisting of two neighboring edges l, t , taking into account the boundary law $\{(z_{0,l}, z_{1,l}, z_t), l \notin \mathbb{Z}\text{-path}, t \in \mathbb{Z}\text{-path}\}$, i.e. solutions to the (2) system. This boundary law is normalized to -1 , i.e., $z_{-1,l} = 1$. We have:

$$\mu(\sigma(l) = a, \sigma(t) = b) = \frac{1}{Z} z_{a,l} \exp(J\beta(a - b)^2) z_{b,t}, \quad a, b = -1, 0, +1,$$

where Z is normalizing factor.

From this, using formulas (3) and (4) for solutions (u, v, w) to (7) we write the matrices of the tree-indexed Markov chains (related to Gibbs measures, see [4]) $\mathbb{P}^{[l,t]} = (P_{ij}^{[l,t]})$:

$$\begin{aligned} \mathbb{P}^{[l,t]} = \mathbb{P}_{(3 \rightarrow 3)}^{[l,t]} &= \begin{pmatrix} 0 & \frac{\lambda u}{\lambda u + \lambda^4 v} & \frac{\lambda^4 v}{\lambda u + \lambda^4 v} \\ \frac{\lambda}{\lambda + u + \lambda v} & \frac{u}{\lambda + u + \lambda v} & \frac{\lambda v}{\lambda + u + \lambda v} \\ \frac{\lambda^4}{\lambda^4 + \lambda u} & \frac{\lambda u}{\lambda^4 + \lambda u} & 0 \end{pmatrix}, \quad \text{if } l, t \notin \mathbb{Z}\text{-path}. \\ \mathbb{P}^{[l,t]} = \mathbb{P}_{(3 \rightarrow 2)}^{[l,t]} &= \begin{pmatrix} 0 & 0 & 1 \\ \frac{1}{1 + w} & 0 & \frac{w}{1 + w} \\ 1 & 0 & 0 \end{pmatrix}, \quad \text{if } l \notin \mathbb{Z}\text{-path}, t \in \mathbb{Z}\text{-path}. \end{aligned}$$

$$\mathbb{P}^{[l,t]} = \mathbb{P}_{(2 \rightarrow 3)}^{[l,t]} = \begin{pmatrix} 0 & \frac{\lambda u}{\lambda u + \lambda^4 v} & \frac{\lambda^4 v}{\lambda u + \lambda^4 v} \\ * & * & * \\ \frac{\lambda^4}{\lambda^4 + \lambda u} & \frac{\lambda u}{\lambda^4 + \lambda u} & 0 \end{pmatrix}, \quad \text{if } l \in \mathbb{Z}\text{-path}, t \notin \mathbb{Z}\text{-path},$$

where * means that $P_{0j}^{[l,t]}$ is not defined, because $\sigma(l) \neq 0$ for any $l \in \mathbb{Z}\text{-path}$.

$$\mathbb{P}^{[l,t]} = \mathbb{P}_{(2 \rightarrow 2)}^{[l,t]} = \begin{pmatrix} 0 & 1 \\ 1 & 0 \end{pmatrix}, \quad \text{if } l \in \mathbb{Z}\text{-path}, t \in \mathbb{Z}\text{-path}.$$

Here, the matrix element $P_{ij}^{[l,t]}$ is the probability of the transition from the state i on the edge l to the state j on the neighboring edge t .

Matrices $\mathbb{P}_{(2 \rightarrow 3)}^{[l,t]}, \mathbb{P}_{(3 \rightarrow 2)}^{[l,t]}$ do not define standard Markov chain. Therefore, we will not consider them.

For the matrix $\mathbb{P}_{(n \rightarrow m)}^{[l,t]}$ with $n = m$, it is easy to find the following stationary distributions:

$$\pi_{(n \rightarrow m)} = (\pi_{(n \rightarrow m), -1}, \pi_{(n \rightarrow m), 0}, \pi_{(n \rightarrow m), 1}).$$

Namely, we have:

$$\pi_{(3 \rightarrow 3)} = \frac{1}{N} (\lambda u + \lambda^4 v, (\lambda + u + \lambda v)u, (\lambda^4 + \lambda u)v),$$

where N the normalizing factor, and:

$$\pi_{(2 \rightarrow 2)} = \left(\frac{1}{2}, \frac{1}{2}\right).$$

Using the ergodic theorem (see [13]) for non-negative stochastic matrices and the above formulas for matrices and stationary distributions, we obtain.

Theorem 2. *In a stationary state of the set of DNAs, independently on $l \notin \mathbb{Z}\text{-path}$, a Holliday junction through l does not occur with the following probability (with respect to measure μ^*):*

$$\pi_{(3 \rightarrow 3), 0} = \pi_{(3 \rightarrow 3), 0}^{(*)} = \frac{1}{N} (2\lambda + u_*)u_*.$$

(Consequently, a Holliday junction occurs with probability $1 - \pi_{(3 \rightarrow 3), 0}^{(*)}$ where u_* are defined in Lemma 1.

It can be seen that $\pi_{(3 \rightarrow 3), 0}^{(*)}$ is a function only of temperature.

We now find the limits of the stationary distribution vectors $\pi_{(3 \rightarrow 3)}, \pi_{(2 \rightarrow 2)}$ (corresponding to the Markov chain generated by the Gibbs measure μ) as $T \rightarrow 0$ (as $\beta \rightarrow \infty$ and $\lambda \rightarrow 0$) and as $T \rightarrow +\infty$ (as $\beta \rightarrow 0$ and $\lambda \rightarrow 1$). To find the limits, we take the dependence of u_* on $T = 1/\beta$ into account.

Lemma 2. *We have the relations:*

$$\lim_{T \rightarrow 0} \pi_{(3 \rightarrow 3)}^{(k)} = (0, 1, 0), \quad k = 2, 3, 4.$$

$$\lim_{T \rightarrow 0} \pi_{(2 \rightarrow 2)}^{(k)} = \left(\frac{1}{2}, \frac{1}{2}\right), \quad k = 2, 3, 4.$$

in the low-temperature case $T \rightarrow 0$ and:

$$\lim_{T \rightarrow +\infty} \pi_{(3 \rightarrow 3)}^{(2)} = \left(\frac{5}{34}, \frac{12}{17}, \frac{5}{34}\right) \approx (0.14705882, 0.70588235, 0.14705882),$$

$$\lim_{T \rightarrow +\infty} \pi_{(3 \rightarrow 3)}^{(3)} = \left(\frac{5 + \sqrt{41}}{41 + 7\sqrt{41}}, \frac{31 + 5\sqrt{41}}{41 + 7\sqrt{41}}, \frac{5 + \sqrt{41}}{41 + 7\sqrt{41}}\right) \approx (0.13286968, 0.73426064, 0.13286968),$$

$$\lim_{T \rightarrow +\infty} \pi_{(3 \rightarrow 3)}^{(4)} = (E, F, E) = (0.12195036, 0.75609928, 0.12195036),$$

$$\lim_{T \rightarrow +\infty} \pi_{(2 \rightarrow 2)}^{(k)} = \left(\frac{1}{2}, \frac{1}{2}\right), \quad k = 2, 3, 4,$$

in the high-temperature case $T \rightarrow +\infty$, where:

$$E = \frac{36\sqrt{78} + 15(359 + 12\sqrt{78})^{\frac{2}{3}} + 147(359 + 12\sqrt{78})^{\frac{1}{3}} + 1077}{8145 + 144(359 + 12\sqrt{78})^{\frac{2}{3}} + (359 + 12\sqrt{78})^{\frac{4}{3}} + 784(359 + 12\sqrt{78})^{\frac{1}{3}} + 192\sqrt{78}} \approx 0.12195036,$$

$$F = \frac{5991 + 144(359 + 12\sqrt{78})^{\frac{2}{3}} + 490(359 + 12\sqrt{78})^{\frac{1}{3}} + (359 + 12\sqrt{78})^{\frac{4}{3}} + 120\sqrt{78}}{8145 + 144(359 + 12\sqrt{78})^{\frac{2}{3}} + (359 + 12\sqrt{78})^{\frac{4}{3}} + 784(359 + 12\sqrt{78})^{\frac{1}{3}} + 192\sqrt{78}} \approx 0.75609928.$$

By Lemma 2 we have the following structures of the DNA set:

- (i) In the case $T \rightarrow 0$, the DNA set has the following stationary states (configurations):

Case μ ($k = 2, 3, 4$): For all neighboring DNA molecules, the Holliday junction does not occur. The sequence of ± 1 s, in a DNA on the \mathbb{Z} -path is free with independent identically distributed and equiprobable $(1/2) - 1$ and $+1$.

- (ii) In the case $T \rightarrow +\infty$, the DNA set has the following stationary states (configurations):

Case μ ($k = 2$): All neighboring DNA molecules have Holliday junction with probability $5/17$ (more precisely, a junction via state -1 or $+1$ with equiprobable $5/34$) and no junction with probability $12/17$. The sequence of ± 1 s, in a DNA on the \mathbb{Z} -path is free with independent identically distributed and equiprobable $(1/2) - 1$ and $+1$.

Case μ ($k = 3$): All neighboring DNA molecules have Holliday junction with probability 0.26573936 (more precisely, a junction via state -1 or $+1$ with equiprobable 0.13286968) and no junction with probability 0.73426064 . The sequence of ± 1 s, in a DNA on the \mathbb{Z} -path is free with independent identically distributed and equiprobable $(1/2) - 1$ and $+1$.

Case μ ($k = 4$): All neighboring DNA molecules have Holliday junction with probability 0.24390072 (more precisely, a junction via state -1 or $+1$ with equiprobable 0.12195036) and no junction with probability 0.75609928 . The sequence of ± 1 s, in a DNA on the \mathbb{Z} -path is free with independent identically distributed and equiprobable $(1/2) - 1$ and $+1$.

4. Conclusions

On the Cayley tree, the results for DNA were obtained only for cases $k = 2$. In this paper, the results are obtained for the case $k \geq 2$. Following [12] for the HC Blume–Capel model in “one case” in DNA on a Cayley tree of order $k \geq 2$, we proved that at a temperature $T > 0$ there is a unique TIGM.

Since each such measure describes the phase of DNA recruitment. Our results refer to the Gibbs measure allowed us to study the distributions of Holliday junctions DNA compounds. In the previous section, for very high and very low temperatures, we gave stationary distributions and typical configurations of Holliday junctions.

Acknowledgements

The author thanks Professor U. A. Rozikov for his suggestions which were helpful to improve the readability of the paper.

References

- [1] Alberts B., Johnson A., et al. *Molecular biology of the cell*, 4th edn., Garland Science, New York, 2002.
- [2] Holliday R. A mechanism for gene conversion in fungi. *Genet Res.*, 1964, **5**, P. 282–304.
- [3] Khatamov N.M. Holliday junctions in the Blume–Capel model of DNA. *Theoretical and Mathematical Physics*, 2021, **3** (206), P. 383–390.
- [4] Rozikov U.A. Tree-hierarchy of DNA and distribution of Holliday junctions. *J. Math. Biol.*, 2017, **75**, P. 1715–1733.
- [5] Rozikov U.A. Holliday junctions for the Potts model of DNA. *Algebra, Complex Analysis, and Pluripotential Theory*, 2018, **264**, P. 151–165.
- [6] Rozikov U.A. Thermodynamics of interacting systems of DNA molecules. *Theoretical and Mathematical Physics*, 2021, **2** (206), P. 174–183.
- [7] Rozikov U.A. Thermodynamics of DNA-RNA renaturation. *Inter. Jour. Geom. Methods Mod. Phys.*, 2021, **6** (18), 2150096.
- [8] Cirillo E.N., Olivieri E. Metastability and nucleation for the Blume–Capel model. Different mechanisms of transition. *Journal of Statistical Physics*, 1996, **83**, P. 473–554.
- [9] Khatamov N.M., Khakimov R.M. Translation-invariant Gibbs measures for the Blume–Capel model on a Cayley tree. *JMAG*, 2019, **2** (15), P. 239–255.
- [10] Khatamov N.M. Translation-invariant extreme Gibbs measures for the Blume–Capel model with a wand on a Cayley tree. *Ukrains'kyi Matematychnyi Zhurnal*, 2020, **4** (72), P. 540–556.
- [11] Rozikov U.A., Ishankulov F.T. Description of periodic p-harmonic functions on Cayley trees. *Nonlinear Diff. Equ. Appl.*, 2010, **2** (17), P. 153–160.
- [12] Rozikov U.A. *Gibbs measures on Cayley trees*. World Scientific Publishing, Singapore, 2013.
- [13] Georgii H.O. *Gibbs measures and phase transitions*. De Gruyter studies in Math, Berlin, 1988.

Numerical analysis of the effect of illumination intensity on photoelectric parameters of the silicon solar cell with various metal nanoparticles

J. Gulomov, R. Aliev

Department of physics, Andijan state university, Andijan, 119, St. Universitet, 170100, Uzbekistan
 jasurbekgulomov@yahoo.com, alievuz@yahoo.com

PACS 85.60.Bt, 78.20.Bh, 73.61.Ga

DOI 10.17586/2220-8054-2021-12-5-569-574

It is important to study the effect of light intensity on the main photoelectric parameters of silicon solar cell with various metal nanoparticles because the intensity of sunlight is variable. In this paper, the effect of Cu, Pt, Au, Ag, Ti, Al, Co nanoparticles on dependence of main photoelectric parameters of silicon solar cell on light intensity has been studied by modeling with Sentaurus TCAD. The intensity coefficient of short circuit current densities of Pt and Ti nanoparticles induced silicon solar cells were found to be $K_{J,Pt} = 0.0158$ A/W and $K_{J,Ti} = 0.0164$ A/W. For simple silicon solar cell, this value was found to be $K_J = 0.0071$ A/W. Thus, we have observed that was the two-fold greater the intensity coefficient of short circuit current density and output power for the silicon solar cells with Ti and Pt nanoparticles relative to that of a simple silicon solar cell.

Keywords: metal nanoparticles, solar cell, nanoplasmonics, modeling, intensity.

Received: 10 July 2021

Revised: 17 August 2021

1. Introduction

Solar cells are especially used in the outdoor environment. The changing of seasons has an influence on the operation of solar cells because, luminosity is changed. The influence of light intensity on main photoelectric parameters of silicon solar cells [1] and panels [2] were studied properly. But for nanoparticles induced silicon solar cells (NISSC), it hasn't been thoroughly researched yet. The effect of gold and silver nanoparticles on the optical properties of silicon solar cells was studied experimentally [3] and simulated by using Lumerical TCAD [4]. In our previous papers, the optimal conditions in inserting nanoparticles into silicon solar cells were found. Acceptable size of nanoparticles was 20 nm, while the optimal distance between adjacent nanoparticles was 100 nm. Moreover, nanoparticles should ideally have been inserted into the n region of silicon solar cell [5]. In this paper, the influence of illumination intensity on main photoelectric parameters of NISSCs have been investigated as a logical continuation of our previous research. A modeling method has been used. There are several TCAD programs to model semiconductor devices. The most reliable and best-known programs among them are: Sentaurus TCAD, Lumerical, Silvaco TCAD as well as Comsol Multiphysics. Among their advantages, the obtained results are more reliable and often are similar to experimental results [6–8]. Besides, from prior literature, some information about the comparing experiment results and simulation results, which are obtained by using TCAD programs, are given [9, 10]. Moreover, all types of semiconductor devices can be modeled by using them.

2. Method

To explore NISSCs, simulation methods are mainly used. In this work, models of NISSCs have been created by using Sentaurus TCAD packages.

In Sentaurus TCAD, only four main tools are used to simulate solar cells: Sentaurus Structure Editor, Sentaurus Device, Sentaurus Visual and Sentaurus Workbench. Sentaurus Workbench is environment that assists all interconnected tools to work. From tools, which are added to use in Sentaurus Workbench, is used only by writing codes in tool command language (TCL). For example, the geometrical model of a solar cell is created by writing codes in Sentaurus Structure Editor, which is added to the Sentaurus Workbench environment. This method is more effective, but the Sentaurus Structure Editor has an SDE module to create geometrical model of solar cells by using standard shapes. After creating geometric model in that module, codes can be generated for use in the Sentaurus Structure Editor command file. So, different models must be created for every project. To form geometrical model of various solar cells by creating unique algorithm in TCL is acceptable way. Therefore, in this paper, geometrical model of NISSC has been created by writing codes in TCL. In our previous scientific works, we gave full information about creating geometric models of various solar cells [11].

After creating geometrical model of solar cell, physical properties were given, and then calculations were performed by using Sentaurus Device. Physical properties of all materials were uploaded to model as a parameter file. Physical models were added to simulation by writing the code in the Sentaurus Device command file.

The simplest state among the processes, which occur in the semiconductor devices, is the equilibrium state. In this state, the Poisson equation, which is shown in formula (1), must be solved:

$$\Delta\phi = -\frac{q}{\varepsilon}(p - n + N_D + N_A), \quad (1)$$

where ε is the permittivity, n and p are the concentrations of the electrons and holes, N_D and N_A are the donor and acceptor concentrations, and q is the electron charge.

Electron concentration n as well as hole concentration p are calculated by using Fermi distribution that is shown formula (2) and (3):

$$n = N_c F_{1/2} \left(\frac{E_{F,n} - E_c}{kT} \right), \quad (2)$$

$$p = N_v F_{1/2} \left(\frac{E_v - E_{F,p}}{kT} \right), \quad (3)$$

where: $F_{1/2}$ is the Fermi half integral, E_c is the conduction band energy, E_v is the valence band energy, $E_{F,n}$ is the quasi Fermi energy for electrons, $E_{F,p}$ is the quasi Fermi energy for holes, T is the absolute temperature, N_c is the density of states in conduction band, N_v is the density of states in valence band, and k is Boltzmann constant.

Transportation of carriers occurred due to externally applied voltage, illumination or heating. In these phenomena, the equilibrium state is disrupted; due to solar cells being illuminated, carrier transport should also be calculated during simulation in them. The motion of the carriers forms a current. Basically, connection between carrier concentration and current density is expressed by “general continuity equations” which are shown in formula (4) and (5):

$$\nabla \cdot \vec{J}_n = qR_{net,n} + q \frac{\partial n}{\partial t}, \quad (4)$$

$$-\nabla \cdot \vec{J}_p = qR_{net,p} + q \frac{\partial p}{\partial t}, \quad (5)$$

where: J_n, J_p are the current densities of electron and holes, $R_{net,p}, R_{net,n}$ are the net recombination of electron and holes, t – time.

In Sentaurus Device, “Drift-Diffusion”, “Thermodynamic”, “Hydrodynamic” and “Monte Carlo” models are used to calculate carrier transport. The “Thermodynamic” models, which are given in formulas (6) and (7), have been used to model solar cell, since, generation and recombination rate of carriers is changed when light intensity is changed. Additionally, heat energy or phonon concentration can also be changed. Therefore, heat energy, which is formed due to motion of carriers, also changed. All of these have been taken into account in “Thermodynamic” models, which are given formulas (6) and (7).

$$\vec{J}_n = -nq\mu_n(\nabla\Phi_n + P_n\nabla T), \quad (6)$$

$$\vec{J}_p = -pq\mu_p(\nabla\Phi_p + P_p\nabla T), \quad (7)$$

where: μ_n, μ_p are the mobility of electron and holes, Φ_n, Φ_p are the electron and hole quasi-Fermi potentials, P_n, P_p are thermoelectric power of electron and holes, T is the absolute temperature.

Formula (8) has been used to calculate carriers transport in metal nanoparticles:

$$\vec{J}_M = -\sigma(\nabla\Phi_M + P\nabla T), \quad (8)$$

where: σ is the conductivity of metal, Φ_m is the Fermi potential in metal, P is the metal thermoelectric power, J_M is current density in the metal.

It has been considered that there were ohmic boundary conditions between the metal nanoparticles and silicon interface, due to nanoparticles input into n region of silicon solar cell. Ohmic boundary conditions were calculated by formula (9):

$$\begin{aligned} \vec{J}_M \cdot \hat{n} &= (\vec{J}_n + \vec{J}_p + \vec{J}_D) \cdot \hat{n}, \\ \phi &= \Phi_M - \Phi_0, \\ n &= n_0, \\ p &= p_0, \end{aligned} \quad (9)$$

where: J_D is the diffusion current density, \hat{n} is the normal vector, Φ_0 is the equilibrium electrostatic potential (the built-in potential), ϕ – electrostatic potential; n_0, p_0 are the electron and hole equilibrium concentrations.

In this paper, AM1.5G was chosen as a light source. For AM1.5G spectrum [12], one sun equals 633 W/m^2 . The intensity of light, which is falling on the solar cell, was varied from 0.1 sun to 1 sun, but the quality of the spectrum wasn't changed, as is shown Fig. 1.

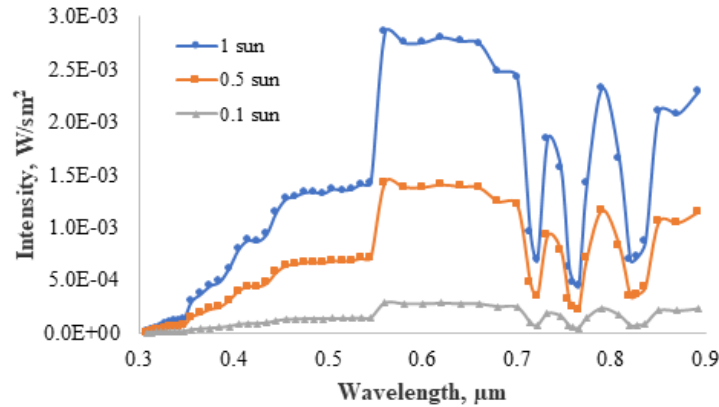


FIG. 1. AM1.5G light spectrum with various intensities

Tables of dependence of complex refractive index of materials on light wavelength were used to calculate the optical properties of silicon solar cells. The total absorption, reflection and transmission factors of solar cells were calculated by using “Transfer matrix method”.

Various AM1.5G spectrum files were created. Then, in Sentaurus Workbench, different values for each file were attached. In Sentaurus Device attached values were checked by the conditional operators, then necessary spectrum file was uploaded to model.

3. Results and discussion

In our previous research work, the optimal conditions of nanoparticles size, the distance between neighboring nanoparticles and their location were found. By using those conditions, the dependence of main photoelectric parameters of NISSCs on illumination intensity have been studied in this paper. In Fig. 2, the dependence of absorption coefficient of SSC and Cu, Au, Ag, Pt NISSCs on light wavelength are given. With light of $0.5 \mu\text{m}$ wavelength, resonance event was occurred for all type NISSCs. In studies by Bonaccorso, the resonance of absorption coefficient of gold nanoparticles with interval of radius 10 to 30 nm occurred with light a wavelength of $0.5 \mu\text{m}$ [13]. These experiments prove the reliability of our simulation results. However, the maximum absorption coefficient was observed in Pt NISSC. In addition, absorption coefficient of Pt NISSC in the infrared field was enhanced. Additionally, in the Brady’s experimental work, influence of nanoparticles on the properties silicon solar cell was properly studied [14].

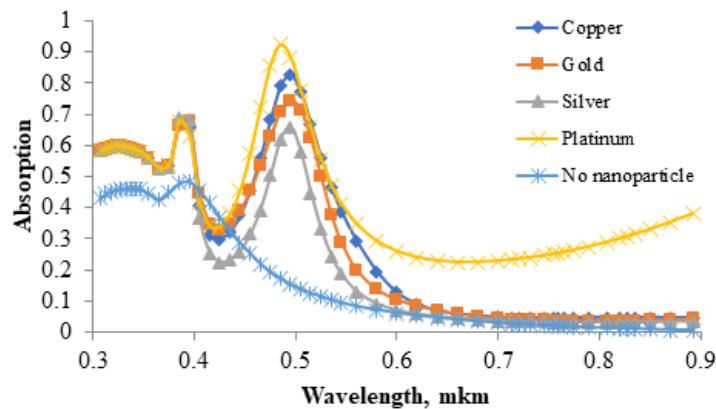


FIG. 2. Dependence of absorption coefficient of SSC and Cu, Au, Ag, Pt NISSCs on light wavelength

The main parameters of solar cells are determined from I–V characteristics. In Fig. 3, I–V characteristics of SSC and Pt, Ag NISSCs are given. Because, only Pt and Ag nanoparticles had a tangible effect on the I–V characteristics

of SSC. Au and Cu nanoparticles had negligible effects. Pt nanoparticle doubled the current density of SSC, due to platinum having a high absorption coefficient. Ag nanoparticle reduced the current density of SSC by 1.2 fold. This phenomenon was observed in Tayyar Dzhaharov's experimental research [15]. The Fano interference can explain this result [16].

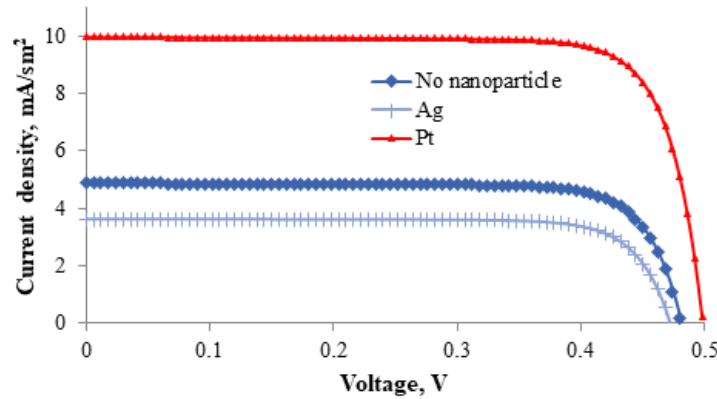


FIG. 3. I-V characteristics of SSC and Ag, Pt NISSCs

Photoelectric parameters change due to varying light intensity. In Fig. 4, the dependence of short circuit current density of SSC and Ag, Pt, Cu NISSCs on the illumination intensity is shown. Light intensity coefficient of short circuit current was found to be $K_J = 0.0071$ A/W for SSC, $K_{J,Pt} = 0.0158$ A/W for Pt NISSC, $K_{J,Ag} = 0.000575$ A/W for Ag NISSC and $K_{J,Cu} = 0.00831$ A/W for Cu NISSC. In Chegari's experimental work, the intensity coefficient of short circuit current found was $K_J = 0.0051$ A/W for SSC and the dependence of short circuit current on light intensity was linear [17]. It was found to be intensity coefficient of Pt NISSC 2.05 times greater than that of SSC. In the research of Bao, it was found that short circuit current of solar cell, in which Pt nanoparticles were deposited by using one minute electroless deposition, was 2.27 times greater than that of solar cell without Pt nanoparticles [18]. In the Au nanoparticles, the dependence of short circuit current of SSC on light intensity was hardly ever affected. The intensity coefficient of short circuit current of Au NISSC was found to be 1.34 times worse than that of SSC.

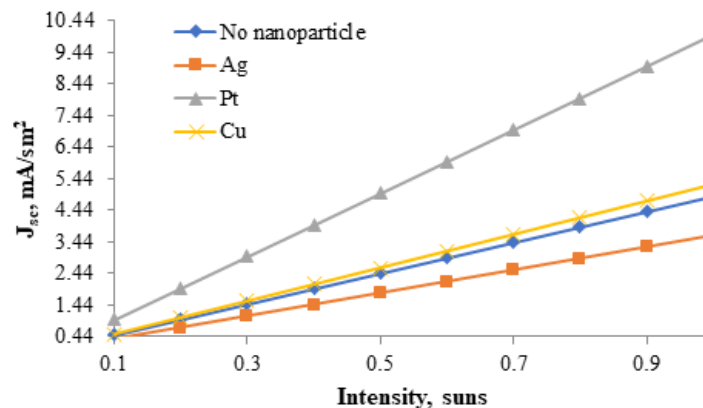


FIG. 4. Dependence of short circuit current density of SSC and NISSC on light intensity

Dependence of the open circuit voltage of SSC on light intensity is known from other research works to be nonlinear [19]. In Fig. 5, dependence of open circuit voltage of SSC and Au, Ag, Pt NISSCs on light intensity are shown. The intensity coefficients of open circuit voltage of SSC and NISSCs were determined to be the same, $K_U = 1.05E-4$ Vcm²/W. Thus, the nanoparticles affected the value of open circuit voltage of SSC, but they did not affect the intensity coefficient of open circuit voltage of SSC. In some studies, the dependence of open circuit voltage on light intensity is explained with changing short circuit current density. So, short circuit current linearly depends on light intensity. As shown formula (10), the open circuit voltage has a logarithmic dependence on the short circuit

current [20]. So, between open circuit voltage and light intensity has logarithmic dependence:

$$V'_{OC} = \frac{nkT}{q} \ln \left(\frac{XI_{SC}}{I_0} \right) = \frac{nkT}{q} \left[\ln \left(\frac{I_{SC}}{I_0} \right) + \ln X \right] = V_{OC} + \frac{nkT}{q} \ln X, \quad (10)$$

where: V_{OC} is open circuit voltage in one sun intensity, V'_{OC} is the open circuit voltage, X is concentration coefficient, I_{SC} is short circuit current, I_0 is dark current.

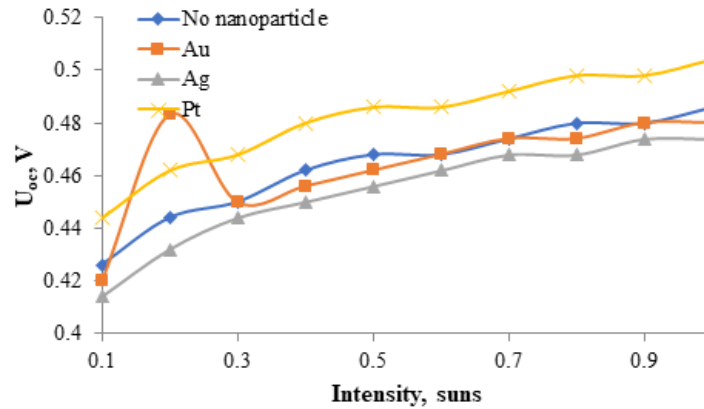


FIG. 5. Dependence of open circuit voltage of SSC and Au, Ag, Pt NISSCs on light intensity

The quality of solar cells is evaluated by their fill factor. In Fig. 6, dependence of fill factor of SSC and Au, Ag, Pt, Cu NISSCs on light intensity is shown. The dependence of fill factor on light intensity is not linear. In this paper, it was found that fill factor increased until 0.6 solar intensity, then it decreased. This occurred due to increasing of series resistance in high intensity [21]. These obtained results are similar to those obtained by Khan [22].

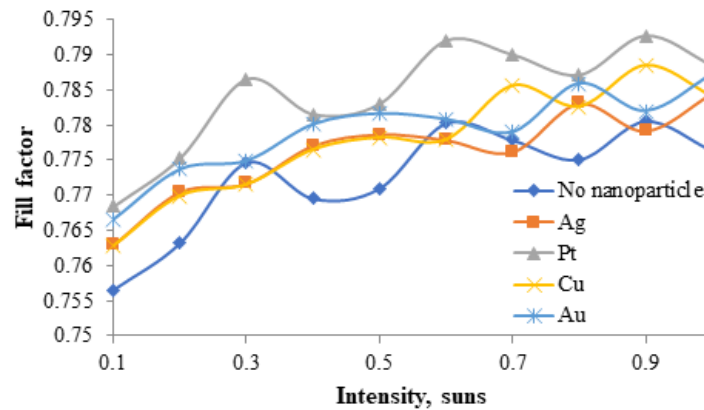


FIG. 6. Dependence of fill factor of SSC and Au, Ag, Pt, Cu NISSCs on light intensity

Various metals can be input into silicon solar cells as nanoparticles. Every metal nanoparticle can exert various effects on silicon solar cell properties. In Table 1, light intensity coefficients of main photoelectric parameters of SSC and NISSCs are given. Nanoparticles have affected all photoelectric parameters except open circuit voltage and voltage on maximum power point.

4. Conclusion

The spectral sensitivity and efficiency of solar cells have been enhanced due to considerable research. In this paper, effects of light intensity on photoelectric parameters of various NISSCs have been studied. Thus, it was determined that the effects of Pt, Ti nanoparticles were favorable, the effects of Ag, Co nanoparticles were deleterious, and the effects of Au, Cu were negligible. The obtained results show that properties of SSCs can be changed by inputting palpable nanoparticles. It is purposeful to use silicon material, which nanoparticles is input, not only to make solar cells but also other semiconductor materials. For instance, silicon material, to which Pt and Ti nanoparticles can be input, has potential for use in a next-generation pyrometer, which has twice sensitivity.

TABLE 1. Light intensity coefficients of main photoelectric parameters of SSC and NISSCs

Nanoparticles	dU_{oc}/dW , Vsm^2/mW	dI_{sc}/sW , A/W	dU_{mpp}/dW , Vsm^2/mW	dI_{mpp}/dW , A/W	dP_{mpp}/dW	dFF/dW , sm^2/mW
—	1.05E-02	7.71E-01	1.05E-02	7.13E-01	2.96E-01	3.49E-03
Cu	1.05E-02	8.31E-01	9.48E-03	7.78E-01	3.22E-01	3.74E-03
Au	1.05E-02	7.40E-01	1.05E-02	6.86E-01	2.84E-01	3.62E-03
Ag	1.05E-02	5.75E-01	1.05E-02	5.32E-01	2.17E-01	3.77E-03
Pt	1.05E-02	1.58E+00	1.05E-02	1.47E+00	6.37E-01	3.53E-03
Al	1.05E-02	9.20E-01	1.05E-02	8.54E-01	3.59E-01	3.62E-03
Co	1.05E-02	6.11E-01	1.05E-02	5.62E-01	2.30E-01	3.49E-03
Ti	1.05E-02	1.64E+00	1.05E-02	1.53E+00	6.64E-01	3.51E-03

References

- [1] Stamenic L., Smiley E., Karim K. Low light conditions modelling for building integrated photovoltaic (BIPV) systems. *Solar Energy*, 2004, **77** (1), P. 37–45.
- [2] Bayhan H., Bayhan M. A simple approach to determine the solar cell diode ideality factor under illumination. *Solar Energy*, 2011, **85** (5), P. 769–775.
- [3] Jeng M.J., Chen Z.Y., et al. Improving Efficiency of Multicrystalline Silicon and CIGS Solar Cells by Incorporating Metal Nanoparticles. *Materials*, 2015, **8** (10), P. 6761–6771.
- [4] Shilpa G.D., Subramanyam T.K., Sreelakshmi K., Uttarakumari. Study and Optimization of Metal Nanoparticles for the Enhanced Efficiency Thin Film Solar Cells. *IOP Conference Series: Materials Science and Engineering*, 2016, **149**, 012074.
- [5] Aliev R., Gulomov J., et al. Stimulation of Photoactive Absorption of Sunlight in Thin Layers of Silicon Structures by Metal Nanoparticles. *Applied Solar Energy*, 2020, **56**, P. 364–370.
- [6] Ghione G. Looking for Quality in TCAD-Based Papers. *IEEE Transactions on Electron Devices*, 2019, **66** (8), P. 3252–3253.
- [7] Pfäffli P., Wong H.Y., et al. TCAD modeling for reliability. *Microelectronics Reliability*, 2018, **88–90**, P. 1083–1089.
- [8] Maiti C.K. *Introducing Technology Computer-Aided Design (TCAD): Fundamentals, Simulations, and Applications*. Jenny Stanford Publishing, Boca Raton, Florida, USA, 2017, 438 p.
- [9] Feng P., Kim J., et al. Contact model based on TCAD-experimental interactive algorithm. *Int. Conf. on Simulation of Semiconductor Processes and Devices, SISPAD*, 2015, P. 238–241.
- [10] Korn J., Rücker H., Heinemann B. Experimental verification of TCAD simulation for high-performance SiGe HBTs. *IEEE 17th Topical Meeting on Silicon Monolithic Integrated Circuits in RF Systems*, 2017, P. 94–96.
- [11] Gulomov J., Aliev R., et al. Studying the Effect of Light Incidence Angle on Photoelectric Parameters of Solar Cells by Simulation. *Int. Journal of Renewable Energy Development*, 2021, **10** (4), P. 731–736.
- [12] Gueymard C.A., Myers D., Emery K. Proposed reference irradiance spectra for solar energy systems testing. *Solar Energy*, 2002, **73** (6), P. 443–467.
- [13] Bonaccorso F., Zerbetto M., Ferrari A.C., Amendola V. Sorting Nanoparticles by Centrifugal Fields in Clean Media. *The Journal of Physical Chemistry C*, 2013, **117** (25), P. 13217–13229.
- [14] Brady B., Wang P.H., Steenhoff V., Brolo A.G. Nanostructuring Solar Cells Using Metallic Nanoparticles. *Metal Nanostructures for Photonics*, 2019, P. 197–221.
- [15] Dzhafarov T.D., Pashaev M.A., et al. Influence of silver nanoparticles on the photovoltaic parameters of silicon solar cells. *Advances in Nano Research*, 2015, **3** (3), P. 133–141.
- [16] Giannini V., Francescato Y., et al. Fano resonances in nanoscale plasmonic systems: a parameter-free modeling approach. *Nano Lett.*, 2011, **11** (7), P. 2835–2840.
- [17] Chegaar M., Hamzaoui A., et al. Effect of Illumination Intensity on Solar Cells Parameters. *Energy Procedia*, 2013, **36**, P. 722–729.
- [18] Bao X.Q., Liu L.F. Platinum nanoparticle interlayer promoted improvement in photovoltaic performance of silicon/PEDOT: PSS hybrid solar cells. *Materials Chemistry and Physics*, 2015, **149–150**, P. 309–316.
- [19] Chegaar M., Hamzaoui A., et al. Effect of illumination intensity on solar cells parameters. *Energy Procedia*, 2013, **36**, P. 722–729.
- [20] Bunea G., Wilson K., et al. Low Light Performance of Mono-Crystalline Silicon Solar Cells. *IEEE 4th World Conference on Photovoltaic Energy Conversion*, 2006, P. 1312–1314.
- [21] Saloux E., Teysseidou A., Sorin M. Explicit model of photovoltaic panels to determine voltages and currents at the maximum power point. *Solar Energy*, 2011, **85** (5), P. 713–722.
- [22] Khan F., Singh S.N., Husain M. Effect of illumination intensity on cell parameters of a silicon solar cell. *Solar Energy Materials and Solar Cells*, 2010, **94** (9), P. 1473–1476.

Surface plasmon resonance optical sensor for COVID-19 detection

H. A. Zain¹, M. Batumalay², H. R. A. Rahim³, Z. Harith⁴, M. Yasin⁵, S. W. Harun¹

¹Photonics Engineering Laboratory, Department of Electrical Engineering, University of Malaya, 50603 Kuala Lumpur, Malaysia

²Faculty of IT, INTI International University, 71800 Nilai, Negeri Sembilan, Malaysia

³Faculty of Electronic and Computer Engineering, Universiti Teknikal Malaysia Melaka, Melaka, Malaysia

⁴Faculty of Engineering and QS, INTI International University, 71800 Nilai, Negeri Sembilan, Malaysia

⁵Department of Physics, Faculty of Science and Technology, Airlangga University, Surabaya, Indonesia

swharun@um.edu.my

PACS 42.82.Gw, 42.82.-m, 42.82.Ds

DOI 10.17586/2220-8054-2021-12-5-575-582

The transmission of SARS-CoV-2, the novel severe acute respiratory syndrome corona virus have caused the corona virus disease (Covid-19) worldwide pandemic. Overcoming this pandemic requires identifying patients to avoid further spread of the disease. Real-time, sensitive, and cost-efficient methods for detecting the COVID-19 virus are crucial. Optical sensors provide one such means to achieve this, especially using surface plasmon resonance due to its advantages such as high sensitivity and excellent detection limits. In this paper, we propose a sensor for COVID-19 detection which is based on a simple Kretschmann configuration with gold layers and thiol-tethered DNA for the ligand layer. Angle interrogation was used to obtain the sensitivity of this structure using Matlab numerical analysis. The performance of the sensor was investigated with two types of prisms, SF10 and SF11, while varying the gold layer thickness between 45 – 60 nm. This information was then used to determine which combination of prism and gold thickness are ideal for detecting COVID-19 using thiol-tethered DNA. Thiol-tethered DNA layer sensor showed the highest sensitivity of 137 degree/RIU when a SF10 prism was used with a 50 – 60 nm gold layer and thiol tethered DNA layer.

Keywords: optical sensors, COVID-19, surface plasmon resonance, plasmonic, energy efficiency.

Received: 19 July 2021

Revised: 9 October 2021

1. Introduction

Coronavirus detection is an urgent step in controlling the spread of the COVID-19 pandemic which caused loss of life and disruption of daily life. Identifying infected patients is needed to control the spread of this disease and mitigate its effects. However, the diverse clinical presentations of this disease such as cough, sore throat, diarrhea, and fever [1], make conclusive tests necessary. The long life of this virus on surfaces ranges from 2 – 72 hours [2] shows the continued need to detect the virus early and conclusively. Sensors that fulfill the ASSURED criteria are needed for COVID-19 control; ASSURED stands for affordability, sensitivity, specificity, user-friendliness, rapidity, and robustness, being equipment-free, and deliverability to end-users.

Current methods for detecting COVID-19 suffer from the need of complicated equipment and high cost. Some of the current technologies such as CT examinations show only pneumonia and lung lesions, which are a sign of COVID-19 but can also be caused by other diseases [3–5]. Enzyme-linked immunosorbent assay (ELISA) and reverse-transcription polymerase chain reaction (RT-PCR) are more common tests, but they require multiple steps, trained professionals to conduct them, and have a long response time [6, 7]. RT-PCR, currently the most common testing method; has been shown to give false-negatives before and needed specialized equipment and trained professionals to be performed [3]. This caused the RT-PCR test to be a bottleneck in the efforts to control the COVID-19 pandemic. Additionally, these tests are also expensive and require specialized delicate equipment. Thus, the challenge of detecting COVID-19 with inexpensive reliable equipment is still an unsolved problem.

Optical sensors might provide a potential solution to this challenge due to the improved sensitivities and detection limits of modern optical sensors, especially ones using surface plasmon resonance. Surface plasmon resonance optical sensors are label-free, efficient, and give real-time measurements. Optical sensors have been shown to have good selectivity, short response time, and can be optimized to be cost-beneficial [8–10]. Thus, thoroughly examining the potential of using surface plasmon resonance optical sensors is necessary. Surface plasmon resonance optical sensors use the surface plasmon resonance phenomenon and the resulting wavelength shift, angle shift, or intensity change to detect an analyte [11, 12]. Surface plasmon waves are free-electron density waves in a thin metal surface such as gold or silver [13, 14]. If p-polarized with the matching wave vector, these waves hit the metal boundary, these surface plasmon waves become excited and the light energy gets coupled into them causing the reflectivity of the metal surface

to have a dip. The coupled light needs to match the wave vector of the polaritons and the way to achieve that is the use of a prism, fiber gratings, or D-shaped fiber evanescent mode [15–17].

If a Kretschmann setup is used for the sensor, the light hits the prism and achieves attenuated internal reflection, causing the evanescent mode to penetrate the thin metal coating layer on the prism. If the angle of incident light is the surface plasmon resonance angle, the wave vector of the light and the surface plasmon waves match, light is coupled into these waves. Thus, a dip appears in the light reflected from the prism. This angle is sensitive to changes in the refractive index of the medium surrounding the prism-metal interface, where the analyte is usually applied. Changes in the analyte refractive index, for instance, caused by the ligand and the analyte interacting on the sensor, cause changes in the surface plasmon resonance angle. By tracking these changes, the surface plasmon resonance Kretschmann setup can be used as a sensor [18].

Surface plasmon resonance sensors have been used before to detect many pathogens such as dengue [18, 19], H5N1 [20], Ebola [21], and hepatitis [22, 23] virus surface antibodies. This shows the ability of surface plasmon sensors to detect pathogens in solutions. To detect a virus, there are multiple ways such as detection of elevated biomarkers like immunoglobulin M (IgM) and immunoglobulin G (IgG). A virus can be directly detected by the surface proteins. COVID-19 virus has S (spike), E (envelope), M (membrane), and N (nucleocapsids) proteins. For instance, similar diseases SARS-CoV and MERS-CoV have been detected using the viruses' proteins [24–26]. Viruses can also be detected by thiol tethered DNA. Surface plasmon resonance sensors have good potential to be used to detect the COVID-19 virus in samples.

Various optical methods have also been proposed and used to detect these viruses. For instance, photon counting has been used to improve the sensitivity of lateral flow assay technology. This technique can detect the density of antibodies with good sensitivity [27]. In other research, an nano-plasmonic sensor for detecting SARS-CoV-2 monoclonal antibodies (mAbs) showed a detection limit of up to 370 vp/mL [28]. NP surface protein of the virus was also detected by immobilizing anti-SARS-CoV-2 antibodies on modified gold sensor chips [29]. Additionally, SPR imaging was also used to test the binding of IgM, IgG and IgA antibodies [30]. Plasmonic photothermal (PPT) effect and localized surface plasmon resonance (LSPR) with the help of two-dimensional gold nano islands (AuNIs) functionalized with complementary DNA receptors were also used to detect the virus [31]. Incorporating layers of silver, BaTiO₃, and silicon have been shown to achieve sensitivity up to 130 degree/RIU in simulations [32]. In another simulation, gold nanorods (Au NRs) were used on BK7 prism to detect the virus spike protein with sensitivity of 111.11 degree/RIU [33]. In this work, a sensitivity >120 degree/RIU was reached in simulation. There is big potential for optical sensing of this virus.

In this paper, we present the preliminary design of a surface plasmon resonance sensor using the Kretschmann setup with gold thin layer coating and a thiol tethered DNA layer as a method to detect the COVID-19 in liquid samples. The theoretical and simulation work are our first step towards building this sensor in our laboratory and using the sensor to test actual COVID-19 sample collected from potential patients. These are basic but necessary steps towards developing an optical sensor for COVID-19.

2. Working principle and sensor diagram

In this surface plasmon resonance sensor, a Kretschmann prism configuration with multiple layers was used. To perform the numerical analysis, the transfer matrix method and Fresnel's equation were used [34]. This sensor has four layers: the prism, the thin gold layer, the thiol-tethered DNA, and lastly the test sample. In this work, the boundary condition at the first two layers $Z = Z_1 = 0$ and the last two layers have the boundary condition of $Z = Z_{n-1}$. The transfer matrix is the formula that relates the tangential components of the electric and magnetic fields for the first and last layers of the sensor and it is expressed in the following equation:

$$\begin{bmatrix} E_1 \\ B_1 \end{bmatrix} = M \times \begin{bmatrix} E_{n-1} \\ B_{n-1} \end{bmatrix}. \quad (1)$$

Given that E_1 and B_1 are the tangential components of the electric and magnetic field of the first layer. E_{n-1} and B_{n-1} are the tangential components of the electric and magnetic field of the N and $N - 1$ layer. The M matrix presents the sensing structure's characteristics. The reflection coefficients also depend on M . Since surface plasmon resonance needs p-polarized light (or known as TM polarized light), the M matrix for p-polarized light is given as:

$$M = \left(\prod_{k=2}^{N-1} M_k \right) = \begin{pmatrix} M_{11} & M_{12} \\ M_{21} & M_{22} \end{pmatrix}, \quad (2)$$

$$M_k = \begin{bmatrix} \cos \delta_k & \frac{-i \sin \delta_k}{\gamma_k} \\ -i\gamma_k \times \sin \delta_k & \cos \delta_k \end{bmatrix}, \quad (3)$$

$$\gamma_k = \sqrt{\frac{\mu_k}{\epsilon_k}} \times \cos \theta_k = \frac{\sqrt{\epsilon_k - n_1^2 \sin^2 \theta_1}}{\epsilon_k}, \quad (4)$$

$$\delta_k = \frac{2\pi}{\lambda} n_k \cos \theta_k (Z_k - Z_{k-1}) = \frac{2\pi d_k}{\lambda} \sqrt{\epsilon_k - n_1^2 \sin^2 \theta_1}. \quad (5)$$

Here, μ_k and ϵ_k are the magnetic permeability and the electric permittivity, respectively. λ is the operating wavelength and d_k is the thickness of the k^{th} layer of the sensor system. The total reflection coefficient, r_p will be:

$$r_p = \frac{(M_{11} + M_{12}\gamma_N)\gamma_1 - (M_{21} + M_{22}\gamma_N)}{(M_{11} + M_{12}\gamma_N)\gamma_1 + (M_{21} + M_{22}\gamma_N)}, \quad (6)$$

with M_{11} , M_{12} , M_{21} , M_{22} being the coefficients of the transfer matrix and the reflectivity is given as [32, 34–36]:

$$R_p = |r_p|^2. \quad (7)$$

The sensor system consists of three main components: He–Ne laser source, photo detector and prism as shown in Fig. 1. He–Ne laser source with 632.8 nm wavelength will be used to provide light [13] and a photo detector will be used to receive the light reflected from inside the prism and the reflectivity will be calculated by using Equations (1) to (7). All these calculations were done using a Matlab. The prism is a vital part of the sensor system and for this simulation, SF11 or SF10 were chosen. A very thin layer of gold (with a thickness ranging from 45 to 60 nm) is deposited on the prism surface [14, 15, 37, 38]. After that, the thiol-tethered DNA of the analyte (the virus) will be immobilized on the surface of that gold layer. The assumption is that the solution containing the analyte will be applied to the chip surface by a sealed flow cell to guarantee safety. The virus will take some time to bind with the thiol tethered DNA and cause a refractive index change on the prism surface. Previous work has shown that the thiol tethered DNA has a refractive index of 1.3 – 1.5, depending on the layers' thickness. At a 4 nm thickness, the refractive index will approach 1.4 [32, 39].

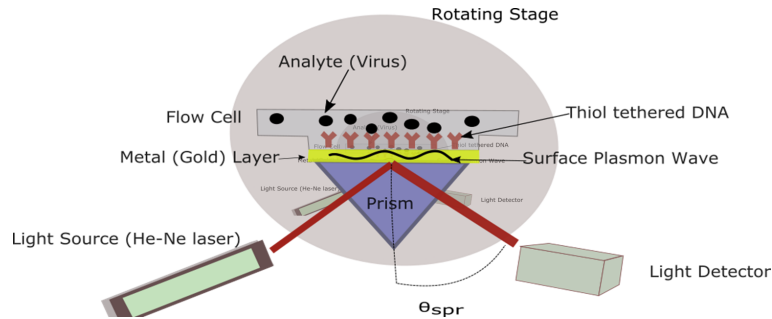


FIG. 1. The proposed sensor system

In this work, the average refractive index of the virus is estimated to be 1.54, the membrane protein has a refractive index of 1.46 ± 0.006 while the virus load density in a liquid sample is estimated to be at average of 7×10^6 [29, 33]. If the virus exists in a sample applied to the coated prism surface, and as time passes, the binding will happen between the layer and the virus, causing a refractive index to change that results in a resonance angle shift. In the calculation, two values of refractive index are used: 1.33 for a clean aqueous sample and 1.34 to show the potential of the sensor to detect the binding between the virus in a sample and the sensing layer of the prism. The resonant angle at the minimum reflectivity is obtained in this work. The change in the resonant angle with the presence of the virus in the sample is investigated. It indicates the ability of this sensor to detect the existence of an analyte (the virus) in a solution.

Several performance parameters such as sensitivity, full width at half maximum/minimum (FWHM), detection accuracy (DA), figure of merit (FOM) and minimum reflectivity (R_{min}) are investigated in this work. These parameters show the feasibility of using this biosensor to detect an analyte or virus in a sample. The sensitivity of the surface plasmon resonance optical sensor is defined as the ratio of the change in resonance angle to the change in the surrounding refractive index. The binding effect of the analyte with the immobilized ligand on the thin metal layer of the sensor results in a change of that layers' refractive index. By tracking that refractive index change and the resonance angle shift, the sensitivity of the sensors can be calculated. The center resonance angle is the location of the minimum

optical power while the FWHM angle is the angle at which the output is 3 dB above the zero level. The quality factor is also related to FWHM by the following formula:

$$\text{Q-factor} = \frac{\theta_0}{\text{FWHM}} \quad (8)$$

DA is the ratio of the total angle shift and the FWHM, and also depends on the sensor's signal to noise ratio (SNR). The FOM of the sensor is defined as the ratio between the sensitivity and the FWHM. The minimum value of reflectivity which happens at the surface plasmon resonance angle can be referred to as R_{\min} . R_{\min} shows how much of the incident light is coupled into the surface plasmon wave. Smaller R_{\min} values indicate better momentum transfer.

3. Results and discussion

A performance comparison between SF10 and SF11 prisms at four different gold layer thicknesses is investigated using MatLab simulation to calculate the reflectivity of the prism setup as the thickness varies between 45 – 60 nm. The main concern is the feasibility of this experiment with readily available setups. The sensor setup performance parameters need to be examined for every potential setup between the two prism types and the thickness variation for the gold layer with the thiol-tethered DNA. Table 1 shows the refractive index of the layers of the sensor.

TABLE 1. The refractive index of the sensor's layers

Layer	Refractive index	Reference
SF10	1.72314	[34, 40]
SF11	1.77860	[34, 41]
Gold	$0.1726 + i3.4218$	[34]
Thiol-tethered DNA at 4 nm thickness	1.40	[32, 39]

Firstly, the reflectivity response of the setup for the SF10 prism at the four determined gold thicknesses is investigated and the results are presented in Figs. 2(a–d) and Table 2. Fig. 2(a) shows the sensor response when the gold layer thickness is 45 nm, the subsequent Figs. 2(b,c,d) show the response when the gold layer thickness is 50, 55, 60 nm respectively. This helps navigating our choices in the laboratory testing stage.

TABLE 2. The SF10 prism performance

SF10 Prism				
Gold thickness (nm)	Sensitivity ($^{\circ}/RIU$)	R_{\min} (%)	FWHM ($^{\circ}$)	FOM
45	133	0.17	8.5	15.65
50	136	0.003	6.7	20.30
55	137	0.05	5.4	25.37
60	137	0.15	5.9	23.22

Figure 2 shows the response of the SF10 prism sensor to the presence of the analyte in a liquid solution. For the 50 nm gold layer, the reflectivity reaches its lowest value as shown in Fig. 2(b). While for 45 nm gold layer, it shows deep dips as shown in Fig. 2(a). The deepest dip with narrow FWHM is achieved with 55 nm gold thickness as shown in Fig. 2(c). As can be seen in Figs. 2(a,b), the minimum reflectivity of the sensor occurs when the gold layer thickness is between 45 – 50 nm. This shows the gold coating with thickness between 45 – 50 nm is suitable to be combined with thiol-tethered DNA. The minimum reflectivity of the sensor is slightly higher when the gold layer thickness is 50 – 60 nm as shown in Figs. 2(c and d) and thus it is less suitable for further experimentation.

Table 2 summarizes the performance of the sensor with SF10 prism. As expected, the 50 nm gold layer has the lowest R_{\min} . Meanwhile, the sensitivity is above 100 for all four thicknesses with the layers of 55 and 60 nm show the highest sensitivity of 137. Fig. 3 shows the sensitivity and figure of merit of the SF10 sensor as a function of

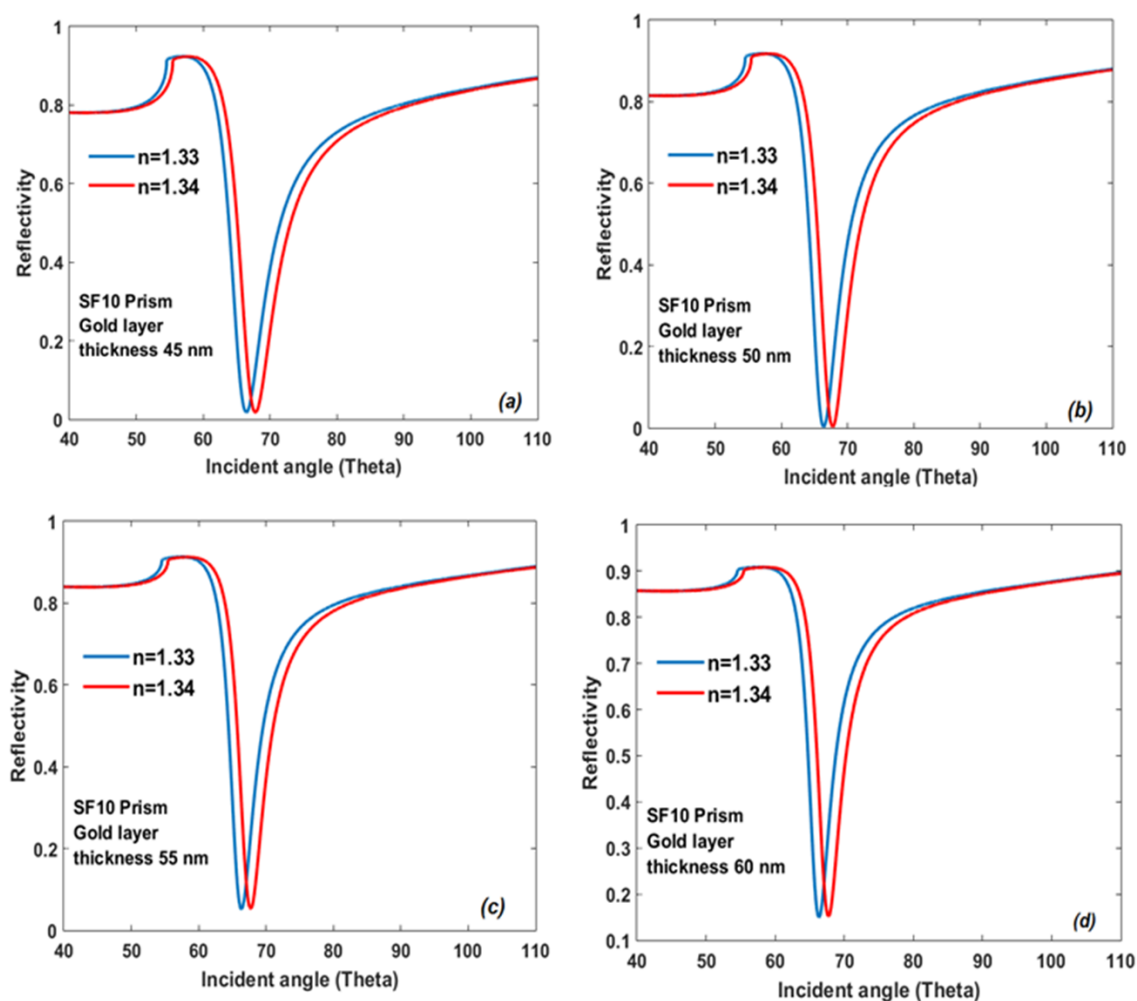


FIG. 2. The SF10 prism sensor response to the analyte with different gold layer thicknesses of (a) 45 nm, (b) 50 nm, (c) 55 nm, and (d) 60 nm

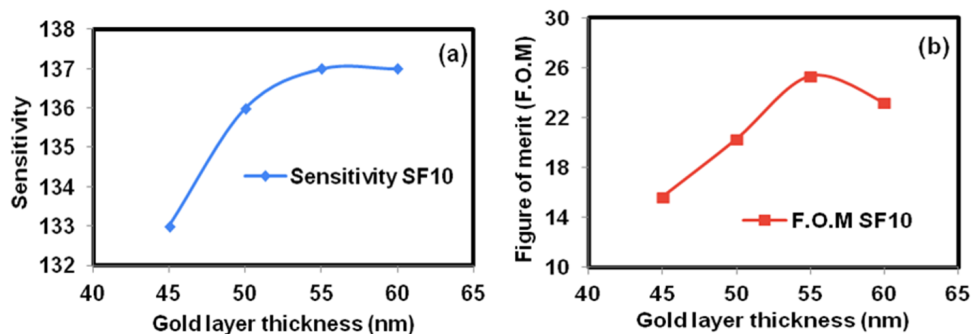


FIG. 3. The sensitivity and FOM against the thickness of gold layer for the sensor with SF10 prism

the gold layer thickness. Choosing the ideal sensor setup will be a trade-off between reflectivity, FOM and FWHM performances. If the best FOM is needed, then better option is to proceed with a 50 – 60 nm layer with an SF10 prism.

Figure 4 shows the sensor's response when an SF11 prism is used. This prism has a higher refractive index but can be costly, so a comparison between them and SF10 is necessary to decide which is better for detecting the analyte using thiol tethered DNA. Figs. 4(a,b,c and d) show the sensor response when the gold layer thickness is exactly 45, 50, 55, 60 nm respectively. Similar resonance dip and FWHM patterns are obtained as compared to the previous

sensor with SF10 prism. However, the FWHM for the SF10 sensor was smaller. As can be seen in Fig. 4, the smaller reflectivity of the sensor occurs at the resonance angle when the gold layer thickness is between 45 and 50 nm as compared to the thicker thicknesses of 55 and 60 nm. This indicates that the gold coating with thickness between 45 –50 nm is suitable to be combined with thiol-tethered DNA for sensing application.

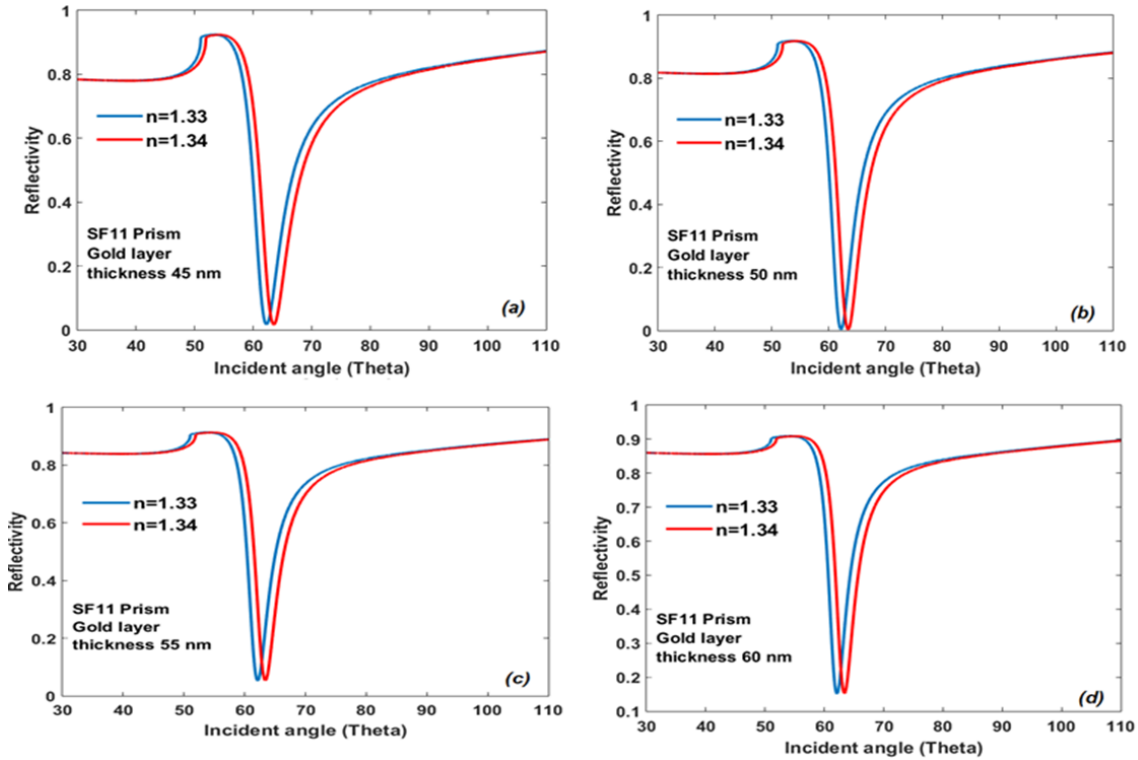


FIG. 4. The SF11 sensor performance with different gold layer thicknesses a) gold layer thickness 45 nm, b) gold layer thickness 50 nm, c) gold layer thickness 55 nm, d) gold layer thickness 60 nm

Figure 5 shows the sensitivity and FOM for the SF11 sensor. For this prism, the thiol-tethered DNA sensor has a lower but more stable sensitivity compared to the previous SF10 prism. The sensitivity varies within 125 to $126^\circ/RIU$ as the gold layer thickness was changed from 45 to 60 nm. However, the FOM peaks at 55 nm. Table 3 summarizes the performance of the sensor with SF11 prism. It indicates a similar performance with the previous prism.

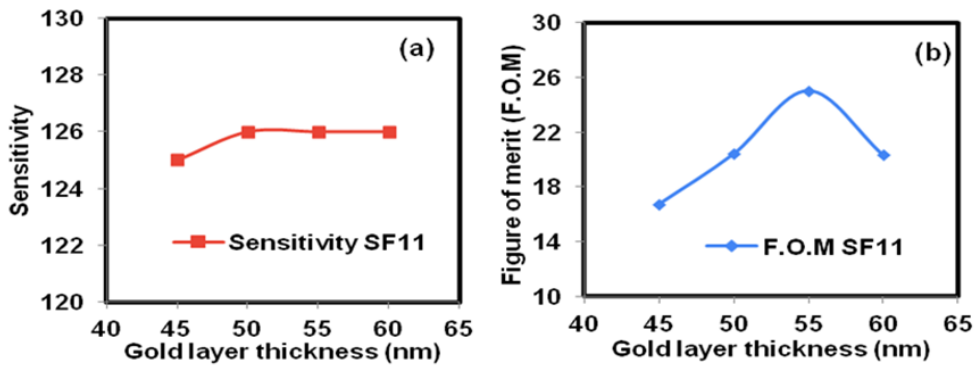


FIG. 5. (a) Sensitivity and (b) figure of merit against the gold thickness for the SF11 sensor

TABLE 3. The SF11 sensor performance

SF11prism				
Metal thickness (nm)	Sensitivity SF11(°/RIU)	R_{\min} (%)	FWHM (°)	F.O.M
45	125	0.016	7.440	16.801
50	126	0.003	6.160	20.455
55	126	0.054	5.030	25.050
60	126	0.153	6.180	20.388

4. Conclusion

In this paper, a COVID-19 sensor using thiol-tethered DNA as a ligand layer with two types of prisms; SF10 and SF11 is proposed. Numerical analysis was completed using MATLAB, to study the response of the sensor. The aim was to determine the type of prism and the thickness of the gold layer which is ideal for thiol-tethered DNA detection of Covid-19. The two prisms were found to have comparable performance. However, SF10 prisms with gold coating between 50 – 60 nm demonstrated a superior performance in terms of sensitivity. Future work will focus on optimizing the layers to improve the FWHM and FOM of the proposed design.

Acknowledgements

This work was supported by the Airlangga University Research Grant (2021) and the University of Malaya (Grant No: ST036-2020).

References

- [1] Menni C., Valdes A.M., et al. Real-time tracking of self-reported symptoms to predict potential COVID-19. *Nature Medicine*, 2020, **26** (7), P. 1037–1040.
- [2] Van Doremalen N., Bushmaker T., et al. Aerosol and Surface Stability of SARS-CoV-2 as Compared with SARS-CoV-1. *New England Journal of Medicine*, 2020, **382** (16), P. 1564–1567.
- [3] Xie X., Zhong Z., et al. Chest CT for Typical Coronavirus Disease 2019 (COVID-19) Pneumonia: Relationship to Negative RT-PCR Testing. *Radiology*, 2020, **296** (2), E41–E45.
- [4] Li X., Zeng W., et al. CT imaging changes of corona virus disease 2019(COVID-19): a multi-center study in Southwest China. *Journal of Translational Medicine*, 2020, **18** (1), 154.
- [5] Fang Y., Zhang H., et al. Sensitivity of Chest CT for COVID-19: Comparison to RT-PCR. *Radiology*, 2020, **296** (2), E115–E117.
- [6] Nguyen T., Duong Bang D., Wolff A. 2019 Novel Coronavirus Disease (COVID-19): Paving the Road for Rapid Detection and Point-of-Care Diagnostics. *Micromachines (Basel)*, 2020, **11** (3), 306.
- [7] Kaur M., Tiwari S., Jain R. Protein based biomarkers for non-invasive Covid-19 detection. *Sens Biosensing Res*, 2020, **29**, 100362.
- [8] Jing J.-Y., Wang Q., Zhao W.-M., Wang B.-T. Long-range surface plasmon resonance and its sensing applications: A review. *Optics and Lasers in Engineering*, 2019, **112**, P. 103–118.
- [9] Lukose J., Chidangil S., George S.D. Optical technologies for the detection of viruses like COVID-19: Progress and prospects. *Biosensors and Bioelectronics*, 2021, **178**, 113004.
- [10] Amendola V., Pilot R., et al. Surface plasmon resonance in gold nanoparticles: a review. *J. Phys. Condens. Matter*, 2017, **29** (20), 203002.
- [11] Drobysch M., Ramanaviciene A., Viter R., Ramanavicius A. Affinity Sensors for the Diagnosis of COVID-19. *Micromachines (Basel)*, 2021, **12** (4), 390.
- [12] Abid S.A., Ahmed Muneer A., et al. Biosensors as a future diagnostic approach for COVID-19. *Life Sciences*, 2021, **273**, 119117.
- [13] Prabowo B.A., Purwidyantri A., Liu K.C. Surface Plasmon Resonance Optical Sensor: A Review on Light Source Technology. *Biosensors (Basel)*, 2018, **8** (3), 80.
- [14] Gupta G., Kondoh J. Tuning and sensitivity enhancement of surface plasmon resonance sensor. *Sensors and Actuators B: Chemical*, 2007, **122** (2), P. 381–388.
- [15] Sharma A.K., Jha R., Gupta B.D. Fiber-Optic Sensors Based on Surface Plasmon Resonance: A Comprehensive Review. *IEEE Sensors Journal*, 2007, **7** (8), P. 1118–1129.
- [16] Roh S., Chung T., Lee B. Overview of the characteristics of micro- and nano-structured surface plasmon resonance sensors. *Sensors (Basel)*, 2011, **11** (2), P. 1565–1588.
- [17] Patil P.O., Pandey G.R., et al. Graphene-based nanocomposites for sensitivity enhancement of surface plasmon resonance sensor for biological and chemical sensing: A review. *Biosensors and Bioelectronics*, 2019, **139**, 111324.
- [18] Omar N.A.S., Fen Y.W., et al. Quantitative and selective surface plasmon resonance response based on a reduced graphene oxide-polyamidoamine nanocomposite for detection of dengue virus e-proteins. *J. Nanomaterials*, 2020, **10** (3), 569.
- [19] Jahanshahi P., Zalnezhad E., Sekaran S.D., Adikan F.R. Rapid immunoglobulin M-based dengue diagnostic test using surface plasmon resonance biosensor. *Scientific Reports*, 2014, **4**, 3851.
- [20] Bai H., Wang R., et al. A SPR aptasensor for detection of avian influenza virus H5N1. *Sensors (Basel)*, 2012, **12** (9), P. 12506–12518.

- [21] Wang S., Shan X., et al. Label-free imaging, detection, and mass measurement of single viruses by surface plasmon resonance. *Proceedings of the National Academy of Sciences of the USA*, 2010, **107** (37), P. 16028–16032.
- [22] Uzun L., Say R., Unal S., Denizli A. Production of surface plasmon resonance based assay kit for hepatitis diagnosis. *Biosensors and Bioelectronics*, 2009, **24** (9), P. 2878–2884.
- [23] Tam Y.J., Zeenathul N.A., et al. Wide dynamic range of surface-plasmon-resonance-based assay for hepatitis B surface antigen antibody optimal detection in comparison with ELISA. *Biotechnology and Applied Biochemistry*, 2017, **64** (5), P. 735–744.
- [24] Zhao G., He L., et al. A novel nanobody targeting Middle East respiratory syndrome coronavirus (MERS-CoV) receptor-binding domain has potent cross-neutralizing activity and protective efficacy against MERS-CoV. *Journal of Virology*, 2018, **92** (18), e00837–18.
- [25] Ahn D.G., Jeon I.J., et al. RNA aptamer-based sensitive detection of SARS coronavirus nucleocapsid protein. *Analyst*, 2009, **134** (9), P. 1896–1901.
- [26] Chandra S., Bharadwaj R., Mukherji S. Label free ultrasensitive optical sensor decorated with polyaniline nanofibers: Characterization and immunosensing application. *Sensors and Actuators B: Chemical*, 2017, **240**, P. 443–450.
- [27] Peng T., Liu X., et al. Enhancing sensitivity of lateral flow assay with application to SARS-CoV-2. *Applied Physics Letters*, 2020, **117** (12), 120601.
- [28] Huang L., Ding L., et al. One-step rapid quantification of SARS-CoV-2 virus particles via low-cost nanoplasmonic sensors in generic microplate reader and point-of-care device. *Biosensors and Bioelectronics*, 2021, **171**, 112685.
- [29] Bong J.-H., Kim T.-H., et al. Pig Sera-derived Anti-SARS-CoV-2 Antibodies in Surface Plasmon Resonance Biosensors. *BioChip Journal*, 2020, **14** (4), P. 358–368.
- [30] Schasfoort R.B.M., van Weperen J., et al. High throughput surface plasmon resonance imaging method for clinical detection of presence and strength of binding of IgM, IgG and IgA antibodies against SARS-CoV-2 during CoViD-19 infection. *Methods X*, 2021, **8**, 101432.
- [31] Qiu G., Gai Z., et al. Dual-functional plasmonic photothermal biosensors for highly accurate severe acute respiratory syndrome coronavirus 2 detection. *ACS nano*, 2020, **14** (5), P. 5268–5277.
- [32] Uddin S.M.A., Chowdhury S.S., Kabir E. Numerical Analysis of a Highly Sensitive Surface Plasmon Resonance Sensor for SARS-CoV-2 Detection. *Plasmonics*, 2021, P. 1–13.
- [33] Das C.M., Guo Y., et al. Gold Nanorod Assisted Enhanced Plasmonic Detection Scheme of COVID-19 SARS-CoV-2 Spike Protein. *Advanced theory and simulations*, 2020, **3** (11), 2000185.
- [34] Yamamoto M. Surface plasmon resonance (SPR) theory: tutorial. *Review of Polarography*, 2002, **48** (3), P. 209–237.
- [35] Rahman M.S., Anower M.S., et al. Design and numerical analysis of highly sensitive Au-MoS₂-graphene based hybrid surface plasmon resonance biosensor. *Optics Communications*, 2017, **396**, P. 36–43.
- [36] Saifur Rahman M., Rikta K.A., Bashar L.B., Anower M.S. Numerical analysis of graphene coated surface plasmon resonance biosensors for biomedical applications. *Optik*, 2018, **156**, P. 384–390.
- [37] Brahmachari K., Ray M. Effect of prism material on design of surface plasmon resonance sensor by admittance loci method. *Frontiers of Optoelectronics*, 2013, **6** (2), P. 185–193.
- [38] Sharma N.K., Yadav S., Sajal V. Theoretical analysis of highly sensitive prism based surface plasmon resonance sensor with indium tin oxide. *Optics Communications*, 2014, **318**, P. 74–78.
- [39] Peterlinz K.A., Georgiadis R.M., Herne T.M., Tarlov M.J. Observation of Hybridization and Dehybridization of Thiol-Tethered DNA Using Two-Color Surface Plasmon Resonance Spectroscopy. *Journal of the American Chemical Society*, 1997, **119** (14), P. 3401–3402.
- [40] SCHOTT, Optical Glass Collection N-SF10, in 728284.428, ed, 2014, URL: https://shop.schott.com/advanced_optics/en/Optical-Glass/N-SF10/c/optical-glass/glass-N-SF10.
- [41] SCHOTT, Optical Glass Collection N-SF11, in 785257.322, ed, 2014, https://shop.schott.com/advanced_optics/en/N-SF11/c/glass-N-SF11.

Realization of combinational logic circuits using standard functions in quantum dot cellular automata

Ratna Chakrabarty, Niranjana Kumar Mandal

Institute of Engineering & Management, Department of Electronics & Communication Engineering,
Salt Lake Electronics Complex, Sector V, Kolkata, 700091, India
ratna.chakrabarty@iemcal.com, niranjanmandal54@gmail.com

DOI 10.17586/2220-8054-2021-12-5-583-597

A set of functions commonly used in basic circuits are defined as standard functions. They are so called because different combinations of different logic circuits are designed using these functions. They are also used to realize combinational logic circuits and most Boolean expressions. In this paper, 13 standard functions are discussed with their various applications using Quantum Dot Cellular Automata known as QCA which is currently a familiar nanotechnology for its ultra-low power consumption and high speed operations. The designed functions are analyzed with area, latency and cell count. Energy calculations have been done with the suitable input for its stable operation. Algorithms are also established for the designed functions to realize in QCA technology.

Keywords: standard functions, majority gate, universal gate, encoder, adder, comparator.

Received: 16 September 2021

Revised: 27 September 2021

1. Introduction

Quantum Dot Cellular Automata technology aimed to provide an alternative to current silicon transistor technology for its low power operation. It has created a system in which electrons are bound in cells; polarization is the alignment of electrons within them. Each piece of information will be transmitted through the wire as a change in polarization. It also developed majority voters, inverters and wires. When the first phase of development was completed, it became the priority of designers and technologists to surpass previous work. The major challenge of the development phase is increasing spatial and temporal efficiency. Scientists aimed to find a more sophisticated design that could perform the same task faster. Also, during the dawn of the VLSI era, using less and less space to implement more and more logic would become unavoidable in order to stay competitive in the shrinking race. Quantum Dot Cellular Automata is mainly implemented in software program. But some researchers in early 1990's, mainly C. S. Lent, exclaimed for a physical realization of quantum dot cells. This technique, since its inception, gained tremendous popularity and it was first fabricated in 1993 [1]. By using the concepts of physics and nanotechnology, Lent realized quantum cells for computation using very low power. The fundamental structural unit of Quantum Dot Cellular Automata is the QCA Cell. Each cell consists of four conductors in the form of metal islands [2, 3] that forms the quantum dots. The paper is framed with the overview of the basic concept of Quantum dot cellular automata, and then it discussed 13 standard functions. The designs are implemented with the help of layered NAND and NOR gates in QCA. Next, it describes the QCA based circuit implementation and energy analysis of the 13 standard functions and different parameters of the designed circuits. The last section concludes the paper with the future applications.

2. Materials and methods

2.1. QCA cell

A Quantum Dot cell has 4 dots with two additional electrons. It has two configurations; one of which is used to transmit the +1 binary information and another as 0. The four phase clock scheme is needed to carry the information through the cells. Cells and clocks together can act as a medium to create device-device interaction with very low power dissipation (on the order of 10 to 20 Joules). QCA devices exist and multi-device circuits have been demonstrated at low temperatures. Fig. 1 shows the four-dot QCA cell.

In a QCA cell, two ground state polarizations are possible. They are labeled as +1 and -1. The formula for calculating polarization is given below:

$$P = \frac{(p_1 + p_3) - (p_2 + p_4)}{p_1 + p_2 + p_3 + p_4}$$

The equation given above shows the calculation of polarization of a QCA cell. Here, p_i is the charge of the i -th quantum-dot ($p_i = 1$ if an electron is present, otherwise it is 0). These polarizations are represented by logic-0 and logic-1 (in other words, binary 0 and binary 1).

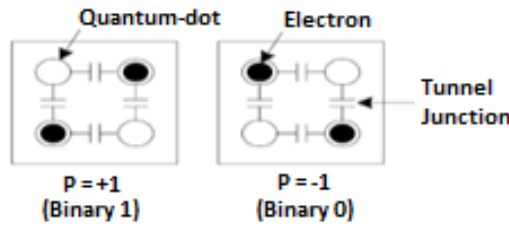


FIG. 1. QCA cells

2.2. Basic components of QCA

The QCA cells and wires can be used to realize the basic components of Quantum dot cellular automata which are used to implement all the combinational and sequential logic circuits of QCA. The first stepping stone of digital electronics is a basic gate. The tools to make basic gates are Majority Gate or Majority voter and Inverter.

Majority Gate or Majority Voter is the fundamental component of QCA [4]. It takes odd numbers of inputs and processes them to find the majority of them and sends that bit to the output pin. Depending on the application, different kinds of majority gates are possible: 3-input majority gate A three-input majority gate has three inputs A, B and C and output Y. The output expression Y can be given by $Y = AB + BC + CA$. Therefore, if more than one input of them is HIGH, output is HIGH. Fig. 2 shows the majority gates implemented in QCA.

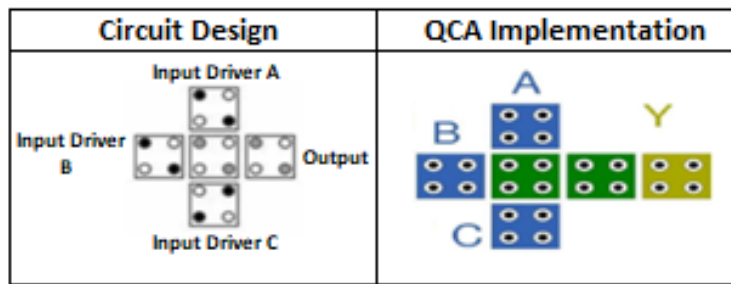


FIG. 2. 3 input Majority gate in QCA

2.3. QCA Clocking

Clocking is an integral part of Quantum-dot Cellular Automata logic circuit design. It not only provides the synchronization and power to run the circuit, it also helps to propagate the input in a pre-defined way. A proper electric field should be introduced for clocking to regulate the electron flow through the channel. By applying the correct time-varying voltage, we can clock the circuit's activity to produce a chain of information. The clocking electric field at the QCA surface is referred to as the clocking field and the signal on the buried wires that will provide such a field is the four-phase signal. Every cycle consists of 4 phases, namely SWITCH, HOLD, RELEASE and RELAX [5]. In traditional electronic systems, timing is controlled through a reference signal (i.e., the clock); however, timing in QCA is accomplished by clocking in four distinct and periodic phases [6, 7]. Fig. 3 shows the clocking scheme of QCA.

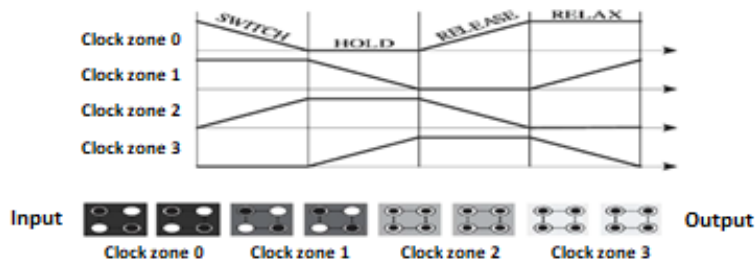


FIG. 3. Different clocking zones in QCA

3. Need for creation of Universal Logic

The two basic needs behind the modification of QCA designs are space complexity and time complexity. Space complexity happens if a simple design takes many cells and hence large space. In that case, it becomes the target of a designer to reduce the circuit without sacrificing its efficiency or input output relation. Moreover, the larger the design more will be the potential energy. Therefore, smaller circuits are also required to attain stability. Time complexity is the amount of time for the input to reach output. If a circuit becomes big, the time to reach the input state to the output increases. This also increases the delay in the circuit and the computation time. In today's world, we always seek for a design with better speed and low computation time, i.e., the speed of operation must be high. Also, the big circuit increases the latency, i.e., the number of clocks required to accomplish any job. NAND and NOR gates are considered to be universal gates, i.e., any logic gate can be generated using NAND and NOR gate. Though the majority voter actually can contain 3 elements, we generally use only 2 elements to generate AND and OR gate. To generate this, we need 6 cells. But we can get the NAND and NOR gates using our modified method using 5 cells [8]. Thus, in a big circuit, this new approach reduces the cell number and the area covered drastically. Also, any Boolean function is expressed using canonical sum-of product (SOP) or canonical product-of sum (POS) form. SOP and POS are generally realized using NAND logic and NOR logic respectively. Therefore, it is always better to use universal gates, because not only it simplifies Boolean expression, it reduces area covered and cell count as well. Fig. 4 shows the QCA implementation of Layered NAND and NOR gate.

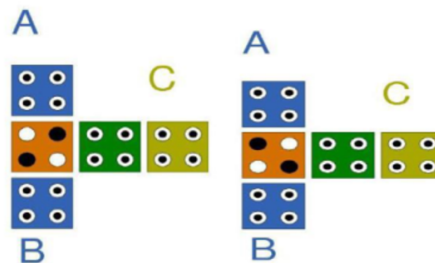


FIG. 4. QCA implementation of (a) Layered NAND Gate (b) Layered NOR Gate

4. Standard functions

The commonly used standard functions [9] are listed below:

1. $D = AB'C$;
2. $D = AB$;
3. $D = A'B'C' + A'BC$;
4. $D = A'BC + AB'C'$;
5. $D = A'B + BC'$;
6. $D = AB' + A'BC$;
7. $D = A'B'C' + A'BC + ABC'$;
8. $D = A$;
9. $D = AB + BC + CA$;
10. $D = A'B + B'C$;
11. $D = A'B + BC + AB'C'$;
12. $D = AB + A'B'$;
13. $D = A'B'C' + ABC' + AB'C + A'BC$.

Implementation of Combinational Logic Digital Circuits using Standard Functions:

- *Half Adder*: Here we are using standard function 2 i.e. $C = AB$ for carry and complement of function 12 i.e. $S = A'B + AB'$ for sum.
- *Full Adder*: The sum is $S = A \text{ XOR } B \text{ XOR } C$, which is the complement of function 13 and carry is $D = AB + BC + CA$ which is standard function 9.
- *Half Subtractor*: Here we are using complement of standard function 12 i.e. $D = A'B + AB'$ for difference and an indirect application of standard function 2, $B_{out} = A'B$ for borrow.
- *Full Subtractor*: The difference is $D = A \text{ XOR } B \text{ XOR } C$, which is the complement of function 13 and borrow is $D = C \times (A \text{ XNOR } B) + A'B$. ($A \text{ XNOR } B$) comes from standard function 12.
- *Binary to Gray Code Converter*: The basic logic gate used is XOR gate which is the complement of function 12.
- *Gray to Binary Code Converter*: 4 bit gray to binary code converter uses 3 XOR gates which is the complement of standard function 12.
- *1 bit Comparator*: It has 3 outputs; equal, greater than and less than; denoted by E, G & L respectively. $E = AB + A'B'$, which is standard function 12. $G = AB'$ and $L = A'B$ which are indirect application of standard function 2.
- *1: 2 Demultiplexer*: It has two outputs; D_0 and D_1 where $D_0 = S'D$ and $D_1 = SD$ which are indirect application of standard function 2.
- *1: 4 Demultiplexer using 1:2 Demultiplexer*: 1:4 demultiplexer requires 3 1:2 demultiplexers. It has 4 output lines which are chosen according to the status of control lines and uses the application of standard function 1.
- *2: 4 Decoder*: A 2:4 decoder circuit has 2 inputs and 4 outputs; denoted by X, Y, A, B, C and D respectively. Here $A = X'Y'$, $B = X'Y$, $C = XY'$, $D = XY$ which are indirect application of standard function 2.
- *4: 2 Encoder*: A 4: 2 encoder has 4 inputs and 2 outputs; namely A, B, C, D, X & Y respectively. Here $X = A + B$ [i.e. $(A'B')$] and $Y = \text{NOT}(B + D)$ [i.e. $(B'D')$] which are indirect application of standard function 2.
- *Even Parity Generator/Checker*: If number of 1's present in input data is even, the parity bit is 1, otherwise 0. This is established using XOR gate which is the complement of standard function 12. Therefore, for a 3 bit number, the parity generator output will be $P = A \text{ XOR } B \text{ XOR } C$.
- *Odd Parity Generator/ Checker*: If number of 1's present in input data is odd, the parity bit is 1, otherwise 0. This is established using XOR gate which is the standard function 12. Therefore, for a 3 bit number, the parity generator output will be $P = \text{NOT}(A \text{ XOR } B \text{ XOR } C)$.
- *2:1 Multiplexer*: A 2:1 multiplexer has 2 inputs and 1 select line denoted by A, B and S respectively and only 1 output denoted by Y. The output is written as $Y = S'A + SB$ which is an indirect application of standard function 10.
- *Basic Gates*: All the basic Gates, e.g. AND, OR, XOR etc. can be realized using the standard functions.

5. Analysis of 13 standard functions

13 standard functions have been discussed previously [9] with the use of NAND and NOR gates in QCA. Table 1 show the functions and algorithm behind it for making that function in QCA based circuits.

Table 1: Realization of standard functions

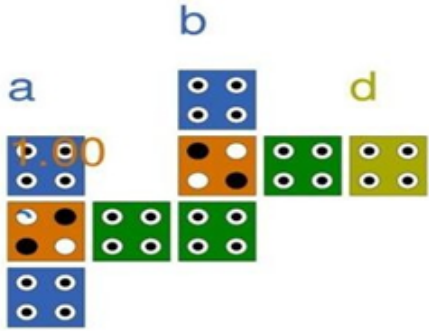
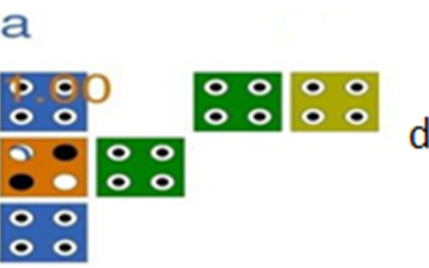
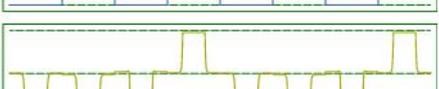
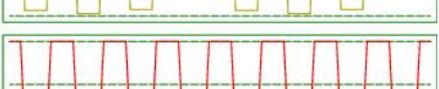
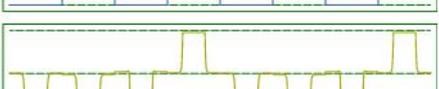
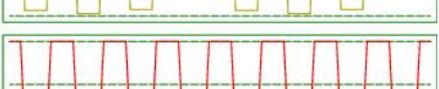
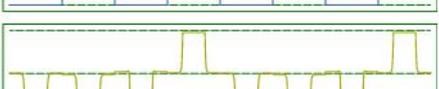
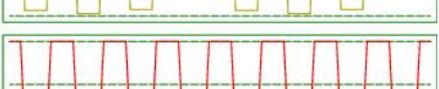
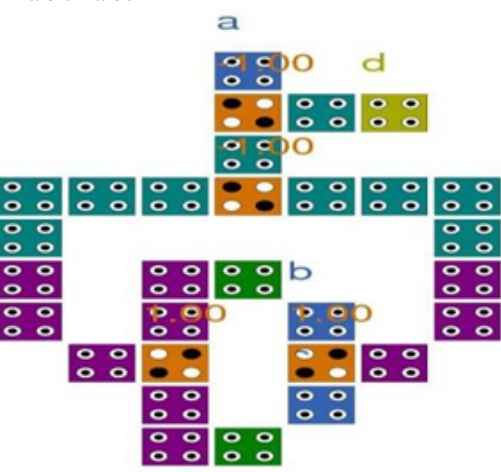
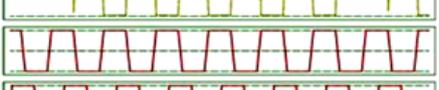
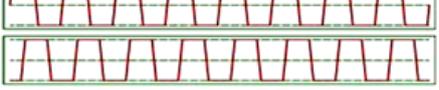
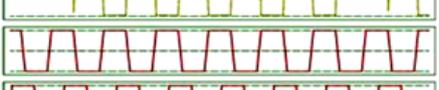
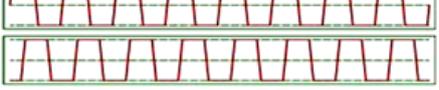
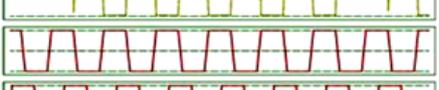
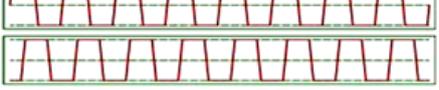
Function	Algorithm
<p>Function: $D = AB'C$ Inputs A and C will be sent to a universal gate with polarization +1 to create intermediate value $i1 = \text{NAND}(A, C)$. Then, the output will be passed through a NOR gate along with input B to get final result. $D = \text{NOR}(i1, B)$.</p>	<p>S1: $i1 = \text{UG}(A, C, +1)$; S2: $D = \text{UG}(B, i1, -1)$.</p>
<p>Function: $D = AB$ First of all, inputs A and B will be sent to a universal gate with polarization +1 to create intermediate value $i1 = \text{NAND}(A, B)$. Then, the output will be passed through a NOT gate along to get final result. $D = \text{NOT}(i1)$.</p>	<p>S1: $i1 = \text{UG}(A, B, +1)$; S2: $D = \text{NOT}(i1)$.</p>
<p>Function: $D = A'B'C' + A'BC$ First of all, inputs C and B will be sent to a universal gate with polarization +1 to create intermediate value $i1 = \text{NAND}(C, B)$. Then, this intermediate value will be used to form another two intermediate values $i2$ and $i3$. $i2 = \text{NAND}(C, i1)$; $i3 = \text{NAND}(B, i1)$. Next, these two values will be passed through a NAND gate to get another intermediate result. $i4 = \text{NAND}(i2, i3)$. Finally, the output will be passed through a NOR gate along with input A to get final result. $D = \text{NOR}(i4, A)$.</p>	<p>S1: $i1 = \text{UG}(C, B, +1)$; S2: $i2 = \text{UG}(C, i1, +1)$; S3: $i3 = \text{UG}(i1, B, +1)$; S4: $i4 = \text{UG}(i2, i3, +1)$; S5: $D = \text{UG}(i4, A, -1)$.</p>
<p>Function: $D = A'BC + AB'C'$ First of all, inputs C and B will be sent to 2 universal gates with polarization +1 and -1 to create intermediate value $i1 = \text{NAND}(C, B)$ and $i2 = \text{NOR}(C, B)$. Then, these intermediate values will be used to form another two intermediate values $i3$ and $i4$. $i3 = \text{NOR}(A, i1)$; $i4 = \text{NAND}(A, i2)$. Next, $i3$ will be passed through a NOR gate to get another intermediate result. $i5 = \text{NOT}(i3)$. Finally, $i5$ and $i4$ will be passed through a NAND gate along with input A to get final result. $D = \text{NAND}(i5, i3)$.</p>	<p>S1: $i1 = \text{UG}(C, B, +1)$; S2: $i2 = \text{UG}(C, B, -1)$; S3: $i3 = \text{UG}(i1, A, -1)$; S4: $i4 = \text{UG}(i2, A, +1)$; S5: $i5 = \text{NOT}(i3)$; S6: $D = \text{UG}(i4, i5, +1)$.</p>
<p>Function: $D = A'B + BC'$ First of all, inputs A and C will be sent to a universal gate with polarization +1 to create intermediate value $i1 = \text{NAND}(A, C)$. Then, the output will be passed again through a NAND gate along with input B to get final result. $i2 = \text{NAND}(i1, B)$, finally, the output will be passed through a NOT gate along to get final result. $D = \text{NOT}(i2)$.</p>	<p>S1: $i1 = \text{UG}(A, C, +1)$; S2: $i2 = \text{UG}(i1, B, +1)$; S3: $D = \text{NOT}(i2)$.</p>
<p>Function: $D = AB' + A'BC$ Let us consider AB' as $d1$ and $A'BC$ as $d2$. For decomposing $d1$, firstly, inputs A and complement of B will be sent to a universal gate with polarization +1 to create intermediate value $i1 = \text{NAND}(A, \text{NOT}(B))$. Then, the output $d1$ is generated by complementing the previous output $i1$ i.e. $d1 = \text{NOT}(i1)$. For decomposing $d2$, firstly, inputs B and C will be sent to a universal gate with polarization +1 to create intermediate value $i2 = \text{NAND}(B, C)$. Then, the output $i3$ is generated by complementing the previous output $i2$ i.e. $i3 = \text{NOT}(i2)$. Next, $i3$ will be passed through another NAND gate along with complement of A i.e. $i4 = \text{NAND}(i3, A)$. Then, the output $d2$ is generated by complementing the previous output $i4$ i.e. $d2 = \text{NOT}(i4)$. The final output D is produced by passing the outputs $d1$ and $d2$ through an NOR gate using polarization -1 and complementing the output. $D = \text{NOT}(\text{NOR}(d1, d2))$.</p>	<p>S1: $i1 = \text{UG}(A, \text{NOT}(B), +1)$; S2: $d1 = \text{NOT}(i1)$; S3: $i2 = \text{UG}(B, C, +1)$; S4: $i3 = \text{NOT}(i2)$; S5: $i4 = \text{UG}(i3, \text{NOT}(A), +1)$; S6: $d2 = \text{NOT}(i4)$; S7: $D = \text{UG}(d1, d2, -1)$.</p>

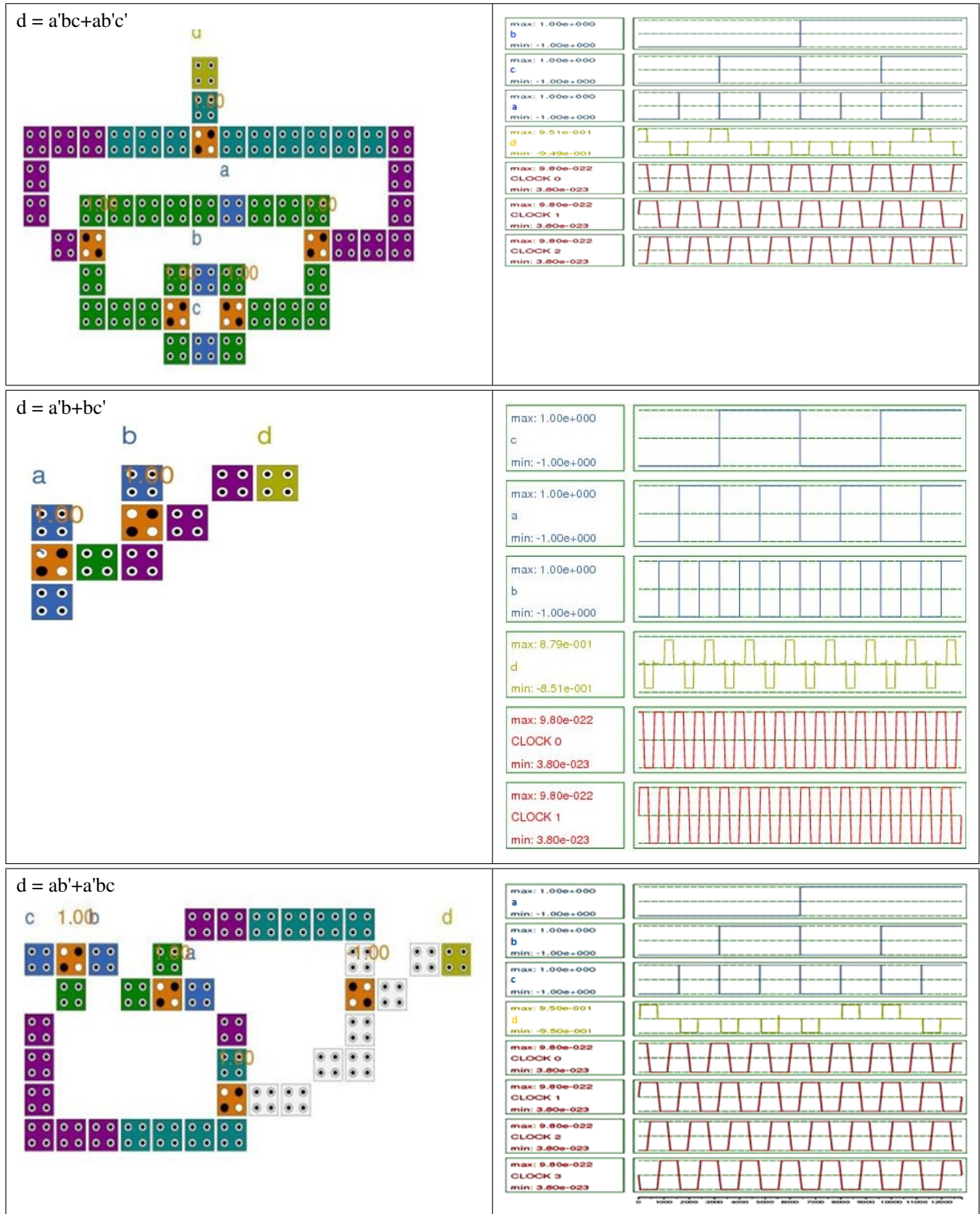
<p>Function: $D = A'B'C' + A'BC + ABC'$ Firstly, we calculate the XOR function, in a similar way, as in function no. 3 (up to step 4). Inputs C and A will be sent to a universal gate with polarization +1 to create intermediate value $i1 = \text{NAND}(C, A)$ and at the same they are sent to NOR gate using polarization -1 i.e. $i5 = \text{NOR}(A,C)$. Then, this intermediate value will be used to form another two intermediate values $i2$ and $i3$. $i2 = \text{NAND}(C, i1)$; $i3 = \text{NAND}(A, i1)$. Next, these two values will be passed through a NAND gate to get another intermediate result. $i4 = \text{NAND}(i2, i3)$. Next, the $i4$ is passed through a NAND gate along with B i.e. $i6 = \text{NAND}(B,i4)$ and its complement is passed along with $i5$ i.e. $i7 = \text{NAND}(i5,\text{NOT}(B))$. Finally, both the outputs are passed through another NAND gate. $D = \text{NAND}(i6,i7)$.</p>	<p>S1: $i1 = \text{UG}(C, A, +1)$; S2: $i2 = \text{UG}(C, i1, +1)$; S3: $i3 = \text{UG}(i1, A, +1)$; S4: $i4 = \text{UG}(i2, i3, +1)$; S5: $i5 = \text{UG}(C, A, -1)$; S6: $i6 = \text{UG}(i4, B, +1)$; S7: $i7 = \text{UG}(\text{NOT}(B), i5, +1)$; S8: $D = \text{UG}(i6, i7, +1)$.</p>
<p>Function: $D = A$ Firstly the single input A is passed through a NAND gate i.e. polarization +1 with positive Boolean value 1. Then the output is complemented.</p>	<p>S1: $i1 = \text{UG}(A, 1, +1)$; S2: $D = \text{NOT}(i1)$.</p>
<p>Function: $D = AB + BC + CA$ First of all, inputs A, B and C will be sent to different combinations of universal NAND gate with polarization +1 to create intermediate value $i1 = \text{NAND}(A, C)$, $i2 = \text{NAND}(A, B)$ and $i3 = \text{NAND}(B, C)$. The 2 out of 3 outputs are then passed through another NAND gate to produce another output which is passed with the remaining of the first 3 output to give the final one.</p>	<p>S1: $i1 = \text{UG}(C, A, +1)$; S2: $i2 = \text{UG}(C, B, +1)$; S3: $i3 = \text{UG}(B, +1, A)$; S4: $i4 = \text{UG}(i2, i3, +1)$; S5: $D = \text{UG}(i4, i1, +1)$.</p>
<p>Function: $D = A'B + B'C$ First of all, inputs A and B will be sent to a universal gate with polarization +1 to create intermediate value $i1 = \text{NAND}(A, B)$. Then, another output will be produced using a NAND gate using complement of B and C as input. $i2 = \text{NAND}(C, B)$. Finally, the 2 outputs will be passed through a NAND gate along to get final result. $D = \text{NAND}(i1,i2)$.</p>	<p>S1: $i1 = \text{UG}(B, A, +1)$; S2: $i2 = \text{UG}(A, \text{NOT}(B), +1)$; S3: $D = \text{UG}(i1, i2, +1)$.</p>
<p>Function: $D = A'B + BC + AB'C'$ Firstly, let us take M as $\text{NAND}(A,C')$ i.e., the inputs A and the complement of C are passed through a NAND gate i.e. with polarization +1. Then, this resultant is passed with B twice, once through a NOR gate and another through NAND gate i.e. $i1 = \text{NAND}(B,M)$ and $i2 = \text{NOR}(B,M)$. The final output is formed when $i1$ and $i2$ are passed again through a NAND gate.</p>	<p>S1: $M = \text{UG}(\text{NOT}(C), A, +1)$; S2: $i1 = \text{UG}(M, B, +1)$; S3: $i2 = \text{UG}(B, M, -1)$; S4: $D = \text{UG}(i2, i3, +1)$.</p>
<p>Function: $D = AB + A'B'$ First of all, inputs A and B will be sent to a universal gate with polarization +1 to create intermediate value $i1 = \text{NAND}(A, B)$. Then, this intermediate value will be used to form another two intermediate values $i2$ and $i3$. $i2 = \text{NAND}(A, i1)$; $i3 = \text{NAND}(B, i1)$. Next, these two values will be passed through a NAND gate to get final result. $i4 = \text{NAND}(i2, i3)$. Finally, the output $i4$ is complemented to produce the desired outcome.</p>	<p>S1: $i1 = \text{UG}(C, A, +1)$; S2: $i2 = \text{UG}(C, i1, +1)$; S3: $i3 = \text{UG}(i1, A, +1)$; S4: $i4 = \text{UG}(i2, i3, +1)$; S5: $D = \text{NOT}(i4)$.</p>
<p>Function: $D = A'B'C' + ABC' + AB'C + A'BC$ Firstly let us take M as $\text{NOR}(\text{NAND}(B',C'), \text{NAND}(B,C))$ i.e., the inputs B and C and their complements are passed through 2 NAND gates i.e., with polarization +1 i.e., $i1 = \text{NAND}(B,C)$ and $i2 = \text{NAND}(B',C')$. After that, the resultants $i1$ and $i2$ is passed through a NOR gates (-1 polarization) i.e. $M = \text{NOR}(i1,i2)$. Then this resultant is passed with A twice, once through a NOR gate and another through NAND gate i.e. $i3 = \text{NAND}(A,M)$ and $i4 = \text{NOR}(A,M)$. The final output is formed when $i3$ and $i4$ are passed again through a NAND gate.</p>	<p>S1: $i1 = \text{UG}(C, B, +1)$; S2: $i2 = \text{UG}(\text{NOT}(C), \text{NOT}(B), +1)$; S3: $M = \text{UG}(i1, i2, -1)$; S4: $i3 = \text{UG}(A, M, +1)$; S5: $i4 = \text{UG}(A, M, -1)$; S6: $D = \text{UG}(i3, i4, +1)$.</p>

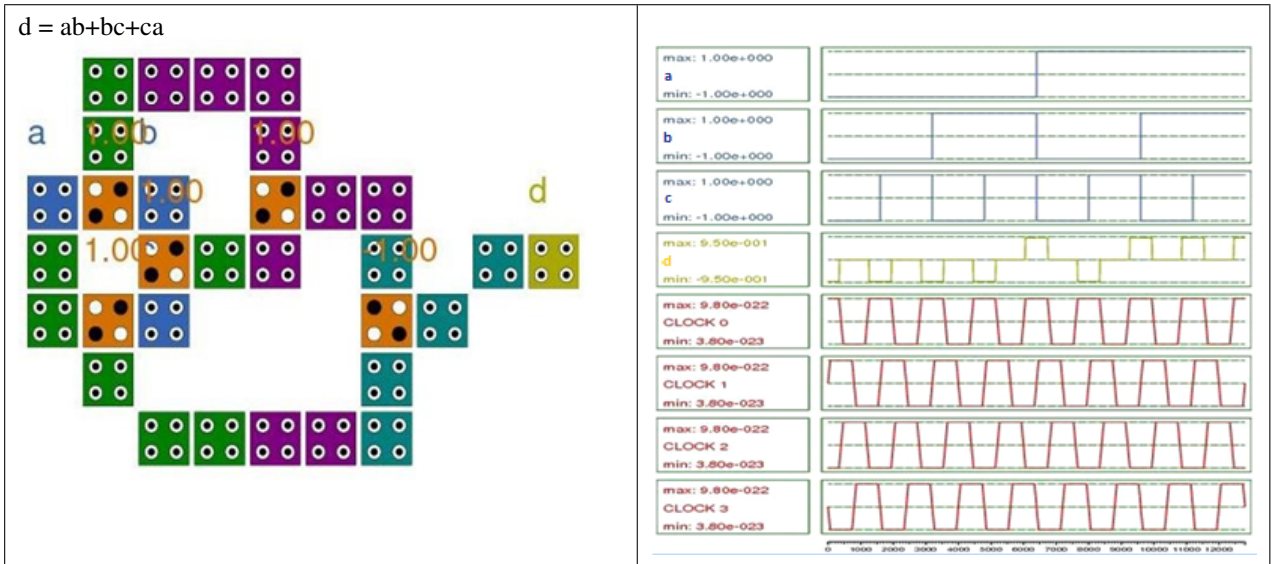
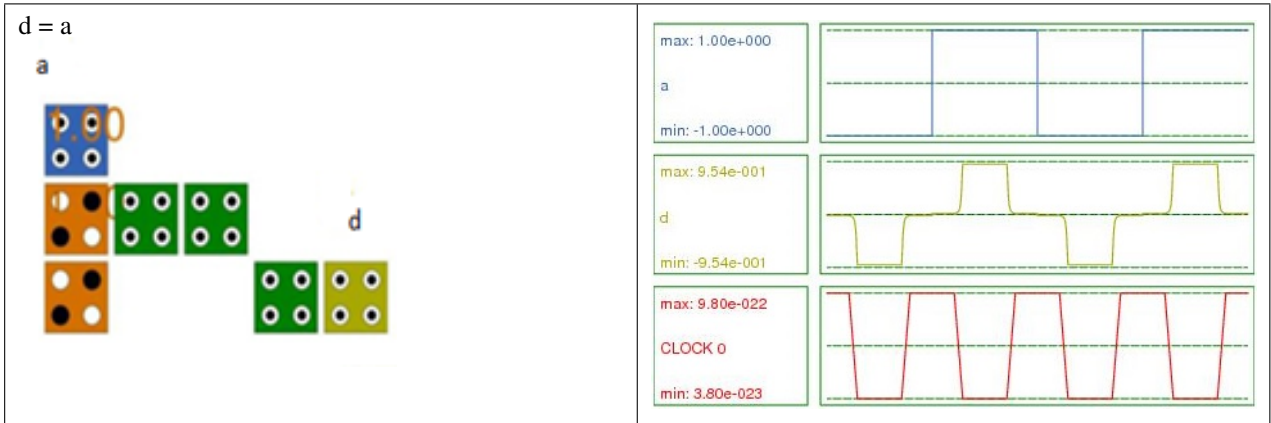
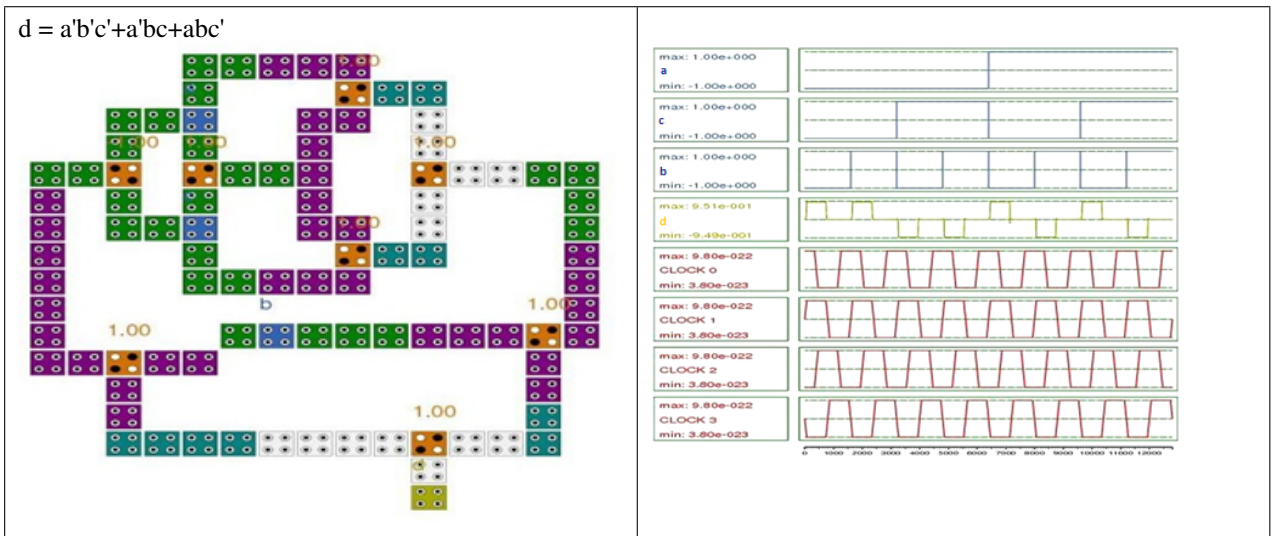
6. Results and discussion

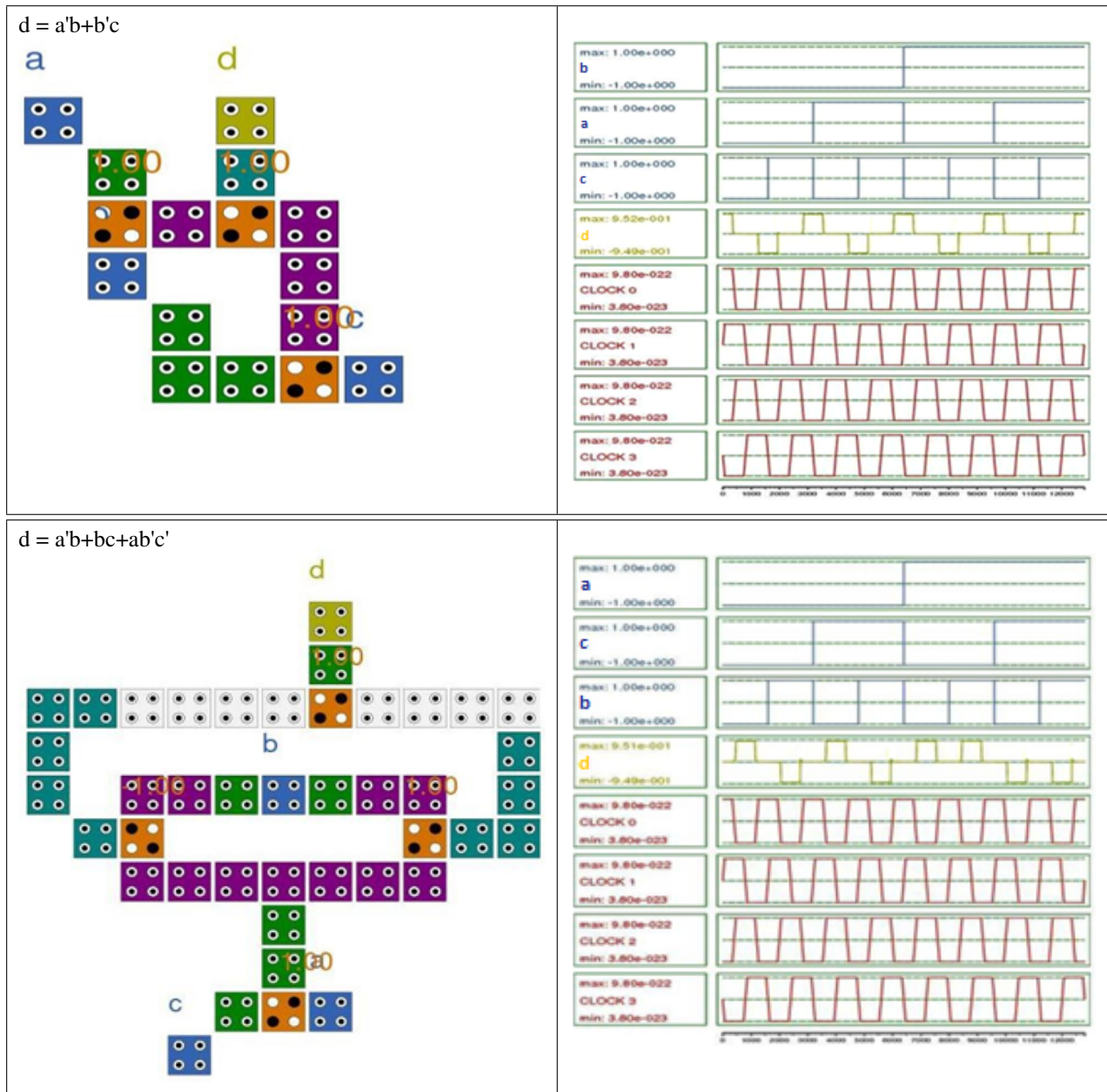
Table 2 shows the circuit diagrams using QCA and the simulated outputs of the corresponding circuits

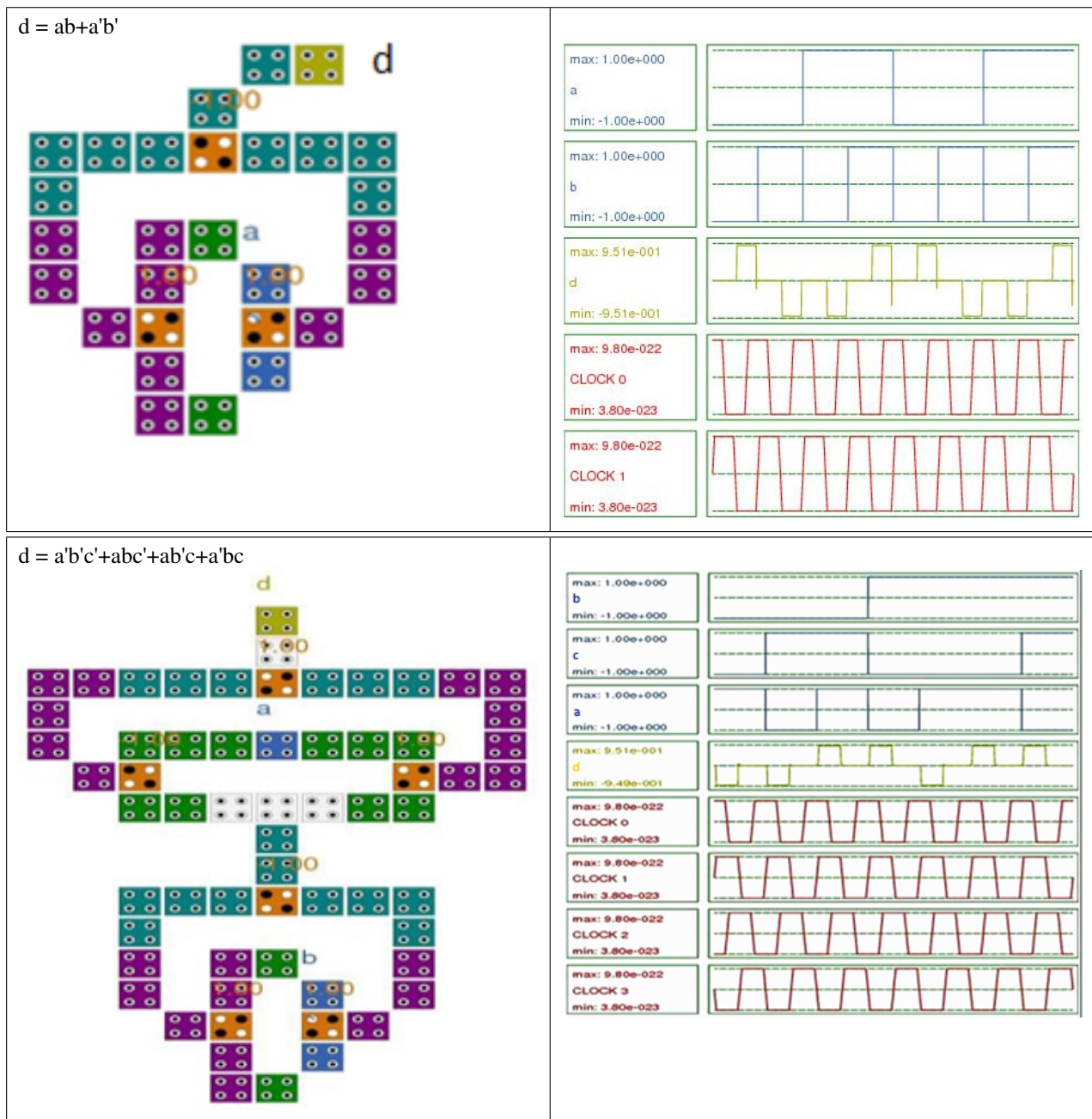
Table 2: Circuit implementation in QCA and their simulated output

QCA Layout	Simulation Result														
<p>$d = ab'c$</p> 	<table border="1"> <tr> <td>max: 1.00e+000 a min: -1.00e+000</td> <td></td> </tr> <tr> <td>max: 1.00e+000 b min: -1.00e+000</td> <td></td> </tr> <tr> <td>max: 1.00e+000 c min: -1.00e+000</td> <td></td> </tr> <tr> <td>max: 8.48e-001 d min: -9.53e-001</td> <td></td> </tr> <tr> <td>max: 9.80e-022 CLOCK 0 min: 3.80e-023</td> <td></td> </tr> </table>	max: 1.00e+000 a min: -1.00e+000		max: 1.00e+000 b min: -1.00e+000		max: 1.00e+000 c min: -1.00e+000		max: 8.48e-001 d min: -9.53e-001		max: 9.80e-022 CLOCK 0 min: 3.80e-023					
max: 1.00e+000 a min: -1.00e+000															
max: 1.00e+000 b min: -1.00e+000															
max: 1.00e+000 c min: -1.00e+000															
max: 8.48e-001 d min: -9.53e-001															
max: 9.80e-022 CLOCK 0 min: 3.80e-023															
<p>$d = ab$</p> 	<table border="1"> <tr> <td>max: 1.00e+000 a min: -1.00e+000</td> <td></td> </tr> <tr> <td>max: 1.00e+000 b min: -1.00e+000</td> <td></td> </tr> <tr> <td>max: 9.54e-001 d min: -9.54e-001</td> <td></td> </tr> <tr> <td>max: 9.80e-022 CLOCK 0 min: 3.80e-023</td> <td></td> </tr> </table>	max: 1.00e+000 a min: -1.00e+000		max: 1.00e+000 b min: -1.00e+000		max: 9.54e-001 d min: -9.54e-001		max: 9.80e-022 CLOCK 0 min: 3.80e-023							
max: 1.00e+000 a min: -1.00e+000															
max: 1.00e+000 b min: -1.00e+000															
max: 9.54e-001 d min: -9.54e-001															
max: 9.80e-022 CLOCK 0 min: 3.80e-023															
<p>$d = a'b'c' + a'bc$</p> 	<table border="1"> <tr> <td>max: 1.00e+000 b min: -1.00e+000</td> <td></td> </tr> <tr> <td>max: 1.00e+000 c min: -1.00e+000</td> <td></td> </tr> <tr> <td>max: 1.00e+000 a min: -1.00e+000</td> <td></td> </tr> <tr> <td>max: 9.50e-001 d min: -9.54e-001</td> <td></td> </tr> <tr> <td>max: 9.80e-022 CLOCK 0 min: 3.80e-023</td> <td></td> </tr> <tr> <td>max: 9.80e-022 CLOCK 1 min: 3.80e-023</td> <td></td> </tr> <tr> <td>max: 9.80e-022 CLOCK 2 min: 3.80e-023</td> <td></td> </tr> </table>	max: 1.00e+000 b min: -1.00e+000		max: 1.00e+000 c min: -1.00e+000		max: 1.00e+000 a min: -1.00e+000		max: 9.50e-001 d min: -9.54e-001		max: 9.80e-022 CLOCK 0 min: 3.80e-023		max: 9.80e-022 CLOCK 1 min: 3.80e-023		max: 9.80e-022 CLOCK 2 min: 3.80e-023	
max: 1.00e+000 b min: -1.00e+000															
max: 1.00e+000 c min: -1.00e+000															
max: 1.00e+000 a min: -1.00e+000															
max: 9.50e-001 d min: -9.54e-001															
max: 9.80e-022 CLOCK 0 min: 3.80e-023															
max: 9.80e-022 CLOCK 1 min: 3.80e-023															
max: 9.80e-022 CLOCK 2 min: 3.80e-023															









7. Observation

From the implementation of standard functions, the following parameters can be found which is shown in Table 3.

8. Energy Analysis of 13 standard functions using QCA

In this section, we deal with the energy calculations and analysis based on said calculations of 13 standard functions as specified below.

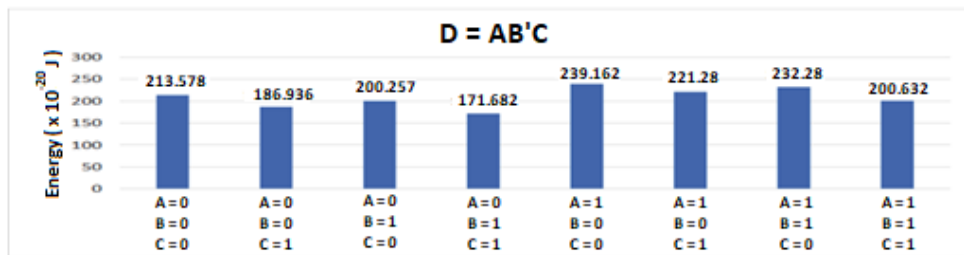
8.1. Analysis for $D = AB'C$

Figure 5 shows the energy calculation bar chart for the function $D = AB'C$.

As we see, this function has 3 inputs, A, B, and C. So we have to find the potential energy for the $2^3 = 8$ different resultant states. Firstly, we fix the input as (0, 0, 0), and determine the configuration of the electrons in the cells. This gives us the total potential energy for this particular state of device cells. Similarly, we find the total potential energy for all the remaining states of device cells.

TABLE 3. Information obtained from 13 Standard Function design using QCA designer tool

Design Name	Length (in nm)	Breadth (in nm)	Cell Count	Area(in nm ²)	Latency
$d = ab'c$	105	98	9	10290	0.25
$d = ab$	85	78	6	6630	0.25
$d = a'b'c'+a'bc$	221	138	30	30498	0.75
$d = a'bc+ab'c'$	278	201	51	55878	0.75
$d = a'b+bc'$	118	101	10	11918	0.50
$d = ab'+a'bc$	278	141	37	39198	1.00
$d = a'b'c'+a'bc+abc'$	341	304	95	103664	1.00
$d = a$	81	78	6	6318	0.25
$d = ab+bc+ca$	198	138	26	27324	0.75
$d = a'b+b'c$	145	134	16	19430	0.75
$d = a'b+bc+ab'c'$	241	218	42	52538	1.25
$d = ab+a'b'$	201	138	28	27738	0.75
$d = a'b'c'+abc'+ab'c+a'bc$	341	218	63	74338	1.00

FIG. 5. Energy calculation for the function $D = AB'C$

The graph showing the energy (10^{-20} Joules) and the state configuration is represented in Fig. 5.

So, we see that the potential energy associated with the state ($A = 0, B = 1, C = 1$) is minimum (171.688 u), in comparison to the energy of the other device states.

Thus, we can conclude that it is the most stable operating state for this particular function, $D = AB'C$.

8.2. Analysis for $D = AB$

The function $D = AB$, has 2 inputs, A and B. So we have to find the potential energy for the $2^2 = 4$ different resultant states. Firstly, we fix the input as (0, 0), and determine the configuration of the electrons in the cells. This gives us the total potential energy for this particular state of device cells. From Fig. 6, we see that the potential energy associated with the state ($A = 0, B = 1$) is minimum (120.863 u), in comparison to the energy of the other device states. Thus, we can conclude that it is the most stable operating state for this particular function, $D = AB$.

8.3. Analysis for $D = A'B'C'+A'BC$

The function $D = AB'C'+A'BC$ has 3 inputs, A, B, and C. So we have to find the potential energy for the $2^3 = 8$ different resultant states. As, mentioned above, after finding the potential energy for different cell states of the device, the resulting output is plotted. The graph from Fig. 7 is showing the energy axis as (10^{-20} Joules) in y axis and the state comparison as x axis

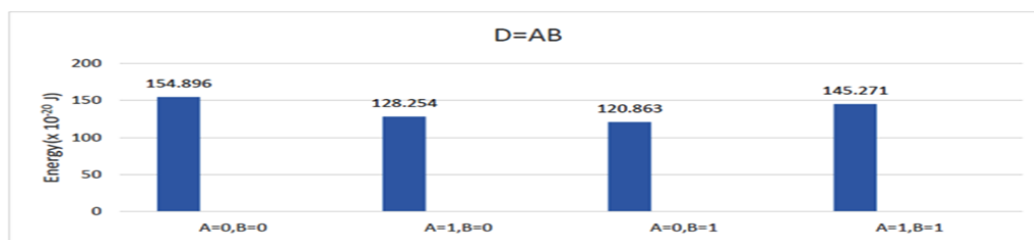


FIG. 6. Energy calculation for the function D = AB

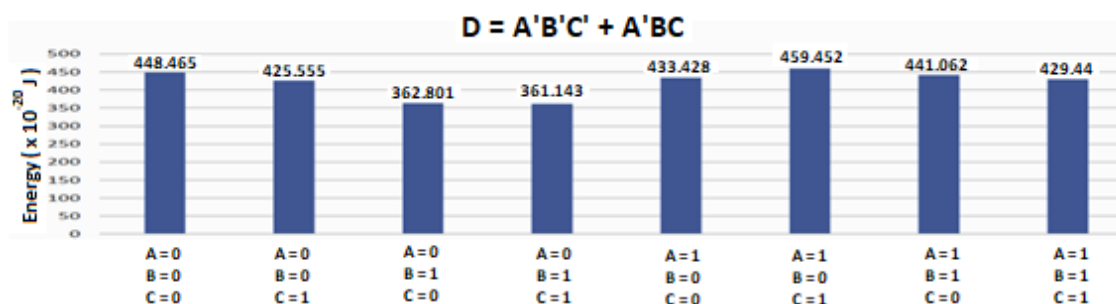


FIG. 7. Energy calculation for the function D = A'B'C'+A'BC'

So, we see that the potential energy associated with the state (A = 0, B = 1, C = 1) is minimum (361.143 u), in comparison to the energy of the other device states. Thus, we can conclude that it is the most stable operating state for this particular function, D = A'B'C'+A'BC'.

8.4. Analysis for D = A'BC+AB'C'

The function D = A'BC+AB'C' has 3 inputs, A, B, and C. So we have to find the potential energy for the 2³ = 8 different resultant states. Depending on the configuration of the input states, which defines the configuration of the electrons in the cells, we'll again have different potential energy for those states. The total energy for those states is then plotted. The graph showing the energy (10⁻²⁰ Joules) and the state configuration is represented as Fig. 8.

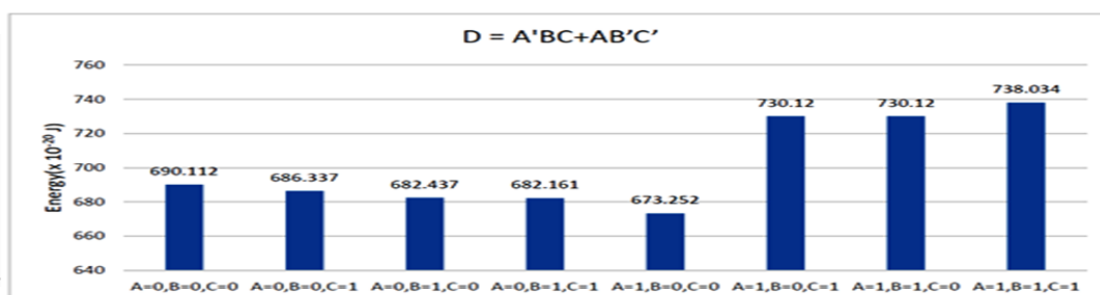


FIG. 8. Energy calculation for the function D = A'BC+AB'C'

So, we see that the potential energy associated with the state (A = 1, B = 0, C = 1) is minimum (673.252 u), in comparison to the energy of the other device states. Thus, we can conclude that it is the most stable operating state for this particular function, D = A'BC+AB'C'.

In this way, we calculate the energy analysis for every standard functions which is shown in Table 4.

9. Comparative study

A comparative study of the existing methodology and the proposed methodology is given in tabular form. The other methods are already implemented and they are reversible gates. Different numbers of unit blocks required to

TABLE 4. Energy analysis of the standard function

Standard function	Input condition	Minimum energy
$D = AB'C$	$A = 0, B = 1, C = 1$	171.688 u
$D = AB$	$A = 0, B = 1$	120.863 u
$D = A'B'C' + A'BC$	$A = 0, B = 1, C = 1$	361.143 u
$D = A'BC + AB'C'$	$A = 1, B = 0, C = 1$	673.252 u
$D = A'B + BC'$	$A = 0, B = 1, C = 1$	220.574 u
$D = AB' + A'BC$	$A = 1, B = 0, C = 1$	480.87 u
$D = A'B'C' + A'BC + ABC'$	$A = 1, B = 1, C = 1$	1004.012 u
$D = A$	$A = 1$	111.931 u
$D = AB + BC + CA$	$A = 0, B = 1, C = 1$	494.544u
$D = A'B + B'C$	$A = 0, B = 0, C = 1$	299.402 u
$D = A'B + BC + AB'C'$	$A = 1, B = 0, C = 1$	439.262 u
$D = AB + A'B'$	$A = 1, B = 0$	536.628 u
$D = A'B'C' + ABC' + AB'C + A'BC$	$A = 0, B = 1, C = 1$	985.084 u

implement 13 standard functions for each of them as well as the number of blocks used by proposed logic design are given in Table 5.

TABLE 5. Comparison with different gates [11]

Functions	CQCA	FREDKIN	PERES	Proposed design
$D = AB'C$	2	2	2	2
$D = AB$	1	1	1	1
$D = A'B'C' + A'BC$	6	3	4	4
$D = A'BC + AB'C'$	4	4	3	5
$D = A'B + BC'$	3	5	5	2
$D = AB' + A'BC$	3	3	8	4
$D = A'B'C' + A'BC + ABC'$	7	5	5	8
$D = A$	1	1	1	1
$D = AB + BC + CA$	1	8	11	5
$D = A'B + B'C$	3	1	4	3
$D = A'B + BC + AB'C'$	6	4	2	4
$D = AB + A'B'$	3	2	3	3
$D = A'B'C' + ABC' + AB'C + A'BC$	9	11	4	6
Average number of gates	3.7692	3.8462	4.0769	3.6923

Here, it can be observed that an average number of gates in our proposed design are mostly less than the average number of gates in other logic realization. The less the average number of gates used, the more will be the efficiency and less will be the space complexity.

10. Conclusions

In this article, we have described 13 standard functions which are the necessary building blocks for various combinational and sequential circuits. This work is an extension of the previous work as referred in [9]. Here, we have shown the energy calculations to verify the robustness of the design and also calculated the cell count, area consumption and latency to complete the design. We have also discussed the implementation of various combinational and sequential circuits using the standard functions. Comparative study has been done with the other gates. In future work, we will show the applications of standard functions for other logic circuits and detail design and simulations using QCA based nanotechnology.

References

- [1] Lent C.S., Tougaw P.D., Porod W., Bernstein G.H. Quantum cellular automata. *Nanotechnology*, 1993, **4**, P. 49–57.
- [2] Majeed A.H., Zainal M.S., Bernstein E.A. Quantum-dot Cellular Automata: Review Paper. *Int. Journal of Integrated Engineering*, 2019, **11** (8), P. 143–158.
- [3] Laajimi R. Nano architecture of Quantum-Dot Cellular Automata (QCA) Using Small Area for Digital Circuits. In *Advanced Electronic Circuits, Principles, Architectures and Applications on Emerging Technologies*, 2018.
- [4] Jayalakshmi R., Amutha R. An Optimized High Input Majority Gate Design in Quantum-Dot Cellular Automata. *Int. Journal of Engineering and Manufacturing Science*, 2018, **8** (1), P. 63–75.
- [5] Sheikhfaal S., Angizi S., et al. Designing efficient QCA logical circuits with power dissipation analysis. *Microelectronics Journal*, 2015, **46** (6), P. 462–471.
- [6] Sridharan K., Pudi, Vikramkumar. *Design of Arithmetic Circuits in Quantum Dot Cellular Automata Nanotechnology*, Springer, 2015.
- [7] Macucci M. *Quantum Cellular Automata. Theory, Experimentation and Prospects*. Imperial college Press, 2006.
- [8] Mukherjee C., Sukla A.S., et al. Layered T full adder using Quantum-dot Cellular Automata. *IEEE International Conference on Electronics, Computing and Communication Technologies (CONECCT)*, 2015, P. 1–6.
- [9] Chakrabarty R., Bhattacharjee A., Kundu A., Ganguly R. Implementation of Standard Functions Using Universal Gate in QCA Designer. *1st Int. Conf. on Electronics, Materials Engineering and Nano-Technology (IEMENTech)*, 2017, 8076966.
- [10] QCADesigner 2.0. URL: <https://qcadesigner.software.informer.com/2.0/>.
- [11] Das J., De D. Optimized Design of Reversible Gates in Quantum Dot-Cellular Automata: A Review. *Reviews in Theoretical Science*, 2016, **4** (3), P. 279–286.

Energy relaxation in molecular systems containing salt ions

M. A. Baranov¹, E. N. Velichko¹, E. K. Nepomnyashchaya¹, I. V. Pleshakov²

¹Peter the Great St. Petersburg Polytechnic University,
Polytechnicheskaya, 29, Saint Petersburg, 195251, Russia

²Ioffe Institute, 26 Politechnicheskaya str., Saint Petersburg, 194021, Russia

baranovma1993@gmail.com, velichko-spbstu@yandex.ru, elina.nep@gmail.com, ivanple@yandex.ru

PACS 05.40.-a, 05.65.+b, 02.70.Ns, 87.14.Ee, 87.15.He

DOI 10.17586/2220-8054-2021-12-5-598-602

In this paper, we consider relaxation processes in molecular systems containing single biomolecule and salt ions. The energy fluctuations in such systems were evaluated using computer simulations. The comparative analysis of the free energy dynamics of alanine, tryptophan, and albumin biomolecules in constructed molecular systems (aqueous solutions with different degrees of ionization) resulted in high influence of ionizing impurities on the full energy of the system and on the energy relaxation time. The results obtained can be used for development of hybrid micro and nanoelectronic devices with built-in biomolecular objects, for example, biochemical sensors, devices with microflow of liquids, technology for the preparation of molecular films, etc.

Keywords: self-organization, proteins, molecular dynamics, biomolecular electronics, energy relaxation.

Received: 1 October 2021

Revised: 16 October 2021

1. Introduction

Like in the living systems, the characteristics of hybrid micro and nanoelectronic devices with organic molecules are determined by specific realizations of the structure, dynamics and function of biomolecules and their ensembles [1]. The key influence on the biomolecular properties of the proteins and peptides, is determined by biomolecular conformation, energy, and dipole moment. These parameters of the molecules in ionized solutions are required for development of highly-efficient modern bioelectronic devices, such as biochemical sensors. The computer modeling is to be used to investigate biomolecules, and in particular, to determine the probability of establishing a certain conformation [2–5], since conformational changes are correlated with changes in the dipole moment and with total energy of molecule or molecular cluster [6–9].

In this study we use the molecular modeling method to investigate changes of the molecular conformation and of the ionization degree of their clusters during the relaxation processes.

2. Calculation methods

Visual Molecular Dynamics software was utilized to develop molecular system models of different structure. This method is usually used for a computer modelling of the free energy of large molecules [2, 10, 11]. The model of the molecular system was presented by one biomolecule placed in a water cube. In all considered systems, the distance from the molecule to the cube faces (box padding) was equal to 15 Å.

In this study, we used albumin, glycine, and tryptophan molecules the modelling. In considering the dissolution of the molecules, the TIP3W model of water was used. This model assumes three atoms of a water at three points of interaction. To create salt solutions with concentration n [mol/L] in the water cube, the standard VMD function of adding ions was used. Changing of the concentration of ions was achieved by introduction of the NaCl ions with a minimum distance of 5 Å. Similar methods are also utilized in other published experiments [12–14]. The addition of Na^+ and Cl^- ions was used to change salt concentration in the interval from 1.71×10^{-4} to 1.71 mol/L, which corresponds to 0.001 – 10%. The maximum concentration of ions in this case was about 3200 ions per molecule in the water cube.

All simulations were performed with a CHARMM27 force field using the NAMD package with the periodic boundary conditions and with the cutoff radius for unrelated interactions with a switching function, starting at 9 Å and reaching zero at 12 Å for the aqueous medium. To establish equilibrium in the system, the energy was minimized and the conformational state of the molecules was stabilized for 50 ps. As a result, the stable conformational states

of molecules were obtained. For the Energy minimization and following calculation of the molecular relaxation, the Langevin equation was used:

$$m_i \frac{d^2 x_i(t)}{dt^2} = F_i(x_i(t)) - \gamma_i \frac{dx_i(t)}{dt} m_i + R_i(t), \quad (1)$$

here, $\gamma_i m_i$ is the system damping factor, γ_i is a friction coefficient, m_i is the particle mass, F_i stands for the force acting on the particle by the electric field (for example, ions), and R_i is the random force that acts on the particle. The Langevin method enables calculation of the kinetic energy of the system while simultaneously controlling the temperature of the molecular object and the pressure. A change in the concentration of ions in the solution leads to a change in the relaxation and the stabilization times.

Calculation of the energy value of the molecular cluster in an aqueous solution was based on the Free Energy Perturbation algorithm in the Nanoscale Molecular Dynamics program. The algorithm consists in evaluation of the energy difference between two states of the system at each moment of time that allows prediction of the system dynamic scenario. Since the calculations were performed for a constant pressure, the free energy is associated with the Gibbs energy [15].

Simulation of the relaxation begins immediately after energy minimization. The relaxation step was analyzed for 150 ps using an NPT ensemble. The instantaneous pressure in the water cube was presented by the root mean square fluctuations of $\frac{kT}{V\beta}$ value, where β is compressibility. The pressure was obtained by spatio-temporal averaging of the kinetic pressure $\frac{nRT}{V}$ and the compensating negative static pressure.

As a result, the values of the total energy of molecular clusters were obtained depending on the simulation time. The total energy can be represented as a sum of the kinetic and the potential energies (Eqs. 2,3):

$$H(p, r) = K(p) + U(r), \quad (2)$$

$$K(p) = \sum_{i=1}^N \frac{p_i^2}{2m_i}. \quad (3)$$

The potential energy is presented by the sum of various potential energies, describing the bound and the unbound interactions between the particles (Eq. 4):

$$U_{total} = U_{bond} + U_{angle} + U_{dihedral} + U_{vdW} + U_{Coulomb} \quad (4)$$

The first three terms describe the stretching, bending, and torsional bonded interactions, where the bonds count includes each covalent bond in the system, angles are the angles between each pair of covalent bonds sharing a single atom at the vertex, and dihedral describes atom pairs separated by exactly three covalent bonds with the central bond subject to the torsion angle. The final two terms in eq. (4) describe interactions between nonbonded atom pairs: van der Waal's forces and electrostatic interactions.

Based on these values, the expected experimental dependences of the relaxation energies on time and on the concentration of salt ions in solutions were obtained and analyzed.

3. Results and discussion

As a result of our calculations, the dependences of the total energy on the simulation time were obtained. Fig. 1 shows typical time dependences of full energy of the molecular clusters for the albumin, glycine, and tryptophan with concentration of NaCl salt ions equal to 0.15 mol/L. It is assumed that oscillations of the molecular cluster occur at the relaxation site, when the energy from the protein molecules is transferred to the aqueous environment. Fig. 1 shows that the larger the molecule, the less time it takes for its oscillation energy to relax. The relaxation time of molecular system was determined from the values of the energies of molecular system when the amplitude of vibrations of the total energy of molecules became less than 10% of the maximum value.

Fig. 2 shows the dependence of the relaxation energy (that corresponds to the relaxation time) on the salt concentration in the molecular cluster. The salt concentration is presented in dimensionless values and was calculated as the decimal logarithm of the ratio of the salt concentration to the initial salt concentration.

The energy value established as a result of relaxation is proportional to the number of molecules in the water cube and the mass of the biomolecule under study. The total energy E also depends on the concentration of ions and decreases upon stabilization by an amount of ΔE , which is much smaller than E . The rate of the energy decline depends on the size of the molecule that for glycine consists of 3202 atoms, for tryptophan of 4131 atoms and for albumin has 169169 atoms. This means that in the process of relaxation, only a small part of the initial total energy is lost. Most likely, this part refers to kinetic energy. In Fig. 3 kinetic energy of molecular system is presented. One

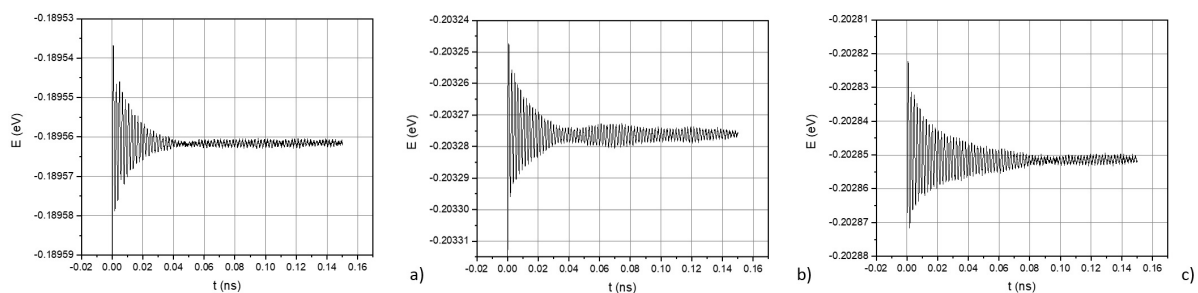


FIG. 1. Relaxation of molecular cluster energy shown as a function of time for a) albumin molecule b) glycine molecule c) tryptophan molecule

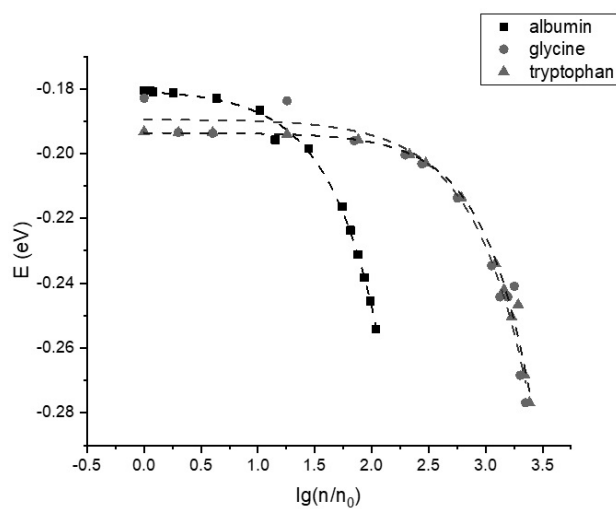


FIG. 2. Relaxation energy of tryptophan, albumin and glycine molecules shown as function of $n(\text{NaCl})$

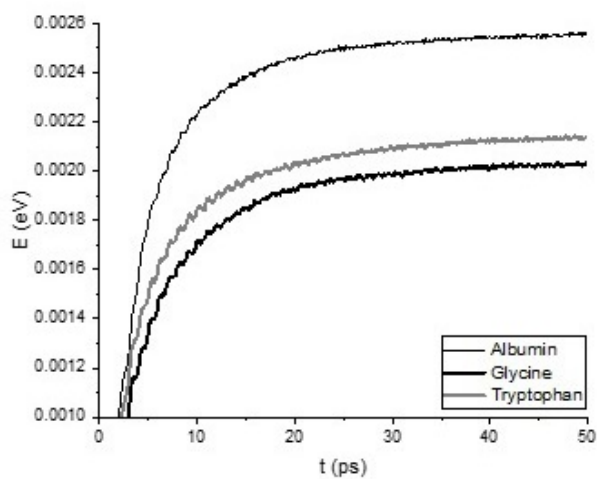


FIG. 3. Kinetic energy of tryptophan, albumin and glycine molecules shown as function of time

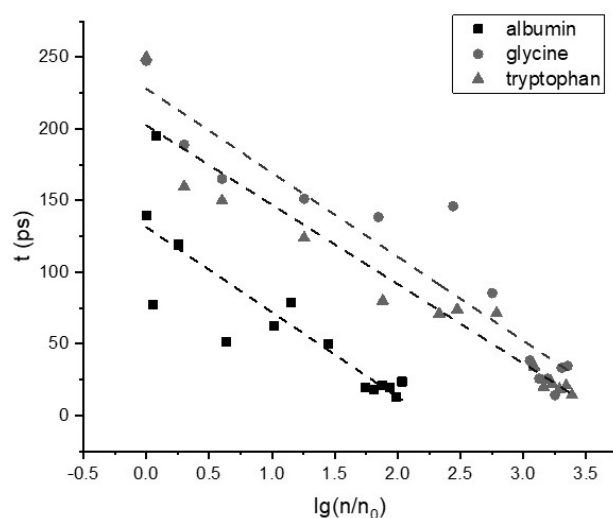


FIG. 4. Relaxation time of tryptophan, albumin and glycine molecules shown as function of $n(\text{NaCl})$

can notice, that in the process of relaxation of the total energy of a molecular cluster, the energy is transferred from the protein to ions. As a result, there is an increase in the kinetic energy.

The characteristic time of energy relaxation was also investigated for the studied molecular systems. Fig. 4 shows the dependences of the relaxation times on the logarithm of the salt ion concentration in the molecular system. As can be seen from Fig. 3, with an increase of the salt concentration, the relaxation time of the energy in studied molecular systems decreases. Analyzing these dependences, the smaller molecules reach the saturation level more slowly at the same ion concentration. However, the larger molecules require more ions to achieve equilibrium.

As can be seen from our modeling, presented in this section, the total energy and energy relaxation time depend on the type of protein and the number of atoms in the system. The energy relaxation process is caused by the initial nonequilibrium state of the molecular cluster with respect to the solution. As a result, we observe energy flux from the cluster to the solution.

4. Conclusion

Summarizing, in our research, we have applied the molecular simulation method to study relaxation processes in molecular systems. It was shown that the initial free energy of a molecular cluster decreases spontaneously during the dissipation time, when the cluster energy is mainly lost to the solution. It reaches the quasi-stationary level when the equilibrium of energy fluxes from the cluster to the solution and back is established.

The relaxation energy of the solution is transferred into the ionic component, or in other words, into the ion vibrations during the salt dissociation. The relaxation energy proves to be much smaller than the total energy of the system. Therefore, we can conclude that the kinetic energy is mainly transferred during these processes.

The characteristic time of the energy reduction to the stable state varies with the salt concentration. As the salt concentration in the solvation cube increases, the relaxation time decreases. In addition, the free energy of a molecular cluster also decreases with an increase in the salt concentration in the solution. This corresponds to a further decrease in the electric field at the cluster surface due to an increase in the pH and electrical conductivity of the aqueous saline solution.

Energy relaxation that occurs with slow aperiodic oscillations corresponds to relaxation of a dissipative dynamic system with low electrical conductivity and increased “friction”. Apparently, this corresponds to an electric field at the cluster surface created by polar water molecules and dissolved salt ions.

The results provided by this study can be useful for the development of modern biomolecular electronic elements constructed from single molecules and molecular layers.

Acknowledgement

This research was funded by RSF, grant number No 21-72-20029. The results were obtained using computational resources of Peter the Great Saint Petersburg Polytechnic University Supercomputing Center (www.spbstu.ru).

The Authors express their deep gratitude to Prof. O. Yu. Tsybin for many fruitful discussions and invaluable advices which have helped us to plan the experiments and explain experimental data.

References

- [1] Zotti L.A. Molecular Electronics. *Applied Sciences*, 2021, **11**, P. 4828.
- [2] Wang Y., Harrison C.B., Schulten K., McCammon J.A. Implementation of accelerated molecular dynamics in NAMD. *Comput. Sci. Discov.*, 2011, P. 4.
- [3] Vilorio J.S., Allega M.F., Lambrughi M., Papaleo E. An optimal distance cutoff for contact-based Protein Structure Networks using side-chain centers of mass. *Sci. Rep.*, 2017, **7**, P 1–11.
- [4] Petty M.C., Nagase T., Suzuki H., Naito H. *Molecular electronics*. Springer Handbooks, 2017, 1.
- [5] Hasani H.J., Ganesan A., Ahmed M., Barakat K.H. Effects of protein-protein interactions and ligand binding on the ion permeation in KCNQ1 potassium channel. *PLoS One*, 2018, **13**.
- [6] Baranov M., Tsybin O. and Velichko E. Structured biomolecular films for microelectronics. *Saint Petersburg Polytech. State Univ. Journal. Phys. Math.*, 2021, **14**, P. 85–99.
- [7] Bibi F., Villain M., Guillaume C., Sorli B., Gontard N.A. Review: Origins of the Dielectric Properties of Proteins and Potential Development as Bio-Sensors. *Sensors*, 2016, **16**(8), P. 1232.
- [8] Taylor P.A., Jayaraman A. Molecular Modeling and Simulations of Peptide-Polymer Conjugates *Annu. Rev. Chem. Biomol. Eng.*, 2020, **11**, P. 257–76.
- [9] Xiao B.L., Ning Y.N., Niu N.N., Li D., Moosavi-Movahedi A.A., Sheibani N., Hong J. Steered molecular dynamic simulations of conformational lock of Cu, Zn-superoxide dismutase. *Sci. Rep.*, 2019, **9**, P. 1-11.
- [10] Tavanti F., Pedone A., Menziani M.C. A closer look into the ubiquitin corona on gold nanoparticles by computational studies. *New J. Chem.*, 2015, **39**, P. 2474–82.
- [11] Tavanti F., Pedone A. and Menziani M. C. Competitive Binding of Proteins to Gold Nanoparticles Disclosed by Molecular Dynamics Simulations *J. Phys. Chem. C*, 2015, 119, 22172-80
- [12] Baranov M., Velichko E., Rozov S. Dehydrated films of protein solutions: structural properties. *Saint Petersburg Polytech. State Univ. Journal. Phys. Mathematics*, 2019, **12**, P. 25–37.
- [13] Dyubo D., Tsybin O.Y., Baranov M.A., Alekseenko A.P., Velichko E.N. Study of electric properties of self-assembled films of albumin during their dehydration Recent citations Study of electric properties of self-assembled films of albumin during their dehydration. *J. Phys*, 2018, **1124**, P. 31013.
- [14] Phillips J.C., Braun R., Wang W., Gumbart J., Tajkhorshid E., Villa E., Chipot C., Skeel R. D., Kalé L., Schulten K. Scalable molecular dynamics with NAMD. *J. Comput. Chem.*, 2005, **26**, P. 1781–802.
- [15] Sanchez C., Galo G.J., Ribot F. and Grosso D. Design of functional nano-structured materials through the use of controlled hybrid organic-inorganic interfaces. *Comptes Rendus Chim.*, 2003, **6**, P. 1131-51.

Modeling the evolution of surface nanobubbles

I. A. Nesterenko, I. Y. Popov

ITMO University, Kronverkskiy, 49, Saint Petersburg, 197101, Russia

nesterok123a@rambler.ru, popov1955@gmail.com

DOI 10.17586/2220-8054-2021-12-5-603-611

Surface nanobubbles are gaseous formations on solid-liquid interfaces. They are interesting in that their lifetime can reach several days, although initially it was assumed only a few nanoseconds. We built a mathematical and computer model of the nanobubble and performed a series of simulations to see how the nanobubble behaves when various external factors change.

Keywords: surface nanobubbles, molecular dynamics, nanosystems.

Received: 7 August 2021

Revised: 5 October 2021

1. Introduction

Gaseous formations – bubbles often appear as a result of various physical processes in a liquid. About 25 years ago, it was found that in addition to visible bubbles, nanobubbles invisible human eyes also appear in the liquid. In addition to spherical nanobubbles in bulk, surface nanobubbles also arise, which are located at the liquid-solid interface. It is surprising that these bubbles have long lifetime [1–13]. They can last several hours, in some cases several days. The initially predicted approximate lifetimes of nanobubbles described in [4] are orders of magnitude shorter than those practically observed [5].

Surface nanobubbles in most cases form a hemispherical shape. Some experiments [8, 14–18] have also shown that the shape of a nanobubble can be spherical with a small flat area at the top. It can also be seen from [3, 6, 7] that the shape of a nanobubble is often not always ideally spherical. Due to their size, nanobubbles have unique properties that may improve many physical, chemical and biological processes [5, 19, 20]. The presence of bubbles on a hydrophobic solid contributes to a change in the behavior of the liquid near the liquid-solid interface.

As for modern modeling methods, the most useful one is the molecular dynamics [3], since it allows one to obtain the most accurate description of processes occurring in objects that do not exceed hundreds of nanometers in size, as well as the simulated nanobubbles. But this method also has its limitation; for example, significantly complex calculations, which, on a regular computer, can take a huge amount of time. Therefore, for this method, various highly efficient algorithms are used which make it possible to reduce the number of computer calculations by an order of magnitude [1–3]. Analogously to [21], we construct two-dimensional molecular dynamics model which is an approximation only but, nevertheless, allows one to determine the properties of real physical system.

2. Description of the model

The simulated nanobubble consists of many gas molecules. In this model, we will assume that the gas is ideal. All collisions of a gas molecule with the upper boundary of the nanobubble are absolutely elastic, without energy loss.

The model is a two-dimensional section of the bubble. The lower boundary is the boundary of the rigid body, specified by the function $l(x) = 0$, where x is the horizontal coordinate. The upper boundary – the “roof” of the nanobubble, is introduced as a set of points, i.e. pairs of numbers (x, y) , where x is the point horizontal coordinate, y is the vertical coordinate. The initial position of the upper boundary is given by the function:

$$h(x) = \frac{4h_s x(w_s - x)}{w_s^2},$$

where h_s is the initial value of the nanobubble height in nanometers, w_s is the initial nanobubble diameter in nanometers, x is the horizontal coordinate, and $h(x)$ is the nanobubble height at point x .

There are N gas molecules inside the bubble. Each molecule has its own normalized direction vector, the coordinate of its location in the system, velocity modulus and mass. The modulus of the velocity v of each molecule is chosen on the basis of the Maxwell distribution function for the absolute values of the velocities:

$$F(v) = 4\pi \left(\frac{m_0}{2\pi kT} \right)^{3/2} \cdot v^2 \cdot \exp \left(-\frac{m_0 v^2}{2kT} \right),$$

where T is the temperature, $k = 1.380649 \cdot 10^{-23} \text{ JK}^{-1}$ is the Boltzmann constant, m_0 is the mass of a gas molecule.

The number of gas molecules in a nanobubble: $N = nV$, where n is the concentration of molecules, and

$$V = \frac{\pi h_s(3w_s^2 + 4h_s^2)}{24}$$

is the volume of a nanobubble (based on work [3]).

In turn, the concentration can be calculated using the following formula

$$n = \frac{\rho}{m},$$

where ρ is the density of the gas, and m is the mass of the gas molecule.

As a result, we come to the following formula:

$$N = \frac{\rho}{m} \frac{\pi h_s(3w_s^2 + 4h_s^2)}{24}$$

As for the dynamics for each molecule, we assume that colliding with the bubble boundary, the molecule does not lose velocity and the velocity vector is mirrored:

$$\vec{b} = \vec{a} - 2\vec{n} \frac{(\vec{n}, \vec{a})}{(\vec{n}, \vec{n})},$$

where \vec{a} is the direction vector of the gas molecule, \vec{n} is the normal vector at the point of collision of the molecule and the upper boundary of the bubble, \vec{b} is the reflected vector of the molecule.

At each moment of time, three main forces act on each point of the upper boundary of the bubble: F_p is the pressure force which is directed vertically downward; F_m is caused by elastic collision of gas molecules; F_a is the force of attraction of molecules. The pressure force is as follows:

$$F_p = \rho g H S,$$

where ρ is the density of the liquid, H is the height of the layer of the simulated liquid above the liquid solid interface with the nanobubbles, S is the unit of area, $g = 9.81 \frac{\text{m}}{\text{s}^2}$ is the acceleration due to gravity. The force caused by elastic collision of gas molecules with the border:

$$\vec{F}_m = \sum_{j=1}^{n_c} \vec{F}_{m_j},$$

where n_c is the number of molecules which collide with the current upper boundary point, and:

$$F_{m_j} = \frac{d\vec{p}_j}{dt},$$

The third force is as follows:

$$F_a = \alpha l,$$

where α is the liquid surface tension coefficient, l – distance between molecules.

3. Results

3.1. Behavior of a nanobubble over flat substrate

Firstly, let us simulate the bubble under normal conditions:

$$T = 300 \text{ K}, \quad H = 0.2 \text{ m},$$

$$\rho_w = 1000 \text{ kg} \cdot \text{m}^{-3}, \quad \alpha = 7.2 \cdot 10^{-2} \text{ H} \cdot \text{m}^{-1}.$$

Let us choose the initial width and height of the simulated nanobubble in the following way:

$$h_s = 20 \cdot 10^{-9} \text{ m},$$

$$w_s = 200 \cdot 10^{-9} \text{ m}.$$

As for the gas molecules, we consider two cases: nitrogen molecules and carbon dioxide molecules. The mass of one nitrogen molecule and the density is as follows:

$$m = 4.67 \cdot 10^{-26} \text{ kg}, \quad \rho = 1.1649 \text{ kg} \cdot \text{m}^{-3}.$$

We simulate the state of a nanobubble in 20 microseconds and collect the results in Table 1, where h is the height of the nanobubble and s is the volume.

The same simulation results for the carbon dioxide instead of the nitrogen are collected in Table 2.

TABLE 1. Parameters of nanobubble with nitrogen in water in the equilibrium state

	$T = 300 \text{ K}$	$T = 330 \text{ K}$	$T = 380 \text{ K}$
$H = 0.2 \text{ m}$	$h = 12 \text{ nm}, s = 8000 \text{ nm}^3$	$h = 13 \text{ nm}, s = 8500 \text{ nm}^3$	$h = 15 \text{ nm}, s = 10000 \text{ nm}^3$
$H = 0.4 \text{ m}$	$h = 8 \text{ nm}, s = 4200 \text{ nm}^3$	$h = 8.5 \text{ nm}, s = 5000 \text{ nm}^3$	$h = 9 \text{ nm}, s = 6000 \text{ nm}^3$

TABLE 2. Parameters of a nanobubble with carbon dioxide in water in the equilibrium state

	$T = 300 \text{ K}$	$T = 330 \text{ K}$	$T = 380 \text{ K}$
$H = 0.2 \text{ m}$	$h = 11 \text{ nm}, s = 6800 \text{ nm}^3$	$h = 12 \text{ nm}, s = 7200 \text{ nm}^3$	$h = 14 \text{ nm}, s = 8800 \text{ nm}^3$
$H = 0.4 \text{ m}$	$h = 8 \text{ nm}, s = 4500 \text{ nm}^3$	$h = 8.5 \text{ nm}, s = 4650 \text{ nm}^3$	$h = 9 \text{ nm}, s = 5200 \text{ nm}^3$

The same simulations were performed for ethanol instead of water. Parameters of the nanobubble are shown in Table 3 and Table 4.

TABLE 3. Parameters of a nanobubble with nitrogen in ethanol in the equilibrium state

	$T = 300 \text{ K}$	$T = 330 \text{ K}$	$T = 380 \text{ K}$
$H = 0.2 \text{ m}$	$h = 11 \text{ nm}, s = 6800 \text{ nm}^3$	$h = 12 \text{ nm}, s = 7200 \text{ nm}^3$	$h = 14 \text{ nm}, s = 8800 \text{ nm}^3$
$H = 0.4 \text{ m}$	$h = 8 \text{ nm}, s = 4500 \text{ nm}^3$	$h = 8.5 \text{ nm}, s = 4650 \text{ nm}^3$	$h = 9 \text{ nm}, s = 5200 \text{ nm}^3$

TABLE 4. Parameters of a nanobubble with the carbon dioxide in ethanol in the equilibrium state

	$T = 300 \text{ K}$	$T = 330 \text{ K}$	$T = 380 \text{ K}$
$H = 0.2 \text{ m}$	$h = 14.9 \text{ nm}, s = 9200 \text{ nm}^3$	$h = 15.5 \text{ nm}, s = 9400 \text{ nm}^3$	$h = 16.3 \text{ nm}, s = 9640 \text{ nm}^3$
$H = 0.4 \text{ m}$	$h = 8.6 \text{ nm}, s = 8100 \text{ nm}^3$	$h = 8.8 \text{ nm}, s = 8250 \text{ nm}^3$	$h = 9.1 \text{ nm}, s = 8400 \text{ nm}^3$

The tables show obvious dependencies: as the temperature in both simulated liquids increases, the nanobubble, as expected, increases its volume due to the increase in the internal energy of the gas molecules. And with a relatively small increase in depth in both simulated fluids, the nanobubble volume significantly decreases due to an increase in external pressure.

3.2. Behavior of nanobubble over rough substrate

In practice, a solid border is almost never perfectly flat. To see what will happen to the nanobubble with “rough” solid boundary, we change the function $l(x) = 0$, which defines the lower bound, to a piecewise linear function $g(x)$, which is presented below:

$$g(x) = \begin{cases} 0, & x \geq 150; \\ -5, & 50 < x < 150; \\ 0, & x \leq 50. \end{cases}$$

The parameters of the nanobubble are the same as in the simulation with water above: the temperature $T = 300 \text{ K}$, depth $H = 0.2 \text{ m}$. The modeled gas molecules are nitrogen and carbon dioxide. The form of nanobubble is shown in the Figs. 1,2.

The simulation results turned out to be quite interesting. The height of the bubble has indeed decreased, but the diameter increased significantly. This can be explained by the fact that the surface tension tries to reduce the contact angle, despite the fact that there is no interaction between the substrate and the liquid. But in this model, we assumed that the substrate is hydrophobic, which means that the external contact angle between the liquid and the substrate is always greater than $\pi/2$; therefore, the only way to reduce this angle is to increase the nanobubble diameter. The figures also show that the bubble has become less streamlined. Probably, such transformations occurred precisely because the molecular motion changed sufficiently and after collision with the lower boundary the molecule cannot get into the left or the right part of the bubble because it is blocked by the wall of the lower boundary. This assumption is confirmed by atomic force microscope measurements carried out in [3, 6]. An image of a nanobubble from [3] is shown in Fig. 3.

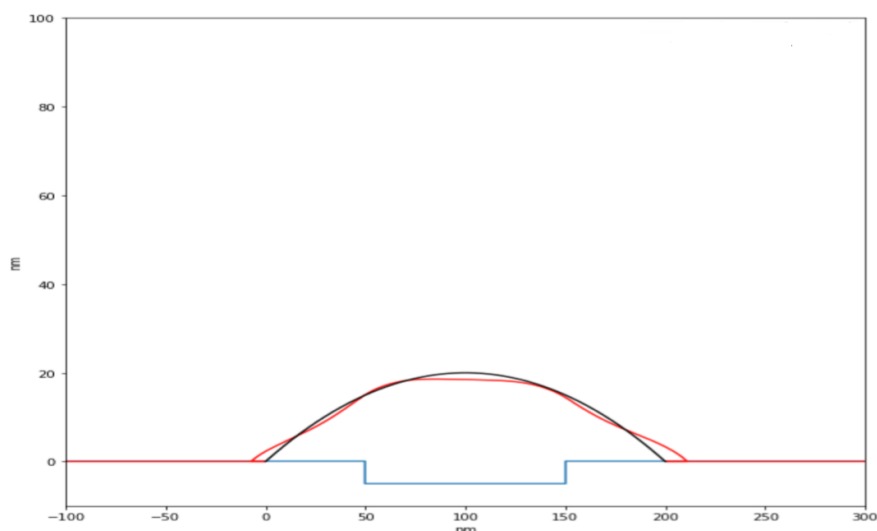


FIG. 1. Changing a nanobubble with nitrogen over the rough substrate. Black line is the initial form of the nanobubble, red line corresponds to the nanobubble in the equilibrium state

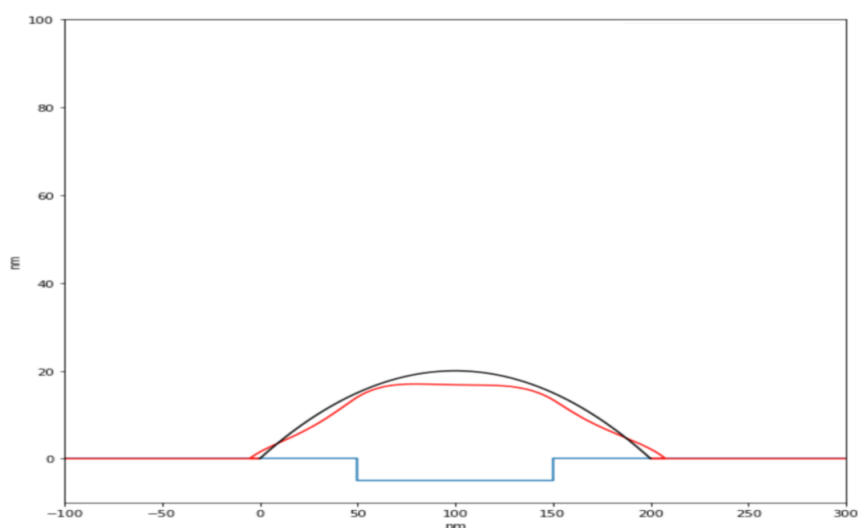


FIG. 2. Changing a nanobubble with carbon dioxide over the rough substrate. Black line is the initial form of the nanobubble, red line corresponds to the nanobubble in the equilibrium state

Figure 3 shows that the shape of the nanobubble is not just spherical, but the same as in Fig. 1,2. The base of the nanobubble is flat, and closer to the point with the maximum height, a small, almost flat area appears at the bubble. Moreover, proceeding from Fig. 3, it cannot be said that this local maximum occurs over the entire cross section of the nanobubble. In our model, the local maximum are almost symmetric, since the notch in the substrate was symmetrical and exactly in the center of the nanobubble. This suggests that the substrate is often not perfectly flat, and the shape of the nanobubble does not always represent an ideal hemisphere and depends very much on the shape of the substrate. Fig. 4 shows a possible reason for the appearance of two maximum at the liquid-gas interface.

3.3. Heating and cooling the substrate and liquid

We add some parameters to our model:

1. $T(x)$ – function of substrate temperature at point x ;
2. T_w – water temperature.

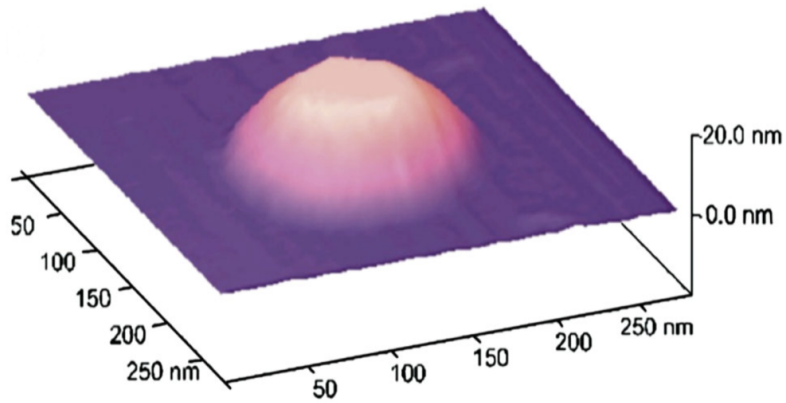


FIG. 3. Atomic force microscopy image of a nanobubble in work [3]

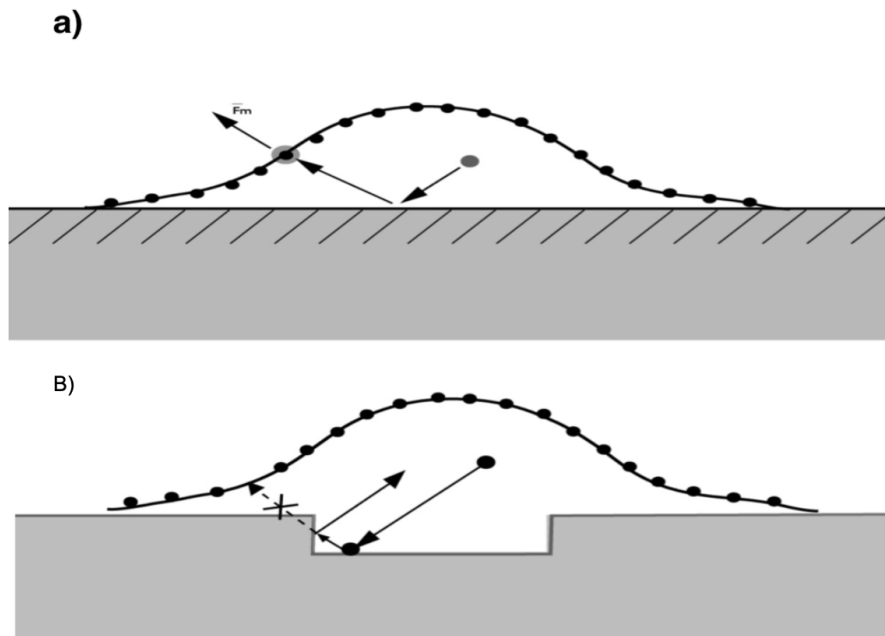


FIG. 4. Demonstration of the movement of a molecule in the case of a) an flat substrate, b) a rough substrate

We will assume that a gas molecule, when struck with the boundary of a liquid, receives a velocity:

$$v = \sqrt{\frac{3kT_w}{m_0}},$$

and upon collision with the boundary of a rigid body, the velocity is obtained:

$$v = \sqrt{\frac{3kT(x)}{m_0}}.$$

Let $T_w = 300$ K and set the $T(x)$ function like:

$$T(x) = \begin{cases} 300, & x \leq 150; \\ 350, & 150 < x < 300; \\ 300, & x \geq 300. \end{cases}$$

Figure 5 clearly shows a tendency to move to the right and an increase in the height of the nanobubble to the right, although the left part is in no hurry to move to the right, this is because the nanobubble is in a near-equilibrium position and when gas molecules collide with a heated region, the internal energy increases and this energy enough to maintain the current volume of the nanobubble until the bubble expands to the right even more.

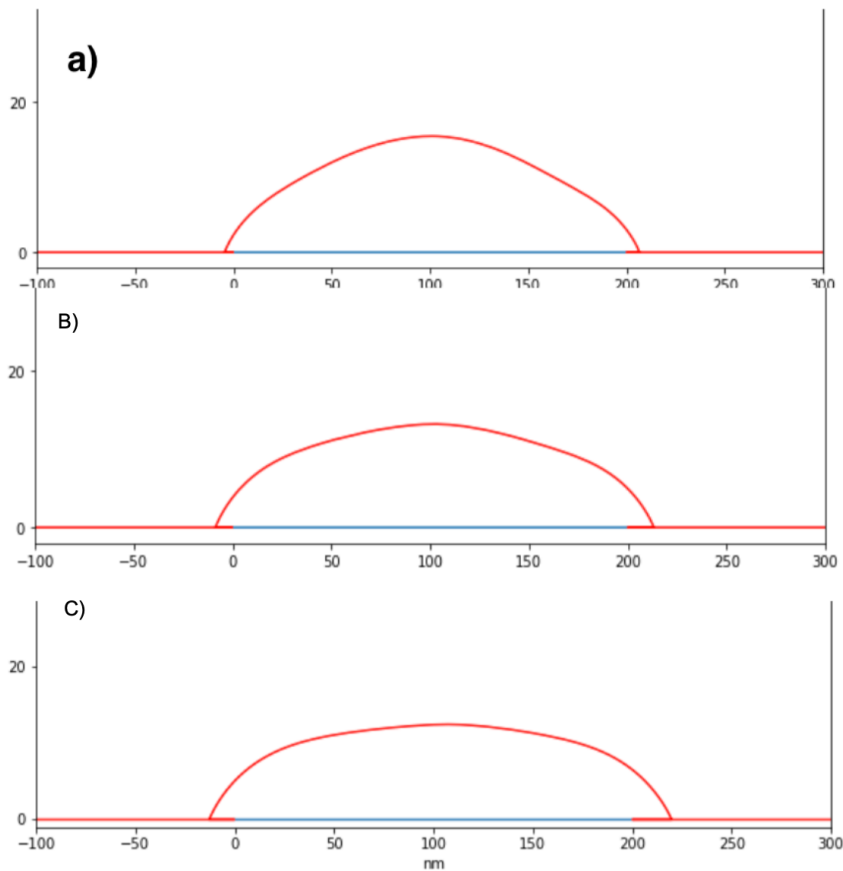


FIG. 5. Changes in the shape and position of a nanobubble over time a) $t = 5 \mu s$, b) $t = 10 \mu s$, c) $t = 15 \mu s$

Now construct the temperature gradient, which at the point $x = 100$ takes the highest temperature, and decreases in both directions according to the following formula:

$$T(x) = T_{\max} - \gamma|100 - x|,$$

where γ temperature gradient $K \cdot nm^{-1}$.

Let $T_{\max} = 350$ K and $\gamma = 0.3 K \cdot nm^{-1}$. Fig. 6 shows the expected formation of the elongated tip of the nanobubble, as well as the absence of lateral movement. The diameter only increased by about 15 nm due to the fact that the nanobubble tends to the equilibrium position.

The data in Table 5 show the height of the nanobubble at various parameters, provided that $T_{\max} = 350$ K.

Instead of T_{\max} , put T_{\min} . The coldest point will be at $x = 100$. In this case, the bubble at the point $x = 100$ will have a lower height compared to other points and a tendency for the bubble to burst by 2 will be seen. Let's try to find

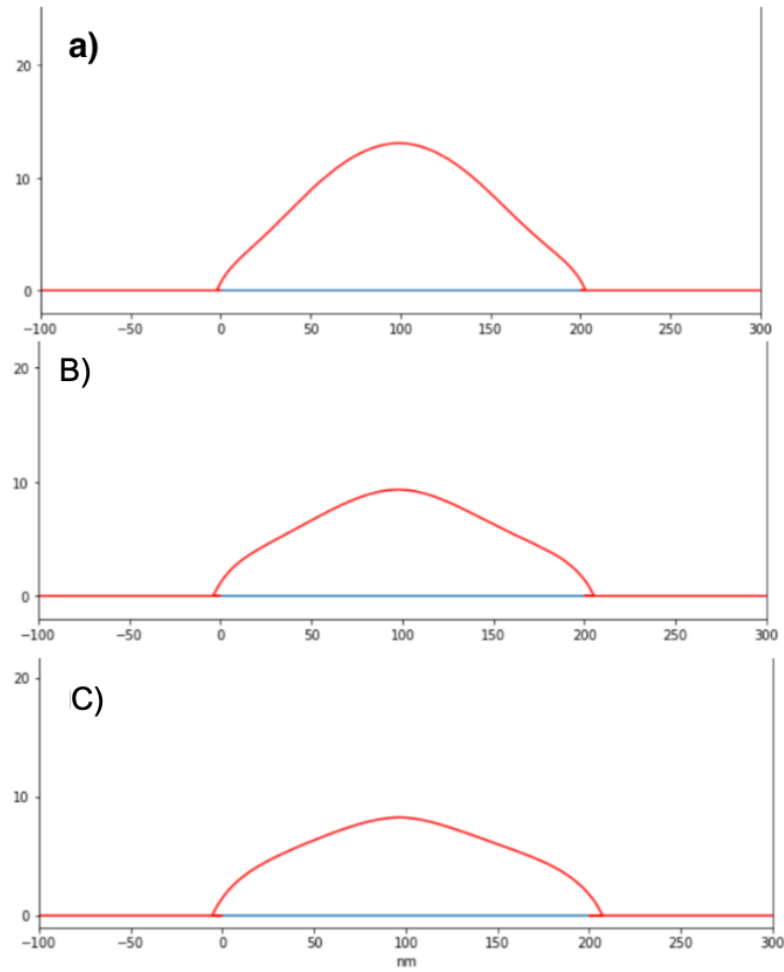


FIG. 6. Change in the shape and position of a nanobubble with a heated substrate over time a) $t = 5 \mu\text{s}$, b) $t = 10 \mu\text{s}$, c) $t = 15 \mu\text{s}$

TABLE 5. Maximum height of a nanobubble in water at different temperature gradients and water temperature T_w

	$\gamma = 0.3 \text{ K}\cdot\text{nm}^{-1}$	$\gamma = 0.1 \text{ K}\cdot\text{nm}^{-1}$	$\gamma = 0.05 \text{ K}\cdot\text{nm}^{-1}$
$T_w = 300 \text{ K}$	$h = 9.2 \text{ nm}$	$h = 11.3 \text{ nm}$	$h = 12.4 \text{ nm}$
$T_w = 330 \text{ K}$	$h = 11.5 \text{ nm}$	$h = 12.4 \text{ nm}$	$h = 13.1 \text{ nm}$
$T_w = 350 \text{ K}$	$h = 12.7 \text{ nm}$	$h = 13.4 \text{ nm}$	$h = 13.8 \text{ nm}$

the critical parameters. Let us increase the depth of the liquid column to $H = 0.4 \text{ m}$ and change $T(x)$ function in the following way:

$$T(x) = T_{\min} + \gamma|100 - x|,$$

$$T_{\min} = 260 \text{ K}, \gamma = 0.5 \text{ K} \cdot \text{nm}^{-1}$$

Simulation data shown on Table 6

What happened to the nanobubble in the case of $H = 1.5$ is shown in Fig. 7.

the nanobubble on the verge of rupture after $13 \mu\text{s}$ does not split in half, but moves in the direction where there are more gas molecules present. From the figure above, it follows that surface tension plays an important role in the formation of a nanobubble. In general, this behavior of a nanobubble can be justified by the fact that when a molecule enters the largest of the forming nanobubbles, it is more difficult for it to get out of it and enter another. Therefore, with sufficient surface tension, it is only a matter of time before one of the forming nanobubbles overflows into another.

TABLE 6. Change in the maximum height at the assumed point of rupture $x = 100$ over time at different depths of the liquid. Temperature gradient $\gamma = 0.5 \text{ K}\cdot\text{nm}^{-1}$, $T_{\min} = 260 \text{ K}$, $T_w = 300 \text{ K}$

	$t = 5 \mu\text{s}$	$t = 10 \mu\text{s}$	$t = 15 \mu\text{s}$
$H = 0.4 \text{ m}$	$h = 5.2 \text{ nm}$	$h = 3.6 \text{ nm}$	$h = 3.4 \text{ nm}$
$H = 0.6 \text{ m}$	$h = 4.5 \text{ nm}$	$h = 3.1 \text{ nm}$	$h = 2.88 \text{ nm}$
$H = 1 \text{ m}$	$h = 2.19 \text{ nm}$	$h = 1.5 \text{ nm}$	$h = 1.44 \text{ nm}$
$H = 1.25 \text{ m}$	$h = 1.3 \text{ nm}$	$h = 1.22 \text{ nm}$	$h = 1.14 \text{ nm}$
$H = 1.35 \text{ m}$	$h = 0.9 \text{ nm}$	$h = 0.95 \text{ nm}$	$h = 1.11 \text{ nm}$
$H = 1.45 \text{ m}$	$h = 0.92 \text{ nm}$	$h = 0.97 \text{ nm}$	$h = 0.6 \text{ nm}$
$H = 1.5 \text{ m}$	$h = 0.8 \text{ nm}$	$h = 0.88 \text{ nm}$	$h = 0 \text{ nm}$

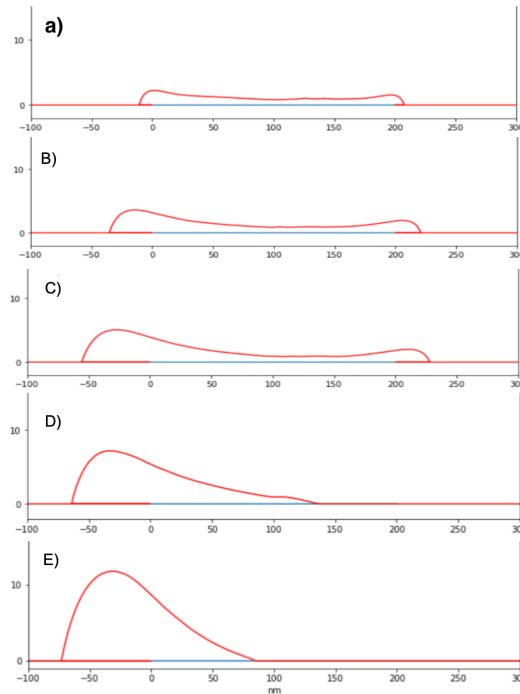


FIG. 7. change in a nanobubble at a depth of $H = 1.5 \text{ m}$ with a temperature gradient. a) $5 \mu\text{s}$, b) $10 \mu\text{s}$, c) $13 \mu\text{s}$, d) $14 \mu\text{s}$, e) $15 \mu\text{s}$

At $H = 1.35 \text{ m}$, the height at the supposed rupture point does not decrease with time, but, on the contrary, increases, which indicates that the bubble began to completely shift to the left.

The table shows that up to a depth of 1 m , the dependence is almost linear. After that, the altitude remains approximately at the same level and a sharp jump occurs at approximately $H = 1.47$. At this depth, the bubble overflows completely to the left side, forming a new one. There was no break in 2 nanobubbles.

Let $H = 0.4 \text{ m}$, $T_{\min} = 260 \text{ K}$, $T_w = 300 \text{ K}$. We will change the parameter of the temperature gradient. The simulation results are in Table 7.

It was not possible to rupture the bubble again. It can be seen from Table 7 that the closest gradient to the separation of the bubble into two is the value: $\gamma 0.5 \text{ K}\cdot\text{nm}^{-1}$. With a gradient greater than 0.5 , the temperature rises rapidly and the center of the bubble sags less and less in height due to the rapid growth of internal energy inside the bubble. With a gradient of less than 0.5 , the temperature, on the contrary, grows more slowly and, accordingly, there is almost no movement to the sides, and therefore more energy is spent on maintaining the current volume of the nanobubble.

TABLE 7. Change in the maximum height at the assumed break point $x = 100$ over time for various parameters of the temperature gradient. $H = 0.4$ m, $T_{\min} = 260$ K, $T_w = 300$ K

	$t = 5 \mu s$	$t = 10 \mu s$	$t = 15 \mu s$
$\gamma = 1 \text{ K}\cdot\text{nm}^{-1}$	$h = 8.7 \text{ nm}$	$h = 4.0 \text{ nm}$	$h = 3.9 \text{ nm}$
$\gamma = 0.8 \text{ K}\cdot\text{nm}^{-1}$	$h = 9.4 \text{ nm}$	$h = 4.1 \text{ nm}$	$h = 3.8 \text{ nm}$
$\gamma = 0.5 \text{ K}\cdot\text{nm}^{-1}$	$h = 5.2 \text{ nm}$	$h = 3.6 \text{ nm}$	$h = 3.4 \text{ nm}$
$\gamma = 0.3 \text{ K}\cdot\text{nm}^{-1}$	$h = 8.0 \text{ nm}$	$h = 3.8 \text{ nm}$	$h = 5.65 \text{ nm}$
$\gamma = 0.1 \text{ K}\cdot\text{nm}^{-1}$	$h = 7.9 \text{ nm}$	$h = 6.1 \text{ nm}$	$h = 4.3 \text{ nm}$
$\gamma = 0.05 \text{ K}\cdot\text{nm}^{-1}$	$h = 7.95 \text{ nm}$	$h = 6.15 \text{ nm}$	$h = 5.2 \text{ nm}$

It makes no sense to consider the situation at $T_{\min} < 260$ K, since this temperature already is a bit lower than freezing point of water and, therefore, it can be concluded that a nanobubble with current parameters at any temperature gradient in water cannot be divided into two parts.

4. Conclusion

In this work, using the molecular dynamics method in combination with highly efficient algorithms a model of a surface nanobubbles was constructed. The model shows how the shape and behavior of the bubble changes over time. The models include various parameters such as liquid and gas temperatures, initial nanobubble shape, solid boundary shape, temperature gradient, liquid surface tension, and other important factors influencing nanobubble evolution. The model demonstrates the stable shape of the nanobubble and establishes the relationship between liquid, gas and the size of the nanobubble in a stable shape. The behavior of a nanobubble with a more real, rough surface of the substrate is shown, which was confirmed by studies carried out years earlier. When heating and cooling different parts of the substrate and liquid, the motion of the nanobubble was substantiated. It is shown that, with the simulated parameters, it is impossible to divide the bubble into two parts with such small sizes and temperature gradient in water: the tension force plays a significant role.

References

- [1] Dockar D., Borg M. K., Reese J. M. Mechanical stability of surface nanobubbles. *Langmuir*, 2018, **35**, 29, P. 9325–9333.
- [2] Joost H. Weijs, Detlef Lohse. Why Surface Nanobubbles Live for Hours. *Phys. Rev. Lett.*, 2013, **110**, P. 054501.
- [3] Lohse D., Zhang X. Surface Nanobubbles and Nanodroplets. *Rev.Mod.Phys.*, 2015, **87**, P. 981–1035.
- [4] Epstein P. S., Plesset M. S. On the Stability of Gas Bubbles in Liquid-Gas Solutions. *J. Chem. Phys.*, 1950, **18**, P. 1505.
- [5] Tsuge H. *Micro-and Nanobubbles: Fundamentals and Applications*. Jenny Stanford Publishing, Stanford, 2019.
- [6] Yang S., Dammer S.M., Bremond N., Zandvliet H.J.W., Kooij E.S., Lohse D. Characterization of Nanobubbles on Hydrophobic Surfaces in Water. *Langmuir*, 2007, **23**(13), P. 7072–7077.
- [7] Zhang X.H., Maeda N., Craig V.S.J. Physical Properties of Nanobubbles on Hydrophobic Surfaces in Water and Aqueous Solutions. *Langmuir*, 2006, **22**(11), P. 5025–5035.
- [8] Borkent B.M., de Beer S., Mugele F., Lohse D. On the Shape of Surface Nanobubbles. *Langmuir*, 2010, **26**(1), P. 260–268.
- [9] Maheshwari S., van der Hoef M., Zhang X., Lohse D. Stability of Surface Nanobubbles: A Molecular Dynamics Study. *Langmuir*, 2016, **32**(43), P. 11116–11122.
- [10] Zhang X., Lhuissier H., Sun C., Lohse D. Surface Nanobubbles Nucleate Microdroplets. *Phys. Rev. Lett.*, 2014, **112**, P. 144503.
- [11] Che Z., Theodorakis P.E. Formation, dissolution and properties of surface nanobubbles. *Journal of Colloid and Interface Science*, 2017, **487**, P. 123–129.
- [12] Zhang X., Chan D.Y.C., Wang D., Maeda N. Stability of Interfacial Nanobubbles. *Langmuir*, 2013, **29**(4), P. 1017–1023.
- [13] Alheshibri M., Qian J., Jehannin M., Craig V.S.J. A History of Nanobubbles. *Langmuir*, 2016, **32**(43), P. 11086–11100.
- [14] Jadhav A.J., Barigou M. Bulk Nanobubbles or Not Nanobubbles: That is the Question. *Langmuir*, 2020, **36**, 7, P. 1699–1708.
- [15] Beng H.T., Hongjie A., C.D. Ohl. How Bulk Nanobubbles Might Survive. *Phys. Rev. Lett.*, 2020, **124**, P. 134503.
- [16] Nirmalkar N., Pacey A. W., Barigou M. On the Existence and Stability of Bulk Nanobubbles. *Langmuir*, 2018, **34**, 37, P. 10964–10973.
- [17] Meegoda J.N., Hewage S.A., Batagoda J.H. Stability of Nanobubbles. *Environmental Engineering Science*, 2018, **53**, P. 1216–1223.
- [18] Lou S.-T., Ouyang Z.-Q., Zhang Y., Li X.-J., Hu J., Li M.-Q., Yang F.-J. Nanobubbles on solid surface imaged by atomic force microscopy. *Journal of Vacuum Science and Technology B: Microelectronics and Nanometer Structures*, 2000, **18**(5), P. 2573.
- [19] Oh S. H., Kim J.-M. Generation and Stability of Bulk Nanobubbles. *Langmuir*, 2017, **33**(15), P. 3818–3823.
- [20] Liu S., Kawagoe Y., Makino Y., Oshita S. Effects of nanobubbles on the physicochemical properties of water: The basis for peculiar properties of water containing nanobubbles. *Chemical Engineering Science*, 2013, **93**, P. 250–256.
- [21] Vorontsov I.V., Chivilikhin S.A., Popov I.Y. Modelling of nanobubbles at the liquid-solid interface in water and oil. *Meccanica*, 2021, **56**, P. 2517–2532.

Structural and energetic analysis of cyclic peptide-gold nano-drug delivery system: a DFT study

B. Khoshbayan, A. Morsali, M. R. Bozorgmehr, S. A. Beyramabadi

Department of Chemistry, Mashhad Branch, Islamic Azad University, Mashhad, Iran

bahareh.khoshbayan@gmail.com, almorsali@yahoo.com, mr_bozorgmehr@yahoo.com, abeyramabadi@gmail.com

PACS 78.67.-n, 78.67.Ch

DOI 10.17586/2220-8054-2021-12-5-612-622

By applying cyclooctaglycine model for cyclic peptide (CP) and cluster Au₆ model for gold nanoparticles (GN), seven different configurations of cyclic peptide-gold nanoparticles (CPGN) with 5-fluorouracil (FU) were investigated. Binding energies, quantum molecular descriptors, and solvation energies in the aqueous solution and gas phase were studied at the density functional level of M06-2X/6-31g(d, p). Solvation energies indicate that the solubility of FU increases in CPGN/FU1-7. This subject is considered a key factor for drug transfer, so CPGNs can be used as an appropriate drug delivery system. The large negative values of calculated binding energies show the stability of CPGN/FU1-7 structures, and quantum molecular descriptors, such as electrophilicity (ω) and global hardness (η) indicate that the reactivity of FU in CPGN/FU1-7 structures increases. AIM calculations for all structures also show that intermolecular hydrogen bonding and Au-drug interactions play an important role for this drug delivery system.

Keywords: 5-fluorouracil, AIM, drug delivery, DFT, cyclic peptide-gold nanosystem.

Received: 4 May 2021

Revised: 22 July 2021

1. Introduction

Drug delivery systems have recently been used as new structures for better drug performance. Various organic and inorganic drug delivery systems such as drug-polymer conjugates [1, 2], carbon nanotubes [3, 4], gold nanoparticles (NPs) [5], magnetic NPs [6, 7], silica NPs [8] and other inorganic nanosystems [9–11] have been investigated due to their chemical stability and environmental compatibility as well as reduced toxicity in medical activities.

In recent studies, gold nanoparticles (GNs) have received significant attention because they have the ability to select and identify cancer cells compared to normal cells [12]. For this reason, GNs have been employed as nanocarriers of different anticancer drugs [5, 13]. In addition to targeted drug delivery, they can perform a controlled release [14, 15].

Cyclic peptides are polypeptide chains with a circular structure and have many uses in various contexts such as drug delivery, nanoscience, optical sensors, and electronic devices. The ring structure is formed by the end of one peptide to the other section with an amide coupling. The cyclic structure with different chain amino acids is a good pattern for encapsulating medicines [16–19]. These structures have been useful in many applications such as molecular transport systems [20, 21], antibacterial agents [22, 23] and other applications [24]. Peptides are less toxic than synthetic molecules and therefore do not accumulate in the tissue. Cyclic peptide-based drugs can cause less harm and usually show better biological activities than their linear counterparts due to their rigid configuration. These drug delivery systems have a variety of structural properties leading to their use as a target drug binder in medical applications [24–26]. Also, they have the ability to penetrate cells more than their linear counterparts and therefore, cellular uptake is significantly increased [27, 28].

Over the past few years, the use of cyclic peptides in the transport of a wide range of therapeutic agents (including anticancer drugs, anti-HIV drugs, and essential phosphopeptides) has been investigated [26, 29, 30]. Recently, gold nanoparticles along with cyclic peptides (CPGNs) have been used as drug transporters for anticancer drugs [31].

Along with experimental methods, quantum mechanical methods are used to better understand drug delivery and biochemical systems [32–37]. In this study, density functional theory (DFT) was applied for exploring gold nanoparticles-cyclic peptide (CPGNs) with 5-fluorouracil (FU) as a drug delivery system. Although this drug (FU) was introduced more than thirty years ago, it is still one of the most widely used anti-cancer drugs for the treatment of many different malignancies alone or in combination with other drugs. FU has shown activity in breast, brain, gastrointestinal (especially colon cancer) and ovarian cancers [38–42].

2. Computational details

DFT calculations were performed at the density functional level of M06-2X with 6-31G(d, p) basis set by GAUSSIAN 09 [43]. For all structures, the optimization of the degrees of freedom in the gas phase and aqueous solution has been performed. Solvent effects were investigated using the polarized continuum model (PCM). Solvation energies (ΔE_{solv}) were calculated by the following equation:

$$\Delta E_{solv} = E_{sol} - E_{gas}, \quad (1)$$

where E_{sol} and E_{gas} represent the total energy for the solution and gas phases. Calculations for cyclic peptide (CP), gold nanoparticles (GN), and 5-fluorouracil (FU) as well as seven CPGN/FU 1-7 configurations were examined.

Quantum molecular descriptors are used to study the stability of different structures. The global hardness (η) indicates the resistance to changing electronic structure and it is determined by the following equation:

$$\eta = \frac{I - A}{2}, \quad (2)$$

where $A = -E_{LUMO}$ and $I = -E_{HOMO}$ are the electron affinity and the ionization potential, in the respective order. The term HOMO-LUMO refers to the highest occupied molecular orbital-lowest unoccupied molecular orbital energy. The electrophilicity index (ω) [44] is obtained by the following equation:

$$\omega = \frac{(I + A)^2}{8\eta}. \quad (3)$$

We used the quantum theory of atom in molecules (QTAIMs) to study the nature of created bonds. QTAIM is based on electron density analysis, $\rho(r)$. AIM calculations were performed using AIMAll software [45]. Different values of electron density such as potential energy density (V_b), kinetic energy density (G_b), total energy density (H_b) and Laplacian of electron density ($\nabla^2 \rho$) at the bond critical point (BCP) were examined for specifying the nature of the bond in different structures.

3. Results and discussion

Cyclooctaglycine [46] and Au₆ cluster [47] were used for cyclic peptide (CP) and gold nanoparticles (GN) modelling, respectively. The different configurations of small Au clusters with 3 to 20 atoms are well known due to numerous experimental and theoretical studies [48–53]. The interaction of gold nanoparticles – cyclic peptide (CPGN) with 5-fluorouracil (FU) was investigated from seven different directions. 5-fluorouracil (Fig. 1) has functional groups such as (F, NH and CO). The various configurations in which 5-fluorouracil approaches CPGN through its functional groups are called CPGN/FU1-7. The optimized structures of (FU), (GN), (CP) and (CPGN/FU1-7) in the aqueous solution are shown in Fig. 2.

The binding energies (ΔE) for different structures were calculated using the following equation:

$$\Delta E = E_{CPGN/FU1-7} - (E_{CP} + E_{GN} + E_{FU}). \quad (4)$$

Table 1 shows the binding energies in the gas phase ($-278.341 \text{ kJ}\cdot\text{mol}^{-1}$ on average) and aqueous solution ($-234.219 \text{ kJ}\cdot\text{mol}^{-1}$ on average) at the M06-2X level. The amounts of these energies in the aqueous solution are lower than in the gas phase; however, their large negative values in both phases indicate the exothermic and optimal performance of CPGN with FU drug. Binding energies depend on the orientation of the drug relative to CPGN. Of the seven species studied in the solution phase, CPGN/FU2 is the most stable configuration. In this configuration, the FU drug is parallel to CPGN, and the NH and OH functional groups of CP interact with the FU drug (Fig. 2). The values of binding energies show the stability of the structures in which FU drug interacts simultaneously with CP and GN. In species where FU interacts only with GN, such as CPGN/FU7, the least stability is observed.

In this research, we evaluated the solvation energy (ΔE_{solv}) for all species (Table 1). The obtained values are negative, indicating the spontaneous solvation, which is very important in drug delivery systems and it is an essential factor for an effective anti-cancer drug. In order to determine the share of each of the two carriers (CP and GN) in the binding and solvation energies, the FU drug was optimized separately near CP and GN (CP/FU and GN/FU in Fig. 1 and Table 1). The solvation of the drug and GN increases in the presence of CP. An important feature of the cyclic peptide is its NH and CO functional groups, which form a hydrogen bond between the FU drug, solvent molecules, and CP. In fact, CP and GN complement each other. GN increases binding energy, and CP increases solvation, and the two become together as a carrier, with better properties.

The stability of various configurations was also investigated using quantum molecular descriptors such as electrophilicity index (ω) and global hardness (η) using the HOMO-LUMO energy gap (E_g). Table 1 shows quantum molecular descriptors such as global hardness (η) and electrophilicity strength (ω) for FU, CP, GN, CP/FU, GN/FU and CPGN/FU1-7 in aqueous solution and gas phases. According to Table 1, in the solution phase, the FU drug and

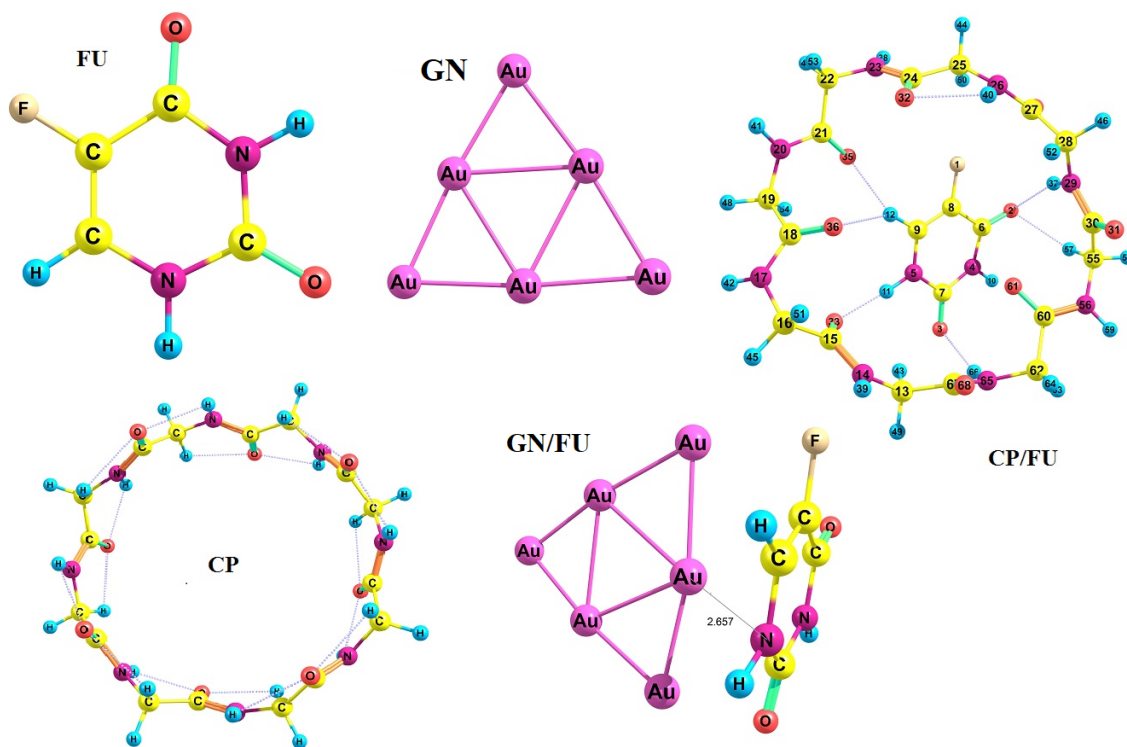


FIG. 1. Optimized structures of FU, GN, CP/FU, CP and GN/FU

CP have high hardness values of 3.97 and 4.95 eV and have high energy gap values of 7.95 and 9.89 eV, and they are considered highly stable species. However, GN is less stable than FU and CP due to hardness value of 2.69 eV and gap energy of 5.38 eV. For CPGN/FU1-7 configurations, the obtained values of E_g and η are less than CP and FU drug, indicating a decrease in the stability of FU drug in the presence of gold nanoparticles and cyclic peptide. According to Table 1, the values of ω in CPGN/FU1-7 structures are higher than FU drug in both phases, which indicates the role of 5-fluorouracil drug as an electron acceptor in the drug delivery system and therefore, the charge is flowing from the carrier to the drug.

Now, a comprehensive review of intermolecular interactions is done using AIM analysis about the nature and strength of interactions through analysis of bond critical points BCP. The electron density $\rho(r)$ and its Laplacian $\nabla^2\rho$ are related to the strength and nature of a bond, respectively. The larger the value of $\rho(r)$, the stronger the bond. Also $\nabla^2\rho$ and H_b show more information about the nature of the interactions. When $(\nabla^2\rho < 0, H_b < 0)$, $(\nabla^2\rho > 0, H_b < 0)$ and $(\nabla^2\rho > 0, H_b > 0)$, the reactions will be strong, medium and weak, respectively. For parameter of $-G_b/V_b$. If $-G_b/V_b > 1$, $0.5 < -G_b/V_b < 1$ and $-G_b/V_b < 0.5$, the bonds will be noncovalent, partially covalent and covalent, respectively [54].

The structure of CPGN/FU2 as the most stable configuration and the structure of CPGN/FU7 as the most unstable configuration in details have been reported by AIM analysis. The values obtained from $\rho(r)$, $\nabla^2\rho$, H_b , G_b , V_b and $-G_b/V_b$ at the bond critical points for the CPGN/FU2 structure are shown in Table 2. The molecular diagram for the most stable state in the solution phase is also shown in Fig. 3. By using $E_{HB} = V_b/2$, hydrogen bond energies can be calculated [55]. The Au–Au interactions in GN, according to Table 2 with the values of $\nabla^2\rho > 0$, $H_b < 0$ and $0.5 < -G_b/V_b < 1$ represent partially covalent bonds, which is the same for other structures. Negative values of H_b indicate covalent bonds (even though closed shell interactions are also involved). Positive values of $\nabla^2\rho$ indicate the electrostatic interactions of the Au–Au interaction [56].

In the CPGN/FU1-7 configurations, we encounter two groups of important interactions, the first of which is between GN and CP or GN and the FU drug. These interactions are in the form of Au–A in which A includes H, O, F, C and N atoms. The higher the Au–A interactions and the higher the values of $\rho(r)$ and $\nabla^2\rho$, the more stable the configuration.

The CPGN/FU2 configuration has 20 Au–A interactions with values of $\rho_{av} = 0.0113$ and $\nabla^2\rho_{av} = 0.0392$ (as average). 3 interactions of Au–A with $\nabla^2\rho > 0$, $H_b < 0$ and $0.5 < -G_b/V_b < 1$ are partially covalent interactions (medium interactions) and 17 Au–A interactions, according to Table 2, are components of weak interactions with

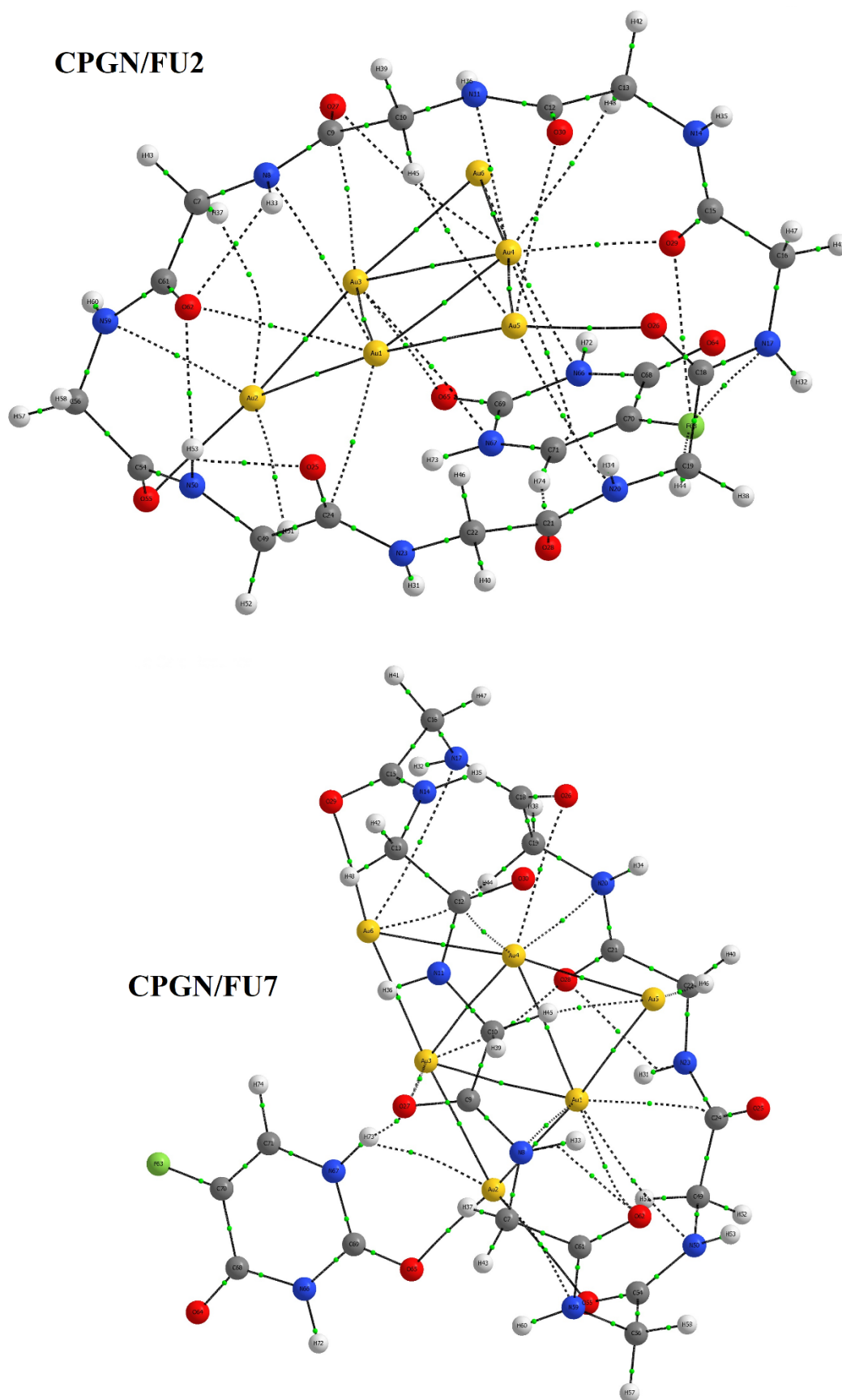


FIG. 3. Molecular graphs of CPGN/FU2 and CPGN/FU7. Small green spheres and lines related to the bond critical points (BCP) and the bond paths, respectively

TABLE 1. Quantum molecular descriptors (eV), binding (ΔE) and solvation (ΔE_{solv}) energies (kJ mol⁻¹) for all structures

Species	E_{LUMO}	E_{HOMO}	E_g	η	ω	ΔE	ΔE_{solv}
H ₂ O							
FU	-0.119	-8.071	7.952	3.976	2.109	—	-40.9
CP	1.395	-8.499	9.894	4.947	1.275	—	-92.2
GN	-1.556	-6.933	5.377	2.688	3.350	—	-24.4
CP/FU	-0.356	-8.255	7.899	3.949	2.347	-119.8	-122.8
GN/FU	-1.570	-6.862	5.291	2.645	3.360	-42.4	-47.5
CPGN/FU1	-1.531	-6.624	5.092	2.546	3.265	-239.4	-143.1
CPGN/FU2	-1.420	-6.486	5.065	2.532	3.085	-243.6	-151.2
CPGN/FU3	-1.554	-6.504	4.950	2.475	3.279	-235.0	-109.7
CPGN/FU4	-1.643	-6.639	4.995	2.497	3.433	-231.8	-90.2
CPGN/FU5	-1.544	-6.608	5.064	2.532	3.281	-237.1	-101.0
CPGN/FU6	-1.544	-6.654	5.112	2.556	3.285	-217.5	-73.7
CPGN/FU7	-1.595	-6.623	5.027	2.513	3.358	-119.8	-40.9
gas							
FU	-0.256	-8.246	7.990	3.995	2.262	—	—
CP	1.340	-8.575	9.916	4.958	1.319	—	—
GN	-2.317	-7.562	5.244	2.622	4.653	—	—
CP/FU	-0.191	-8.084	7.892	3.946	2.169	-208.8	—
GN/FU	-2.268	-7.416	5.147	2.573	4.554	-60.2	—
CPGN/FU1	-1.750	-6.571	4.821	2.410	3.591	-299.2	—
CPGN/FU2	-1.436	-6.454	5.017	2.508	3.102	-301.4	—
CPGN/FU3	-1.779	-6.753	4.973	2.486	3.660	-282.9	—
CPGN/FU4	-1.633	-6.595	4.961	2.480	3.411	-253.8	—
CPGN/FU5	-1.622	-6.494	4.872	2.436	3.381	-293.6	—
CPGN/FU6	-1.672	-6.666	4.993	2.496	3.481	-250.0	—
CPGN/FU7	-1.882	-6.638	4.755	2.377	3.816	-208.8	—

($\nabla^2\rho > 0$, $H_b > 0$ and $-G_b/V_b > 1$). The second group is the interaction between FU drug and CP via hydrogen bonding. In the CPGN/FU2 configuration, the H44 \cdots F63 and H74 \cdots O28 bonds with $\nabla^2\rho > 0$, $H_b > 0$ and $-G_b/V_b > 1$, are related to weak hydrogen bonds.

CPGN/FU7 is the most unstable structure in which there is no interaction between the drug and the cyclic peptide. For this structure, the molecular diagram and the values of $\rho(r)$, $\nabla^2\rho$, H_b , G_b , V_b and $-G_b/V_b$ in the solution phase are presented in Fig. 3 and Table 3. In this configuration, the drug approaches GN from the NH and OH groups. Considering Table 3, this configuration has 19 Au–A interactions with the values of $\rho_{av} = 0.0120$ and $\nabla^2\rho_{av} = 0.0419$ (on average). 3 Au–A interactions are medium and 16 Au–A interactions are weak. In this structure, there is no hydrogen bond between CP and FU.

TABLE 2. Topological parameters in a.u. for CPGN/FU2

Atoms	$\rho(r)$	$\nabla^2\rho$	V_b	G_b	$-G_b/V_b$	H_b
Au–Au interactions						
Au1 – Au3	0.03196	0.08931	–0.03225	0.02729	0.84613	–0.00496
Au1 – Au2	0.04150	0.09884	–0.04457	0.03464	0.77717	–0.00993
Au1 – Au4	0.03460	0.09201	–0.03541	0.02920	0.82480	–0.00620
Au2 – Au3	0.06320	0.12105	–0.07302	0.05164	0.70721	–0.02138
Au3 – Au4	0.03318	0.08992	–0.03376	0.02812	0.83288	–0.00564
Au1 – Au5	0.06291	0.11411	–0.07120	0.04986	0.70033	–0.02133
Au4 – Au5	0.04371	0.10296	–0.04806	0.03690	0.76777	–0.01116
Au3 – Au6	0.04720	0.10709	–0.05265	0.03971	0.75423	–0.01294
Au4 – Au6	0.05339	0.11867	–0.06184	0.04575	0.73984	–0.01609
Au–A interactions						
N8 – Au1	0.00728	0.01999	–0.00408	0.00454	1.11190	0.00045
H37 – Au2	0.00640	0.01510	–0.00252	0.00315	1.24703	0.00062
O27 – Au3	0.00593	0.01884	–0.00328	0.00399	1.21717	0.00071
N11 – Au4	0.01155	0.03406	–0.00747	0.00799	1.06970	0.00052
H45 – Au5	0.00707	0.02089	–0.00321	0.00421	1.31329	0.00100
O30 – Au5	0.00759	0.02432	–0.00460	0.00534	1.16083	0.00074
H48 – Au4	0.00763	0.02725	–0.00406	0.00544	1.33751	0.00137
H29 – Au4	0.02409	0.09375	–0.02439	0.02391	0.98048	–0.00047
N20 – Au5	0.01095	0.03403	–0.00717	0.00783	1.09330	0.00066
C24 – Au1	0.00642	0.02172	–0.00311	0.00427	1.37107	0.00115
O26 – Au5	0.03851	0.16091	–0.04559	0.04291	0.94111	–0.00268
O27 – Au4	0.00507	0.01423	–0.00247	0.00301	1.21742	0.00053
H51 – Au2	0.00763	0.02531	–0.00390	0.00511	1.31029	0.00121
O62 – Au1	0.00489	0.01497	–0.00235	0.00305	1.29334	0.00069
O55 – Au2	0.03218	0.12694	–0.03593	0.03383	0.94153	–0.00210
N59 – Au2	0.01010	0.02853	–0.00619	0.00666	1.07570	0.00046
C71 – Au4	0.00923	0.02823	–0.00477	0.00591	1.23895	0.00114
O65 – Au3	0.01033	0.03463	–0.00730	0.00798	1.09235	0.00067
N66 – Au6	0.00593	0.01448	–0.00284	0.00323	1.13593	0.00038
N67 – Au3	0.00848	0.02716	–0.00518	0.00598	1.15559	0.00080
Intermolecular hydrogen bonds						
H44 – F63	0.01072	0.04407	–0.00897	0.00999	1.11415	0.00102
O28 – H74	0.01842	0.05928	–0.01479	0.01476	1.00176	–0.00002

Table 3: Topological parameters in a.u. for CPGN/FU1, CPGN/FU3-7 and GN/H₂O

Atoms	$\rho(r)$	$\nabla^2\rho$	V_b	G_b	$-G_b/V_b$	H_b
Au-Au interactions (CPGN/FU3-7)						
Au1 – Au3	0.03801	0.10021	-0.04071	0.03288	0.80769	-0.00782
Au1 – Au2	0.05995	0.11259	-0.06754	0.04784	0.70836	-0.01969
Au2 – Au3	0.05361	0.10714	-0.05929	0.04304	0.72585	-0.01625
Au1 – Au4	0.03207	0.08994	-0.03267	0.02758	0.84407	-0.00509
Au3 – Au4	0.03387	0.09317	-0.03504	0.02916	0.83237	-0.00587
Au1 – Au5	0.04794	0.10850	-0.05379	0.04045	0.75215	-0.01333
Au4 – Au5	0.05377	0.11737	-0.06196	0.04565	0.73679	-0.01630
Au3 - Au6	0.05861	0.11364	-0.06633	0.04737	0.71414	-0.01896
Au4 - Au6	0.04927	0.11032	-0.05550	0.04154	0.74844	-0.01396
Au-A interactions (CPGN/FU3-7)						
N8 – Au1	0.00768	0.02278	-0.00464	0.00516	1.11328	0.00052
O27 – Au3	0.00403	0.01234	-0.00188	0.00248	1.31709	0.00059
H45 – Au5	0.00790	0.02284	-0.00360	0.00465	1.29165	0.00105
C12 – Au4	0.01024	0.03900	-0.00654	0.00814	1.24472	0.00160
N17 - Au6	0.00693	0.01894	-0.00377	0.00425	1.12678	0.00047
O26 – Au4	0.01296	0.04391	-0.01000	0.01049	1.04857	0.00048
H44 - Au6	0.00608	0.01571	-0.00246	0.00319	1.29643	0.00073
N20 – Au4	0.00825	0.02395	-0.00502	0.00550	1.09639	0.00048
H46 - Au5	0.00854	0.02575	-0.00416	0.00530	1.27292	0.00113
C24 – Au1	0.01088	0.04032	-0.00696	0.00852	1.22407	0.00156
O28 – Au3	0.00386	0.01149	-0.00177	0.00232	1.30929	0.00054
O29 - Au6	0.03139	0.12372	-0.03478	0.03285	0.94460	-0.00192
N50 – Au1	0.00689	0.01815	-0.00379	0.00416	1.09833	0.00037
O55 - Au2	0.02696	0.10319	-0.02838	0.02709	0.95447	-0.00129
N59 - Au2	0.00646	0.01718	-0.00343	0.00386	1.12580	0.00043
O62 – Au1	0.01209	0.04199	-0.00883	0.00966	1.09391	0.00083
H73 – Au3	0.00968	0.02810	-0.00504	0.00603	1.19674	0.00099
O65 – Au2	0.03707	0.15481	-0.04359	0.04115	0.94389	-0.00244
H73 – Au2	0.01030	0.03341	-0.00587	0.00711	1.21065	0.00123
Medium Au-A interactions (CPGN/FU1)						
O29 - Au6	0.02995	0.11675	-0.03266	0.03092	0.94676	-0.00173
O55 – Au2	0.02901	0.11205	-0.03126	0.02964	0.94796	-0.00162
Medium Au-A interactions (CPGN/FU3)						
O29 – Au6	0.02710	0.10324	-0.02844	0.02712	0.95379	-0.00131
O25 – Au1	0.01758	0.06279	-0.01570	0.01571	0.99974	-0.00001

O55 - Au2	0.03180	0.12638	-0.03538	0.03349	0.94642	-0.00189
O65 - Au2	0.03061	0.11855	-0.03336	0.03150	0.94416	-0.00186
O28 - H72	0.02050	0.06254	-0.01615	0.01589	0.98390	-0.00026
O64 - H31	0.02882	0.08955	-0.02293	0.02266	0.98805	-0.00027
Medium Au-A interactions (CPGN/FU4)						
O29 - Au6	0.03087	0.12110	-0.03399	0.03213	0.94528	-0.00186
O55 - Au2	0.02239	0.08028	-0.02205	0.02106	0.95493	-0.00099
H51 - O64	0.01568	0.04680	-0.01196	0.01183	0.98896	-0.00013
H31 - O64	0.01637	0.05301	-0.01331	0.01328	0.99759	-0.00003
Medium Au-A interactions (CPGN/FU5)						
O29 - Au6	0.03135	0.12342	-0.03472	0.03278	0.94435	-0.00193
O64 - Au2	0.04041	0.17285	-0.04867	0.04594	0.94389	-0.00273
Medium Au-A interactions (CPGN/FU6)						
O29 - Au6	0.03336	0.13357	-0.03771	0.03555	0.94272	-0.00216
O65 - Au2	0.03794	0.15756	-0.04471	0.04205	0.94048	-0.00266
GN/H ₂ O						
O7-Au5	0.04766	0.21010	-0.06032	0.05642	0.93535	-0.00390

The values of $\rho(r)$, $\nabla^2\rho$, H_b , G_b , V_b and $-G_b/V_b$ along with Au-A interactions ($H_b < 0$) and medium hydrogen bonds in other structures were investigated, as shown in Table 3. CPGN/FU1 is the second stable configuration which has 2 medium Au-A interactions and 19 weak interactions with $\rho_{av} = 0.0106$ and $\nabla^2\rho_{av} = 0.0355$ and it consists of 2 weak hydrogen bonds. Concerning the structure of CPGN/FU2, the strength and nature of Au-A interactions have higher values and this has made this structure more stable than CPGN/FU1.

CPGN/FU6 is the third stable configuration. In this structure, there are 17 Au-A interactions with 2 medium interactions and 15 weak interactions of Au-A with $\rho_{av} = 0.0118$ and $\nabla^2\rho_{av} = 0.0412$. CPGN/FU6 has 2 weak hydrogen bonds. The order of stability of the other configurations is as follows (Table 3).

CPGN/FU4 has 2 medium Au-A interactions and 16 weak interactions with values of $\rho_{av} = 0.0111$ and $\nabla^2\rho_{av} = 0.0372$. Also, this structure has 2 hydrogen bonds of H51 \cdots O64 and H31 \cdots O64 as a medium hydrogen bond and one weak hydrogen bond. CPGN/FU3 has 4 medium Au-A interactions and 15 weak interactions with $\rho_{av} = 0.0120$ and $\nabla^2\rho_{av} = 0.0409$ and 2 medium hydrogen bonds of H31 \cdots O64 and H72 \cdots O28 and one weak hydrogen bond. CPGN/FU5 has 2 medium interactions of Au-A and 16 weak interactions with the values of $\rho_{av} = 0.0117$ and $\nabla^2\rho_{av} = 0.0415$. In this structure, there is 1 weak hydrogen bond.

As previously mentioned, we used PCM to consider the implicit effect of the solvent. QTAIM calculations can be used to justify that there is no need to consider the explicit effect of the solvent. To do this, we must show that there is no chemical bond between GN and H₂O molecules (solvent). The GN structure was optimized next to H₂O (GN/H₂O) and then AIM calculations were performed. The optimized structure of GN/H₂O along with the molecular graph and the values of $\rho(r)$, $\nabla^2\rho$, H_b , G_b , V_b and $-G_b/V_b$ are represented in Fig. 4 and Table 3, respectively. According to the bond length in Fig. 4 (Au-O) and the values in Table 3, no chemical bond is formed between GN and H₂O.

4. Conclusion

In this study, seven gold nanoparticle-cyclic peptide configurations with the anticancer drug FU were investigated in the aqueous solution and gas phase at the M06-2X level. The values of binding energy indicate that the performance of CPGN with FU drug in CPGN/FU1-7 configurations is appropriate and the simultaneous interaction of the drug with CP and GN results in greater stability. The data obtained from solvation and binding energies show that the solubility of FU and GN increases in the presence of CP. The global hardness (η) and energy gap (E_g) for FU decrease in the presence of GN and CP (CPGN/FU1-7), indicating the reactivity FU increases. According to AIM studies, FU can interact with CPGN as Au-A (A = N, O, F, C, H) and hydrogen bonding. Most Au-A interactions with $-G_b/V_b > 1$, $H_b > 0$ and $\nabla^2\rho > 0$ are weak interactions. AIM results showed that in the most unstable configuration (CPGN/FU7),

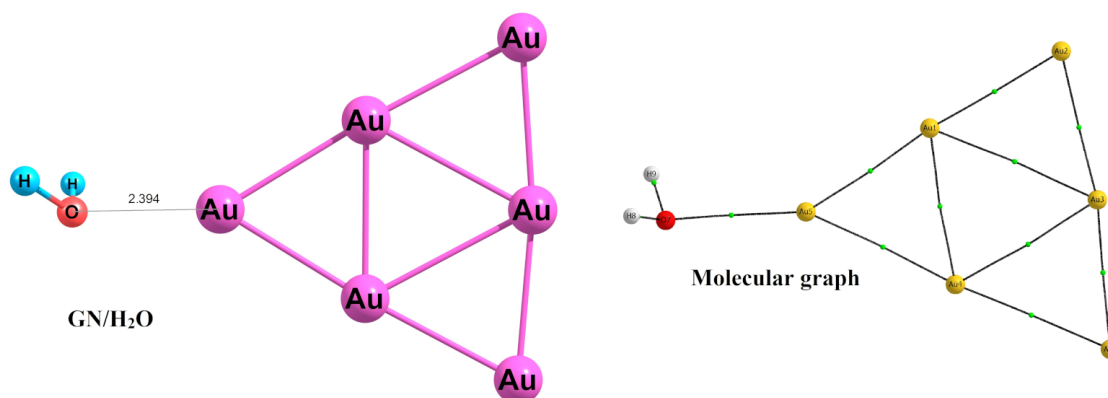


FIG. 4. Optimized structure and molecular graph of GN/H₂O. Small green spheres and lines related to the bond critical points (BCP) and the bond paths, respectively

the drug interacts only with GN, and in the most stable configuration (CPGN/FU2), Au–A interactions are stronger and are accompanied by hydrogen bonds.

Acknowledgements

We thank the Research Centre for Animal Development Applied Biology for allocation of computer time.

References

- [1] Girase M.L., Patil P.G., Ige P.P., Biomaterials P. Polymer-drug conjugates as nanomedicine: a review. *Int. J. Polymer. Mater.*, 2020, **69**, P. 990–1014.
- [2] Rahbar M., Morsali A., Bozorgmehr M.R., Beyramabadi S.A. Quantum chemical studies of chitosan nanoparticles as effective drug delivery systems for 5-fluorouracil anticancer drug. *J. Mol. Liq.*, 2020, **302**, 112495.
- [3] Lotfi M., Morsali A., Bozorgmehr M.R. Comprehensive quantum chemical insight into the mechanistic understanding of the surface functionalization of carbon nanotube as a nanocarrier with cladribine anticancer drug. *Appl. Surf. Sci.*, 2018, **462**, P. 720–729.
- [4] Samal S.K. Cancer and Carbon Nano Tubes: A Promising Hope of Future. *Scientific Review*, 2018, **4**, P. 64–67.
- [5] Connor D.M., Broome A.-M. Gold Nanoparticles for the Delivery of Cancer Therapeutics. *Adv. Cancer Res.*, 2018, **139**, P. 163–184.
- [6] Roohi R., Emdad H., Jafarpur K. A comprehensive study and optimization of magnetic nanoparticle drug delivery to cancerous tissues via external magnetic field. *J. Test. Eval.*, 2019, **47**, P. 681–703.
- [7] Shabani Z., Morsali A., Bozorgmehr M.R., Beyramabadi S.A. Quantum chemical modeling of iron oxide magnetic nanoparticles functionalized with cytarabine. *Chem. Phys. Lett.*, 2019, **719**, P. 12–21.
- [8] Foglia L.M., Alvarez S.G., et al. Recent patents on the synthesis and application of silica nanoparticles for drug delivery. *Recent Pat. Biotechnol.*, 2011, **5**, P. 54–61.
- [9] Singh R.K., Kim H.W. Inorganic nanobiomaterial drug carriers for medicine. *Tissue Eng. Regen. Med.*, 2013, **10**, P. 296–309.
- [10] Ostroshko A.A., Gagarin I.y.D., Danilova I.G., Gette I.F. The use of nanocluster polyoxometalates in the bioactive substance delivery systems. *Nanosystems: Phys. Chem. Math.*, 2019, **10**, P. 318–349.
- [11] Popova N., Popov A., Shcherbakov A., Ivanov V. Layer-by-layer capsules as smart delivery systems of CeO₂ nanoparticle-based theranostic agents. *Nanosystems: Phys. Chem. Math.*, 2017, **8**, P. 282–289.
- [12] Fan M., Han Y., et al. Ultrasmall gold nanoparticles in cancer diagnosis and therapy. *Theranostics*, 2020, **10**, 4944.
- [13] Haume K., Rosa S., et al. Gold nanoparticles for cancer radiotherapy: a review. *Cancer Nanotechnol.*, 2016, **7**, P. 8–28.
- [14] Xu Y., He R., et al. Laser beam controlled drug release from Ce6-gold nanorod composites in living cells: a FLIM study. *Nanoscale*, 2015, **7**, P. 2433–2441.
- [15] Khutale G.V., Casey A. Synthesis and characterization of a multifunctional gold-doxorubicin nanoparticle system for pH triggered intracellular anticancer drug release. *Eur. J. Pharm. Biopharm.*, 2017, **119**, P. 372–380.
- [16] Fernandez-Lopez S., Kim H.-S., et al. Antibacterial agents based on the cyclic D, L- α -peptide architecture. *Nature*, 2001, **412**, 452.
- [17] Larnaudie S.C., Brendel J.C., et al. Cyclic Peptide-Polymer Nanotubes as Efficient and Highly Potent Drug Delivery Systems for Organometallic Anticancer Complexes. *Biomacromolecules*, 2018, **19**, P. 239–247.
- [18] Ellison A.J., Tanrikulu I.C., Dones J.M., Raines R.T. Cyclic Peptide Mimetic of Damaged Collagen. *Biomacromolecules*, 2020, **21**, P. 1539–1547.
- [19] Shahabi M., Raissi H. Assessment of solvent effects on the inclusion behavior of pyrazinamide drug into cyclic peptide based nanotubes as novel drug delivery vehicles. *J. Mol. Liq.*, 2018, **268**, P. 326–334.
- [20] Nasrolahi Shirazi A., Tiwari R.K., et al. Cyclic peptide-selenium nanoparticles as drug transporters. *Mol. Pharm.*, 2014, **11**, P. 3631–3641.
- [21] Chermahini A.N., Farrokhpour H., Shahangi F., Dabbagh H.A. Cyclic peptide nanocapsule as ion carrier for halides: a theoretical survey. *Struct. Chem.*, 2018, **29**, P. 1351–1357.
- [22] Dartois V., Sanchez-Quesada J., et al. Systemic antibacterial activity of novel synthetic cyclic peptides. *Antimicrob. Agents Chemother.*, 2005, **49**, P. 3302–3310.
- [23] Khalfa A., Tarek M. On the antibacterial action of cyclic peptides: insights from coarse-grained MD simulations. *J. Phys. Chem. B*, 2010, **114**, P. 2676–2684.

- [24] Claro B., Bastos M., Garcia-Fandino R. Design and applications of cyclic peptides. In *Peptide Applications in Biomedicine, Biotechnology and Bioengineering*, 2018, Elsevier, P. 87–129.
- [25] Zorzi A., Deyle K., Heinis C. Cyclic peptide therapeutics: past, present and future. *Curr. Opin. Chem. Biol.*, 2017, **38**, P. 24–29.
- [26] Park S.E., Sajid M.I., Parang K., Tiwari R.K.M.p. Cyclic Cell-Penetrating Peptides as Efficient Intracellular Drug Delivery Tools. *Mol. Pharm.*, 2019, **16**, P. 3727–3743.
- [27] Oh D., Nasrolahi Shirazi A., et al. Enhanced cellular uptake of short polyarginine peptides through fatty acylation and cyclization. *Mol. Pharm.*, 2014, **11**, P. 2845–2854.
- [28] Mandal D., Nasrolahi Shirazi A., Parang K. Cell-penetrating homochiral cyclic peptides as nuclear-targeting molecular transporters. *Angew. Chem. Int. Ed.*, 2011, **50**, P. 9633–9637.
- [29] Jing X., Jin K.J.M.R.R. A gold mine for drug discovery: Strategies to develop cyclic peptides into therapies. *Med. Res. Rev.*, 2020, **40**, P. 753–810.
- [30] Dougherty P.G., Sahni A., Pei D. Understanding cell penetration of cyclic peptides. *Chem. Rev.*, 2019, **119**, P. 10241–10287.
- [31] Nasrolahi Shirazi A., Tiwari R.K., et al. Surface decorated gold nanoparticles by linear and cyclic peptides as molecular transporters. *Mol. Pharm.*, 2013, **10**, P. 3137–3151.
- [32] Naghavi F., Morsali A., Bozorgmehr M.R., Beyramabadi S.A. Quantum molecular study of mesoporous silica nanoparticle as a delivery system for troxacitabine anticancer drug. *J. Mol. Liq.*, 2020, **310**, 113155.
- [33] Nasrabadi M., Morsali A., Beyramabadi S.A. An applied quantum-chemical model for genipin-crosslinked chitosan (GCS) nanocarrier. *Int. J. Biol. Macromol.*, 2020, **165**, P. 1229–1240.
- [34] Bokarev A., Plastun I. Possibility of drug delivery due to hydrogen bonds formation in nanodiamonds and doxorubicin: molecular modeling. *Nanosystems: Phys. Chem. Math.*, 2018, **9**, P. 370–377.
- [35] Nasrabadi M., Beyramabadi S.A., Morsali A. Surface functionalization of chitosan with 5-nitroisatin. *Int. J. Biol. Macromol.*, 2020, **147**, P. 534–536.
- [36] Naghavi F., Morsali A., Bozorgmehr M.R. Molecular mechanism study of surface functionalization of silica nanoparticle as an anticancer drug nanocarrier in aqueous solution. *J. Mol. Liq.*, 2019, **282**, P. 392–400.
- [37] Hadi L., Ali M., Momen H.M. The prediction of COOH functionalized carbon nanotube application in melphalan drug delivery. *Nanosystems: Phys. Chem. Math.*, 2019, **10**, P. 438–446.
- [38] Sara J.D., Kaur J., et al. 5-fluorouracil and cardiotoxicity: a review. *Ther. Adv. Med. Oncol.*, 2018, **10**, 1758835918780140.
- [39] Longley D.B., Harkin D.P., Johnston P.G. 5-fluorouracil: mechanisms of action and clinical strategies. *Nat. Rev. Cancer*, 2003, **3**, P. 330–338.
- [40] Metterle L., Nelson C., Patel N. Intralesional 5-fluorouracil (FU) as a treatment for nonmelanoma skin cancer (NMSC): a review. *J. Am. Acad. Dermatol.*, 2016, **74**, P. 552–557.
- [41] Lee J.J., Beumer J.H., Chu E. Therapeutic drug monitoring of 5-fluorouracil. *Cancer Chemother. Pharmacol.*, 2016, **78**, P. 447–464.
- [42] Chen L., Yu H., et al. Fabrication of a microporous Dy (III)-organic framework with polar channels for 5-Fu (fluorouracil) delivery and inhibiting human brain tumor cells. *Struct. Chem.*, 2018, **29**, P. 1885–1891.
- [43] Frisch M., Trucks G., et al. G09 Gaussian Inc. Gaussian 09, revision B.01. Gaussian, Inc., Wallingford, CT, 2009.
- [44] Parr R.G., Szentpaly L.v., Liu S. Electrophilicity index. *J. Am. Chem. Soc.*, 1999, **121**, P. 1922–1924.
- [45] AIMAll TK Gristmill Software. Overland Park KS, USA, 2016, URL: aim.tkgristmill.com.
- [46] Poteau R., Trinquier G. All-cis cyclic peptides. *J. Am. Chem. Soc.*, 2005, **127**, P. 13875–13889.
- [47] Manzoor D., Pal S., Krishnamurty S. Influence of charge and ligand on the finite temperature behavior of gold clusters: a BOMD study on Au₆ cluster. *J. Phys. Chem. C*, 2013, **117**, P. 20982–20990.
- [48] Fagan J.W., Weerawardene K.D.M., et al. Toward quantitative electronic structure in small gold nanoclusters. *J. Chem. Phys.*, 2021, **155**, 014301.
- [49] Shi H.X., Sun W.G., et al. Probing the Interactions of O₂ with Small Gold Cluster Au_nQ (n = 2–10, Q= 0–1): A Neutral Chemisorbed Complex Au₅O₂ Cluster Predicted. *J. Phys. Chem. C*, 2017, **121**, P. 24886–24893.
- [50] Ligare M.R., Morrison K.A., et al. Ion Mobility Spectrometry Characterization of the Intermediate Hydrogen-Containing Gold Cluster Au₇(PPh₃)₇H₅²⁺. *J. Phys. Chem. Lett.*, 2021, **12**, P. 2502–2508.
- [51] Lang S.M., Bernhardt T.M., et al. Selective C-H bond cleavage in methane by small gold clusters. *Angew. Chem. Int. Ed. Engl.*, 2017, **129**, P. 13591–13595.
- [52] Gilb S., Weis P., et al. Structures of small gold cluster cations (Au_n⁺, n < 14): Ion mobility measurements versus density functional calculations. *J. Chem. Phys.*, 2002, **116**, P. 4094–4101.
- [53] Lechtken A., Neiss C., Kappes M.M., Schooss D. Structure determination of gold clusters by trapped ion electron diffraction: Au₁₄–Au₁₉⁻. *Phys. Chem. Chem. Phys.*, 2009, **11**, P. 4344–4350.
- [54] Rozas I., Alkorta I., Elguero J. Behavior of ylides containing N, O, and C atoms as hydrogen bond acceptors. *J. Am. Chem. Soc.*, 2000, **122**, P. 11154–11161.
- [55] Espinosa E., Souhassou M., Lachekar H., Lecomte C. Topological analysis of the electron density in hydrogen bonds. *Acta Crystallogr. Sect. B: Struct. Sci.*, 1999, **55**, P. 563–572.
- [56] Espinosa E., Alkorta I., Elguero J., Molins E. From weak to strong interactions: A comprehensive analysis of the topological and energetic properties of the electron density distribution involving X-H F-Y systems. *J. Chem. Phys.*, 2002, **117**, P. 5529–5542.

The influence of edge specific surface energy on the direction of hydrosilicate layers scrolling

A. A. Krasilin

Ioffe Institute, Politekhnikeskaya 26, St.-Petersburg, 194021, Russia

ikrasilin@mail.ioffe.ru

PACS 61.46.+w**DOI 10.17586/2220-8054-2021-12-5-623-629**

The present study reports on energy modeling of morphological features of hydrosilicate nanoscrolls with chrysotile structure. It considers a possibility of scrolling direction change driven by difference in specific surface energies on the hydrosilicate layer edges. Specific surface energy estimation together with energy modeling of the scrolling process reveal several directions, which are preferable in comparison to the [010] or [100] directions of scrolling. The results obtained may help to better understand correlation between morphology, structural features, and mechanical behavior of hydrosilicate nanoscrolls.

Keywords: inorganic nanotube, modeling, phyllosilicate, morphology.

Received: 11 August 2021

Revised: 25 September 2021

1. Introduction

Hydrosilicate layers like imogolite, halloysite, chrysotile, and their structural analogs may scroll due to size mismatch between octahedral and tetrahedral sheets and surface structure difference on the opposite sides of a layer [1]. The scrolling process yields nanoparticles of high specific surface area [2–5] having good mechanical properties [6–11] and oppositely charged inner and outer surfaces [5, 12]. These remarkable features have promoted hydrosilicate nanoscrolls and nanotubes applications as catalysts [13–16], nanoreactors [17, 18] and containers [19–21], polymer [22, 23] and other functional materials [24] fillers.

Despite large variety of applications, formation mechanism, hydrosilicate nanoscrolls structure description, and understanding of related properties remain challenging. One particular problem relates to the form of cross-section (concentric rings, spiral or more complex forms [25]) and the direction of scrolling. A number of X-ray diffraction studies of chrysotile [26, 27] and halloysite [28] came to the conclusion that the scrolling occurred along b or seldom along a axes (of monoclinic or triclinic unit cells). While this method gave integral information about nanotubes and nanoscrolls powders, electron diffraction patterns obtained on individual hydrosilicate and chalcogenide nanoscrolls [29–31] demonstrated deviations of scrolling direction from a or b axes. Concurrently, those particles were recognized as of cylindrical form. Strong deviations of scrolling direction or inequality of the scrolling driving force along the layer frequently led to formation of conical nanoscrolls [32–36]. An arbitrariness of scrolling direction may affect quality of hydrogen bonding between the adjacent layers [26], which, in turn, can play an important role in the mechanical behavior of hydrosilicate nanotubes and nanoscrolls [8, 10, 11].

The present study has attempted to investigate the issue with scrolling direction of hydrosilicate layers from an energy modeling [37–42] perspective. Recent developments in the field of phenomenological modeling of scrolling [42] have revealed a crucial role for the specific surface energy σ of the hydrosilicate layer edges in the choice between platy and scrolled particle shape. That study, however, operated with arbitrary range of edge σ values. Here, edge σ values have been estimated relative to certain $(hk0)$ planes intersecting chrysotile unit cell. Thus, an assumption has been tested, that the direction of scrolling may deviate from directions of a or b axes because of energy preference of edges formed by $(hk0)$ planes in comparison to the edges formed by (100) and (010) planes.

2. Calculation concept**2.1. Energy model of scrolling**

An energy model of finite mass rectangular plate scrolling [41] was adopted for the calculation of energy effect value and preferable size parameters (number of layers and length) for cylindrical nanoscrolls with different σ values on the edges. The model relied on three energy components, namely strain energy E_s , surface energy Σ , and adhesion energy U_a :

$$\Delta E_j^{\textcircled{a}} = \frac{M}{m} \left[\left(E_s^{\textcircled{a}} - E_s' \right) + \left(\Sigma^{\textcircled{a}} - \Sigma' \right) - U_a^{\textcircled{a}} \right], \quad (1)$$

where M is molar mass of the layer, m is mass of the layer, @ sign denotes scrolled state, and / sign denotes flat state of the layer. The layer mass was held constant during the calculation and was determined as follows:

$$m=L_1L_2h_s\rho=\text{const}, \quad (2)$$

where L_1 is the length, along which the scrolling process occurred (equals to spiral length measured at $h_s/2$), L_2 is the length of cylinder, h_s is the layer thickness, and ρ is density of the layer.

The strain energy of the scrolled state was determined within the continuous mechanics approach [43]:

$$E_s^{\textcircled{}}=\frac{Yh_s^3L_2}{24(1-\mu)}\int_0^{2\pi n}\left(\frac{1}{r_{in}+f\varphi}-\frac{1}{r_0}\right)^2\sqrt{f^2+(r_{in}+f\varphi)^2}d\varphi, \quad (3)$$

where Y is the Young's modulus, μ is the Poisson's ratio, n is the number of layers (wraps), r_{in} is the inner radius of the nanoscroll, measured at $h_s/2$, r_0 is the radius, at which size difference between octahedral and tetrahedral sheets is fully compensated by curvature (in the direction of scrolling), and $f=(h_s+t)/2\pi$ is the Archimedean spiral constant (t is the gap between adjacent layers). Square layer of side length L_{ref} was chosen as the reference flat state with the following strain energy:

$$E_s^/= \frac{Yh_s^3L_{ref}^2}{24(1-\mu)r_0^2}. \quad (4)$$

The surface energy was determined as sum of all surface areas multiplied by specific surface energy values:

$$\Sigma^{\textcircled{}}=\sigma_{out}L_1^{out}L_2+\sigma_{in}L_1^{in}L_2+2\sigma_1L_1h_s+2\sigma_2L_2h_s, \quad (5)$$

where σ_{out} , σ_{in} , σ_1 , σ_2 are specific surface energies of outer, inner, and two different edge surfaces, respectively, L_1^{out} and L_1^{in} are lengths of the spiral beginning at $r=r_{in}\pm h_s/2$, respectively. The surface energy of the reference flat layer was written assuming $\sigma_1=\sigma_2=\sigma_{ref}$:

$$\Sigma^/=L_{ref}^2(\sigma_{out}+\sigma_{in})+4\sigma_{ref}L_{ref}h_s. \quad (6)$$

The adhesion energy at $n > 1$ was estimated as follows:

$$U_a^{\textcircled{}}=u_aL_2\int_0^{2\pi(n-1)}\sqrt{f^2+\left(r_{in}+\frac{h_s+t}{2}+f\varphi\right)^2}d\varphi, \quad (7)$$

where u_a is the specific adhesion energy.

2.2. Parametrization

To determine energy effect of scrolling, the model must be parameterized. The mass of the layer (eq. (2)) was set to 10^{-15} g, and the molar mass 277 g/mol was calculated in accordance with the chemical formula $\text{Mg}_3\text{Si}_2\text{O}_5(\text{OH})_4$. The layer thickness $h_s=0.4$ nm and the gap between adjacent layers $t=0.3$ nm were chosen in accordance with electron microscopy study [10]. Density of the layer was set to 2.5 g/cm³ [41]. The Young's modulus $Y=280$ GPa was calculated as an average of the data represented in theoretical paper [44], and the Poisson's ratio was set to 0.2 [45]. The stress-free radius $r_0=8.8$ nm was taken from study [46]. Specific surface energies were chosen as follows: $\sigma_{out}=0.05$ J/m² for (0001) surface of $\text{Mg}(\text{OH})_2$ brucite [47], $\sigma_{in}=1.51$ J/m² for (111) surface of α - SiO_2 cristobalite [48]. An approach to calculation of specific surface energies at the edges of the layer is described in the subsection below. For the reference layer $\sigma_{ref}=5.5$ J/m² was chosen.

2.3. Specific surface energy of the edges

Specific surface energy calculation approach was based on the work of Shchupalov [48]. The σ value was estimated as a quantity of broken chemical bonds per surface area. For an arbitrary (hkl) plane specific surface energy was written as follows:

$$\sigma_{hkl}=\frac{0.5}{N_A S_{hkl}}\sum_i E_i n_i^{br}, \quad (8)$$

where N_A is the Avogadro constant, E_i is the energy of a single bond, n_i^{br} is the number of chemical bonds, intersected by the (hkl) plane, and S_{hkl} is the surface area of the (hkl) plane, limited by periodicity condition. It was assumed that the edges of the layer are formed only by the ($hk0$) planes parallel to c axis. Fig. 1 demonstrates an example of the S_{hk0} value determination. Whereas the relative position of chemical bonds and (010) or (110) planes reproduced from

cell to cell, the (130) plane intersected the cell in 3 unique ways, so 3 cells must be considered. The final equation for the surface area was written as follows:

$$S_{hk0} = \sqrt{(hb)^2 + (ka)^2} \cdot c \cdot \sin\beta, \quad (9)$$

where a , b , c , and β are lattice parameters. In the case shown in Fig. 1 $a = 0.5340$ nm, $b = 0.9241$ nm, $c = 1.4689$ nm, and $\beta = 93.66^\circ$ ($\sin\beta \cong 1$).

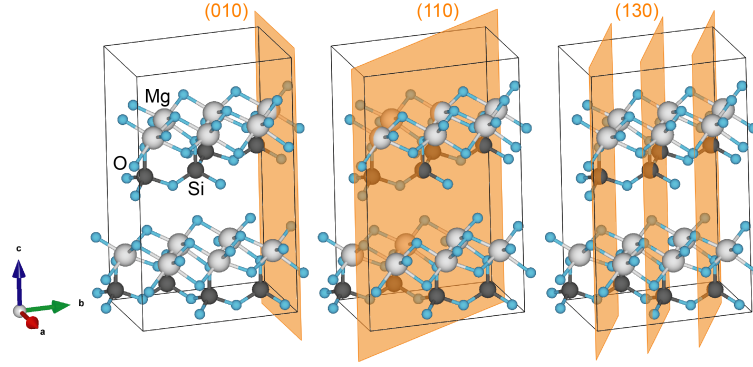


FIG. 1. Example of several lattice planes intersecting $\text{Mg}_3\text{Si}_2\text{O}_5(\text{OH})_4$ unit cell (hydrogen bonds between the layers are not shown). Structural data was adopted from [27] and visualized by VESTA software [50]

Only Mg–O and Si–O bonds were taken into account having bond energies $E_{\text{Mg-O}} = 401 \pm 13$ kJ/mol [49] and $E_{\text{Si-O}} = 444 \pm 18$ kJ/mol [48], respectively. Some of the $(hk0)$ planes may intersect hydrogen bonds, however, their estimated energy (5.2 kJ/mol [42]) was almost two orders of magnitude less than those of Mg–O and Si–O bonds. In this regard, hydrogen bonds were omitted during the calculation. Edge surfaces were assumed to be oxide surfaces, without OH-groups or water molecules adsorbed on them.

An angle between the (100) plane and $(hk0)$ planes was calculated by using the following equations:

$$\varphi_{100 \wedge hk0} = \begin{cases} \frac{180}{\pi} \arccos \left(\frac{b}{\sqrt{(hb)^2 + (ka)^2}} \right), & h = \pm 1, k \geq 1; \\ 90 - \frac{180}{\pi} \arccos \left(\frac{b}{\sqrt{(hb)^2 + (ka)^2}} \right), & h > 1, k = \pm 1. \end{cases} \quad (10)$$

To model a rectangular plate, several $\sigma_{hk0}/\sigma_{h'k'0}$ pairs were chosen in accordance with a condition:

$$\varphi_{100 \wedge hk0} + \varphi_{100 \wedge h'k'0} = 90 \pm 3^\circ, \quad (11)$$

where either h' or k' should be negative. Then σ_{hk0} substituted σ_1 , and $\sigma_{h'k'0}$ substituted σ_2 in the eq. (5).

3. Results and discussion

The choice of different $\sigma_{hk0}/\sigma_{h'k'0}$ pairs as specific surface energies of the edges (σ_1 and σ_2 , see eq. (5)) means that the rotation of the model rectangular plate undergoes in the ab plane relative to the crystal structure. Consequently, direction of scrolling of the model plate would also change with the respect to the a and b axes. The results presented below were obtained within two important assumptions. The first one is that the r_0 value (eq. (3)) does not change with change in direction of scrolling, in other words, that the size difference between octahedral and tetrahedral sheets along any direction is the same. This assumption leads us to conclude that the hydrosilicate plate could be strained along any direction within the ab plane. The second assumption is that the scrolling process occurs in only one direction, whereas strains along other directions either remain uncompensated or find another relaxation routes. One of these routes could be tetrahedron rotation yielding a tetrahedral sheet size change [37]. An alternative way for the crystal structure relaxation, strained in multiple directions, would be curving with formation of spherical particles. However, this case is rarely observed in practice: up to date, only allophane [51–53] demonstrates spherical morphology among hydrosilicates with the ability of curving. This feature could be related with the fact that allophane has the smallest r_0 value (~ 1 nm) in comparison with other hydrosilicates [1].

Figure 2 shows the results of σ_{hk0} calculations. Both positive and negative $hk0$ branches possessed several minima, which were relatively deep for the positive branch. The $hk0$ values in the energy minima were 510, 110, 130, 1100 for the positive branch, and $4\bar{1}0$, $\bar{1}20$, $\bar{1}100$ for the negative branch. Both branches demonstrated similar trends at $\varphi_{100} \wedge_{hk0}$ being close to 0° or 90° , whereas the trends were approximately opposite beyond that region. It is interesting to note, that σ_{100} and σ_{010} were among the highest values calculated. In the view of the necessity to choose $\sigma_{hk0}/\sigma_{h'k'0}$ pairs in accordance with the eq. (11), this feature would make the particle with the edges formed by (100) and (010) planes comparatively less energetically preferable.

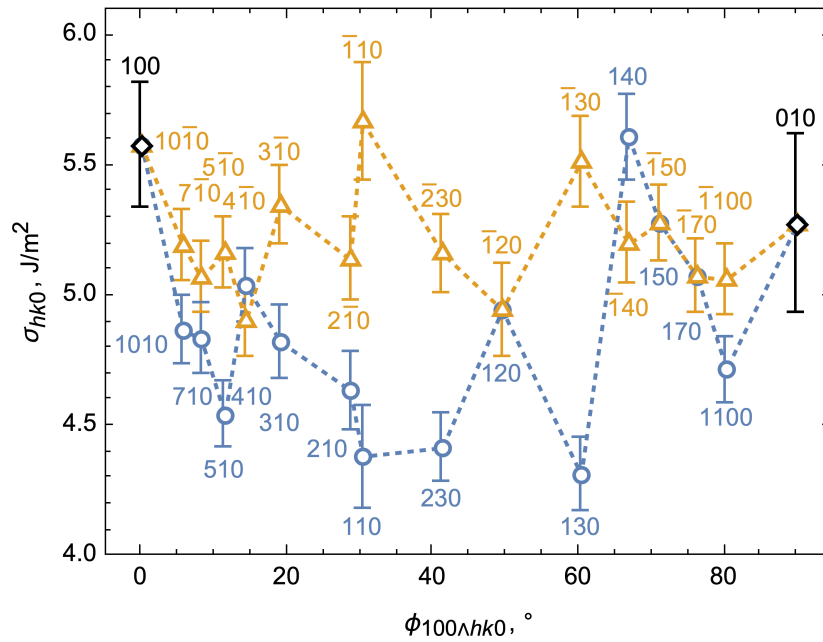


FIG. 2. Specific surface energies of $(hk0)$ planes vs. angle between the (100) and the $(hk0)$ plane. The positive branch (both h and k are positive) is marked by blue circles, the negative branch (either h or k are negative) is marked by orange triangles. Dashed lines join points for guidance.

Figure 3(a) shows positions of energy minima of scrolled layers with the edges, formed by different pairs of $hk0$ planes (110/ $\bar{1}30$ pair as an example), perpendicular to each other (see eq. (11)). The angle $\varphi_{100} \wedge_{hk0}$ is pointed for the plane with both h and k being positive (positive branch on Fig. 2). The relatively high value of energy effect was partially caused by the adhesion energy component (eq. (1)). The case of a multiwalled-nanoscroll is compared with that of a multilayered plate, for which the energy gap between them would be lower [42]. Depending on the $\sigma_{hk0}/\sigma_{h'k'0}$ pair, the energy effect could differ on approximately 400 J/mol, whereas the preferable spiral length L_1 almost did not change. Fig. 3(b) confirms miserable change of other energy preferable size parameters. The biggest change (200 nm) was revealed for cylinder length L_2 . The results of calculation allow to assume that the hydrosilicate layers with different edge surfaces – within current approximation, scrolled in different directions – could be morphologically indistinguishable, especially in the view of inner and outer diameters. On the other hand, variability of scrolling directions could broaden the nanoscroll length distribution. There is still a chance to determine scrolling direction by using the electron diffraction technique [30, 54].

Figure 4 shows energy effect of scrolling (eq. (1)) of rectangular plates with edges formed by different $(hk0)$ planes perpendicular to each other. The calculation revealed several energy minima with the deepest belonging to scrolling of 230/ $\bar{1}20$ plate. The general trend is almost symmetrical from both sides of this minimum. The 100/010 and 010/100 pairs, which are considered to be the most probable for scrolling of hydrosilicates like chrysotile and halloysite [28], were energetically unfavorable in the view of specific surface energy. At the same time, the 100/010 pair is slightly preferable than the 010/100 pair. The nearest to 100/010 pair energy minimum was formed by (510) and complementary ($\bar{1}70$) planes and was situated at $\varphi_{100} \wedge_{hk0} \cong 10^\circ$.

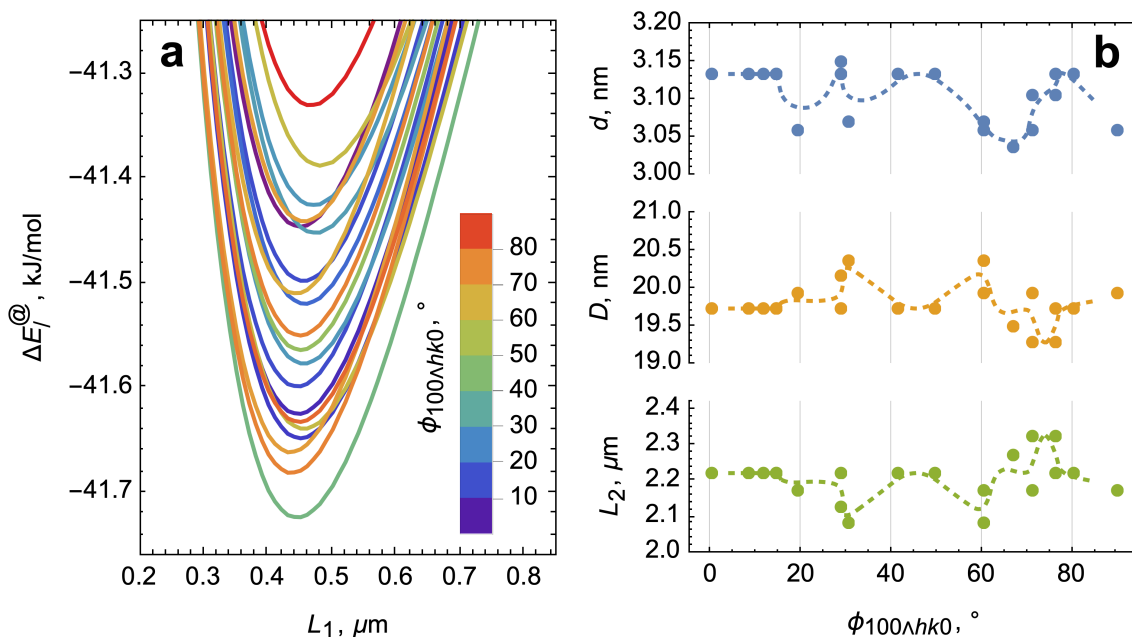


FIG. 3. (a) Change of energy minimum position for different $\sigma_{hk0}/\sigma_{h'k'0}$ pairs. Color denotes the angle between the (100) plane and the plane with positive h and k . Complementary angle is determined by the eq. (11). (b) Energy preferable size parameters (inner diameter d , outer diameter D , and cylinder length L_2) of multiwalled nanoscrolls having different edge surfaces. Dashed lines join moving average values for guidance

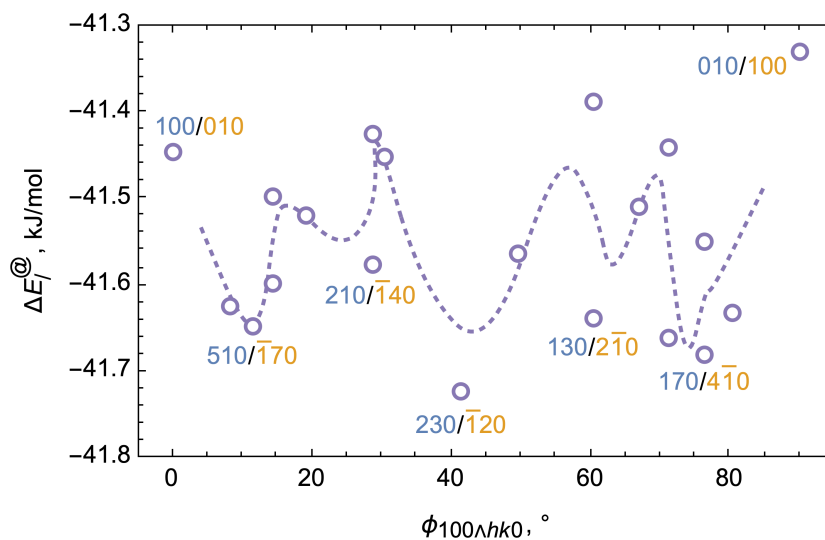


FIG. 4. Energy effect of scrolling for model rectangular plates with different edge surfaces. Local energy minima and 100/010 pairs are marked. Scrolling occurs along direction signed by orange text, whereas the spiral edge obtained is signed by blue text. Dashed line joins moving average values for guidance

4. Concluding remarks

Specific surface energies of a family of ($hk0$) planes in $\text{Mg}_3\text{Si}_2\text{O}_5(\text{OH})_4$ chrysotile were estimated using a phenomenological approach and information on Mg–O and Si–O bond energies. It was shown that the specific surface energies of the main crystallographic planes (100) and (010) were among the highest among other values. The smallest values of σ_{hk0} were obtained for the (110), (230), and (130) planes.

The obtained data was used in calculation of energy effect of scrolling for a rectangular hydrosilicate model plate with the edge surfaces formed by ($hk0$) plane and complementary ($\bar{h}k0$) or ($h\bar{k}0$) plane. The calculations, carried out by the developed energy model, revealed several pairs of planes, at which energy effect of scrolling was maximal. All these pairs differed from 100/010 pair, although [010] direction is generally accepted as the main direction of hydrosilicate layer scrolling. The biggest energy effect of scrolling was revealed for 230/ $\bar{1}20$ pair of planes, and the nearest to 100/010 pair local energy minimum was revealed for 510/ $\bar{1}70$ pair.

Preferable size parameters of nanoscroll models with different edge surfaces almost did not change being a possible obstacle for experimental distinguishing of nanoscrolls, which are cylindrically shaped but scrolled along different crystallographic directions, by electron microscopy. Energy modeling was carried out assuming direction of scrolling was always parallel to crystallographic direction of complementary plane. If this assumption is not correct because, for example, scrolling occurs along the crystallographic direction with maximal strains, then the formed scroll might still deviate from its cylindrical form. This deviation can be described as complication of the nanoscroll ends shape and formation of downward spiral on the side surface of the nanoscroll.

In the view of powder X-ray diffraction experiment, the direction of scrolling could be related with the crystallite size along certain direction. Crystallite size is expected to be the highest along that direction or in proximity to it.

Acknowledgements

The research was supported by the President of the Russian Federation grant MK-1962.2021.1.3. The author thanks Dr. A. V. Ankudinov, Dr. A. A. Levin, and Prof. V. V. Gusarov for fruitful discussions.

References

- [1] Krasilin A.A., Khrapova E.K., Maslennikova T.P. Cation doping approach for nanotubular hydrosilicates curvature control and related applications. *Crystals*, 2020, **10** (8), 654.
- [2] Shafia E., Esposito S., et al. Al/Fe isomorphic substitution versus Fe₂O₃ clusters formation in Fe-doped aluminosilicate nanotubes (imogolite). *J. Nanopart. Res.*, 2015, **17** (8), 336.
- [3] Zsirka B., Táborosi A., et al. Surface characterization of mechanochemically modified exfoliated halloysite nanoscrolls. *Langmuir*, 2017, **33** (14), P. 3534–3547.
- [4] Lesci I.G., Balducci G., et al. Surface features and thermal stability of mesoporous Fe doped geoinspired synthetic chrysotile nanotubes. *Micropor. Mesopor. Mat.*, 2014, **197**, P. 8–16.
- [5] Krasilin A.A., Danilovich D.P., et al. Crystal violet adsorption by oppositely twisted heat-treated halloysite and pecoraite nanoscrolls. *Appl. Clay Sci.*, 2019, **173**, P. 1–11.
- [6] Guimarães L., Enyashin A.N., et al. Imogolite nanotubes: stability, electronic, and mechanical properties. *ACS Nano*, 2007, **1** (4), P. 362–368.
- [7] Guimarães L., Enyashin A.N., Seifert G., Duarte H.A. Structural, electronic, and mechanical properties of single-walled halloysite nanotube models. *J. Phys. Chem. C*, 2010, **114** (26), P. 11358–11363.
- [8] Lecouvet B., Horion J., et al. Elastic modulus of halloysite nanotubes. *Nanotechnology*, 2013, **24** (10), 105704.
- [9] Kumzerov Y.A., Parfen'eva L.S., et al. Thermal and acoustic properties of chrysotile asbestos. *Phys. Solid State*, 2005, **47** (2), P. 370–373.
- [10] Piperno S., Kaplan-Ashiri I., et al. Characterization of geoinspired and synthetic chrysotile nanotubes by atomic force microscopy and transmission electron microscopy. *Adv. Funct. Mater.*, 2007, **17** (16), P. 3332–3338.
- [11] Khalisov M.M., Lebedev V.A., et al. Young's modulus of phyllosilicate nanoscrolls measured by the AFM and by the in-situ TEM indentation. *Nanosystems: Phys. Chem. Math.*, 2021, **12** (1), P. 118–127.
- [12] Lisuzzo L., Cavallaro G., et al. Colloidal stability of halloysite clay nanotubes. *Ceram. Int.*, 2019, **45** (2), P. 2858–2865.
- [13] Bonelli B., Bottero I., et al. IR spectroscopic and catalytic characterization of the acidity of imogolite-based systems. *J. Catal.*, 2009, **264** (1), P. 15–30.
- [14] Mahajan A., Gupta P. Halloysite nanotubes based heterogeneous solid acid catalysts. *New J. Chem.*, 2020, **44** (30), P. 12897–12908.
- [15] Bian Z., Kawi S. Preparation, characterization and catalytic application of phyllosilicate: A review. *Catal. Today*, 2020, **339**, P. 3–23.
- [16] Khrapova E.K., Ugolkov V.L., et al. Thermal behavior of Mg–Ni-phyllosilicate nanoscrolls and performance of the resulting composites in hexene-1 and acetone hydrogenation. *ChemNanoMat*, 2021, **7** (3), P. 257–269.
- [17] Monet G., Paineau E., et al. Solid wetting-layers in inorganic nano-reactors: the water in imogolite nanotube case. *Nanoscale Adv.*, 2020, **2** (5), P. 1869–1877.
- [18] Pignié M.-C., Shcherbakov V., et al. Confined water radiolysis in aluminosilicate nanotubes: the importance of charge separation effects. *Nanoscale*, 2021, **13** (5), P. 3092–3105.
- [19] Lvov Y., Wang W., Zhang L., Fakhru'llin R. Halloysite clay nanotubes for loading and sustained release of functional compounds. *Adv. Mater.*, 2016, **28** (6), P. 1227–1250.
- [20] Cavallaro G., Milioto S., Lazzara G. Halloysite nanotubes: interfacial properties and applications in cultural heritage. *Langmuir*, 2020, **36** (14), P. 3677–3689.

- [21] Maslennikova T.P., Korytkova E.N. Aqueous solutions of cesium salts and cesium hydroxide in hydrosilicate nanotubes of the $\text{Mg}_3\text{Si}_2\text{O}_5(\text{OH})_4$ composition. *Glass Phys. Chem.*, 2010, **36** (3), P. 345–350.
- [22] Kononova S.V., Korytkova E.N., et al. Polymer-inorganic nanocomposites based on aromatic polyamidoimides effective in the processes of liquids separation. *Russ. J. Gen. Chem.*, 2010, **80** (6), P. 1136–1142.
- [23] Lvov Y., Abdullayev E. Functional polymer–clay nanotube composites with sustained release of chemical agents. *Prog. Polym. Sci.*, 2013, **38** (10–11), P. 1690–1719.
- [24] Khrapova E.K., Ezhov I.S., et al. Nanotubular nickel hydrosilicate and its thermal annealing products as anode materials for lithium ion batteries. *Inorg. Mater.*, 2020, **56** (12), P. 1248–1257.
- [25] Yada K. Study of microstructure of chrysotile asbestos by high-resolution electron microscopy. *Acta Crystallogr. A*, 1971, **27** (6), P. 659–664.
- [26] Wicks F.J., Whittaker E.J.W. A reappraisal of the structures of the serpentine minerals. *Can. Mineral.*, 1975, **13** (3), P. 227–243.
- [27] Falini G., Foresti E., et al. Tubular-shaped stoichiometric chrysotile nanocrystals. *Chem. Eur. J.*, 2004, **10** (12), P. 3043–3049.
- [28] Drits V.A., Sakharov B.A., Hillier S. Phase and structural features of tubular halloysite (7 Å). *Clay Miner.*, 2018, **53** (4), P. 691–720.
- [29] Niu J., Qiang Y., et al. Morphology and orientation of curling of kaolinite layer in hydrate. *Appl. Clay Sci.*, 2014, **101**, P. 215–222.
- [30] Khalitov Z., Khadiev A., Pashin D. Electron diffraction patterns from scroll nanotubes: interpretation peculiarities. *J. Appl. Crystallogr.*, 2015, **48** (1), P. 29–36.
- [31] Makó É., Dódney L., et al. Nanoscale structural and morphological features of kaolinite nanoscrolls. *Appl. Clay Sci.*, 2020, **198**, 105800.
- [32] Korytkova E.N., Maslov A.V., et al. Formation of $\text{Mg}_3\text{Si}_2\text{O}_5(\text{OH})_4$ nanotubes under hydrothermal conditions. *Glass Phys. Chem.*, 2004, **30** (1), P. 51–55.
- [33] Krasilin A.A., Suprun A.M., Nevedomsky V.N., Gusarov V.V. Formation of conical $(\text{Mg,Ni})_3\text{Si}_2\text{O}_5(\text{OH})_4$ nanoscrolls. *Dokl. Phys. Chem.*, 2015, **460** (2), P. 42–44.
- [34] Krasilin A.A., Gusarov V.V. Redistribution of Mg and Ni cations in crystal lattice of conical nanotube with chrysotile structure. *Nanosystems: Phys. Chem. Math.*, 2017, **8** (5), P. 620–627.
- [35] Bloise A., Barrese E., Apollaro C. Hydrothermal alteration of Ti-doped forsterite to chrysotile and characterization of the resulting chrysotile fibers. *Neues Jb. Miner. Abh.*, 2009, **185** (3), P. 297–304.
- [36] Bloise A., Belluso E., et al. Hydrothermal alteration of glass to chrysotile. *J. Am. Ceram. Soc.*, 2012, **95** (10), P. 3050–3055.
- [37] Singh B. Why does halloysite roll? – A new model. *Clay. Clay Miner.*, 1996, **44** (2), P. 191–196.
- [38] Perbost R., Amouric M., Olives J. Influence of cation size on the curvature of serpentine minerals: HRTEM-AEM study and elastic theory. *Clay. Clay Miner.*, 2003, **51** (4), P. 430–438.
- [39] Chivilikhin S.A., Popov I.Y., Gusarov V.V. Dynamics of nanotube twisting in a viscous fluid. *Dokl. Phys.*, 2007, **52** (1), P. 60–62.
- [40] Thill A., Guiose B., et al. How the diameter and structure of $(\text{OH})_3\text{Al}_2\text{O}_3\text{Si}_x\text{Ge}_{1-x}\text{OH}$ imogolite nanotubes are controlled by an adhesion versus curvature competition. *J. Phys. Chem. C*, 2012, **116** (51), P. 26841–26849.
- [41] Krasilin A.A., Nevedomsky V.N., Gusarov V.V. Comparative energy modeling of multiwalled $\text{Mg}_3\text{Si}_2\text{O}_5(\text{OH})_4$ and $\text{Ni}_3\text{Si}_2\text{O}_5(\text{OH})_4$ nanoscroll growth. *J. Phys. Chem. C*, 2017, **121** (22), P. 12495–12502.
- [42] Krasilin A.A. Energy modeling of competition between tubular and platy morphologies of chrysotile and halloysite layers. *Clay. Clay Miner.*, 2020, **68** (5), P. 436–445.
- [43] Landau L.D., Pitaevskii L.P., Kosevich A.M., Lifshitz E.M. *Theory of Elasticity, Third Edition: Volume 7 (Course of Theoretical Physics)*, Butterworth-Heinemann, Oxford, 1986, 195 p.
- [44] Lourenço M.P., de Oliveira C., et al. Structural, electronic, and mechanical properties of single-walled chrysotile nanotube models. *J. Phys. Chem. C*, 2012, **116** (17), P. 9405–9411.
- [45] Cressey B.A., Whittaker E.J.W. Five-fold symmetry in chrysotile asbestos revealed by transmission electron microscopy. *Mineral. Mag.*, 1993, **57** (389), P. 729–732.
- [46] Demichelis R., De La Pierre M., et al. Serpentine polymorphism: a quantitative insight from first-principles calculations. *CrystEngComm*, 2016, **18** (23), P. 4412–4419.
- [47] Churakov S.V., Iannuzzi M., Parrinello M. Ab initio study of dehydroxylation/carbonation reaction on brucite surface. *J. Phys. Chem. B*, 2004, **108** (31), P. 11567–11574.
- [48] Shchupalov Y.K. Surface energy of crystalline and vitreous silica. *Glass Ceram.*, 2000, **57** (11–12), P. 374–377.
- [49] Cotton D.H., Jenkins D.R. Bond-dissociation energy of gaseous magnesium oxide. *T. Faraday Soc.*, 1969, **65**, P. 376–379.
- [50] Momma K., Izumi F. VESTA 3 for three-dimensional visualization of crystal, volumetric and morphology data. *J. Appl. Crystallogr.*, 2011, **44** (6), P. 1272–1276.
- [51] Parfitt R.L. Allophane and imogolite: role in soil biogeochemical processes. *Clay Miner.*, 2009, **44** (1), P. 135–155.
- [52] Du P., Yuan P., et al. Insights into the formation mechanism of imogolite from a full-range observation of its sol-gel growth. *Appl. Clay Sci.*, 2017, **150**, P. 115–124.
- [53] Thill A., Picot P., Belloni L. A mechanism for the sphere/tube shape transition of nanoparticles with an imogolite local structure (imogolite and allophane). *Appl. Clay Sci.*, 2017, **141**, P. 308–315.
- [54] Khadiev A., Khalitov Z. Quantitative theory of diffraction by cylindrical scroll nanotubes. *Acta Crystallogr. A*, 2018, **74** (3), P. 233–244.

The “rolling up” effect of platinum layer obtained on nickel surface by interaction with solution of H_2PtCl_6 and its electrocatalytic properties in hydrogen evolution reaction during water electrolysis in alkaline medium

M. V. Kaneva, V. P. Tolstoy*

Institute of Chemistry, Saint Petersburg State University,
26 University Prosp, St. Peterhof, Saint Petersburg, 198504, Russia
skt94@bk.ru, *v.tolstoy@spbu.ru

PACS 82.33.Pt, 82.45.Mp, 82.45.Yz

DOI 10.17586/2220-8054-2021-12-5-630-633

We have shown for the first time that a platinum layer has been obtained on the surface of nickel foil as a result of Galvanic Replacement Reaction (GRR) when interacting with an aqueous solution of H_2PtCl_6 , during drying in air, partially rolling up into incompletely formed microscrolls with a unique 3D morphology. Analysis of the wall of these microscrolls by FESEM, TEM, HR-TEM, and SAED methods showed that they are porous and formed by platinum nanocrystals with sizes of 5 – 10 nm, and their packing density over the wall thickness differs. Nickel foil samples with the layer of platinum microscrolls deposited on their surface exhibit high electrocatalytic activity in hydrogen evolution reaction (HER) during water electrolysis in the alkaline medium. In particular, the overpotential value is 32 mV and the Tafel slope is 32.5 mV/dec for an electrode with the platinum layer with a thickness of 120 – 140 nm.

Keywords: Platinum, nanocrystals, microscrolls, galvanic replacement reaction, hydrogen evolution reaction, nickel electrode.

Received: 14 July 2021

Revised: 7 September 2021

1. Introduction

As is known, the processes of “rolling up” planar structures into more complex geometric shapes are the basis of various methodological techniques for obtaining new nanoscale materials. For example, novel metamaterials were obtained using this approach [1] and new types of 3D devices with small form factors [2–4]. There are also known works devoted to the synthesis and research of nanoscrolls of hydrosilicates of metals [5–8], as well as microtube of a number of oxides [9, 10], fluorides [11] and sulfides of metals [12]. As shown by the authors of these works, the reason for this rolling up is mechanical forces that arise inside planar structures due to density or composition gradients.

The aim of this work was to synthesize platinum nanocrystals under the conditions of galvanic replacement reaction (GRR) on the surface of a polycrystalline nickel foil with the participation of an H_2PtCl_6 solution and to determine the conditions for carrying out this reaction under which the planar geometry of the resulting nanocrystal layer is distorted and 3D microstructures are formed on the surface. The study of such a reaction is of undoubted practical interest, since platinum nanocrystals are, for example, active electrocatalysts of various electrochemical processes. One would expect such 3D microstructures to have unique electrocatalytic properties, for example, in HER during water electrolysis. Previously, GRR with the participation of these reagents was studied, in particular, in articles [13, 14] on the examples of nickel nanoparticles and nickel foam.

2. Experimental

Dihydrogen hexachloroplatinate (IV) hydrate ($\text{H}_2\text{PtCl}_6 \cdot 6\text{H}_2\text{O}$, JSC “Aurat”) and Ni foil with a size of $0.5 \times 7.0 \times 20.0$ mm were used as precursor and a substrate, respectively, to synthesize the platinum layer by GRR. Ni plates were degreased with acetone by ultrasonic treatment for 30 min and treated according to [15] in hydrochloric acid (HCl, 3 M). Then the substrates were washed in deionized water. Thereafter, Ni plates were immersed into a solution of H_2PtCl_6 ($C = 0.005$ M) for 20 min. The GRR was carried out at room temperature and atmospheric pressure. As a result, the platinum nanolayer is formed on the surface and during drying in air rolls up into microscrolls.

FESEM and TEM methods were used to characterize the samples. FESEM micrographs were obtained using a Zeiss Merlin electron microscope. TEM and HR-TEM micrographs were obtained using a Zeiss Libra 200 microscope. Electrochemical experiments were conducted at room temperature using a standard three-electrode cell connected to an ElinsP-45X-FRA-24M potentiostat. Carbon rod and an Ag/AgCl (aq. KCl sat.) electrode were used as the counter electrode and the reference electrode, respectively. The sample of Ni foil with the platinum layer obtained by GRR was used as the working electrode. The electrolyte was Ar-saturated 1 M KOH solution ($\text{pH} \approx 14.0$). The polarization curves were recorded at a scan rate of 5 mV/s. The electrochemical measurements were performed

with iR compensation. The overpotential from the Ag/AgCl electrode scale was converted to a reversible hydrogen electrode (RHE) scale according to the Nernst equation. The equation $|\eta| = b \log(|j|) + a$, was used to calculate the Tafel slope (b – Tafel slope, η – overpotential, j – current density and a – intercept).

3. Results and discussions

As a result of GRR, when nickel interacts with a 0.005 M H_2PtCl_6 solution, a light gray platinum layer is formed on its surface. FESEM studies of this layer have shown it is formed by nanocrystals. A sample of chemically polished nickel obtained with a treatment time of 20 minutes or more has a morphology different from planar due to partial “rolling up” with the formation of incompletely formed microscrolls (Fig. 1). The wall thickness of such a microscroll is 120 – 140 nm (Fig. 1b) and its cross-section shows that it consists of nanoparticles with a size of 5 – 10 nm and is porous. Moreover, the packing density of such nanoparticles changes over the layer thickness and the pores are partially oriented across the wall. In the micrographs 1c and 1d, showing a top view of the substrate surface, it can be seen that these nanoparticles also form microglobules with a size of 20 – 80 nm and their shape on the outer and inner surface of the layer with respect to the substrate is different. So, on the outer surface, these globules have a certain asymmetry, and some of them contain acute-angled vertices oriented perpendicular to the plane of the layer. The study of fragments of this layer by the TEM and HR-TEM methods also showed that the sizes of nanoparticles are 5 – 10 nm (Fig. 2a,b) and, as follows from the micrographs shown in Fig. 2b and Fig. 2c, these nanoparticles are platinum nanocrystals.

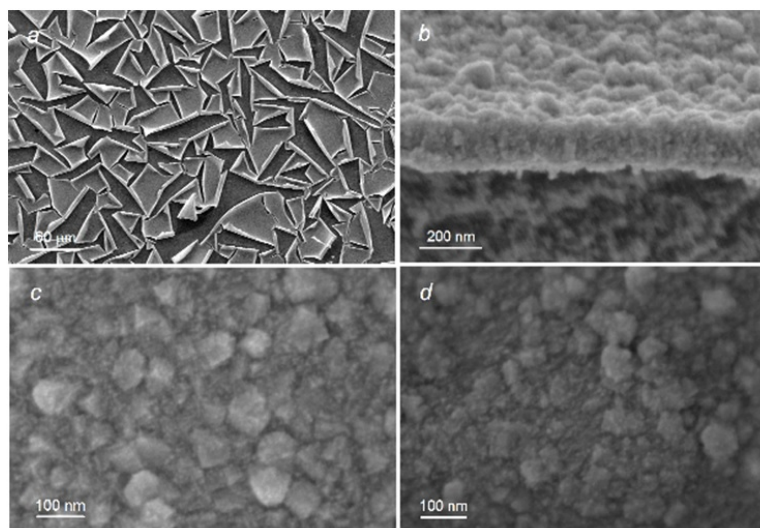


FIG. 1. FESEM images of the platinum layer on the nickel surface obtained by treating it for 20 minutes with a 0.005 M H_2PtCl_6 solution. (a) – general top view, (b) – side view of the platinum layer, (c) – top view of the layer area inside the scroll, (d) – top view of the layer area outside the scroll

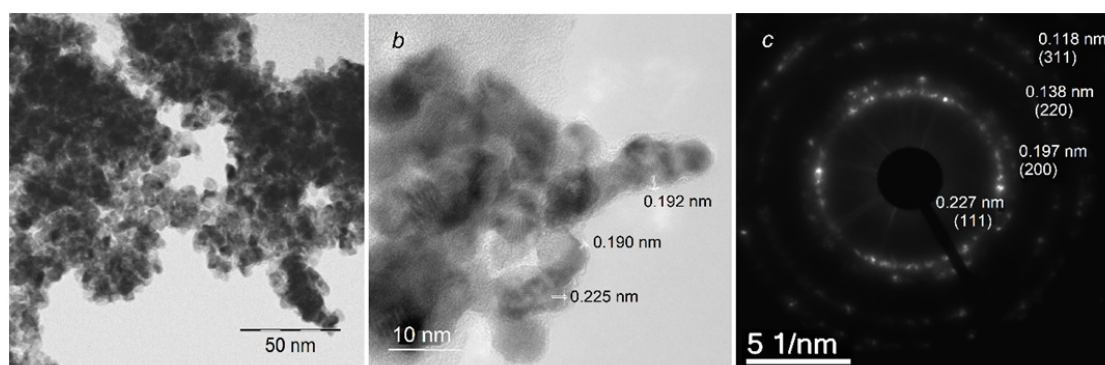


FIG. 2. (a) – TEM image of platinum nanocrystals, (b) – HR-TEM image of platinum nanoparticles, (c) – SAED pattern of platinum nanoparticles

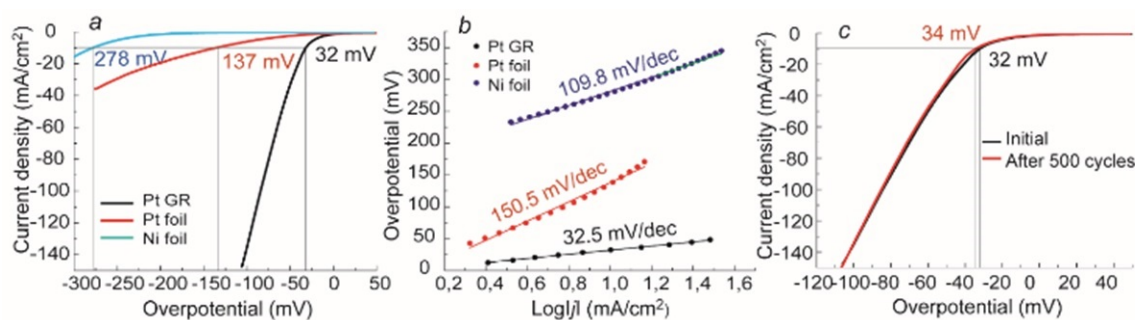


FIG. 3. HER polarization curves (a) and Tafel plots (b) of the platinum layer on the nickel surface obtained by treating it for 20 minutes, Pt foil and Ni foil in 1 M KOH solution. (c) – HER polarization curves of the platinum layer on the nickel surface before and after 500 potential cycling

TABLE 1. Comparison of overpotential and Tafel slope values for platinum-based electrocatalysts in HER during water electrolysis in 1 M KOH solution

Electrocatalyst	Synthesis method	Substrate	Overpotential (mV at 10 mA/cm ²)	Tafel slope (mV/dec)	Reference
Pt	GRR	Ni foil	32	32.5	This work
Pt/NiO@Ni/NF	Electrodeposition, electrochemical reduction	Ni foam	34	40	[16]
Pt _{SA} -Ni ₃ S ₂	Electrochemical process	Ni foam	≈50	43.29	[17]
Pt _{SA} -Ni ₃ S ₂ @Ag NWs		flexible cloth	33	34.7	
Pt/NiRu-OH	Hydrothermal method, electrochemical atom trapping method	Ni foam	38	39.0	[18]
Pt-Fe-Na	Corrosion engineering approach	Ni foam	31	35.98	[19]
Pt NSs/CNTs	Electrochemical reduction	GC electrode	36	44.0	[20]
PtSA/NC-DG	Pyrolysis, electroless deposition	GC electrode	41	40.0	[21]

Explaining the observed effects, it should be noted, first of all, that upon contact of the nickel surface with the H₂PtCl₆ solution, GRR occurs at the interface with the formation of platinum nanocrystals and Ni²⁺ cations. Over time, the number of such nanocrystals increases, and they eventually form the porous layer on the nickel surface, which also consists of agglomerates of such nanocrystals. Through the pores of this layer PtCl₆⁻ anions enter the interface and nickel cations are removed. In this case, the degree of porosity near the interface and on the outer side with respect to the substrate are different. This fact and the noted asymmetry of the microglobules' shapes lead to the appearance of mechanical forces that contribute to cracking and partial twisting of this layer during its drying.

The study of the electrocatalytic properties of such a layer showed (Fig. 3) that the values of the overpotential and the Tafel slope are 32 mV and 32.5 mV/dec, respectively, in HER. Comparison of these values with the results of other authors shown in Table 1 indicates that the noted values are currently among the best. In our opinion, the observed effect of reducing the overpotential values is due to the unique morphology of the electrode surface. In particular, the surface has many points at the tops of the microscrolls present, on which HER occurs, as well as the presence of an internal space in the microscrolls, in which bubbles are formed at a lower concentration of dissolved hydrogen.

It is important that the overpotential value increases by only 2 mV upon repeated 500-fold potential cycling (Fig. 3c) and this indicates a high stability of the electrocatalyst properties over a relatively long time. This result shows that these incompletely formed platinum microscrolls are relatively tightly bound to the nickel surface and are

not removed from it when immersed in an aqueous solution of KOH and during the operation of the electrolyzer electrode.

4. Conclusion

Under the proposed GRR conditions between nickel and an aqueous solution of H_2PtCl_6 , the porous platinum layer forms on its surface, which cracks during drying and partially rolls up into incompletely formed microscrolls with a unique 3D morphology. Electrodes created on their basis exhibit high electrocatalytic activity in HER during electrolysis of an aqueous alkaline medium. In particular, the overpotential value is 32 mV and the Tafel slope is 32.5 mV/dec for an electrode with the platinum layer with a thickness of 120 – 140 nm.

Acknowledgement

This work was supported by the RSF grant (project #18-19-00370-P). We are grateful to the “Nanotechnology” Research Parks of Saint-Petersburg State University, for their technical assistance with the synthesized samples investigation.

References

- [1] Prinz V.Y., Naumova E.V., Golod S.V., Seleznev V.A., Bocharov A.A., Kubarev V.V. Terahertz metamaterials and systems based on rolled-up 3D elements: designs, technological approaches, and properties. *Scientific reports*, 2017, **7**, P. 43334.
- [2] Xu C., Wu X., Huang G., Mei Y. Rolled-up Nanotechnology: Materials Issue and Geometry Capability. *Advanced materials technologies*, 2019, **4**, P. 1800486.
- [3] Zhang Z., Tian Z., Mei Y., Di Z. Shaping and structuring 2D materials via kirigami and origami. *Materials Science and Engineering: R: Reports*, 2021, **145**, P. 100621.
- [4] Bolaños Quiñones V.A., Zhu H., Solovev A.A., Mei Y., Gracias D.H. Origami Biosystems: 3D Assembly Methods for Biomedical Applications. *Advanced Biosystems*, 2018, P. 1800230.
- [5] Krasilin A.A., Khrapova E.K., Nomine A., Ghanbaja J., Belmonte T., Gusarov V.V. Cations redistribution along the spiral of Ni-doped phyllosilicate nanoscrolls: energy modelling and STEM/EDS study. *ChemPhysChem*, 2019, **20**(5), P. 719–726.
- [6] Krasilin A.A., Gusarov V.V. Redistribution of Mg and Ni cations in crystal lattice of conical nanotube with chrysotile structure. *Nanosystems: Physics, Chemistry, Mathematics*, 2017, **8**(5), P. 620–627.
- [7] Khalisov M.M., Lebedev V.A., Poluboyarinov A.S., Garshev A.V., Khrapova E.K., Krasilin A.A., Ankudinov A.V. Young’s modulus of phyllosilicate nanoscrolls measured by the AFM and by the in-situ TEM indentation. *Nanosystems: physics, chemistry, mathematics*, 2021, **12**(1), P. 118–127.
- [8] Krasilin A.A., Nevedomsky V.N., Gusarov V.V. Comparative Energy Modeling of Multi-Walled $\text{Mg}_3\text{Si}_2\text{O}_5(\text{OH})_4$ and $\text{Ni}_3\text{Si}_2\text{O}_5(\text{OH})_4$ Nanoscrolls Growth. *The Journal of Physical Chemistry C*, 2017, **121**(22), P. 12495–12502.
- [9] Gurenko V.E., Tolstoy V.P., Gulina L.B. The effect of microtube formation with walls, containing Fe_3O_4 nanoparticles, via gassolution interface technique by hydrolysis of the FeCl_2 and FeCl_3 mixed solution with gaseous ammonia. *Nanosystems: physics, chemistry, mathematics*, 2017, **8**(4), P. 471–475.
- [10] Gulina L.B., Gurenko V.E., Tolstoy V.P., Mikhailovskii V.Y., Koroleva A.V. Interface-Assisted Synthesis of the $\text{Mn}_{3-x}\text{Fe}_x\text{O}_4$ Gradient Film with Multifunctional Properties. *Langmuir*, 2019, **35**, P. 14983–14989.
- [11] Gulina L.B., Tolstoy V.P., Kasatkin I.A., Petrov Y.V. Facile synthesis of LaF_3 strained 2D nanoparticles and microtubes at solution-gas interface. *Journal of Fluorine Chemistry*, 2015, **180**, P. 117–121.
- [12] Gulina L.B., Tolstoy V.P., Solovev A.A., Gurenko V.E., Huang G., Mei Y. Gas-Solution Interface Technique as a simple method to produce inorganic microtubes with scroll morphology. *Progress in Natural Science: Materials International*, 2020, **30**(3), P. 279–288.
- [13] Caballero-Manrique G., Garcia-Cardona J., Brillas E., Jaén J.A., Sánchez J.M., Cabot P.L. Synthesis and Evaluation of PtNi Electrocatalysts for CO and Methanol Oxidation in Low Temperature Fuel Cells. *Catalysts*, 2020, **10**(5), P. 563.
- [14] Lyu X., Jia Y., Mao X., Li D., Li G., Zhuang L., Wang X., Yang D., Wang Q., Du A., Yao X. Gradient-Concentration Design of Stable Core-Shell Nanostructure for Acidic Oxygen Reduction Electrocatalysis. *Advanced Materials*, 2020, **32**, P. 2003493.
- [15] Tolstoy V.P., Lobinsky A.A., Kaneva M.V. Features of inorganic nanocrystals formation in conditions of successive ionic layers deposition in water solutions and the Co(II)Co(III) 2D layered double hydroxide synthesis. *Journal of Molecular Liquids*, 2019, **282**, P. 32–38.
- [16] Chen Z.-J., Cao G.-X., Gan L., Dai H., Xu N., Zang M.-J., Wang P. Highly dispersed platinum on honeycomb-like NiO@Ni film as a synergistic electrocatalyst for hydrogen evolution reaction. *ACS Catalysis*, 2018, **8**(9), P. 8866–8872.
- [17] Zhou K. L., Han C. B., Wang Z., Ke X., Wang C., Jin Y., Yan H. Atomically Dispersed Platinum Modulated by Sulfide as an Efficient Electrocatalyst for Hydrogen Evolution Reaction. *Advanced Science*, 2021, **8**(12), P. 2100347.
- [18] Li D., Chen X., Lv Y., Hang G., Huang Y., Liu W., Ni H. An effective hybrid electrocatalyst for the alkaline HER: Highly dispersed Pt sites immobilized by a functionalized NiRu-hydroxide. *Applied Catalysis B: Environmental*, 2020, **269**, P. 118824.
- [19] Zhao Y., Gao Y., Chen Z., Li Z., Ma T., Wu Z., Wang L. Triflex Pt coupled with NiFe hydroxide synthesized via corrosion engineering to boost the cleavage of water molecule for alkaline water-splitting. *Applied Catalysis B: Environmental*, 2021, **297**, P. 120395.
- [20] Bao X., Gong Y., Zheng X., Chen J., Mao S., Wang Y. Highly performed platinum nanosheets synthesized under in situ reaction conditions for hydrogen generation. *Journal of Energy Chemistry*, 2020, **51**, P. 272–279.
- [21] Yihui Z., Pengfei T., Hongliang J., Jingren M., Lu M., Xiaozhi S., Yu W., Yunxiang L., Yihua Z., Li S., Chunzhong L. Synergistic Effect of Platinum Single Atoms and Nanoclusters Boosting Electrocatalytic Hydrogen Evolution. *CCS Chemistry*, 2020, **3**(10), P. 2539–2547.

Two-step combustion synthesis of nanocrystalline $\text{Zn}_{1-x}\text{Mn}_x\text{Fe}_2\text{O}_4$ ($0 \leq x \leq 1$) spinel ferrites with linear tuning of magnetic parameters

K. D. Martinson, V. I. Popkov

Ioffe Institute, St. Petersburg, 194021, Russia

martinsonkirill@mail.ru

PACS 61.46.+w, 75.50.Bb, 75.60.-d

DOI 10.17586/2220-8054-2021-12-5-634-640

Multicomponent zinc ferrites are of great applied value due to their functional features, due to which they are widely used in the production of microwave devices. In this regard, the development of new methods for obtaining initial pre-ceramic nanopowders in a nanostructured form is especially urgent. In this work, multicomponent zinc-manganese ferrites of the $\text{Zn}_{1-x}\text{Mn}_x\text{Fe}_2\text{O}_4$ ($x = 0, 0.2, \dots, 1.0$) composition were obtained by thermal treatment of X-ray amorphous products of solution combustion synthesis at a temperature of 750 °C and a holding time of 6 hours. The synthesized powders were analyzed by PXRD, FT-IR, and SEM methods. The magnetic characteristics were determined by vibration magnetometry. It was shown that the obtained samples contain one-phase spinel ferrite without any noticeable impurities. Depending on the number of Mn^{2+} cations in the crystal lattice, the unit cell parameters varied from 8.485(2) to 8.451(2) Å. The average crystallite size of the powders varied from 29.4 nm in the case of zinc ferrite to 36.8 nm in the case of MnFe_2O_4 . Residual magnetization (M_s), saturation magnetization (M_T), and coercive force (H_c) also depend on the content of manganese cations in spinel and varied from 4.9 to 12.3 emu/g, from 22.4 to 76.4 emu/g, and from 47.5 to 81.3 Oe, respectively and these dependencies are almost linear. The highest magnetic parameters were found in simple manganese ferrite, which has the largest crystallite size.

Keywords: zinc-manganese ferrite, solution combustion, nanocrystals, structure transformation, magnetic properties.

Received: 25 August 2021

Revised: 14 September 2021

1. Introduction

Ferrites are well-known spinel compounds with the general formula MFe_2O_4 ($\text{M} = \text{Co}, \text{Ni}, \text{Zn}, \text{Mn}, \text{et al.}$). The peculiarities of their functional behavior are associated with their structural features, namely the cubic system, which contains 32 oxygen anions occupying 8 regions (4 anions in each), 8 M^{2+} cations (one cation each in 8 regions), and 16 Fe^{3+} cations (two cations each in 8 regions) [1]. The unique magnetic properties of ferrites arise primarily due to a divalent transition metal cation introduced into the crystal structure, which occupies the tetrahedral position (A) in the case of normal spinel and the octahedral position (B) in the case of inverted spinel [2]. Inverted spinels are a more complex structural unit in this case, since the M^{2+} cation can replace both the A and B positions. Such spinels are called mixed and their magnetic behavior can change significantly depending on composition and structural features [3].

Multicomponent zinc ferrites correspond to the structure of normal spinel in which the Zn^{2+} cation occupies a tetrahedral position, while the Fe^{3+} cations are located in the octahedral regions. The magnetic behavior of zinc ferrite is based on its antiferrimagnetic nature, which is characterized by a weak super exchange interaction due to an angle of 90° in the $\text{Fe}^{3+}\text{-O-Fe}^{3+}$ bond [4]. In the case of multicomponent zinc ferrites, cations of transition metals, including Mn^{2+} , Co^{2+} , Ni^{2+} , etc., most often act as an alloying addition [5, 6]. In particular, zinc-manganese ferrites should be highlighted, which have found wide application in the field of microwave technology [7], in the production of magnetic fluids [8], as contrast agents for magnetic resonance imaging [9], for drug delivery [10], etc. In addition, several works have shown the possibility of using nanostructured spinel ferrites as catalysts and photocatalysts [11], for wastewater treatment [12], as antibacterial materials [13]. For the application of this class of compounds in these areas, structural parameters are especially important, among which the size of particles and their size distribution should be singled out separately [14]. In recent years, a large number of methods have been used to obtain ferrite nanopowders of various compositions, including hydrothermal synthesis [15], co-precipitation method [16], solution combustion method [17], sol-gel synthesis [18], and many other methods. Each of these types of synthesis has its advantages and disadvantages, but from the point of view of possible industrial scale-up, various methods of solution combustion are of particular interest [19, 20]. They are most often based on the preparation of a homogeneous solution, which contains cations of the corresponding metals and organic fuel acting as a chelating agent and initiator of the combustion process [21]. Since the combustion process is completed within a few seconds, and the initial reagents are dissolved in the solution, its use makes it possible to obtain nanoparticles with controlled functional characteristics in a wide range of particle

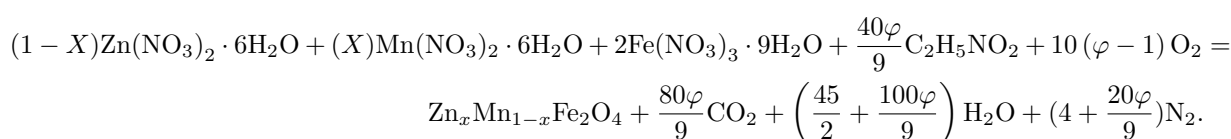
sizes [22–24]. Nevertheless, this technique has some disadvantages, among which is the difficulty of obtaining some complex oxide systems without impurities [25] and the difficulty in obtaining particles less than 30 nm in size.

In this regard, the search for modified multistage methods of solution combustion with a wider set of controlled synthesis parameters, due to which it is possible to obtain pure multicomponent phases with small particle size, becomes especially urgent. One of these methods is the method of thermal treatment of X-ray amorphous products of solution combustion, within which the initial powder is synthesized with a significant excess or shortage of fuel and is thermally treated in an air atmosphere at temperatures from 500 to 800 °C. This original technique was first applied by the authors of this work for the synthesis of holmium and europium orthoferrites [26, 27]. Nevertheless, the question of whether it can be used to obtain multicomponent spinel ferrites remains unanswered.

In this article, the method of thermal treatment of X-ray amorphous products of solution combustion was applied to obtain single-phase nanostructured powders of the composition $Zn_{1-x}Mn_xFe_2O_4$ ($x = 0, 0.2, \dots, 1.0$) with a particle size of up to 29 nm. The starting powders were synthesized under the conditions of glycine-nitrate combustion with a significant lack of organic fuel. The samples obtained were thermally treated under aerobic conditions at 750 °C for 6 hours and studied using a complex of physicochemical methods of analysis.

2. Experimental

The synthesis of nanopowders of zinc-manganese ferrites of the $Zn_{1-x}Mn_xFe_2O_4$ ($x = 0, 0.2, \dots, 1.0$) composition was carried out in two stages. At the first stage, the initial powder was obtained by the method of solution combustion with the addition of a small amount of glycine (redox ratio = 0.2). The following compounds were chosen as the starting reagents for the synthesis: $Zn(NO_3)_2 \cdot 6H_2O$ (puriss., NevaReactiv), $Mn(NO_3)_2 \cdot 6H_2O$ (puriss., NevaReactiv), $Fe(NO_3)_3 \cdot 9H_2O$ (puriss., NevaReactiv), CH_2NH_2COOH (puriss., NevaReactiv) and distilled water. The reagents were dissolved in 50 ml of distilled water with constant mechanical stirring and then heated until the water was almost completely removed and the autoignition process began, during which solid and gaseous reaction products were formed. The weighed portions were taken taking into account the reaction of the formation of the final product ($x = 0, 0.2, \dots, 1.0$):



During the second stage of the synthesis, the powders thus obtained were mechanically ground in a mortar and thermally treated aerobically at 750 °C for 6 hours.

The phase composition of the synthesized samples was studied by powder X-ray diffractometry (PXRD) using $CuK\alpha$ radiation ($\lambda = 0.15406$ nm) on a RigakuSmartLab 3 X-ray diffractometer. The obtained diffractograms were processed in the RigakuSmartLab Studio II software package and using the ICDD PDF 2 powder database. The average crystallite size was calculated using the Scherrer formula, and the crystallite size distribution was constructed using the method of fundamental parameters. The unit cell parameters were determined using the Rietveld method. A Shimadzu IRTracer-100 FT-IR spectrometer was used to obtain infrared spectra (FT-IR) in the wavenumbers ranging from 400 to 1600 cm^{-1} . The morphology and elemental analysis of the synthesized powders were determined by scanning electron microscopy (SEM) and energy dispersive analysis (EDX) using a Tescan Vega 3 SBH electron microscope equipped with an Oxford INCA x-act X-ray spectral microanalysis attachment. Magnetic hysteresis loops were obtained using a LakeShore 7410 vibrating magnetometer in an external magnetic field ranging from –4000 to 4000 Oe.

3. Results and discussion

Diffraction patterns of the synthesized samples of zinc-manganese ferrites of the composition $Zn_{1-x}Mn_xFe_2O_4$ ($x = 0, 0.2, \dots, 1.0$) are shown in Fig. 1. The data obtained indicate that all the obtained powders contain one phase – ferrite of the corresponding composition.

Large values of the line width of the diffraction maxima indicate the nanoscale nature of the obtained crystallites. Refinement of the diffraction patterns performed by the Rietveld method indicates that all samples correspond to the space group $Fd3m$ and contain up to 95 – 97 % of the crystalline phase and from 3 to 5 % of the amorphous phase. With a change in the number of Mn^{2+} cations in the lattice, the diffraction peaks shift, which is clearly shown in Fig. 1b. In the crystallographic direction (111) using the method of fundamental parameters, the size distribution of crystallites was calculated (Fig. 2), which indicates that a narrow distribution is observed in all samples, which is virtually identical in appearance. It is characteristic that the narrowest is the distribution for simple zinc ferrite, while the synthesized $MnFe_2O_4$ nanopowder has a somewhat wider distribution. This may be due to the peculiarities of the

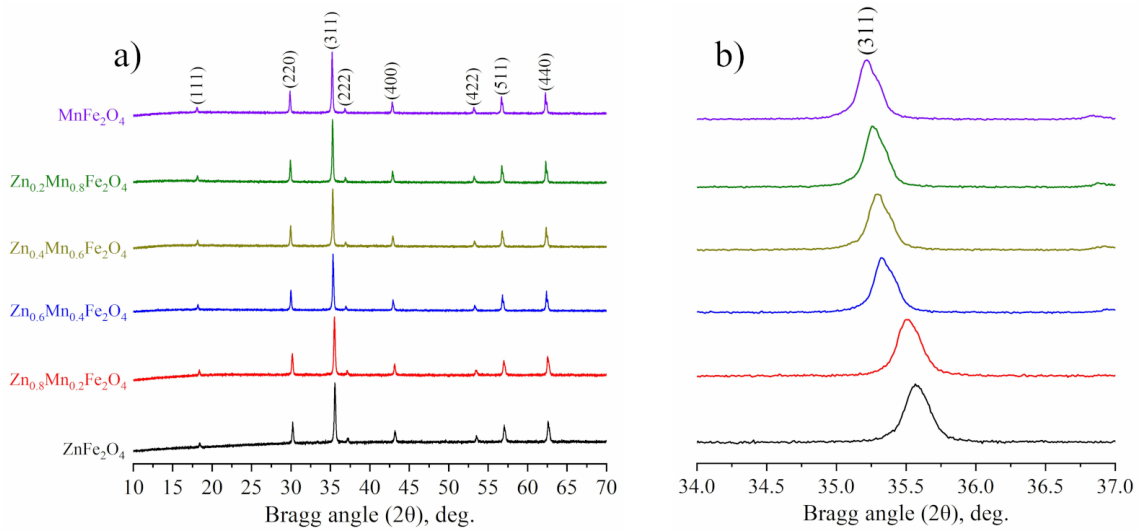


FIG. 1. Survey (a) and local (b) PXRD patterns of the synthesized $Zn_xMn_{1-x}Fe_2O_4$ nanopowders

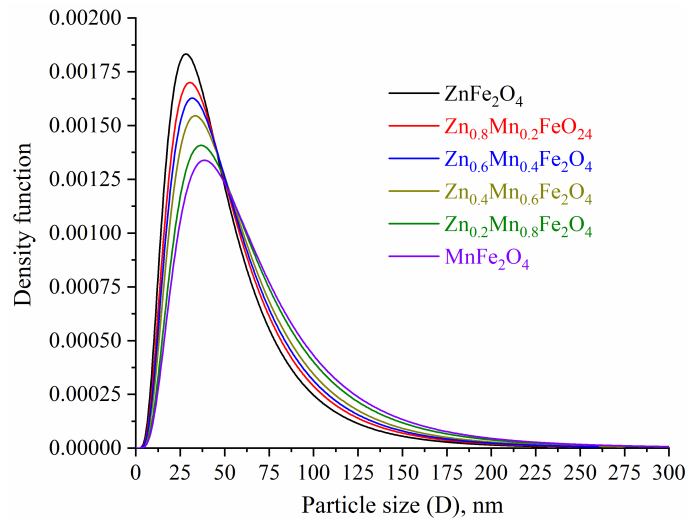


FIG. 2. Lognormal size distribution of the synthesized Zn–Mn ferrite nanocrystals

processes of ferrite formation under conditions of solution combustion and a change in temperature in the combustion front, depending on the chemical composition of the reaction medium [28].

The obtained data for the size distribution of crystallites are in good agreement with the calculations for the average crystallite size according to the Scherrer formula (Fig. 3). It was shown that, in the case of $ZnFe_2O_4$, crystallites with the smallest size (~ 29.4 nm) are formed, while in the case of manganese ferrite, the average crystallite size is somewhat larger and equal to 36.8 nm. It is noteworthy that with a change in the fraction of manganese cations in a multicomponent ferrite, the average crystallite size changes monotonically from larger ($MnFe_2O_4$) to smaller ($ZnFe_2O_4$). This indirectly confirms the effect on the crystallite size of the composition of the initial reaction medium and, as a consequence, the conditions of the combustion reaction.

In addition, using the Rietveld method, the unit cell parameters were calculated, the results of which are shown in Fig. 3b. The data obtained indicate that with an increase in the dopant, Mn^{2+} leads to a decrease in the lattice constant from 8.485(2) for $ZnFe_2O_4$ to 8.451(2) for $MnFe_2O_4$. This is because Mn^{2+} cations have a larger ionic radius (0.082 nm) compared to Zn^{2+} cations (0.074 nm). Separately, it should be noted that in mixed Zn–Mn ferrite, manganese cations are usually randomly distributed at tetrahedral positions (A) and octahedral positions (B), while zinc cations are usually located only in tetrahedral regions (A) [29]. This explains why, in the case of zinc ferrite and

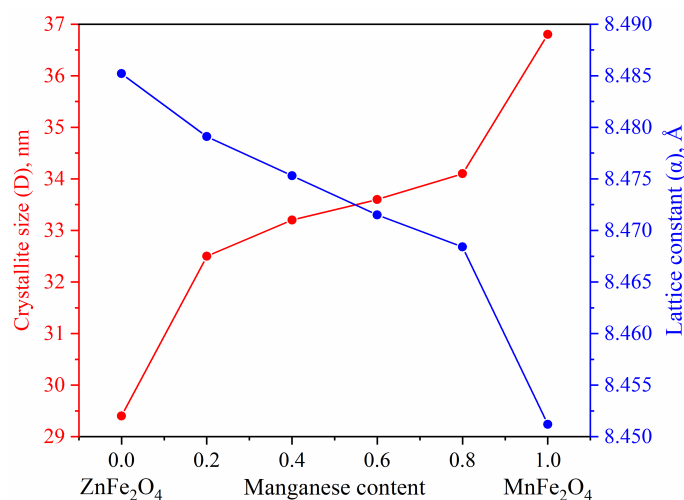


FIG. 3. Average crystallite sizes and lattice constants depending on the Mn content in Zn–Mn ferrites

mixed Zn–Mn ferrite, the change in the lattice constant proceeds linearly, while between the $Zn_{0.2}Mn_{0.8}Fe_2O_4$ and $MnFe_2O_4$ samples there is a significant change in the parameter α .

The FT-IR spectra of all synthesized samples (Fig. 4) show only two main absorption bands in the range of $605 - 404 \text{ cm}^{-1}$. The absence of bending and stretching vibrations related to O–H, C=O bonds, etc., indirectly indicated the complete formation of Zn–Mn ferrites at a temperature of $750 \text{ }^\circ\text{C}$. The set of absorption bands in the range from 568 to 605 cm^{-1} referred to the stretching vibrations of oxygen in the M–O–Fe (M–Zn, Mn) and Fe–O–Fe systems [30].

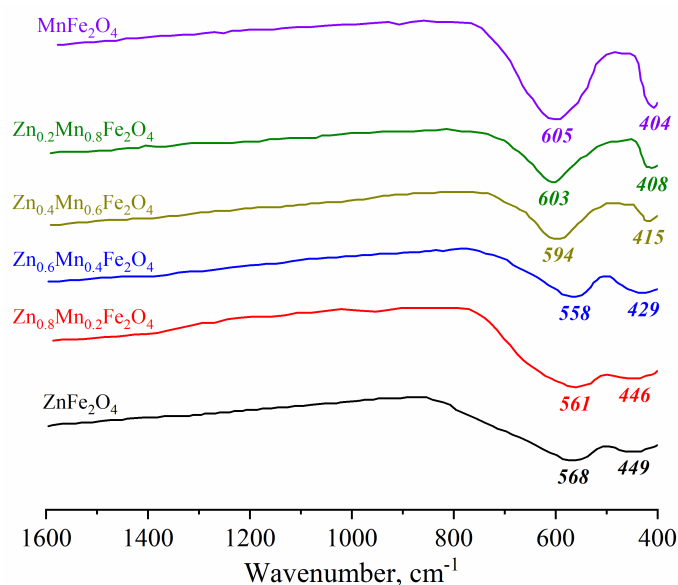


FIG. 4. FT-IR spectra of the obtained $Zn_{1-x}Mn_xFe_2O_4$ ferrites

In turn, absorption bands from 404 to 449 cm^{-1} indicated the presence of bending O–Fe–O vibrations in the synthesized samples [31]. The described two types of vibrations are characteristic of spinel ferrites and their presence in the resulting powders confirmed the successful formation of zinc-manganese ferrites. It should be noted separately that, depending on the composition, there is a slight shift of the absorption bands. As in the case of the diffraction results, this is due to a change in the fraction of manganese cations in the crystal lattice.

Figure 5 shows the results of studying the morphology of synthesized samples of zinc-manganese ferrites of various compositions. The results obtained indicate that simple zinc and manganese ferrites have a typical morphology of solid solution combustion products, which is characteristic of spinel ferrites synthesized by this technique. The most remarkable are samples of mixed Zn–Mn ferrites in which nanoparticles are collected in submicron agglomerates lying

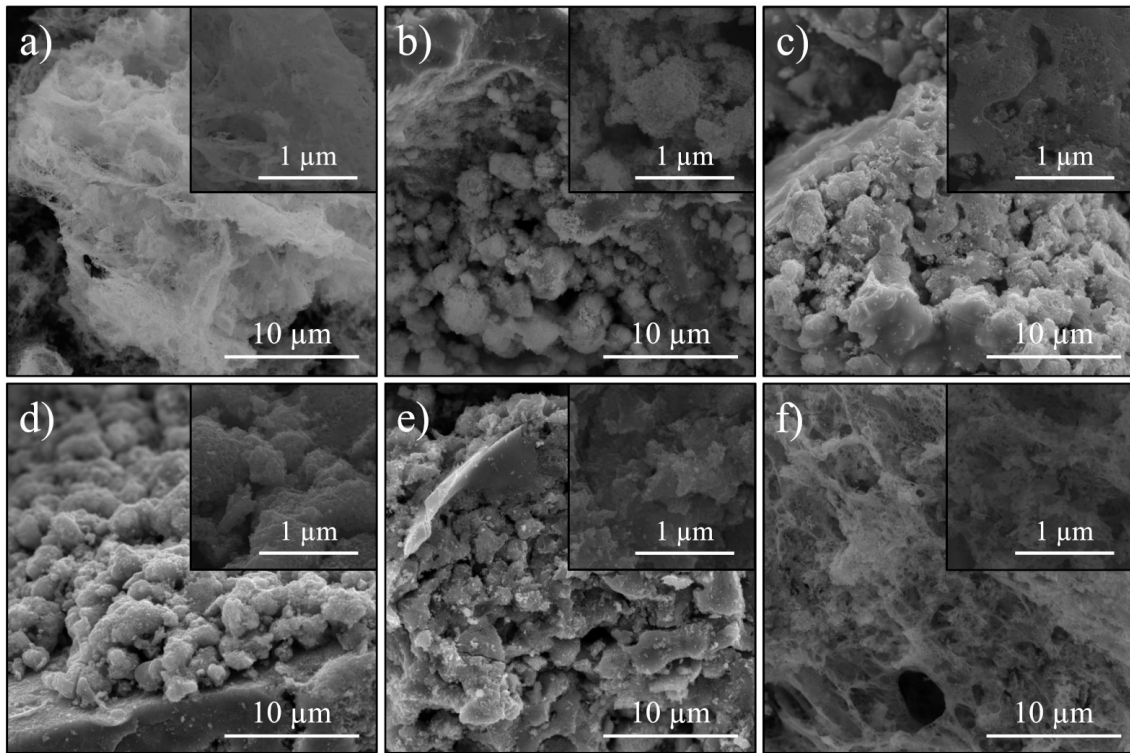


FIG. 5. SEM images of the Zn–Mn ferrite powders synthesized via heat treatment of amorphous combustion products

on the surface of larger irregularly shaped agglomerations several tens of microns in size. In the insets in Fig. 5(b, c and d), you can see the effects of the thermal treatment process, during which the particles are sintered together. According to the elemental analysis data, all synthesized compositions corresponded in their experimental composition to the calculated composition within the experimental error of the determination method.

Magnetic M–H loops of the obtained powders were constructed using a vibration magnetometer and are shown in Fig. 6. According to the presented data, the content of manganese cations significantly changes the magnetic behavior of multicomponent zinc ferrite nanopowders. It is easy to see that the change in the hysteresis loops is linear and their appearance changes significantly in the series $\text{ZnFe}_2\text{O}_4\text{--Zn}_{1-x}\text{Mn}_x\text{Fe}_2\text{O}_4\text{--MnFe}_2\text{O}_4$. As mentioned above, this is due to both the peculiarities of the magnetic behavior of simple zinc and manganese ferrites (which are normal spinels) and mixed Zn–Mn ferrites and the peculiarities of the distribution of Zn^{2+} and Mn^{2+} cations in their lattice.

The largest values of the main magnetic parameters (remanent magnetization, saturation magnetization, and coercive force) were observed in the case of simple zinc ferrite and were 4.9 emu/g, 22/4 emu/g, and 47.5 Oe, respectively (Fig. 7). On the contrary, MnFe_2O_4 nanoparticles exhibited the most pronounced magnetic characteristics ($M_r = 12.3$ emu/g, $M_s = 76.4$ emu/g, $H_c = 81.3$ Oe). The data obtained indicated that an increase in the proportion of manganese cations was accompanied by a linear increase in magnetic characteristics. This is due to the structural features of the obtained powders. It is known that spinel ferrites have three types of magnetic interaction: between metal cations located at tetrahedral positions (A–A), between metal cations located at octahedral positions (B–B), and between metal cations located in both of these regions (A–B). With an increase in the proportion of manganese in spinel, it replaces the Fe^{3+} cations at octahedral and tetrahedral positions, thereby changing the nature of the magnetic behavior of mixed ferrites.

4. Conclusion

Thus, in this work, for the first time, an original method was proposed for obtaining nanoparticles of multicomponent zinc-manganese ferrites of the composition $\text{Zn}_{1-x}\text{Mn}_x\text{Fe}_2\text{O}_4$ ($x = 0, 0.2, \dots, 1.0$) by thermal treatment of X-ray amorphous combustion products. The use of this technique made it possible to obtain nanoparticles in sizes ranging from 29.4 to 36.8 nm with high values of remanent magnetization ($M_r = 4.9 - 12.3$ emu/g), saturation

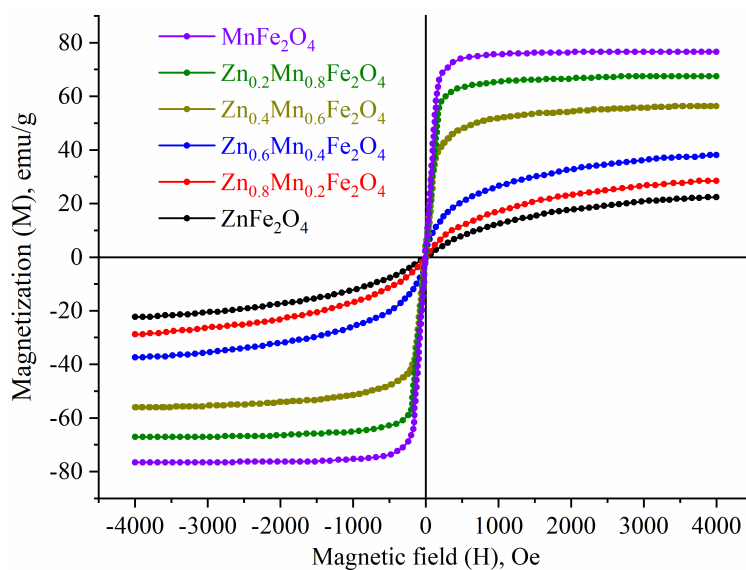


FIG. 6. M–H loops of Mn–Zn ferrite nanopowders at a room temperature

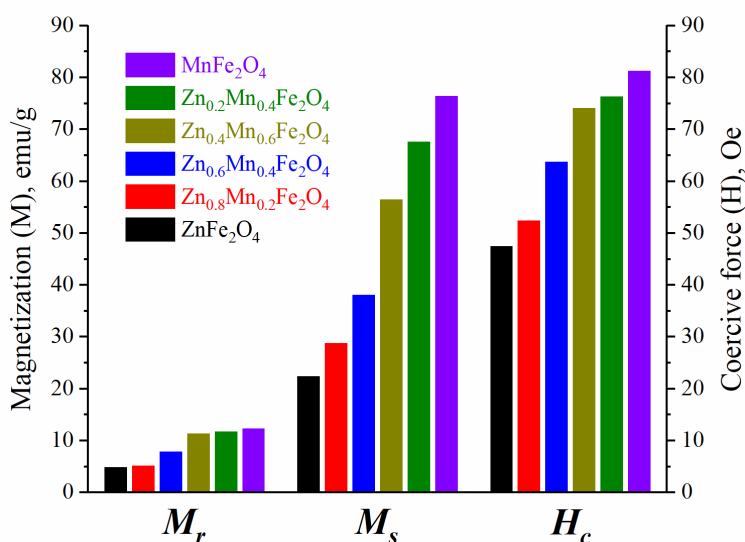


FIG. 7. The main magnetic parameters of the obtained zinc-manganese ferrites of various compositions

magnetization ($M_s = 22.4 - 76.4$ emu/g) and coercive force ($H_c = 47.5 - 81.3$ Oe). The absence of extraneous impurity phases suggests that this synthesis method is promising for obtaining pure multicomponent ferrites of various compositions and linearly tunable magnetic characteristics.

Acknowledgements

The reported study was funded by RFBR, project number 20-03-00976.

References

- [1] Narang S.B., Pubby K. Nickel spinel ferrites: a review. *Journal of Magnetism and Magnetic Materials*, 2021, **519**, 167163.
- [2] Varshney D., Verma K., Kumar A. Structural and vibrational properties of $Zn_xMn_{1-x}Fe_2O_4$ ($x = 0.0, 0.25, 0.50, 0.75, 1.0$) mixed ferrites. *Materials Chemistry and Physics*, 2011, **131**, P. 413-419.
- [3] Martinson K.D., Ivanov A.A., Panteleev I.B., Popkov V.I. Effect of sintering temperature on the synthesis of LiZnMnFe microwave ceramics with controllable electro/magnetic properties. *Ceramics International*, 2021, **47**, P. 30071–30081.
- [4] Hwang J., Choi M., et al. Structural and magnetic properties of NiZn ferrite nanoparticles synthesized by a thermal decomposition method. *Applied Sciences*, 2020, **10**, 6279.

- [5] Msomi J.Z., Nhlapo T.A., et al. Grain size effects on the magnetic properties of $Zn_xMn_{1-x}Fe_2O_4$ nanoferrites. *Journal of Magnetism and Magnetic Materials*, 2015, **373**, P. 74–77.
- [6] Azouaoui A., Haoua M.E., et al. Structural and magnetic properties of Co–Zn ferrites: density functional theory calculations and high-temperature series expansions. *Computational Condensed Matter*, 2020, **23**, 00454.
- [7] Praveena K., Sadhana K., Bharadwaj S., Murthy S.R. Development of nanocrystalline Mn–Zn ferrites for high frequency transformer applications. *J. of Magnetism and Magnetic Materials*, 2009, **321**, P. 2433–2437.
- [8] Dyachenko S.V., Vasishenkov M.A., et al. Synthesis and properties of magnetic fluids produced on the basis of magnetite particles. *Russian J. of Applied Chemistry*, 2016, **89**, P. 690–696.
- [9] Nandwana V., Zhou R., et al. Exchange coupling in soft magnetic nanostructures and its direct effect on their theranostic properties. *ACS Applied Materials & Interfaces*, 2018, **10**, P. 27233–27243.
- [10] Cojocariu A.M., Doaga A., et al. Synthesis and functionalization of magnetic nanoparticles with possible application in drug delivery systems. *Digest J. of Nanomaterials and Biostructures*, 2013, **8**, P. 519–527.
- [11] Tikhanova S.M., Lebedev L.A., et al. The synthesis of novel heterojunction h-YbFeO₃/o-YbFeO₃ photocatalyst with enhanced Fenton-like activity under visible-light. *New J. of Chemistry*, 2021, **45**, P. 1541–1550.
- [12] Kefeni K.K., Mamba B.B., Msagati T.A.M. Application of spinel ferrite nanoparticles in water and wastewater treatment: a review. *Separation and Purification Technology*, 2017, **188**, P. 399–422.
- [13] Haghniaz R., Rabbani A., et al. Anti-bacterial and wound healing-promoting effects of zinc ferrite nanoparticles. *J. of Nanobiotechnology*, 2021, **19**, 38.
- [14] Martinson K.D., Pantelev I.B., Shevchik A.P., Popkov V.I. Effect on the Red/Ox ratio on the structure and magnetic behavior of $Li_{0.5}Fe_{2.5}O_4$ nanocrystals synthesized by solution combustion approach. *Letters on Materials*, 2019, **9**, P. 475–479.
- [15] Hu X., Guan P., Yan X. Hydrothermal synthesis of nano-meter microporous zinc ferrite. *China Particuology*, 2004, **2**, P. 135–137.
- [16] Mello L.B., Varanda L.C., Sigoli F.A., Mazali I.O. Co-precipitation synthesis of (Zn–Mn)-co-doped magnetite nanoparticles and their application in magnetic hyperthermia. *J. of Alloys and Compounds*, 2019, **779**, P. 698–705.
- [17] Martinson K.D., Ivanov V.A., et al. Facile combustion synthesis of $TbFeO_3$ nanocrystals with hexagonal and orthorhombic structure. *Nanosystems: Physics, Chemistry, Mathematics*, 2019, **10**, P. 694–700.
- [18] Waqas H., Qureshi A.H. Influence of pH on nanosized Mn–Zn ferrite synthesized by sol-gel auto combustion process. *J. of Thermal Analysis and Calorimetry*, 2009, **98**, 355.
- [19] Tugova E., Yastrebov S., Karpov O., Smith R., $NdFeO_3$ nanocrystals under glycine nitrate combustion formation. *J. of Crystal Growth*, 2017, **467**, P. 88–92.
- [20] Martinson K.D., Kozyritskaya S.S., Pantelev I.B., Popkov V.I. Low coercivity microwave ceramics based on $LiZnMn$ ferrite synthesized via glycine-nitrate combustion. *Nanosystems: Physics, Chemistry, Mathematics*, 2019, **10**, P. 313–317.
- [21] Varma A., Mukasyan A.S., Rogachev A.S., Manukyan K.V. Solution combustion synthesis of nanoscale materials. *Chemical Reviews*, 2016, **116**, P. 14493–14586.
- [22] Dippong T., Levei E.A., Cadar O. Recent Advances in Synthesis and Applications of MFe_2O_4 (M = Co, Cu, Mn, Ni, Zn) nanoparticles. *Nanomaterials*, 2021, **11**, 1560.
- [23] Novitskaya E., Kelly J.P., Bhaduri S., Graeve O.A. A review of solution combustion synthesis: an analysis of parameters controlling powder characteristics. *International Materials Reviews*, 2018, **66**, P. 188–214.
- [24] Sutka A., Mezinskis G. Sol-gel auto-combustion synthesis of spinel-type ferrite nanomaterials. *Frontiers of Materials Science*, 2012, **6**, P. 128–141.
- [25] Chavarriaga E.A., Lopera A.A., et al. Gel combustion synthesis and magnetic properties of $CoFe_2O_4$, $ZnFe_2O_4$, and $MgFe_2O_4$ using 6-aminohexanoic acid as a new fuel. *J. of Magnetism and Magnetic Materials*, 2020, **497**, 166054.
- [26] Popkov V.I., Martinson K.D., et al. SCS-assisted production of $EuFeO_3$ core-shell nanoparticles: formation process, structural features and magnetic behavior. *J. of Alloys and Compounds*, 2021, **859**, 157812.
- [27] Martinson K.D., Kondrashkova I.S., et al. Magnetically recoverable catalyst based on porous nanocrystalline $HoFeO_3$ for process of n-hexane conversion. *Advanced Powder Technology*, 2020, **31**, P. 402–408.
- [28] Jadhav L.D., Patil S.P., Jamale A.P., Chavan A.U. Solution combustion synthesis: role of oxidant to fuel ratio on powder properties. *Materials Science Forum*, 2013, **757**, P. 85–98.
- [29] Chandra T., Ionescu M., Mantovani D. Structure and magnetic properties of Mn–Zn ferrite synthesized by glycine-nitrate auto-combustion process. *Advanced Materials Research*, 2011, **409**, P. 520–525.
- [30] Albadi A., Ivanova M.S., et al. The influence of co-precipitation technique on the structure, morphology and dual-modal proton relaxivity of $GdFeO_3$ nanoparticles. *Inorganics*, 2021, **9**, 39.
- [31] Sumathi S., Nehru M., Synthesis, characterization, and influence of fuel on dielectric and magnetic properties of cobalt ferrite nanoparticles. *J. of Superconductivity and Novel Magnetism*, 2016, **29**, P. 1317–1323.

Formation of titanium-cobalt nitride $\text{Ti}_{0.7}\text{Co}_{0.3}\text{N}$ under plasma-chemical synthesis conditions in a low-temperature nitrogen plasma

Yu. A. Avdeeva, I. V. Luzhkova, A. N. Ermakov

Institute of Solid State Chemistry, Ural Branch, Russian Academy of Sciences,
Pervomaiskaya Street, 91, Ekaterinburg, 620990, Russia

y-avdeeva@list.ru, key703@yandex.ru, ermakovihim@yandex.ru

PACS 61.46.+w, 61.46.-w, 61.66.Fn

DOI 10.17586/2220-8054-2021-12-5-641-649

Nanocompositions with “core-shell” structure are of interest in different areas of materials science and solid state chemistry, since, along with traditional refractory components in the form of carbides or nitrides and individual metals (Ni, Co), phases of mixed composition of the type $\text{Me}_{1-x}\text{Me}_2_x\text{N}$ (Me1 – a refractory element of IV-VIA subgroup, Me2 – Ni or Co) are formed during synthesis within one highly dispersed particle. It should be noted that such multicomponent phase components are metastable and cannot be obtained in an individual state. At the same time, phases of the $\text{Me}_{1-x}\text{Me}_2_x\text{N}$ type are formed in systems with participation of nitride compounds during extreme processing. In the present work, the technology of plasma-chemical synthesis with subsequent recondensation of gaseous nitrogen in a rotating cylinder was used.

The work is aimed at obtaining metastable complex-substituted titanium-cobalt nitride $\text{Ti}_{0.7}\text{Co}_{0.3}\text{N}$ in the framework of nano- and ultra-dispersed Ti(Mo)C–Co “core-shell” structures. All phase components of the claimed compositions were determined by X-ray diffraction. Additionally, Ti(Mo)C–Co nanoparticles were studied by high-resolution transmission electron microscopy and electron diffraction. It was determined that $\text{Ti}_{0.7}\text{Co}_{0.3}\text{N}$ has a strongly deformed stressed state, as evidenced by a single reflection (101) on the X-ray diffraction pattern. The paper also considers some aspects of crystal chemical design of $\text{Ti}_{0.7}\text{Co}_{0.3}\text{N}$ obtained in the course of structural and morphological certification of the Ti(Mo)C–Co nanocomposition.

Keywords: titanium-cobalt nitride, core-shell structure, plasma recondensation, low temperature plasma, X-ray phase analysis, high-resolution transmission electron microscopy.

Received: 14 October 2021

Revised: 18 October 2021

1. Introduction

Ultra- and nanodispersed materials have attracted much interest in terms of fundamental scientific research and technological applicability of the obtained powder media and samples compacted on their basis [1–5]. Of special interest are nanocrystalline materials obtained using techniques possessing a high productivity, relative simplicity and, what is important, environmental benignness and manufacturability of formation processes, including those in the form of “core-shell” structures [6–10].

One of the first methods for the formation of ultra- and nanodispersed products that meets the above requirements is plasma-chemical synthesis in a low-temperature gas plasma [11]. This technology features a high productivity (from 200 g/h), environmental friendliness and universal segregation procedures aimed at separating powder media in classifiers of the first type (vortex cyclones) and the second type (fabric bag filters). The number of collecting aggregates can be varied depending on the requirements for the final powder products, including distribution into fractions with a narrow particle size distribution. It should be noted that an important issue in the preparation of especially nanocrystalline media with the participation of various metals in the form of surface shells is reduction of the chemical activity and pyrophoricity of “core-shell” structures by different methods. For this purpose, capsulators are used in plasma-chemical installations. Capsulators are aerosol-type devices promoting the coating of active, highly-dispersed particles with vapors of organic compounds with an admixture of highly volatile technical liquids. The ultra- and nanodispersed particles processed in this way are suitable for long-term storage under normal conditions, which is important in the technological process.

In terms of physicochemical laws, plasma-chemical processes in a low-temperature nitrogen plasma are referred to “quasi-equilibrium” processes [12]. Quasi-equilibrium conditions promote the formation of stoichiometric compounds with individual crystallization of metals, regardless of their mutual chemical affinity, despite a substantially high crystallization rate in the quenching chamber of the plasmatron ($\sim 10^5$ °C/s). Under these conditions, ultra- and nanodispersed “core-shell” structures are formed in accordance with the laws set forth in the theory of heterogeneous nucleation by B. Chalmers [13]. In the framework of this theory, some aspects of interaction have been formed, including those between components having no mutual wettability with each other. In these cases, according to [13], during heterogeneous nucleation, crystallization of interlayer phases occurs, which include both elements

representing a refractory core and elements of metal shells. One of the first studies of the crystal-chemical features of complexly substituted hexagonal nitrides based on some elements of IV-VIA subgroups of the Periodic Table are Schonberg's works [14–16], where Ni and Co served as substitute elements in the metal sublattice. Later, nanocrystalline $\text{Ti}_{0.7}\text{Ni}_{0.3}\text{N}$ with a cubic modification was obtained and certified by X-ray diffraction and high-resolution transmission electron microscopy (HRTEM) [17]. In [18], plasma-chemical synthesis of titanium nickelide was carried out according to the plasma recondensation scheme in a low-temperature nitrogen plasma. In the fraction from the filter, a nanocrystalline composition TiN–Ni was recorded and certified, which included a similar nitride $\text{Ti}_{0.7}\text{Ni}_{0.3}\text{N}$. The HRTEM studies showed that the nanocrystalline composition was a “core-shell” structure. The refractory core corresponded to stoichiometric titanium nitride, while the metal shell was cubic modification Ni. Also, the hexagonal phase $\text{Ti}_{0.7}\text{Ni}_{0.3}\text{N}$ was found and certified [14] based on HRTEM studies with the use of profilometric measurements of interplanar distances and Fourier transform method. In particular, according to X-ray and electron microscopy data, titanium-nickel nitride was in a forcedly oriented state along the (101) direction, which is one of the main directions in the crystal structure of the corresponding space group P-6m2. In accordance with [19], the forcedly oriented state of titanium-nickel nitride can be explained by the effect of strong deformations in the process of extreme action during quenching of evaporated components in a rotating cylinder of gaseous nitrogen. Compaction of highly dispersed TiN–Ni powders was carried out under the conditions of liquid-phase vacuum sintering. These experiments showed that the interlayer phase component makes it possible to intensify the sintering processes due to the decomposition of $\text{Ti}_{0.7}\text{Ni}_{0.3}\text{N}$ into the Ti_2Ni intermetallic compound and gaseous nitrogen. The intermetallic phase in the intermediate layer melts at temperatures of 900 – 1100 °C, which intensifies the processes of melting of the metallic nickel shell with simultaneous solid-phase dissolution of the refractory TiN core [20]. Solid-phase dissolution processes proceeded until the solubility products of titanium nitride and metallic nickel were equalized in accordance with Humenik theory of liquid-phase interaction [21].

The aim of this work was to study the structural and morphological features of the $\text{Ti}_{0.7}\text{Co}_{0.3}\text{N}$ phase component, which is present in nanocrystalline Ti(Mo)C–Co compounds of various dispersed compositions depending on the stage of unloading.

2. Materials and methods

Plasma-chemical synthesis in a low-temperature nitrogen plasma taking into account crystallization by plasma recondensation was chosen as the main method for obtaining nanocrystalline materials. The synthesis is based on transferring a mixture of a plasma-forming gas with atomic components of precursor materials to a quenching chamber. The cooler gas in the quenching chamber is in the form of a rotating cylinder, then crystallization of the evaporated components of the initial charge occurs. The rotating cylinder of the coolant gas protects the final products of plasma-chemical synthesis from contamination by elements and compounds that make up the material of the quenching chamber walls. Industrial nitrogen was used as a plasma-forming gas, a cooling gas, and a transport gas. During crystallization, the powder substance is transported by the transport gas to the separating devices. The separating devices represent classifier 1 – a cyclone of vortex type, where the heaviest ultrafine particles settle, and classifier 2 – a bag-type fabric filter, where nanocrystalline fractions of recondensed products of plasma chemical synthesis are collected. The technological parameters of the plasma-chemical installation are shown in Table 1. In the course of the experiment, both single and double recondensations were carried out due to partial sampling of once-processed fractions and subsequent intensive mixing of the fractions from the cyclone and the filter in the dispenser. As the products of extreme synthesis were accumulated and cooled in the separators, the powder fractions were sent to the encapsulation unit. During encapsulation, all the obtained media were chemically treated with organic components to reduce the chemical activity and, accordingly, the pyrophoricity. The finely dispersed powders were encapsulated to provide their long-term storage under normal conditions.

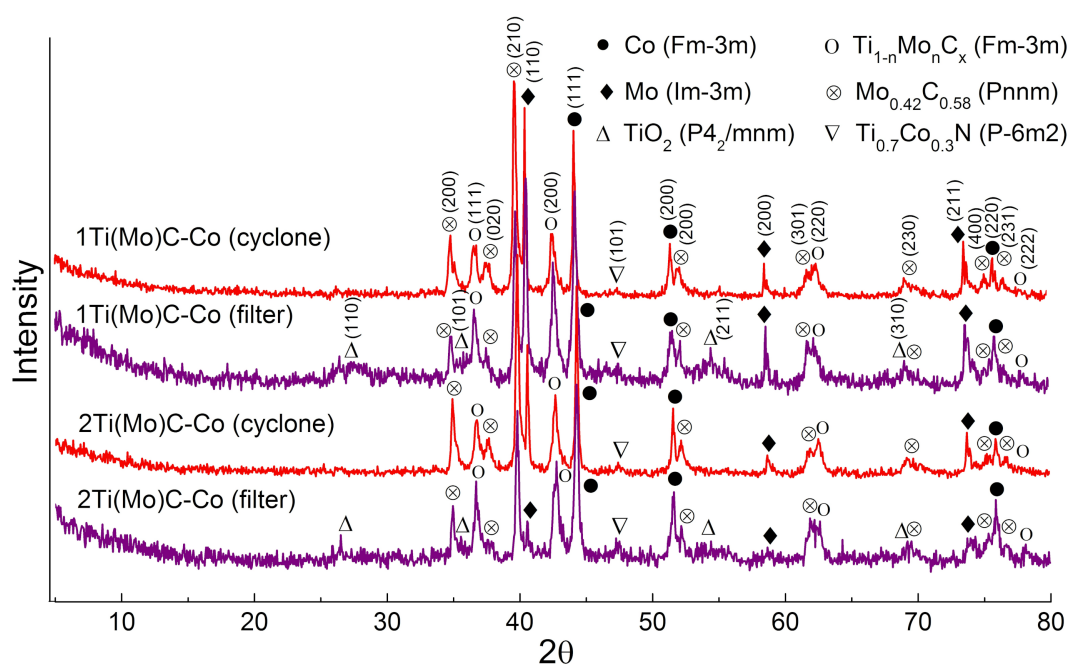
The recondensed ultrafine and nanopowder compositions were studied by X-ray phase analysis (automatic X-ray diffractometer SHIMADZU XRD 7000, $\text{CuK}\alpha$ cathode) and HRTEM (JEOL JED 2100). The obtained research results were processed using the modern software: WinXPOW, PowderCell 2.3 and SP ATOMS for processing X-ray data and constructing octahedral-tetrahedral coordination of the metastable complex nitride $\text{Ti}_{0.7}\text{Co}_{0.3}\text{N}$, as well as the Digital Micrograph 7.0 software package for interpreting atomic planes of various phase components entering into the composition of the nanocrystalline “core-shell” structures Ti(Mo)C–Co.

3. Results and discussion

The results of X-ray diffraction studies of nanocrystalline “core-shell” structures are presented in Fig. 1 and Table 2. Phase analysis and refinement of the unit cell parameters show that titanium-molybdenum carbide $\text{Ti}_{1-n}\text{Mo}_n\text{C}_x$

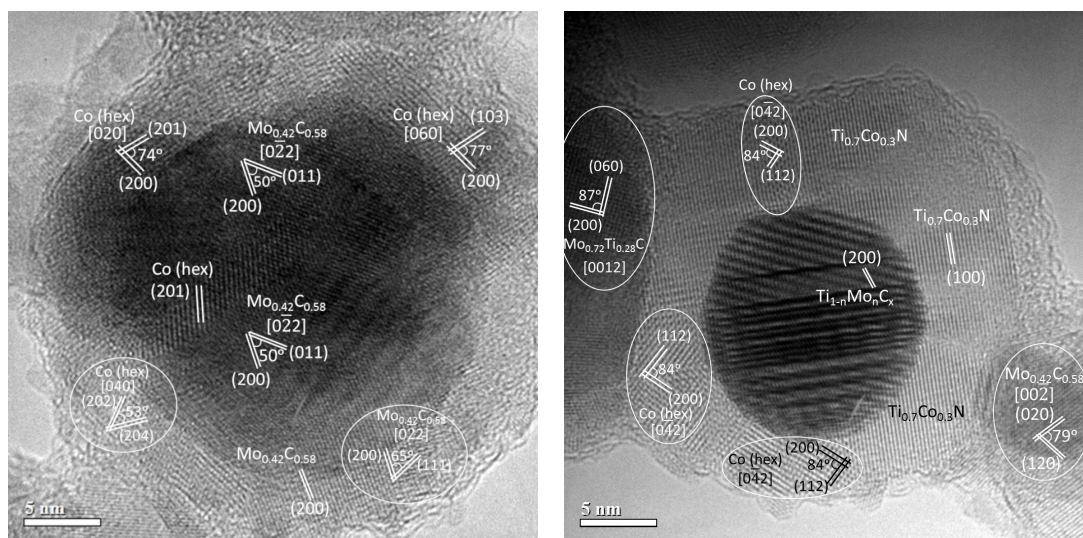
TABLE 1. Technical parameters of the plasma-chemical installation

Consumption of precursor mixture, g/h	200
Power of plasmatron, kW	25
Current strength, A	100 – 110
Voltage, V	200 – 220
Plasma flow velocity, m/s	60 – 100
Total nitrogen consumption in the plasma reactor, nm^3/h	25 – 30
Of the total nitrogen consumption for plasma formation, nm^3/h	6
Of the total nitrogen consumption for stabilization and quenching, nm^3/h	19 – 16

FIG. 1. X-ray diffraction patterns of $Ti(Mo)C-Co$ recondensed fractions in $5 - 80^\circ$

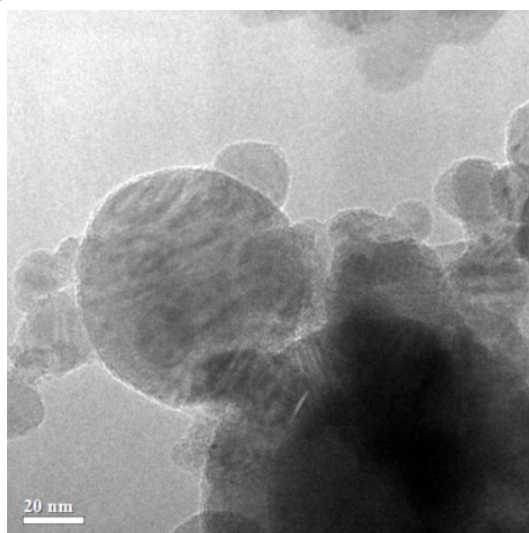
of the cubic modification, metallic Mo and its highly defective carbide $Mo_{0.42}C_{0.58}$ of the orthorhombic modification [22], as well as metallic Co of the cubic modification are formed in the process of plasma recondensation. The crystal chemical model of $Mo_{0.42}C_{0.58}$ is shown in Fig. 3a. A separate item is the phase formation of hexagonal (space group P-6m2) titanium-cobalt nitride $Ti_{0.7}Co_{0.3}N$, the standard crystallographic data of which are given in Table 2. The X-ray diffraction patterns of this phase have a single, considerably broadened reflection (101), which, in accordance with [19], is associated with a strongly deformed state caused by the extreme character of plasma recondensation. At the same time, the presence of a “core-shell” structure was proved using HRTEM by the example of singly recondensed particles of $Ti(Mo)C-Co$ fraction from the filter (Fig. 2a,b). Refractory titanium-molybdenum carbide $Ti_{1-n}Mo_nC_x$ acts as a core, and the shell, according to profilometric measurements and interpretation of the fast Fourier transform, contains metallic Mo, its highly defective carbide $Mo_{0.42}C_{0.58}$, hexagonal and cubic cobalt (Fig. 2b).

The presence of titanium-cobalt nitride $Ti_{0.7}Co_{0.3}N$, the crystal-chemical model of which is shown in Fig. 3b, in the form of a family of planes (101), (011), (100) in the framework of HRTEM was recorded by profilometry, fast Fourier transform, and electron diffraction methods (Fig. 2). In particular, the study of various image areas (Fig. 2b) reveals that titanium-cobalt nitride $Ti_{0.7}Co_{0.3}N$ almost completely covers the entire “core-shell” structure, including

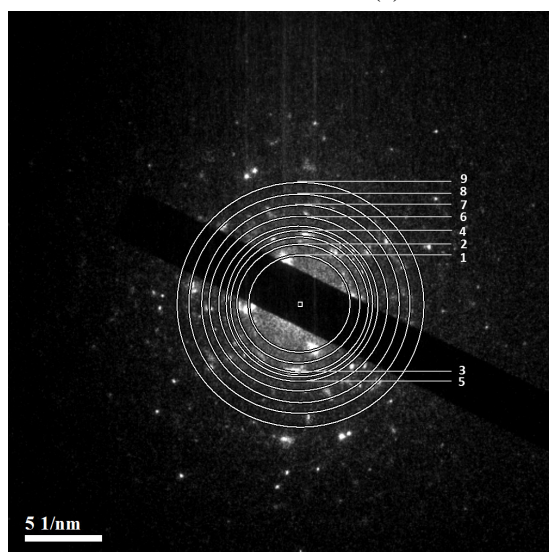


(a)

(b)



(c)



1. (011) $Ti_{0.7}Co_{0.3}N$
2. (100) $Ti_{0.7}Co_{0.3}N$
3. (111) $Mo_{0.42}C_{0.58}$
4. (200) $Ti_{1-n}Mo_nC_x$
5. (101) $Ti_{0.7}Co_{0.3}N$
6. (220) $Mo_{0.42}C_{0.58}$
7. (200) Mo
8. (311) $Mo_{0.42}C_{0.58}$
9. (220) Co

(d)

FIG. 2. HRTEM images of particles with “core-shell” structure (a,b), polycrystalline electron diffraction pattern (d) of the Ti(Mo)C–Co fraction from the filter (c)

TABLE 2. The results of X-ray phase analysis of recondensed fractions of Ti(Mo)C–Co

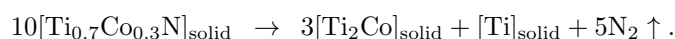
No.	Fraction	Phase composition, (± 2 wt. %), a , b , c , (± 0.001 Å)	ρ , g/cm ³	S_{sp} , m ² /g
1	1Ti(Mo)C–Co (cyclone)	Co (Fm-3m), (13 %), $a = 3.5514$; Ti _{1-n} Mo _n C _x (Fm-3m), (37 %), $a = 4.2459$; Mo (Im-3m), (6 %), $a = 3.1527$; Mo _{0.42} C _{0.58} (Pnnm), (44 %), $a = 5.1535$, $b = 4.8235$, $c = 2.9723$	5.3092	1.5243
2	1Ti(Mo)C–Co (filter)	Co (Fm-3m), (25 %), $a = 3.5494$; Ti _{1-n} Mo _n C _x (Fm-3m), (40 %), $a = 4.2408$; Mo (Im-3m), (2 %), $a = 3.1503$; Mo _{0.42} C _{0.58} (Pnnm), (22 %), $a = 5.1448$, $b = 4.8235$, $c = 2.9702$; TiO ₂ (P42/mnm), (11 %), $a = 4.748$, $c = 2.9349$	4.8778	8.8812
3	2Ti(Mo)C–Co (cyclone)	Co (Fm-3m), (17 %), $a = 3.5398$; Ti _{1-n} Mo _n C _x (Fm-3m), (33 %), $a = 4.2326$; Mo (Im-3m), (5 %), $a = 3.1422$; Mo _{0.42} C _{0.58} (Pnnm), (45 %), $a = 5.1302$, $b = 4.7952$, $c = 2.9638$	5.2619	1.8885
4	2Ti(Mo)C–Co (filter)	Co (Fm-3m), (26 %), $a = 3.5480$; Ti _{1-n} Mo _n C _x (Fm-3m), (45 %), $a = 4.2375$; Mo (Im-3m), (1 %), $a = 3.1474$; Mo _{0.42} C _{0.58} (Pnnm), (26 %), $a = 5.1413$, $b = 4.7960$, $c = 2.9719$; TiO ₂ (P42/mnm), (2 %), $a = 4.7635$, $c = 2.9219$	4.6690	10.9226

the refractory core of titanium-molybdenum carbide Ti_{1-n}Mo_nC_x. This illustration further confirms the layer-by-layer formation of phase components, including metastable compounds of highly defective molybdenum carbide and titanium-cobalt nitride.

Based on the results of experimental studies and previously published findings [18], it can be noted that the formation of metastable nitrides with a hexagonal crystal structure, which is complexly substituted in the metal sublattice, one of which is Ti_{0.7}Co_{0.3}N, takes place during high-speed crystallization with an excessive amount of cooling gas (N₂). In terms of colloidal-chemical regularities, in the process of crystallization of nanocrystalline “core-shell” TiN–Co structures, it is necessary to take into account the absence of mutual wettability effects between complete titanium nitride and metals of the iron subgroup under equilibrium conditions created by vacuum heating. At the same time, it is well known that titanium nitrides TiN_{1-x} in a highly defective state have prerequisites for certain conditions of wettability [23]. One of these formula compositions is TiN_{0.7}, which follows from the conditions of the presence of a wide homogeneity region in the Ti–N phase diagram.

The presence of complex titanium-cobalt nitride is also confirmed in the studies of ultra- and nanodispersed “core-shell” structures by DTA and TGA analysis in a protective argon atmosphere. In prior studies [20], a diffuse exothermic effect is observed at temperatures ranging from 500 – 550 °C, corresponding, according to X-ray phase analysis data, to the decomposition of Ti_{0.7}Ni_{0.3}N.

In the present work, the “core-shell” structures based on titanium carbides and nitrides with molybdenum and cobalt have been investigated by DTA and TGA methods under similar conditions under a protective argon atmosphere. Strongly diffuse exothermic effects were recorded, which correspond to the decomposition of the Ti_{0.7}Co_{0.3}N phase according to the equation:



The decomposition occurs at temperatures of 380 – 450 °C in all the obtained fractions of Ti(Mo)C–Co and TiN–Mo–Co, which is shown in Fig. 4.

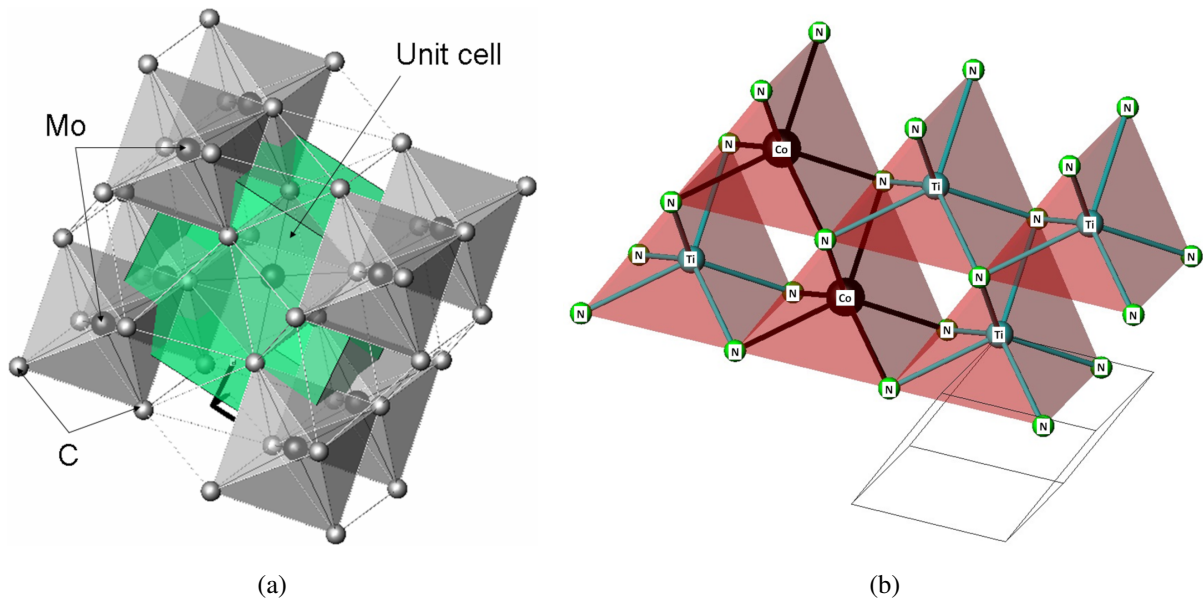


FIG. 3. Crystal-chemical model of orthorhombic $\text{Mo}_{0.42}\text{C}_{0.58}$ (a) and model of prismatic coordination of titanium-cobalt nitride $\text{Ti}_{0.7}\text{Co}_{0.3}\text{N}$ with reduced unit cell (b)

The complex nitride $\text{Mo}_{0.8}\text{Co}_{0.2}\text{N}_{0.9}$ obtained in [14] was not detected under the formation conditions for $\text{Ti}(\text{Mo})\text{C}-\text{Co}$ and $\text{TiN}-\text{Mo}-\text{Co}$ “core-shell” structures. The absence of compounds based on molybdenum nitride can be substantiated by the data of the $-\Delta G_f(T)$ dependence (Fig. 5) for similar nitrides TiN and MoN [24]. As seen from the graphs, the formation of compounds based on molybdenum nitride is virtually impossible due to the proximity of its values to 0.

At the end of the work, the results obtained can be compared with those described in prior literature. Table 3 shows the theoretical and experimental data for the similar metastable $\text{Ti}_{0.7}\text{Ni}_{0.3}\text{N}$ phase of various modifications [17]. Brief information on the complex titanium-cobalt nitride $\text{Ti}_{0.7}\text{Co}_{0.3}\text{N}$ obtained by plasma-chemical synthesis in a low-temperature nitrogen plasma with subsequent recondensation of gaseous nitrogen in a rotating cylinder is also presented.

4. Conclusion

In this work, nano- and ultradispersed $\text{Ti}(\text{Mo})\text{C}-\text{Co}$ compositions were obtained in the process of plasma recondensation in a low-temperature nitrogen plasma. In the course of HRTEM studies, the “core-shell” structure of $\text{Ti}(\text{Mo})\text{C}-\text{Co}$ nanoparticles was determined. In the composition of this structure, the $\text{Ti}_{0.7}\text{Co}_{0.3}\text{N}$ phase (space group P-6m2) of the hexagonal modification was determined with the use of X-ray diffraction and electron diffraction, which cannot be obtained in individual form. It was found that $\text{Ti}_{0.7}\text{Co}_{0.3}\text{N}$ is present as an interfacial layer between the refractory phase of cubic $\text{Ti}_{1-n}\text{Mo}_n\text{C}_x$ and metallic cobalt. The highly defective state of $\text{Ti}_{0.7}\text{Co}_{0.3}\text{N}$ is confirmed by the redistribution of line intensities and the presence of one reflection (101) in the X-ray diffraction patterns.

Nanocrystalline powders can be used as insoluble casting modifiers when pouring steels into molds coated with nanocrystalline powder. In this case, the dissolution of the cobalt shell with simultaneous preservation of the refractory core is allowed on contact of the molten metal with the nanoparticles. The core serves as a crystallization center, which can improve the strength and plastic characteristics of steel.

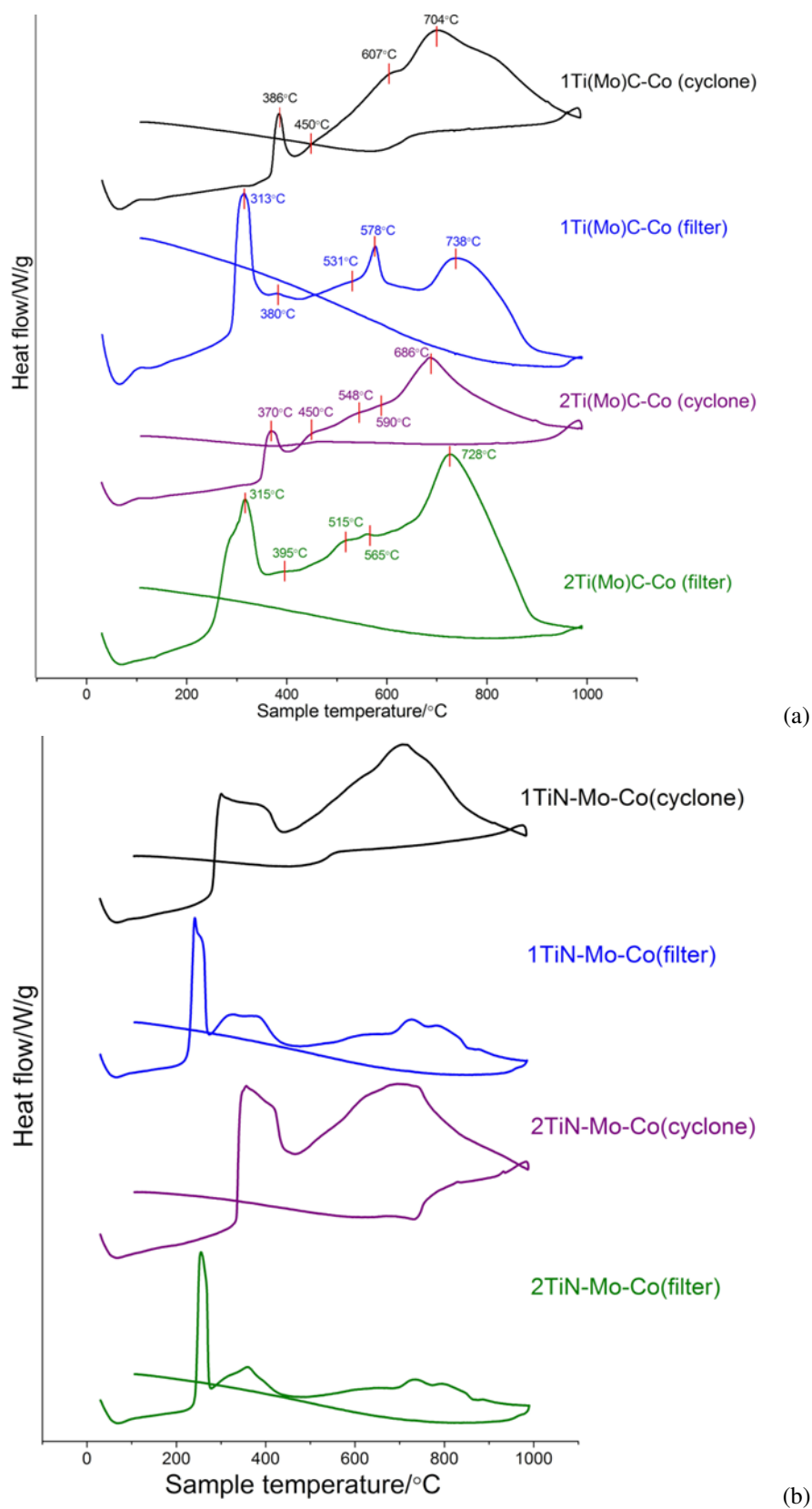


FIG. 4. DTA study of Ti(Mo)C-Co (a) and TiN-Mo-Co (b) fractions

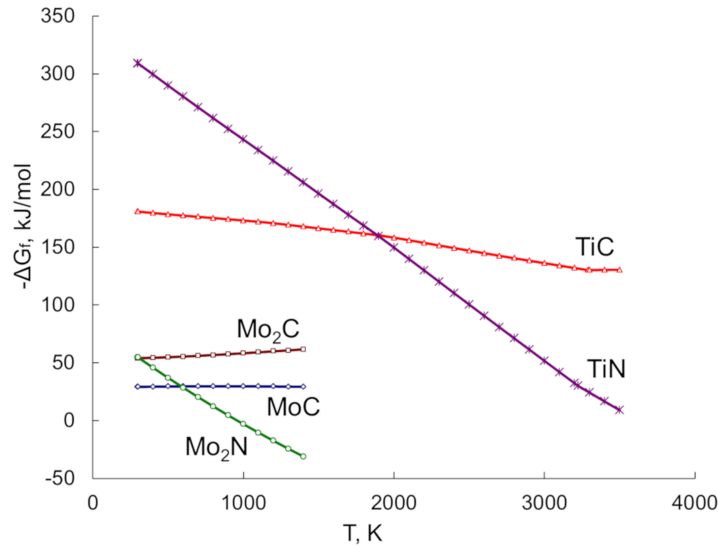


FIG. 5. Dependences $-\Delta G_f(T)$ for Mo_2N , MoC , Mo_2C , TiN and TiC compounds

TABLE 3. Information on the preparation and study of complex nitrides of the type $\text{Me}_1_{1-n}\text{Me}_2_n\text{N}_x$, where Me_1 – Ti, Mo, ... ; Me_2 – Ni, Co; $n \leq 1$

No.	Research performed	Literature source
1	For the first time, a number of complex nitrides $\text{Ti}_{0.7}\text{Co}_{0.3}\text{N}$, $\text{Ti}_{0.7}\text{Ni}_{0.3}\text{N}$, $\text{Mo}_{0.8}\text{Co}_{0.8}\text{N}_{0.9}$, $\text{Mo}_{0.8}\text{Ni}_{0.8}\text{N}_{0.9}$ were obtained and crystallographically certified.	[14]
2	Nanocrystalline $\text{Ti}_{0.7}\text{Ni}_{0.3}\text{N}$ with a cubic lattice was obtained by mechanochemical synthesis in an atmosphere of gaseous nitrogen. The nitride was certified by X-ray and transmission electron microscopy methods.	[17]
3	TiN-Ni powders were obtained by plasma-chemical synthesis in a low-temperature nitrogen plasma followed by recondensation in rotating nitrogen gas. Under conditions of liquid-phase vacuum sintering of nanocrystalline TiN-Ni powders, the role of $\text{Ti}_{0.7}\text{Ni}_{0.3}\text{N}$ was determined. According to additional DTA and TGA studies, it was found that $\text{Ti}_{0.7}\text{Ni}_{0.3}\text{N}$ decomposes into Ti_2Ni and gaseous N_2 . In turn, the decomposition reaction promotes a decrease in the sintering temperature of nanocrystalline samples by 300 °C.	[20]
4	High-resolution transmission electron microscopy of a TiN-Ni nanocrystalline sample obtained by plasma-chemical synthesis in a low-temperature nitrogen plasma was carried out. The $\text{Ti}_{0.7}\text{Ni}_{0.3}\text{N}$ phase is certified under the conditions of profilometric studies and fast Fourier transform.	[18]
5	X-ray and electron microscopic studies (HRTEM) under conditions of plasma recondensation of “core-shell” $\text{Ti}(\text{Mo})\text{C-Co}$ structures revealed the presence of titanium-cobalt nitride $\text{Ti}_{0.7}\text{Co}_{0.3}\text{N}$ in the nanocrystalline fraction from the filter.	The present work

Acknowledgements

The work was carried out in accordance with the state assignment for the Institute of Solid State Chemistry of the Ural Branch of the Russian Academy of Sciences (theme No 0397-2019-0003 “New functional materials for promising technologies: synthesis, properties, spectroscopy and computer simulation”).

The authors are grateful to Dr. A. M. Murzakaev, Ph. D., senior researcher of the Laboratory of impulse processes of the Institute of Electrophysics, Ural Branch of the Russian Academy of Sciences, for conducting electron microscopic studies of nanocrystalline Ti(Mo)C–Co compositions under conditions of high-resolution transmission electron microscopy.

References

- [1] Wang D., Bai Y., et al. Optimization of sintering parameters for fabrication of $Al_2O_3/TiN/TiC$ micro-nano-composite ceramic tool material based on microstructure evolution simulation. *Ceramics international*, 2021, **47**, P. 5776–5785.
- [2] Hao J., Li J., Shi W., Wang B., Tan Y. The novel effect mechanism of Al_2O_3 nano-powder in the pack cementation process to prepare SiC coating on C/C composites. *Journal of the European Ceramic Society*, 2021, **41**, P. 1107–1113.
- [3] Moghanlou F.S., Vajdi M., et al. Spark plasma sinterability and thermal diffusivity of TiN ceramics with graphene additive. *Ceramics International*, 2021, **47**, P. 10057–10062.
- [4] Akinribide O.J., Obadele B.A., et al. Sintering of binderless TiN and TiCN-based cermet for toughness applications: Processing techniques and mechanical properties: A review. *Ceramics International*, 2019, **45**, P. 21077–21090.
- [5] Fu Z., Kong J.H., Gajjala S.R., Koc R. Sintering, mechanical, and oxidation properties of TiC-Ni-Mo cermets obtained from ultra-fine TiC powders. *Journal of Alloys and Compounds*, 2018, **751**, P. 316–323.
- [6] Park K., Hirayama Y., et al. Anisotropic Sm–Co nanopowder prepared by induction thermal plasma. *Journal of Alloys and Compounds*, 2021, **882**, 160633.
- [7] Plohl O., Ajdnik U., et al. Superior stability and high biosorbent efficiency of carboxymethylchitosan covalently linked to silica-coated core-shell magnetic nanoparticles for application in copper removal. *Journal of Environmental Chemical Engineering*, 2019, **7**, 102913.
- [8] Coleman D., Mangolini L. Plasmonic core-shell silicon carbide-graphene nanoparticles. *CS Omega*, 2019, **4**, P. 10089–10093.
- [9] Yu J., Yu H., et al. Synthesis and electrochemical activities of TiC/C core-shell nanocrystals. *Journal of Alloys and Compounds*, 2017, **693**, P. 500–509.
- [10] Lang S.-T., Yan Q.-Z., Sun N.-B., Zhang X.-X. Preparation of W–TiC alloys from core–shell structure powders synthesized by an improved wet chemical method. *Rare Metals*, 2018, **6**.
- [11] Storozhenko P.A., Guseinov Sh.L., Malashin S.I. Nanodispersed powders: synthesis methods and practical applications. *Nanotechnologies in Russia*, 2009, **4**, P. 262–274.
- [12] Polak L. Elementary chemical processes and kinetics in a non-equilibrium and quasi-equilibrium plasma. *Pure and Applied Chemistry*, 1974, **39**, P. 307–342.
- [13] Chalmers B. *Principles of solidification*. John Wiley and Sons, Springer, New York, Dordrecht, Heidelberg, London, 1964, 319 p.
- [14] Schönberg N. The tungsten carbide and nickel arsenide structures. *Acta Metallurgica*, 1954, **2**, P. 427–432.
- [15] Schönberg N. Contributions to the knowledge of the molybdenum-nitrogen and the tungsten-nitrogen systems. *Acta Chemica Scandinavica*, 1954, **8**, P. 204–207.
- [16] Schönberg N. An X-ray investigation on ternary phases in the Ta–Me–N systems (Me = Ti, Cr, Mn, Fe, Co, Ni). *Acta Chemica Scandinavica*, 1954, **8**, P. 213–218.
- [17] Bhaskar U.K., Pradhan S.K. Microstructural evolution of nanostructured $Ti_{0.7}Ni_{0.3}N$ prepared by reactive ball-milling. *Materials Research Bulletin*, 2013, **48**, P. 3129–3135.
- [18] Ermakov A.N., Luzhkova I.V., et al. Formation of complex titanium-nickel nitride $Ti_{0.7}Ni_{0.3}N$ in the ‘core-shell’ structure of TiN–Ni. *Int. J. of Refractory Metals and Hard Materials*, 2019, **84**, 104996.
- [19] Fultz B., Howe J.M. *Transmission electron microscopy and diffractometry of materials*, 3rd ed. Springer, Berlin, Heidelberg, 2008, 758 p.
- [20] Ermakov A.N., Misharina I.V., et al. The peculiarities of phase formation in TiN–Ni system after plasma-chemical treatment of titanium nickelide and sintering of the obtained composition. *Materialovedenie*, 2011, **3**, P. 34–38. [in Russian]
- [21] Gumenik M., Waylen T.J. *Cermets*. Ed. by Tinklepaugh J.R., Crandall W.B. Reinhold Publishing Corporation, Chapman and Hall, Ltd., New York, London, 1960, 244 p.
- [22] Schuster J.C., Nowotny H. Molybdän- und molybdän-wolfram-carbide im temperaturbereich von 600 – 1600 °C. *Monatshefte für Chemie*, 1979, **110**, P. 321–332.
- [23] Kosolapova T.Ya. *Handbook of high temperature compounds: properties, production, applications*. CRC Press, New York, Washington, Philadelphia, London, 1990, 958 p.
- [24] Barin I. *Thermochemical Data of Pure Substances*. Third Edition. In collab. with Gregor Platzki. VCH, Weinheim, New York, Base1, Cambridge, Tokyo, 1995, 2003 p.



NANOSYSTEMS:

PHYSICS, CHEMISTRY, MATHEMATICS

INFORMATION FOR AUTHORS

The journal publishes research articles and reviews, and also short scientific papers (letters) which are unpublished and have not been accepted for publication in other magazines. Articles should be submitted in English. All articles are reviewed, then if necessary come back to the author to completion.

The journal is indexed in Web of Science Core Collection (Emerging Sources Citation Index), Chemical Abstract Service of the American Chemical Society, Zentralblatt MATH and in Russian Scientific Citation Index.

Author should submit the following materials:

1. Article file in English, containing article title, the initials and the surname of the authors, Institute (University), postal address, the electronic address, the summary, keywords, MSC or PACS index, article text, the list of references.
2. Files with illustrations, files with tables.
3. The covering letter in English containing the article information (article name, MSC or PACS index, keywords, the summary, the literature) and about all authors (the surname, names, the full name of places of work, the mailing address with the postal code, contact phone number with a city code, the electronic address).
4. The expert judgement on possibility of publication of the article in open press (for authors from Russia).

Authors can submit a paper and the corresponding files to the following addresses: nanojournal.ifmo@gmail.com, popov1955@gmail.com.

Text requirements

Articles should be prepared with using of text editors MS Word or LaTeX (preferable). It is necessary to submit source file (LaTeX) and a pdf copy. In the name of files the English alphabet is used. The recommended size of short communications (letters) is 4-6 pages, research articles– 6-15 pages, reviews – 30 pages.

Recommendations for text in MS Word:

Formulas should be written using Math Type. Figures and tables with captions should be inserted in the text. Additionally, authors present separate files for all figures and Word files of tables.

Recommendations for text in LaTeX:

Please, use standard LaTeX without macros and additional style files. The list of references should be included in the main LaTeX file. Source LaTeX file of the paper with the corresponding pdf file and files of figures should be submitted.

References in the article text are given in square brackets. The list of references should be prepared in accordance with the following samples:

- [1] Surname N. *Book Title*. Nauka Publishing House, Saint Petersburg, 2000, 281 pp.
- [2] Surname N., Surname N. Paper title. *Journal Name*, 2010, 1 (5), P. 17-23.
- [3] Surname N., Surname N. Lecture title. In: Abstracts/Proceedings of the Conference, Place and Date, 2000, P. 17-23.
- [4] Surname N., Surname N. Paper title, 2000, URL: <http://books.ifmo.ru/ntv>.
- [5] Surname N., Surname N. Patent Name. Patent No. 11111, 2010, Bul. No. 33, 5 pp.
- [6] Surname N., Surname N. Thesis Title. Thesis for full doctor degree in math. and physics, Saint Petersburg, 2000, 105 pp.

Requirements to illustrations

Illustrations should be submitted as separate black-and-white files. Formats of files – jpeg, eps, tiff.



NANOSYSTEMS:

PHYSICS, CHEMISTRY, MATHEMATICS

Журнал зарегистрирован

Федеральной службой по надзору в сфере связи, информационных технологий и массовых коммуникаций
(свидетельство ПИ № ФС 77 - 49048 от 22.03.2012 г.)
ISSN 2220-8054

Учредитель: федеральное государственное автономное образовательное учреждение высшего образования

«Санкт-Петербургский национальный исследовательский университет информационных технологий, механики и оптики»

Издатель: федеральное государственное автономное образовательное учреждение высшего образования

«Санкт-Петербургский национальный исследовательский университет информационных технологий, механики и оптики»

Отпечатано в Учреждении «Университетские телекоммуникации»

Адрес: 197101, Санкт-Петербург, Кронверкский пр., 49

Подписка на журнал НФХМ

На первое полугодие 2022 года подписка осуществляется через
ОАО «АРЗИ», подписной индекс Э57385